REPORT DOCUMENTATION PAG

AFRL-SR-BL-TR-98-
0556

1. AGENCY USE ONLY (Leave blank)	2. REPORT DATE	Technical 1 June 1997 - 31 May 1998
	29 July 1998	

4. TITLE AND SUBTITLE
(U) ARO and AFOSR Contractors Meeting in Chemical Propulsion

5. FUNDING NUMBERS
PE - 61102A
61102F

6. AUTHOR(S)
David M. Mann and Julian M. Tishkoff

7. PERFORMING ORGANIZATION NAME(S) AND ADDRESS(ES)

Army Research Office
Research Triangle Park NC 27709-2211

Air Force Office of Scientific Research
Bolling AFB DC 20332-8050

8. PERFORMING ORGANIZATION REPORT NUMBER

9. SPONSORING / MONITORING AGENCY NAME(S) AND ADDRESS(ES)

10. SPONSORING / MONITORING AGENCY REPORT NUMBER

19980803 103

11. SUPPLEMENTARY NOTES

12a. DISTRIBUTION / AVAILABILITY STATEMENT
Approved for public release; distribution is unlimited.

12b. DISTRIBUTION CODE
-

13. ABSTRACT (Maximum 200 Words)

Abstracts are given for research in chemical propulsion supported by the Air Force Office of Scientific Research and the Army Research Office.

14. SUBJECT TERMS
Flames, Propulsion, Gas Turbines, Diesel Engines, Scramjets, Soot, Sprays, Turbulence, Diagnostics

15. NUMBER OF PAGES
199

16. PRICE CODE

17. SECURITY CLASSIFICATION OF REPORT	18. SECURITY CLASSIFICATION OF THIS PAGE	19. SECURITY CLASSIFICATION OF ABSTRACT	20. LIMITATION OF ABSTRACT
Unclassified	Unclassified	Unclassified	UL

AIR FORCE OF SCIENTIFIC RESEARCH (AFSC)
NOTICE OF TRANSMITTAL TO DTIC
This technical report has been reviewed and is
approved for public release IAW AFR 190-12
Distribution is unlimited.
Joan Boggus
STINFO Program Manager

Approved for public release;
distribution unlimited.

ARMY RESEARCH OFFICE
AND
AIR FORCE OFFICE OF SCIENTIFIC RESEARCH

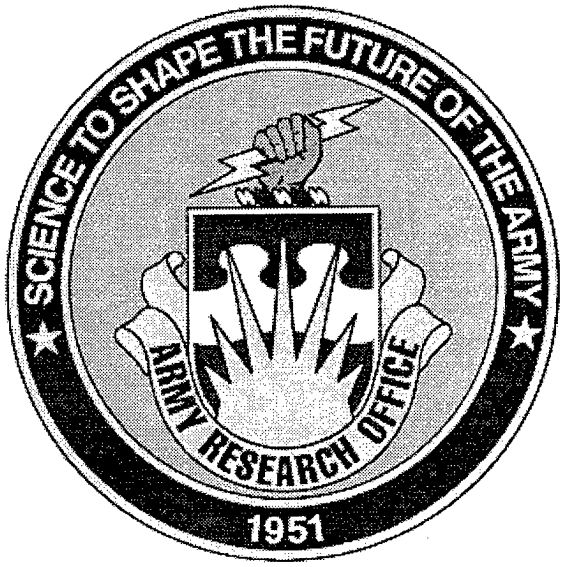

1998

CONTRACTORS' MEETING
IN
CHEMICAL PROPULSION

Air Force Office of Scientific Research
Directorate of Aerospace and Materials Sciences
AFOSR/NA
110 Duncan Avenue, Suite B115
Bolling AFB, DC 20332-8080

Layout & Design by DTI Associates, Inc

ARO/AFSOR Contractors' Meeting in Chemical Propulsion
29 June - 1 July 1998
Long Beach, CA

Table of Contents

ABSTRACTS OF WORK UNITS NOT PRESENTED AT THE MEETING

INVITEES

ARO/AFOSR CONTRACTORS' MEETING

IN

CHEMICAL PROPULSION

Hyatt Regency Hotel
Long Beach, CA
29 June – 1 July 1998

MONDAY, 29 JUNE

12:30 - 12:45 Army Research Office Overview - David Mann

12:45 - 1:00 Air Force Office of Scientific Research Overview - Julian Tishkoff

Session Chairman: Dr. Ernest Schwarz, USA Tank-Automotive Command

Topic: Combustor/Combustion Chamber Design and Characterization

1:00 - 1:30 Mixing Control for Turbine Engine Combustors
Jerry Seitzman, Georgia Institute of Technology

1:30 - 2:00 Analysis of Advanced Direct-Injection Diesel Engine Development Strategies
K. T. Rhee, Rutgers University

2:00 - 2:30 Visualization High Power-Density Diesel Engine Combustion
Ming-Chia Lai, Wayne State University

Topic: Diagnostics

2:30 - 3:00 Development of a Laser-Induced Fluorescence Technique for Characterization of Reaction Zones
Michael Coradini, Pat Farrell, David Foster, Jaal Ghandhi, Jay Martin, John Moskwa, Rolf Reitz, and Chris Rutland, University of Wisconsin, Madison

3:00 - 3:30 Break

3:30 - 4:15 Advanced Diagnostics for Reacting Flows
Ronald Hanson, Stanford University

4:15 - 4:45 Resonant Holographic Interferometry, and Innovative Technique for Combustion Diagnostics
Peter A. DeBarber, MetroLaser

Topic: Interdisciplinary Nonmetallic Materials-Combustion Research

4:45 - 6:00 Alexander Pechenik, Air Force Office of Scientific Research
Walter Bryzik, USA Tank-Automotive Command

6:00 - 8:00 DINNER

8:00 - 10:00 WORKSHOP – Research Needs and Opportunities for Diesel Engine Technology
Dr. Jay Martin, University of Wisconsin

TUESDAY, 30 JUNE

8:15 - 8:30 Announcements

TOPIC: Atomization and Sprays

Session Chairman: Dr. David Mann, Army Research Office

8:30 - 9:00 Modeling and Advanced Fuel Injectors for Control of Turbine Engines
Suresh Menon, Georgia Institute of Technology

9:00 - 9:30 Numerical Modeling of Two-Phase Nozzle Flows
David Foster, Jay Martin, Michael Coradini, Pat Farrell, Jaal Ghandhi, Rolf Reitz, and Chris Rutland, University of Wisconsin, Madison

9:30 - 10:00 Fluorescent Diagnostics and Fundamental Approaches to Droplet, Spray, Engine, and Aerodynamic Behavior
Lynn Melton, University of Texas at Dallas and
Michael Winter, United Technologies Research Center

10:00 - 10:30 BREAK

10:30 - 11:00	The Evaporation of Liquid Droplets in Highly Turbulent Gas Streams Richard Gould, North Carolina State University
11:00 - 11:30	The Effect of Turbulence on Droplet Drag, Dispersion, Vaporization and Secondary Breakup in Diesel Fuel Sprays Domenic Santavicca, Pennsylvania State University
11:30 - 12:00	Particle Dispersion in Turbulent Sprays Ian Kennedy, University of California, Davis
12:00 - 1:30	LUNCH
Session Chairman:	Dr. Doug Talley, AFRL/PRRK
1:30 - 2:00	Nonlinear Distortion and Disintegration of Liquid Sheets for Pressure Atomization Systems William Sirignano, University of California, Irvine
2:00 - 2:30	Secondary Breakup and Turbulence Interactions of Drops Gerard Faeth, University of Michigan
2:30 - 3:00	Computational Investigations of Atomization Gretar Tryggvason, University of Michigan
3:00 - 3:30	BREAK
3:30 - 4:00	Molecular Dynamics Investigation of Supercritical Phenomena Lyle Long, Pennsylvania State University
4:00 - 4:30	Study of the Sub- and Supercritical Behavior of Fuel Droplets and Jets Yaw Yeboah, Clark Atlanta University
4:45 - 5:00	BUSINESS SESSION - Contractors in Dr. Mann's Program Only
5:00 - 5:45	BUSINESS SESSION - Contractors in Dr. Tishkoff's Program Only
6:00 - 8:00	DINNER
8:00 - 10:00	WORKSHOP – Research Needs and Opportunities for Air Force Propulsion Technology W M Roquemore and Ted Fecke, AFRL/PR

WEDNESDAY, 1 JULY

8:15 - 8:30 Announcements

Topic: High Pressure Behavior

Session Chairman: Dr. W.M. Roquenmore, AFRL/PRSC

8:30 - 9:00 The Chemistry Controlling Ignition of Hydrocarbons and Their Mixtures at High Pressures
Nicholas Cernansky, Drexel University

9:00 - 9:30 Chemical Kinetics and Aerodynamics of Ignition
C K Law, Princeton University

9:30 - 10:00 Advanced Supercritical Fuels/Supercritical Combustion
Tim Edwards, AFRL/PR

10:00 - 10:30 BREAK

10:30 - 11:00 Fuels Combustion Research
Irvin Glassman, Princeton University

11:00 - 11:30 Theoretical and Computational Studies of Nucleation in Supercritical Fuels
Pablo Debenedetti, Princeton University

11:30 - 12:00 Experimental Studies on Supercritical Flows
Gregory Faris, SRI International

12:00 - 1:30 LUNCH

Topic: Combustion-Generated Particulates

Session Chairman: Dr. Gabriel Roy, Office of Naval Research

1:30 - 2:00 Phenomenological Soot Model to Predict Particle Size, Number Density, and Total Soot Mass
Michael Coradini, Pat Farrell, David Foster, Jaal Ghandhi, Jay Martin, John Moskwa, Rolf Reitz, and Chris Rutland, University of Wisconsin, Madison

2:00 - 2:30	Transport Phenomena and Interfacial Kinetics in Multiphase Combustion Systems Daniel Rosner, Yale University
2:30 - 3:00	Soot Evolution and Control Richard Dobbins, Brown University
3:00 - 3:30	BREAK
3:30 - 4:00	Soot, Temperature, and OH Measurements in an Unsteady Counterflow Diffusion Flame William Roberts, North Carolina State University
4:00 - 4:30	Mechanisms Controlling Soot Formation in Diffusion Flames Meredith Colket III, United Technologies Research Center
4:30 - 5:00	Soot Formation in Turbulent Combusting Flows Robert Santoro, Pennsylvania State University
5:30	ADJOURN

AFOSR SPONSORED RESEARCH IN COMBUSTION AND DIAGNOSTICS

PROGRAM MANAGER: JULIAN M. TISHKOFF

AFOSR/NA
110 Duncan Avenue, Suite B115
BOLLING AFB DC 20332-8050

SUMMARY/OVERVIEW: The Air Force Office of Scientific Research (AFOSR) program in combustion and diagnostics currently is focused on six areas of study: supersonic combustion, turbulent combustion, soot, sprays, kinetics, and supercritical fuel behavior. An assessment of major research needs in each of these areas is presented.

TECHNICAL DISCUSSION

AFOSR is the single manager for Air Force basic research, including efforts based on external proposals and in-house work at the Air Force Research Laboratory (AFRL). Combustion and Diagnostics is assigned to the AFOSR Directorate of Aerospace and Materials Sciences along with programs in rocket and space propulsion, fluid and solid mechanics, and structural materials.

Interests of the AFOSR Combustion and Diagnostics subarea are given in the SUMMARY section above. Many achievements can be cited for these interests, yet imposing fundamental research challenges remain. The objective of the program is publications in the refereed scientific literature describing significant new understanding of multiphase turbulent reacting flow. Incremental improvements to existing scientific approaches, hardware development, and computer codes fall outside the scope of this objective.

Decisions on support for research proposals are based on scientific opportunities and technology needs. Proposals are submitted for panel review. Therefore, researchers interested in submitting proposals should contact Dr. Tishkoff for information on time constraints associated with proposal evaluations. Further information on research interests and proposal preparation can be found on the AFOSR web site, http://www.afosr.af.mil.

The scope and title of the Combustion and Diagnostics subarea are new. Previously this subarea was identified as Airbreathing Combustion. The change reflects a new Air Force commitment to support space science and technology. Accordingly, the research in this

subarea will address research issues related to chemical propulsion for all Air Force aerospace missions. This program will complement related research activities in space propulsion and energetic materials.

Future airbreathing propulsion systems will require fuels to absorb substantial thermal energy, raising fuel temperatures to supercritical thermodynamic conditions. Understanding and controlling fuel properties at these conditions will be crucial for avoiding thermal degradation and for optimizing subsequent processes within the combustor. Environmental concerns and the availability of petroleum supplies also will contribute to future propulsion system design and operational needs.

Designing propulsion systems that will offer reliability, maintainability and long service life represents a new motivation for propulsion research. Future budgets likely will dictate the acquisition of reduced quantities of new operational aerospace vehicles, with a corresponding increase in requirements for durability. Research topics such as soot and supercritical fuel behavior will be relevant to these new service constraints.

Beginning in fiscal year 1997 AFOSR and the Air Force Scientific Advisory Board established priority research areas to support future Air Force Technology under the New World Vistas (NWV) program. One of the research topics in New World Vistas is Hypersonics. Specific thrusts in Hypersonics address the impact of weakly ionized flows on hypersonic vehicle performance, including combustion, and the utilization of hydrocarbon fuels. Another NWV topic involving propulsion is Family of UAV (uninhabited aerial vehicles).

The purpose of this abstract has been to communicate AFOSR perceptions of research trends to the university and industrial research communities. However, communication from those communities back to AFOSR also is desirable and essential for creating new research opportunities. Therefore, all proposals and inquiries for fundamental research are encouraged even if the content does not fall within the areas of emphasis described herein. Comments and criticisms of current AFOSR programs also are welcome.

INTELLIGENT TURBINE ENGINES

ARO Contract Number DAAH04-96-1-0008

Principal Investigator(s): **B. T. Zinn, M. Allen, M. Brooke, A. Glezer, W. Haddad, J. Jagoda, S. Menon, Y. Neumeier, J. V. R. Prasad, L. Sankar and J. Seitzman**

Georgia Institute of Technology
Schools of Aerospace, Mechanical, and Electrical and Computer Engineering
Atlanta, Georgia, 30332-0150

SUMMARY/OVERVIEW

This program focuses on the fundamental and practical issues that hinder development of intelligent control systems for improving the performance of turbine engines, such as rotorcraft turboshaft engines. Our approach to the development of an intelligent control system hinges on advances in the basic understanding of engine processes through experiments and advanced computational models, refinement of appropriate sensor and actuator technologies, and development of practical control strategies for control of steady-state and transient performance of highly uncertain, nonlinear systems such as compressors and combustors, and the integrated engine itself. Substantial advances have been made on: unsteady modeling of compressor and combustor flows, control strategies for compressor surge and stall; combustor control using synthetic jets and smart fuel injectors; model-based, fuzzy logic and neural network control approaches; and MEMS and optical sensors able to operate in high temperature environments.

TECHNICAL DISCUSSION

The material presented in this year's Contractors meeting focuses on recent accomplishments aimed at improving the combustor's performance. They include: LES modeling of the combustor flow, applications of synthetic jets in the control of mixing processes and pattern factor, development of a smart fuel injector for controlling fuel spray characteristics, development of a wireless MEMS pressure sensor for high temperature applications, and development of non-intrusive, optical, sensors for real time monitoring of water content and temperature profile uniformity at the turbine inlet.

Modeling Efforts (Menon, Jagoda and Seitzman). The modeling efforts included the development of a comprehensive two-phase large-eddy simulation (LES) model. To validate the model, its predictions were compared to results of past experimental and numerical studies of particle transport in a mixing layer. As expected, particles are entrained into the mixing layer at a rate that depends upon their size or Stokes number (St); i.e., particles with St slightly above unity show maximum entrainment. The innovative aspect of the new two-phase LES code is its handling of droplet vaporization. In conventional LES, droplets are tracked using a Lagrangian tracking method only up to some cut-off size and droplets below this cut-off are assumed to *instantaneously vaporize* and mix. It has been shown that this assumption is acceptable only if the cut-off size is very small. However, the computational cost required to achieve this can be quite significant since small droplets imply small time steps. A new, more efficient subgrid vaporization model (denoted LEM here) was developed. Droplets smaller than the cut-off are no longer tracked in a Lagrangian

manner, but vaporization is allowed to continuously occur within the unresolved (subgrid) scales. A reacting mixing layer with infinite rate chemistry was simulated with both conventional droplet tracking and the new LEM model in order to evaluate the ability of the LEM to handle a wider range of cut-off sizes. Results show that as the cut-off size is increased, the product mass fraction predicted by the conventional LES approach increases significantly. As expected, the new LEM subgrid model shows much less sensitivity to cut-off size.

We have also implemented the model into a 3-D compressible, parallel, LES code to begin the next stage of validation using data obtained in a test facility built specifically for this purpose. The facility provides a more comprehensive evaluation of the new LES method in a pseudo-combustor environment. The facility provides a controlled environment for measuring the interaction between sprays and turbulent flow fields, and these measurements are being used to generate a benchmark quality data base for validation of our LES code, as well as other predictive codes. The facility consists of an air jet centered within a secondary, axisymmetric coflow of air. The center jet also contains a dilute liquid fuel spray. The flows are produced with three concentric tubes. The center tube carries the liquid, which is injected under pressure through a nozzle contained inside the middle tube. This middle tube carries the primary air flow that produces the inner jet. The outer duct carries a secondary, turbulent flow that interacts with the center jet. Various levels of turbulence can be generated in the secondary flow by turbulence screens. The complete flow field, including gas and droplet velocity distributions, and droplet size and number density distributions, are measured using a phase Doppler anemometer through windows in the test section walls. Currently water sprays are used to produce data sets with minimal evaporation. Measured data show that small droplets in the 40 micron range follow the flow quite well while 120 micron sized drops require the whole test section to catch up with the air flow. The non-evaporating experiments are almost complete and tests with evaporating sprays will begin soon. Complete flow conditions at the inflow boundary have been provided to the LES code, and simulations based on these input values are currently underway. The validation of the LES code will depend on its ability to reproduce results at various downstream "outflow" locations.

Actuators (Glezer, Jagoda, Neumeier and Seitzman). Two actuator systems are under investigation; synthetic jets technology that periodically "inhale" nearby fluid and inject it back into the flow, and smart injectors that independently control the size of the liquid fuel spray droplets and their spatial distribution in the combustor.

Synthetic Jets Studies. For active control of mixing between two fluids (e.g., fuel and air), we have applied the synthetic jet technology to single and co-axial round jets. The exit plane of a primary jet nozzle is equipped with an insert housing nine individually-controlled synthetic jet actuators equally-spaced around the circumference of the jet that can operate either normal or parallel to the primary jet. The effect of controlled flow manipulation on the flow structure and the concomitant mixing is investigated in parallel in two nearly identical experimental setups. In the first, Schlieren imaging and two-component hot-wire anemometry are being used to study flow structure and acquire detailed measurements of the streamwise and radial velocity components. The second setup uses PLIF of a passive scalar, acetone, seeded into the flow. This direct measure of mixing is used to study the capabilities of the synthetic jets to control mixing (a small-scale process) and entrainment (typically produced by large scale motions). The synthetic jets are used to achieve concurrent manipulation of *both* the small- and large-scale dynamical processes in the flow.

The capability of synthetic jets to form closed recirculating flow regions near the flow boundary is exploited to alter the large-scale structure of the jet where the radial extent and azimuthal locations of these regions can be adaptively tailored to the desired level of mixedness by electronically controlling the actuator jets. Mixing at the molecular level is enhanced by direct (rather than hierarchical) excitation of the small scales in the vicinity of these regions. Hot wire results show that forcing increases the rms velocity fluctuations across the entire jet, and that radial actuation results in larger increases in the rms velocity fluctuations. The power spectra demonstrate that the forcing suppresses the fundamental Kelvin-Helmholtz

instability of the unforced flow and increases the energy throughout the entire frequency range. Large-scale structures within the flow (and thus entrainment) are affected using amplitude modulation of the (high frequency) excitation waveform. For example, the modulating waveform can be advanced in phase azimuthally resulting in a "spinning mode". As a result of the forcing, the peak streamwise velocity is off axis and rotates about the centerline at the modulation frequency, resulting in a net tangential velocity and clockwise swirl in the direction of rotation. Although the swirl number is low (approximately 0.03), it is remarkable that it is possible to provide the flow with angular momentum by phasing of the actuators.

The ability of the synthetic jets to enhance mixing has been also studied using PLIF of acetone imaged with a high-resolution, low-noise CCD camera. The PLIF studies investigated mixing between two coaxial round jets, the outer one seeded with acetone. The inner air jet exits from a 5/8" diameter tube at 10 m/s, and the outer annular jet flows is seeded with ~20% acetone flowing at 2.5 m/s. In these studies, the synthetic jets were directed parallel to the flow with an exit velocity of about 10 m/s. The effect of forcing was studied by comparing PLIF images obtained without forcing, with the synthetic jets on (but without any modulation), and with the synthetic the jets modulated at 50 Hz. These images show significant mixing enhancement for both forced cases, where the fluid from the outer jet quickly mixes just downstream of the exit (mixture fraction is reduced to one-half at about one annulus thickness downstream). Also, the downstream mixture is more uniform and spreads over a greater region. The near field structure is nearly the same for the two forced cases, but there is much more dilution of the outer jet in the pulsed case. It is likely that the pulsing produces large scale structures that enhance the entrainment of ambient fluid into the outer jet.

PLIF images were also obtained for the "spinning" mode of operation. The most noticeable attribute of this forcing mode is the ability to control placement of the outer jet fluid. At the exit plane of the jets, most of the outer jet fluid is pulled toward the active actuators. This pattern control persists downstream of the synthetic jets locations. Combining fuel pattern control with fuel/air mixing control can be used to control local stoichiometry in the combustor, and thereby influence blowoff limits, flame location, temperature profiles at the combustor exhaust and pollutant emissions

Use of synthetic jets to control the temperature profile at the combustor exit is also underway. An experimental facility in which a nonuniform temperature profile is generated by an off-axis propane flame has been designed and built. Synthetic jets are attached at various locations in the combustor walls and their effect on the temperature distribution is measured using a thermocouple rake. The physical mechanisms responsible for the observed changes are being investigated by visualizing the flow field using high speed Schlieren photography.

Smart Injector. The combustor performance can be also controlled using smart fuel injectors that allow independent control of the size and spatial distribution of the liquid fuel spray droplets. For current injectors (pressure and air-blast), the droplet size and fuel pattern change with fuel flow rate and combustor pressure, often degrading combustor performance at off-design operation. This study investigates an internal air mixing atomizer that is not sensitive to g-forces. In this atomizer, droplets are generated by using air injection to accelerate and breakup the liquid. It has been shown that this atomizer can control water droplet sizes between 30 and 110 microns.

Since two-phase flow through an air-assisted atomizer is a very complex process, current efforts include modeling the flowrate through the injector as a function of the liquid supply pressure, air to liquid mass flowrates, and back pressure using mass and energy conservation but with no change of phase. The energy of each phase is not conserved, however, due to interactions between the phases. Model predictions and measurements of the dependence of the total mass flow rate upon the air-to-liquid ratio and back pressure are in excellent and reasonable agreement, respectively. Experiments are underway to study the effects of changes in back pressure and liquid properties; e.g., density, viscosity, and surface tension on droplet size.

Sensors (Allen and Seitzman). This task investigates a MEMS pressure transducer for high temperature applications and non-intrusive optical sensors for real-time monitoring of combustor health and temperature profile uniformity at the turbine inlet.

The MEMS studies seek to optimize design and fabrication procedures for a ceramic MEMS pressure sensor, and develop a wireless data retrieval system. The development of the wireless resonant circuit for the data retrieval and the test-bed for the sensor have been the primary focus of recent work. As a first step, a hybrid-fixed inductor in parallel with a hybrid-variable capacitor was used to test the wireless data retrieval concept. A network analyzer was used to monitor the phase of the impedance as a function of frequency of a wire loop. The hybrid LC resonator circuit is placed inside the loop of wire and the impedance of the wire loop is monitored as a function of frequency. This scheme was successful in reading out the frequency variation of the sensor and thereby the capacitance. Theoretical calculations based on the extracted static pressure data yielded a sensitivity of 560 kilohertz per bar frequency shift as a function of pressure, at a carrier frequency of 100 megahertz. The current status of the work is that the (non-wireless) sensors and the hybrid (i.e., assembled) readout scheme are operational. Our upcoming work will focus on incorporating these two results into a single sensor substrate to form the integrated sensor.

In a parallel study, a sensor approach for monitoring the water mole fraction and temperature uniformity in the exit plane of a high pressure gas turbine combustor has been developed. The sensor is based on infrared line-of-sight absorption measurements of water. Unlike most sensors previously proposed, the current approach would employ broadband IR sources, or perhaps a single source with a tunable bandpass filter. The design and performance of the sensor has so far been based on computer simulations using the HITRAN/HITEMP database for the infrared absorption of water. Three specific regions of interest near 2.5 μm have been identified, based on their relative sensitivity to temperature and lack of interference from other combustor exhaust gases. One, relatively insensitive to temperature, permits monitoring of integrated water mole fraction across the exhaust, without knowledge of the temperature. Two other measurement wavelengths, one more sensitive to hot water, and the other sensitive to cold water can be used to monitor the uniformity of the exhaust temperature profile. Using the measured water concentration and the absorbance at either of these wavelengths, a path averaged temperature can be determined across the combustor exhaust. The difference in the temperatures inferred from the "hot" and "cold" wavelength measurements is a measure of the temperature uniformity. The results of this study were used to develop a strategy for determining a path averaged temperature across the combustor exhaust, and the "degree" of temperature uniformity.

We simulated the performance of this sensor for five combustor exhaust profiles. Each profile has the same path averaged water mole fraction (0.047) and the same path and mass averaged temperature (1300 K). For most of the profiles, the water fraction output by the sensor is within 6.5% of the actual value, and within 10% in the worst case. Furthermore, the simulations showed that the proposed sensor could determine a path integrated water content and temperature uniformity across the combustor using as few as three measurements at different wavelengths. Interferences associated with "dirty" optics and particle extinction can be assessed at nearby wavelengths that have little water absorption, e.g., above 4200 cm^{-1}. The next step in this effort is an experimental verification of the simulation. A facility that should be capable of producing a 40 atm flow of heated (~1000°C) air, seeded with a controllable amount of water has been designed and will be constructed. In addition, a broadband, tunable IR source is under construction.

ANALYSIS OF ADVANCED DIRECT-INJECTION DIESEL ENGINE DEVELOPMENT STRATEGIES

(ARO Contract No. DAAH04-95-1-0430)

Principal Investigator: KT Rhee

Rutgers, The State University of New Jersey
Mechanical and Aerospace Engineering Department
Brett and Bowser Roads
Piscataway, NJ 08855-0909

OVERVIEW:

The present study was directed towards investigation of some engine design strategies to achieve a direct-injection Diesel or compression ignition (DI-CI) engine with high brake mean effective pressure (BMEP), in particular when the engine is equipped with ceramic components for uncooled operations. Two approaches were taken for this objective.

A real world commercial engine (Cummins 903 engine, 140 dia -121mm stroke) was equipped with a new laboratory-built electronically controlled high injection-pressure fuel unit (HIP), which can deliver injection pressures of over 210 MPa (30,625psi). This engine was also mated with a high-temperature induction system for introducing intake air at temperatures as high as 205°C (400°F) to simulate severe thermal conditions expected when an uncooled ceramic engine design strategy is employed. A parametric study was conducted in order to evaluate the engine behaviors for a wide range of variables.

In order to study the in-cylinder processes when such engine alterations were made, a separate single-cylinder engine with optical access was lined up with the Rutgers Super Imaging System (SIS) whose electronic packages and control units were entirely redesigned/fabricated to simultaneously obtain four spectral IR images at high rates. Although the SIS is being further improved, the new system is at present operational with imaging rates of over 1,800 frame/sec/channel.

In addition, a new data analysis method has been developed to efficiently analyze the vast amount of data captured using the SIS as mentioned above.

TECHNICAL DISCUSSION:

Engine Performance Evaluation. An increased air utilization for high BMEP appears to be promising by the use of an HIP as demonstrated in the present study. It was possible to operate an engine having an injection pressure of 210 MPa by using an HIP at air-fuel ratio as low as 18-1 to produce smoke emissions comparable or lower than those from a DI-CI engine equipped with a conventional low pressure injection unit. The high air utilization, however, resulted in several consequences, including high engine block and exhaust temperatures, and increased noise. Note that the temperatures will become higher when an uncooled engine design approach is employed, whose impacts on the goal of developing an HIP are in need of discussion.

Most of all, the volumetric efficiency will greatly deteriorate in an uncooled high air-utilization engine, resulting in a low mean effective pressure as studied in the present work. The use of a high performance turbocharger or supercharger, therefore, may become a precondition for a high BMEP uncooled engine, which also may have to use inter-cooling. In addition, the high engine temperature will undoubtedly increase the injector as well as the fuel temperature. When there is no positive remedy for this, the fuel would attain super critical temperatures. This then will modify the spray formation, affect the lubrication of the injector itself and even damage the nozzle holes by cavitation in the fuel stream.

The high exhaust gas temperature, on the other hand, may be a useful ingredient for achieving a high BMEP engine by facilitating the incorporation of a turbocharger in the engine. Also, the high temperature may offer an opportunity for using an exhaust catalytic converter to produce a cleaner emission, which then may make it possible to further increase the air utilization.

The development strategies of an uncooled high BMEP DI-CI engine using ceramic components is certainly a great challenge involving various technical problems as briefly discussed above. There is no question that they would not be easy to surmount, but they offer an exciting opportunity for advancing the engine technology.

High-speed Spectral IR Images by using SIS. Based on the earlier design experience of the Rutgers SIS system, also a proto-type from which additional system requirements were found, entirely new electronic and control software packages were developed. This was done in order to achieve more accurate quantitative imaging by processing the spectral digital images.

At present, the system is basically functional but delivering a limited versatility in control, which is being further improved. Two sets of sequential spectral images obtained in 2.47 and 3.43 μm at two different injection pressures (23,590 and 30,625 psi) are included here. The set in 2.47 μm represents radiation liberated mainly from water vapor and soot, and the other in 3.43 μm reveals similar radiation plus those from some strong (invisible) preflame reactions as captured during the ignition delay period.

Future Plan. An in-depth parametric study is planned for both the engine evaluation and in-cylinder imaging as outlined above. In particular, the preflame reactions which appear to start immediately after fuel is introduced into the cylinder will be of one of more important topics to be studied during the next period.

The SIS will be further improved: Completion of the new SIS system will never be fully satisfactory in view that additional features were identified to be incorporated while the system was used in the experiment. The improved system is expected to deliver a framing rate of over 2,000 in each channel, which will be equipped with a modern affordable high-speed memory.

REFERENCES

T. Themel, M. Jansons S. Campbell, and KT Rhee, "Diesel Engine Response to High Fuel-Injection Pressures," SAE Paper to be presented at Fuels and Lubes Meeting (October, 1998) to be held in San Francisco.

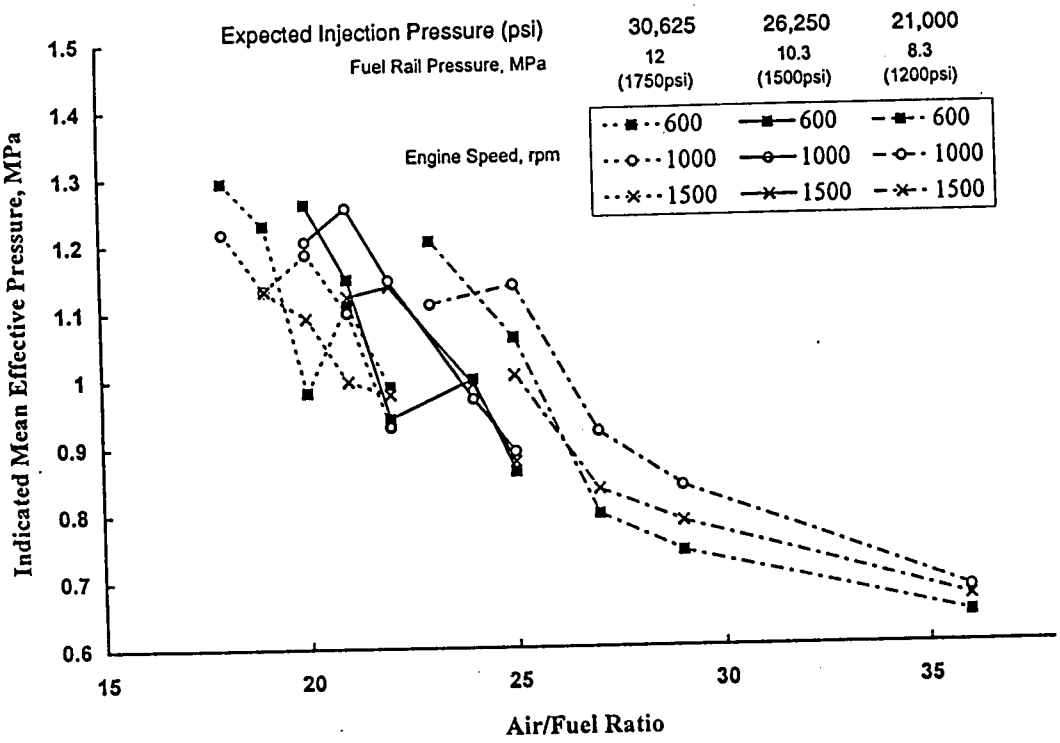

Indicated Mean Effective Pressure (IMEP) as a Function of Air/Fuel Ratio (Intake-air 38°C and Injection timing of 10° bTDC).

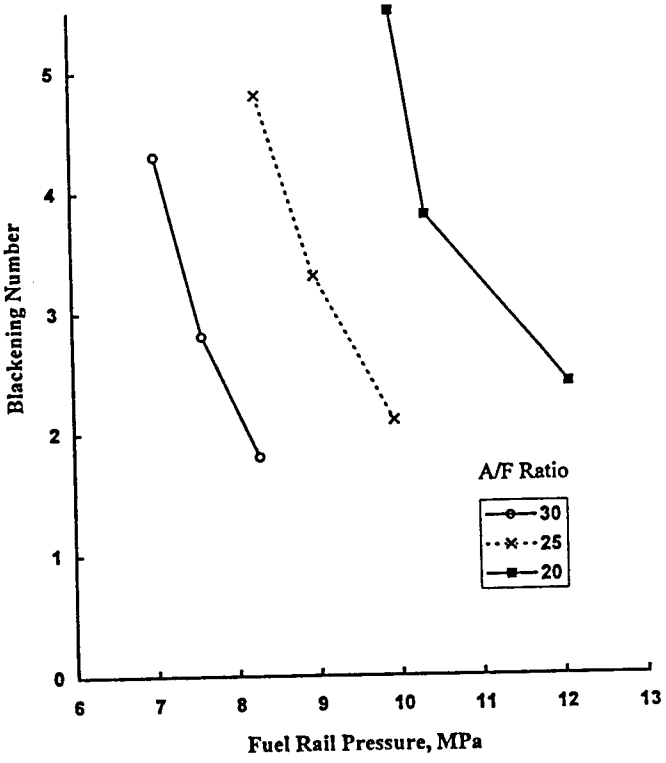

Bosch Smoke Reading of Exhaust Gas at Varied Fuel Injection Pressures.

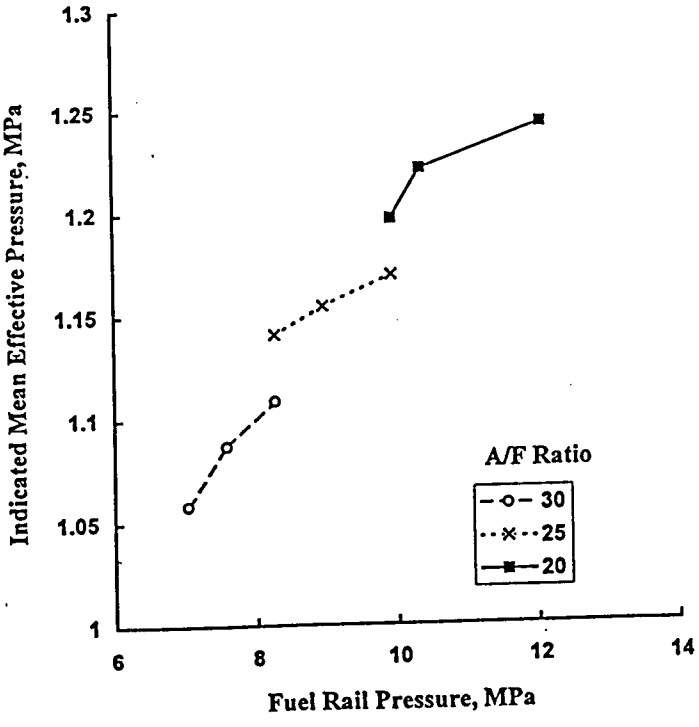

IMEP as a Function of Fuel Injection Pressure (38°C Intake-air Temperature).

High-speed Spectral IR Images
23,590 psi Fuel Injection

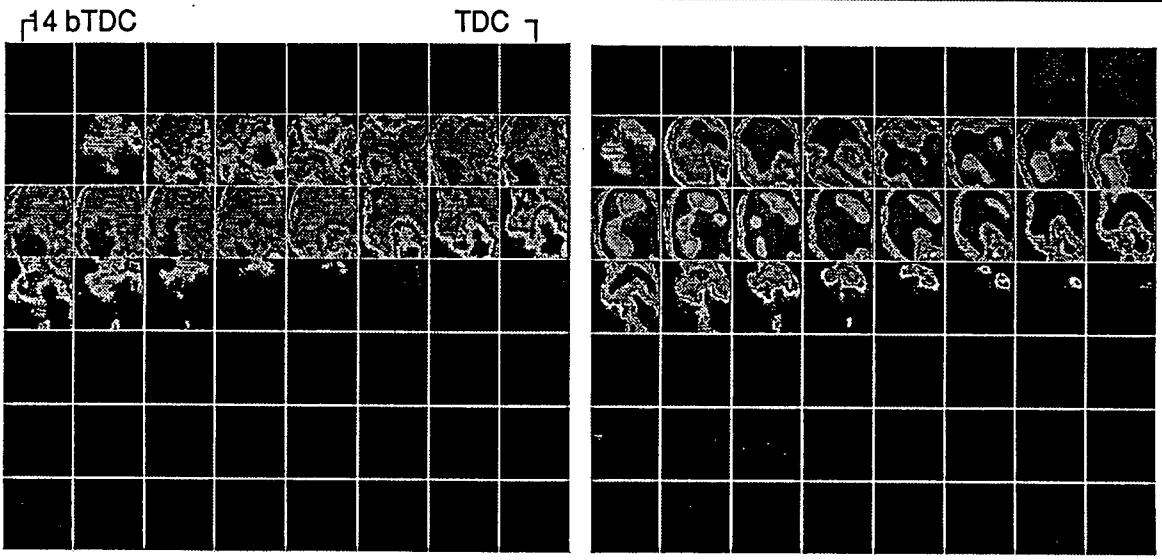

2.47μm 3.42μm

High-speed Spectral IR Images
30,625 psi Fuel Injection

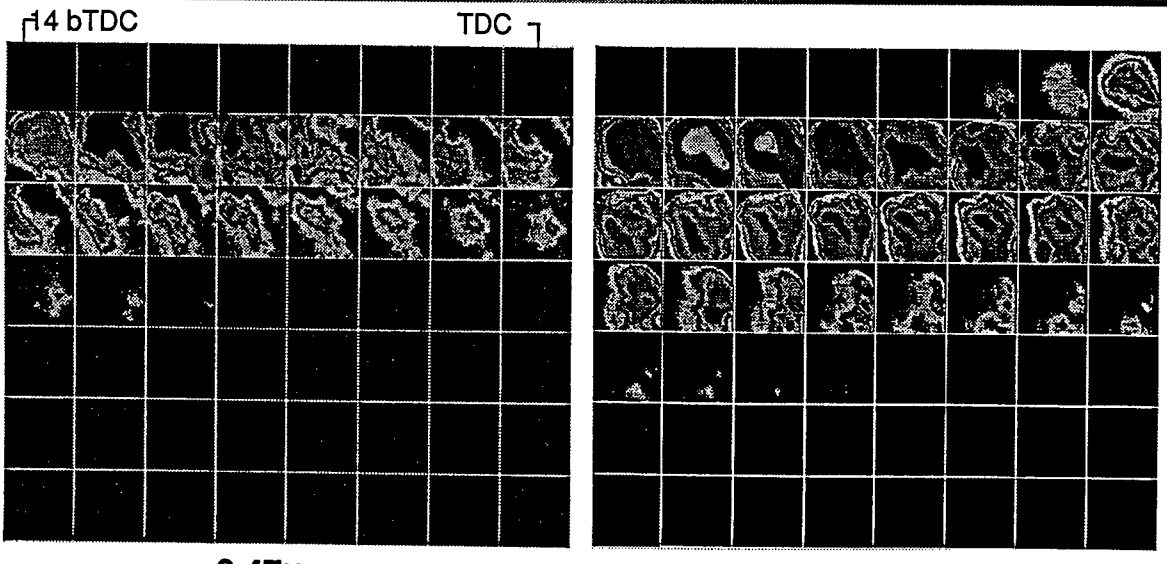

2.47μm 3.42μm

A/F, 25-1; 600rpm; Intake air, room temp.
Injection, 8 bTDC; Imaging Interval 2CA

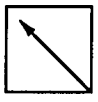

Direction of Sray

TITLE: VISUALIZATION OF HIGH-POWER-DENSITY DIESEL ENGINE COMBUSTION

ARO Grant No.: DAAH04-96-1-0458

Principal Investigators: Ming-Chia Lai, Naeim A. Henein

Mechanical Engineering Department
Center for Automotive Research
Wayne State University
Detroit, Michigan

SUMMARY/OVERVIEW:

The objective of this research is to visualize the fuel injection and combustion processes inside the high-power-density (HPD) diesel engines. Because of their extreme operation conditions, our current understanding of the required high-pressure fuel injection and high-density combustion processes is very limited. Using advanced visualization techniques aided by high-speed pulse-laser and long-distance microscope to characterize the spray and combustion processes inside a modified "see-through" engine, the results of this research are expected to

- better define the role of turbulence and cavitation breakup mechanisms in transient high-pressure rate-shaping fuel injection,
- help the development of new and improved diesel injection systems and injection strategies for advanced Army HPD engines,
- explore the role of combustion chamber geometry and ceramic parts in HPD combustion, and
- improve the accuracy and efficiency of HPD diesel combustion simulation program.

TECHNICAL DISCUSSION:

In this performance period, we conducted microscopic spray visualization in high-pressure chambers and combustion visualization in an optical accessible engine (OAE). The research findings are summarized as follows:

- Microscopic spray visualization provides useful information for spray symmetry and dynamics not seen before.
- Advanced spray modeling needs to incorporate 3D transient flow effects, and turbulent, cavitation and pressure wave break-up mechanisms.
- Combustion visualization shows sensitivity to injection and geometry parameters.
- High-pressure injection and combustion goals achieved in OAE experiments.
- Multi-zone diesel combustion model seems promising as a HPD diesel engine design tool.

MICROSCOPIC SPRAY VISUALIZATION

The optical system setup includes a long-distance microscope, a copper-vapor laser (Oxford CU15), and a still or a high-speed drum camera, both using 35-mm photographic film. The copper laser is expanded into a thin sheet using cylindrical lens and is used as the optical shutter, up to 25kHz with the exposure time as short as 10 nanoseconds. A long-distance microscope is used to magnify the diesel spray structure very close to the nozzle exit. The field of view is 1-2 mm and the diffraction-limit resolution can be as small as 1-2 micron. The optical setup provides great resolution in both time and space. The injectors examined are valve-covered-orifice (VCO) nozzles, from either a common rail (CR) or an electronic-controlled unit injector (EUI), system. For comparison, a mini-sac injector from a HEUI system is also investigated. Diesel fuel No.2 was used in this study.

POOR PILOT AND END OF INJECTIONS Typical high-speed microscopic visualization results are shown in figures 1 and 2. The copper vapor laser was operated at the frequency of 25kHz, *i.e.* each frame is 40 microsecond apart. The field of view extends from the nozzle exit to 1.5mm downstream. At the injection of 25MPa, the pilot barely made it out of the nozzle, resulting in an inconsistent and poorly atomized spray.

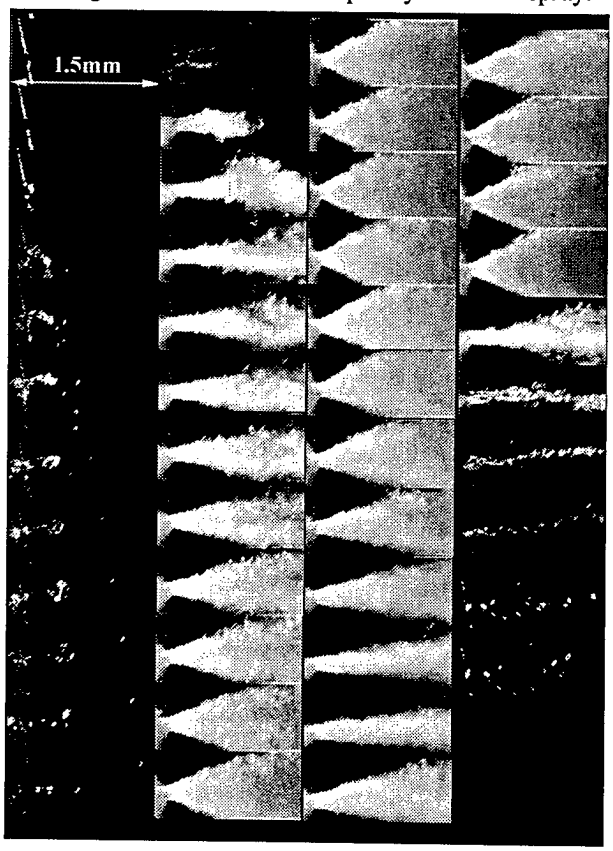

Fig. 1 Microscopic Visualization of CR spray. P_{inj}=25MPa, Injection Event: 0.2ms-pilot/1.0ms-dwell/1.0ms-main, frame 13-23 skipped.

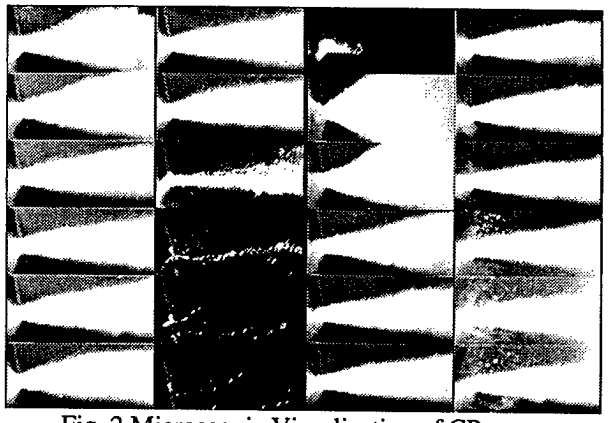

Fig. 2 Microscopic Visualization of CR spray. P_{inj}=135MPa, Injection Event: 0.2ms-pilot/1.0ms-dwell/1.0ms-main, frame 13-28 skipped.

At the injection of 135 MPa in Fig. 2, the pilot is much better atomized, but the 0.2-ms injection command results into an injection duration of more than 0.3 ms. Both figures show that at the end of injection, the spray trickles down and forms larger drops. However, compared with sac nozzles which tend to produce even larger ligaments at end of injection (and consequently higher HC emission in engine tests), the VCO nozzle shows considerable improvement. The lower injection pressure case in Figure 1 also shows poorer atomization and large-eddy structure inside and at the edge of the spray, as is evidenced by the less homogenous light intensity scattered.

SPRAY ANGLE OSCILATION The visualization results in Fig. 1 and 2 also show rapid temporal variations of spray angle, which result into the puffy spray structure at the edge of the spray as observed in the macroscopic visualization. At the high injection pressure of 135 MPa, the spray angles at the start of injection are larger than those of during the mid-injection period; there is also a slight increase at the end of injection. However, the low-pressure spray shows pronounced oscillation in spray angles even during the mid-injection period. Since the spray angle does not correlate very well with injection pressure, the spray angle oscillation is attributed to needle oscillation, which sets up swirling flow motion within the injector hole.

A typical visualization high-speed microscopic visualization result of the EUI spray is shown in Figure 3. The condition in Figure 3 is for a speed of 1500 rpm and a injection duration of 7 crank angle degree. The EUI injector has a sturdy injector construction with a larger nozzle, which generally results into more symmetric spray. Figure 3 shows that it also has very large spray cone angle initially, but quickly stabilizes. Therefore it does not have significant spray-angle variation in the mid-injection compared with the slender CR injector conditions.

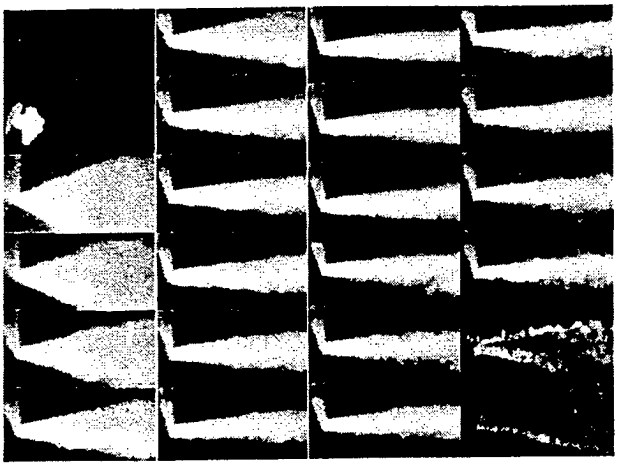

Fig. 3 Microscopic Visualization of EUI spray.

PRIMARY BREAKUP MECHANISMS A inverted microscopic visualization of the EHI spray is shown in Figure 3, which is taken at the peak pressure of 200 MPa. The picture shows that onset of spray breakup start immediately at the injector exit, indicating the presence of turbulent primary breakup. The bottom side of the spray shows droplet formation with a diameter of about 10-20% of that of the nozzle hole, corresponding to the turbulent integral scale within the nozzle.

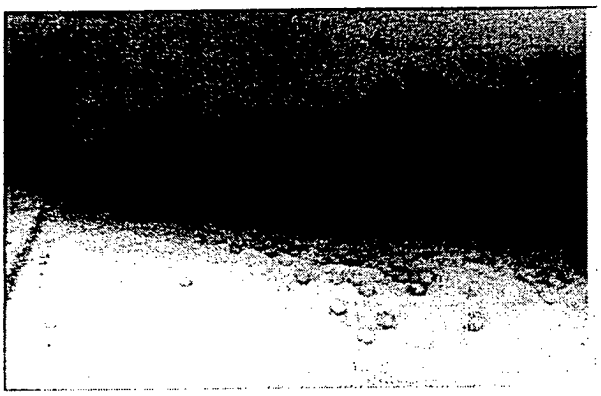

Fig. 3 Inverted microscopic image of EUI spray at peak injection of 200 MPa.

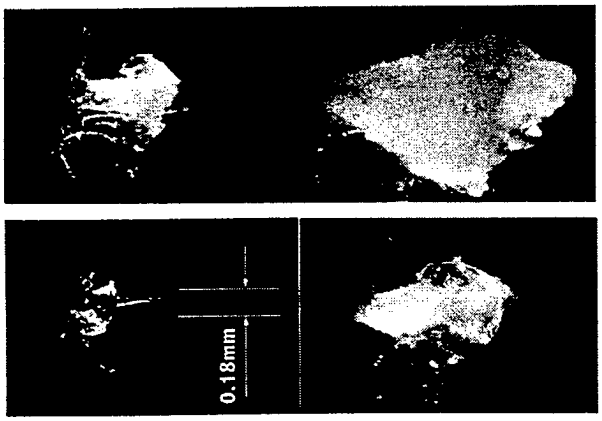

Fig. 4 Early spray breakup photographs of a VCO nozzle spray from an EUI.

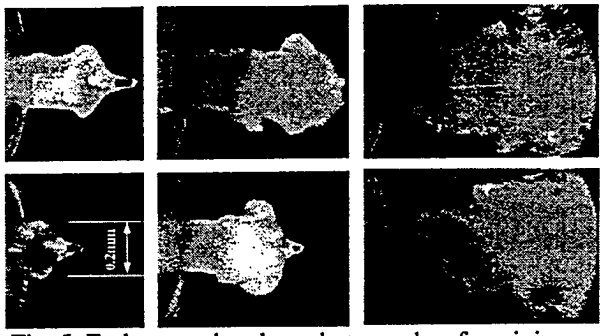

Fig. 5 Early spray breakup photographs of a mini-sac nozzle spray from a HEUI.

Although light attention could be significant across the spray, the top side of spray does not show a symmetric and corresponding distribution of large droplets, but instead shows the formation of a very fine mist. The nozzle internal flow direction is from top to bottom; therefore, the topside spray is directly downstream of the turn-around point, where nozzle internal flow passage dictates that fuel flow must negotiate a sharper inside turn into the VCO hole. The fine mist observed suggests cavitation-enhanced breakup mechanism.

Fig.4 shows a collection of the microscopic photographs taken with a 35 mm SLR camera, which has better spatial resolution but is limited to single shot. These close-ups were taken to catch the onset of spray formation, where the spray just exits the nozzle orifice. The photograph shows very dynamic turbulence- and cavitation-enhanced breakup processes. For comparison, Figure 5 shows a collection of the close-ups of one of the spray from a HEUI mini-sac nozzle. At the onset of injection, the initially low-pressure fuel in the sac volume is squeezed out of the nozzle orifice like the shape of toothpaste. The initial liquid column has quite distinct and clear boundary, but it turns bubbly or milky very quickly. Its surface also rolls up similar to that the eddy rollup processes observed in pure gas jet. Close examination of the interface shows formation of very fine droplets, suggesting very rapid breakup due to pressure wave. Comparing the mini-sac nozzle sprays with those of the VCO show that sac-type nozzle has less turbulent primary breakup features, which is consistent with its internal flow characteristics.

COMBUSTION VISUALIZATION

A four-valve single-cylinder research engine (AVL520, with 120mm-bore, 120mm-stroke, and a compression ratio of 19) was converted for optical access. Optical access into the combustion chamber is provided through a quartz window at the crown of an elongated piston which is mounted piggy-back on the original piston, and a 45-degree stationary mirror which is mounted from the crank case and extends into the extended piston. A quartz ring, which provides laser beam access into the combustion chamber, and an

additional dry liner are sandwiched between the original cylinder head and crank case. Compression pressure of 4.2MPa is achieved under ambient intake condition at the motoring speed of 500 rpm, showing good sealing between the extended piston and the dry liner. A HEUI injection system with a maximum injection pressure of 180MPa is first used in the parametric study. Intake air charge is conditioned by a 100psi compressor, 400-gallon reservoir and a 40kW electrical heater to match the turbo-charged conditions of HPD diesel combustion. Currently, peak combustion pressure of 150MPa has been achieved successfully in the optical engine.

A PC running LABVIEW program controls the synchronization of the injection timing, laser illumination timing, high-speed camera trigger, as well as the data acquisition. Data acquired include cylinder pressure, injection pressure, and injector needle lift. During testing, the engine is motored to a specified speed, and the injection system is fired for at least five consecutive cycles to simulate the residual gas and hot wall effect of actual engine operation. Imaging of the last combustion events is recorded using either a 16-mm high-speed camera or a high-speed digital camera. The charge conditions (intake pressure and temperature) and injection strategies (nozzle design pressure, timing, split-injection and rate-shaping) are varied to study their effect on the HPD combustion.

Figures 6-8 show the typical results of the combustion visualizations obtained using the 16-mm high-speed camera. The time between each frame shown is 0.2 ms. Figures 6 and 7 are for the low injection cases, with a peak injection of 42MPa, and a engine speed of 1000rpm; while Fig. 8 is for the high injection pressure case, with a peak pressure of 110MPa. The effect of injection timing on the auto-ignition sites is also shown in Fig. 6: the top sequence is for the injection timing of 13°BTDC, and the bottom, 20°BTDC. Because of the long ignition delay, ignition sites are observed after the fuel injection has been completed, in the wall impingement areas or the spray tail area. Poor burning speed is evident by the poor air utilization, as shown by the spotty combustion and wall burning phenomena. Fig. 7 shows the effect of intake air temperature. Preheating the temperature to 330°K shortens the ignition delay, but the low injection pressure results into very sooty combustion, as shown by the yellowish radiation.

Fig. 8 shows that at the peak injection pressure of 110MPa, and a supercharged intake condition of 0.16MPa and 333°K, the combustion is significantly improved. Multiple-ignition sites are observed at the spray peripheral, starting at the down wind side due to the swirling air motion inside the combustion chamber. Intense white radiation indicates that Soot emission is reduced by the intense fuel-air mixing, due to the higher injection pressure. Much better air utilization is also observed.

Fig. 6 Combustion visualization: natural aspiration condition, peak injection pressure 42MPa, injection timing = 13°BTDC (top), and 20°BTDC (bottom).

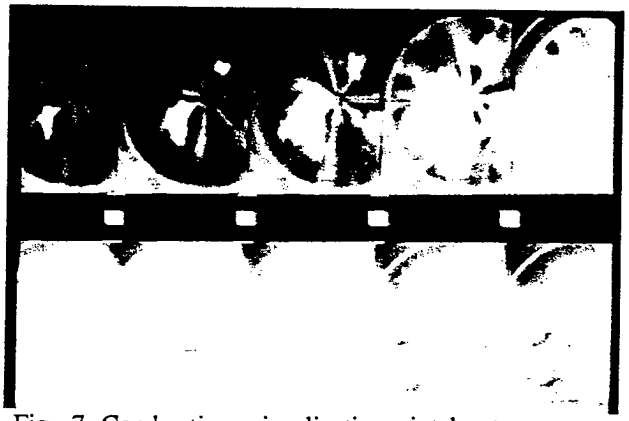

Fig. 7 Combustion visualization: intake temperature 330°K, peak injection pressure 42MPa, injection timing = 10°BTDC.

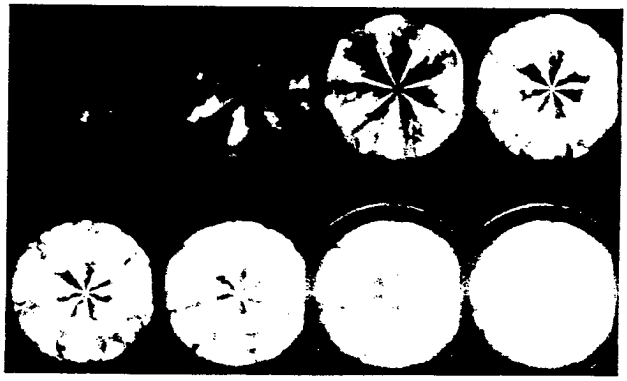

Fig. 8 Combustion visualization: intake temperature 330°K, intake pressure 0.16MPa, peak injection pressure 110MPa, injection timing = 8°BTDC.

REFERENCES

Lai, M.-C., Henein, N. A., Xie, X., Chue, T.-H., Itoh, Y. and Bryzik, W., SAE 952366.

Harrington, D., and Lai, M.-C., (1998) *ILASS AMERICAS '98*, pp. 296-300.

Lai, M.-C., Wang, T.-C., and Xie, X. (1998) *ILASS AMERICAS '98*, pp. 38-42.

DEVELOPMENT OF A LASER-INDUCED FLUORESCENCE TECHNIQUE FOR CHARACTERIZATION OF REACTION ZONES

AFSOR Grant Contract No. DAAH04-94-G-0328

Principal Investigators: Engine Research Center

Mike Corradini, Pat Farrell, Dave Foster, Jaal Ghandhi,
Jay Martin, John Moskwa, Rolf Reitz and Chris Rutland

University of Wisconsin Engine Research Center

1500 Engineering Drive

Madison WI 53706

SUMMARY/OVERVIEW:

AUTHORS: Mark Musculus and David Foster

A Planar Laser-Induced Fluorescence technique was developed to characterize the reaction zones involved in combustion for future application to Diesel engines. A diagonal excitation technique for the CH radical using a holographic notch filter to reject elastic scatter of the laser light allowed imaging of the reaction zones with high excitation efficiency in atmospheric pressure flames. The CH fluorescence images can be used to determine the thickness and character of the reaction zones, as well as the scales of the structures observed in turbulent flames. The technique will continue to be refined and applied to more challenging combustion regimes, to determine its applicability to Diesel combustion. Ultimately, it is hoped that this diagnostic tool will provide better understanding of the mixing controlled combustion of Diesel engines.

TECHNICAL DISCUSSION:

Combustion in Diesel engines occurs in a regime that is difficult to analyze and characterize, and it is still unclear exactly where Diesel combustion resides between the extremes of distributed reactions and thin wrinkled flame sheets. Because of the heterogeneous nature of Diesel combustion, it is very possible that multiple combustion regimes could be defined within a single Diesel combustion event. The enigma of Diesel combustion is evident in the varied modeling strategies employed for Diesel combustion, ranging from the coherent flamelet model to the characteristic time model.

It is the objective of this research to develop a diagnostic tool that can be used to investigate the structures involved in combustion and also to determine the applicability of the technique to Diesel combustion. The diagnostic should provide the ability to characterize reaction zones within the spectrum of combustion from thin sheets to distributed reactions. The scales of observed combustion structures, thickness of reaction zones, and evidence of interaction with turbulence should all be provided by the technique.

Planar laser-induced fluorescence of the CH radical was chosen as a diagnostic technique which may satisfy these requirements. The CH radical is found in a thin region near the leading edge of reaction zones in all hydrocarbon combustion, and is therefore an excellent flame marker. However, CH is a difficult molecule for fluorescence techniques because of the diagonal nature of its vibrational transitions. The diagonal transitions, for which the vibrational state does not change, are at least two orders of magnitude stronger than off-diagonal transitions, for which the vibrational state changes during excitation or emission. Therefore, excitation or observation in off-diagonal bands is not desirable. However, the diagonal vibrational transitions are spectrally overlapped, so the spectral separation between excitation and observation wavelengths using only diagonal vibrational transitions is limited, making spectral filtering quite challenging.

In this diagnostic, excitation is performed in the (0,0) diagonal vibrational band of the CH $A^2\Delta \leftrightarrow X^2P$ electronic transition near 425 nm in the R branch, with observation from 428 nm to 440 nm in the Q- and P- branches of the same vibrational band. A narrow bandwidth, high rejection (10^6) holographic notch filter (HNF) centered at the excitation wavelength is employed to reject elastic scatter of the laser light from various sources. The HNF essentially blocks out scattered laser light as well as most of the emission from the R-branch, while passing emission from the Q- and P- branches, at up to 60% transmittance.

Excitation in the (0,0) band is advantageous because of the high population of the $v'=0$ ground state as well as the relatively strong absorption of this diagonal band. In high pressure combustion regimes where saturation of the excitation is unlikely due to high quenching, the strong absorption of the diagonal bands can yield excited populations 2 orders of magnitude greater than techniques which employ off-diagonal excitation. The excitation wavelength near 425 nm is also outside the reported absorption spectra of many PAH's, potentially reducing the

effect of PAH fluorescence observed in other off-diagonal techniques employing shorter wavelength excitation.

However, even with the high rejection of the holographic notch filter, complete rejection of elastic scatter may be difficult or impossible. Indeed, scatter from metallic surfaces and scatter from outside of the field of view that is not properly collimated can pass through the filter and contribute to the noise level. Although the HNF is narrowband, with a width of only 5-6 nm, the filter blocks most of the R-branch emission, only allowing observation of about 50% of the total fluorescence emission. The spectral purity of the dye laser used for fluorescence excitation is also very important. Since the signal is collected as little as 3 nm away from the excitation wavelength, scatter from dye laser emission outside the primary line (ASE) also contributes to the noise, since it is indistinguishable from the true fluorescence signal.

A Continuum Powerlite 8010 10 Hz pulsed YAG laser delivering 200 mJ per pulse at 355 nm was used to pump a Lambda Physik Scanmate 2E dye laser. The dye laser was operated with a stilbene-3/methanol solution to deliver 30 mJ per pulse at 425.015 nm in a 6 ns pulse. The output of the dye laser was formed into a 200 μm thick by 20 mm high vertical sheet using a combination of spherical and cylindrical lenses. The laser sheet was passed through the turbulent premixed propane-air flame produced by an 11 mm diameter laboratory Bunsen burner. The propane and air flow rates were metered to produce a variety of turbulence intensities and mixture strengths.

The fluorescence emission was collected perpendicular to the flame sheet so that the excited molecules in the sheet were imaged on the face of a 3710-D CidTech gated, intensified CID camera. The HNF was placed in the optical path between the object and image lenses, so that partially collimated light was received by the filter. A custom timing system was constructed which controlled the frequency and phasing of the camera, laser, intensifier gate and PC frame grabber to acquire the fluorescence images. Images were acquired at a rate of 1Hz.

Fluorescence images for the premixed propane-air flame at 1) Re_D=2000, Φ=1.2 and 2) Re_D=5000, Φ=1.5 are shown in Fig. 1. CH fluorescence is not present above 25 mm above the burner for the Re_D=2000, Φ=1.2 images because the flame cone was only about 25 mm high for this flame. The images have been enhanced through post-processing to improve the contrast and remove some noise. The images were acquired at five different heights above the burner exit for this flow condition at a rate of 1 Hz. At this slow acquisition rate, there is no flow continuity between images. Also, images at different heights were not acquired simultaneously, so there is no continuity between images at different heights above the burner. Using these flame images, the combustion regime for this burner can be qualitatively characterized as being composed of thin, wrinkled sheets.

Through post-processing, structures in the flame images can also be quantified. To the right of each of these images is a flame "skeleton," which is a single-pixel wide trace of the center of the flame fronts. Flame skeletons such as these will be used to determine a distribution

of the radii of curvature observed in these flames, which can be used to estimate the scales of the combustion structures. Additionally, the flame skeletons can provide a measure of the flame area density, giving an indication of the degree of wrinkling. The flame skeletons will also be used as an anchor for determination of flame thickness.

After establishing this technique for a premixed, atmospheric pressure flame, it will be applied to more difficult regimes, approaching the conditions of Diesel combustion. Employing the technique in higher pressure and non-premixed conditions will help to determine the eventual applicability of the technique to Diesel combustion.

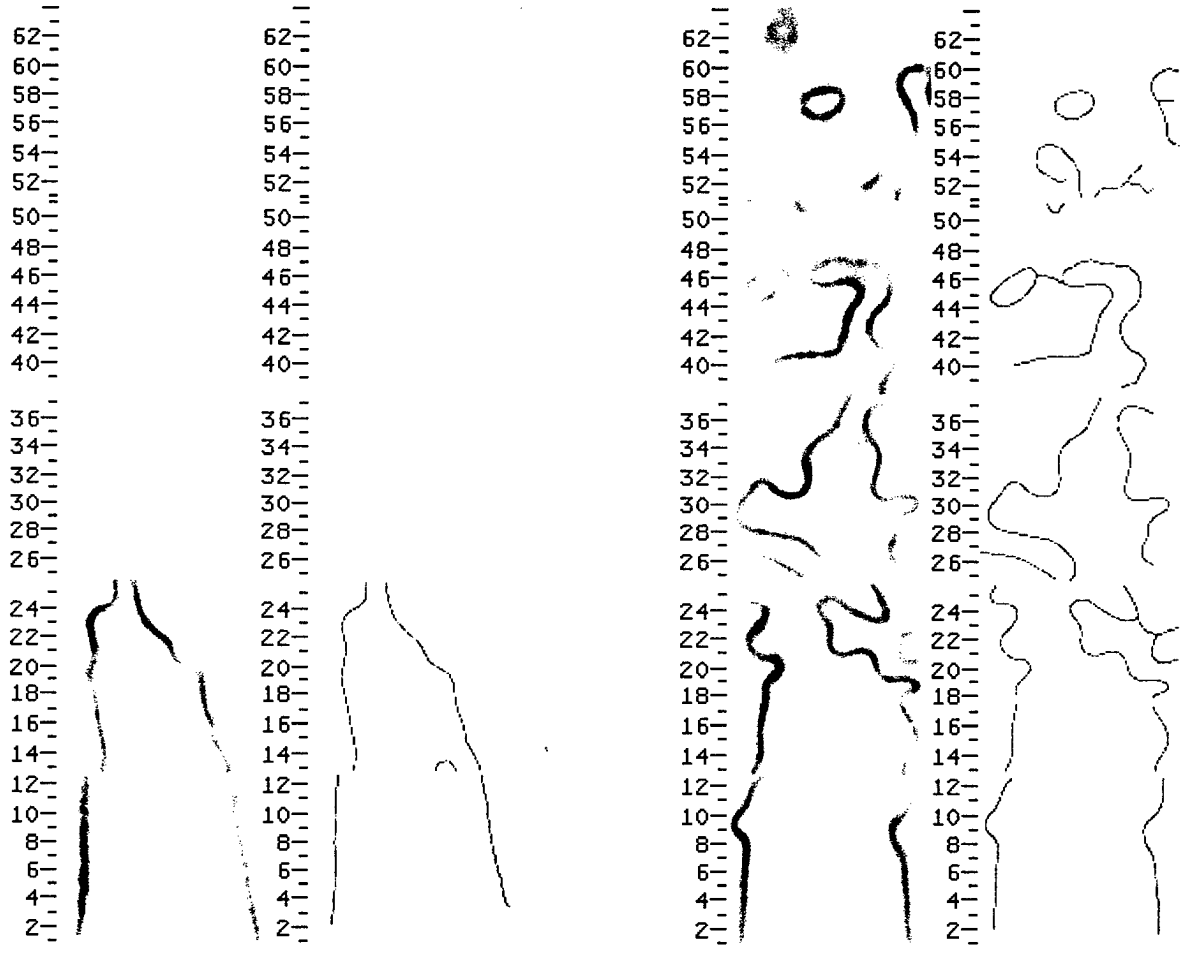

Figure 1: Fluorescence images and flame skeletons for Re_D=2000, Φ=1.2 (pair on left) and Re_D=5000, Φ=1.5 (pair on right). The scale on the left of the images is the distance above the burner exit, in mm. The flame skeletons were created using post processing algorithms developed at the UW Engine Research Center.

ADVANCED DIAGNOSTICS FOR REACTING FLOWS

AFOSR 98-1-0010

Principal Investigator: Ronald K. Hanson

High Temperature Gasdynamics Laboratory
Mechanical Engineering Department
Stanford University, Stanford, CA

SUMMARY/OVERVIEW:

This research is aimed at establishing laser-based absorption and fluorescence techniques for nonintrusive measurements relevant to air-breathing propulsion. Significant progress was made in the development of diode laser absorption diagnostics for combustion sensing and control, and for measurements at high pressures. New PLIF strategies are reported for imaging temperature in acetone-bearing gases and for imaging infrared-active species.

TECHNICAL DISCUSSION:

High-Pressure Diagnostics

Progress has been made on the development of a diode-laser absorption diagnostic to monitor H_2O and temperature in high-pressure environments. A critical step has been assembly of a code for calculation of water vapor spectra over a wide range of conditions. Experiments were conducted in a high-pressure cell to successfully validate the spectral simulation code at pressures to 20 atm and temperatures to 473 K (see paper 1). These experiments also validated use of the impact and additive approximations in modeling line shapes for densities up to 18 amagats.

Experiments in a high-pressure shock tube are underway to validate the spectral simulation code at even higher pressures and temperatures. Preliminary results are shown in Fig. 1. The top panel is a comparison between recorded data and the simulation at 40.4 atm and 1276 K. The bottom panel compares measured and calculated absorbance at 7117.4 cm^{-1} over a range of temperatures at a nominal pressure of 40 atm. Good agreement between the recorded data and the simulation is found. Work is in progress to utilize multiple laser sources at selected fixed wavelengths for simultaneous monitoring of water vapor and temperature at high pressures.

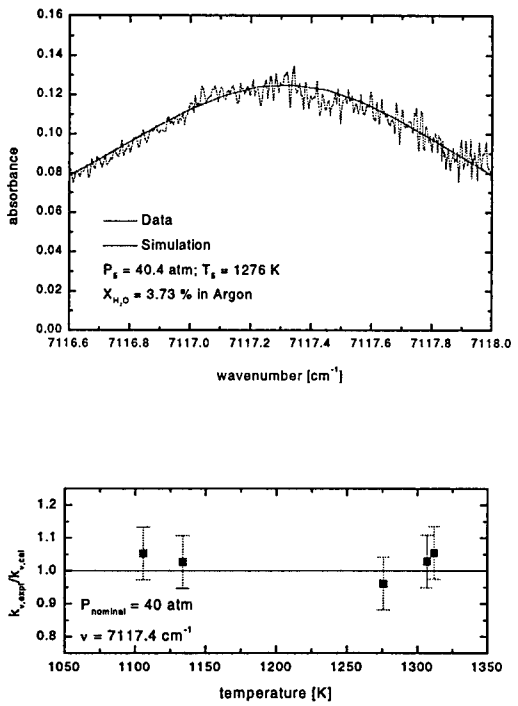

Fig 1. Shown in the top panel is a comparison between recorded data and simulation at 40.4 atm and 1276 K. The bottom panel compares recorded and calculated absorbance at 7117 cm^{-1}over a range of temperatures at a nominal pressure of 40 atm.

In a separate effort, we have completed design and ordered manufacture of a new high-pressure flat-flame burner which will be used for high-resolution spectroscopy of combustion gases at temperatures to 2000 K and pressures to 50 atm.

TDLAS Probe for Hypervelocity Flows

Recent experiments have demonstrated the capability and robustness of tunable diode laser absorption spectroscopy (TDLAS) techniques to measure temperature and velocity in high-enthalpy flowfields (see paper 2). An added benefit of the technique is the ability to diagnose the presence of minor or contaminant species. We have developed two separate TDLAS systems, one based on water vapor and a second based on atomic potassium. Water vapor is a critical contaminant when operating a hypersonic shock tunnel with a hydrogen driver, but of course is present as a product of combustion in scramjet testing. On the other hand, potassium has been discovered to exist naturally in minute quantities in Stanford's expansion-tube facility and in Calspan's 96" hypersonic shock tunnel (HST). This suggests the opportunity to capitalize on such tracer species without a perturbation to flowfield composition.

In Fig. 2, a schematic of a hardened potassium probe is shown. This probe contains the electro-optics required to pitch and catch laser beams through an undisturbed flow. Light is fed to the probe via a fiber-coupled diode laser system located remotely from the test facility.

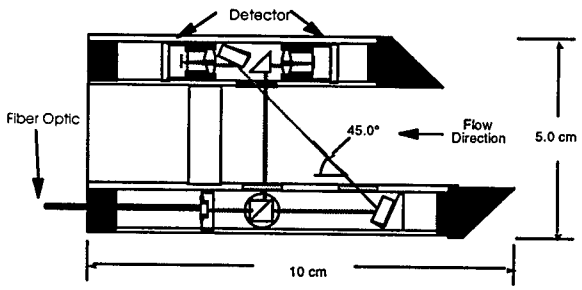

Fig. 2. A schematic of the TDL probe for measurements of potassium in hypervelocity flowfields. Two beams probe the test gas; the beam perpendicular to the flow provides an *in-situ* static absorption trace while the angled beam yields a Doppler shifted absorption for velocity measurements.

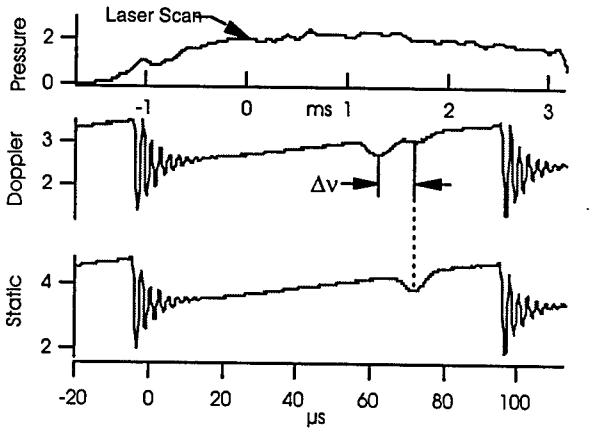

Fig. 3. Data traces from a 10 MJ/kg test at Calspan's 96" Hypersonic Shock Tunnel. The pressure trace (top) illustrates the location in time when the two laser scans (middle, bottom) were taken. The lower trace is a static absorption scan of potassium. The middle trace illustrates the recorded Doppler shifted (Δv) signal, corresponding to V = 4630 m/s.

Recently TDL measurements of water vapor and potassium were obtained in Calspan's 96" HST. The two probes were situated at the exit plane of the facility nozzle and exposed to the following free stream conditions: V = 4600 m/s, T = 600 K, and P = 7 torr. To our knowledge these are the first hypervelocity measurements based on potassium. In Fig. 3, a sample raw data trace demonstrates the Doppler-shifted absorption near the start of the test time.

Infrared PLIF Imaging

Infrared PLIF shows the potential for visualization of important species such as CO, CO_2, and H_2O that cannot be visualized using traditional PLIF techniques. In infrared PLIF, a tunable infrared laser source is used to excite vibrational transitions in molecules, and the resulting vibrational fluorescence is imaged onto an infrared camera. Preliminary analytical and experimental results have been obtained which demonstrate the feasibility of infrared PLIF for species concentration imaging.

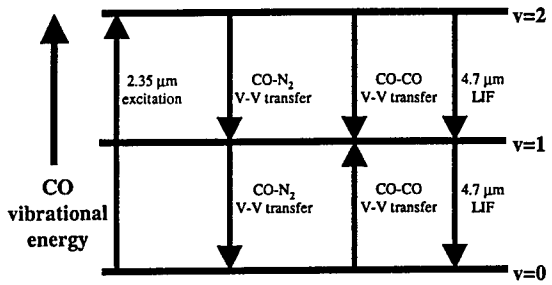

Fig. 4 Energy level diagram for energy transfer in the CO-air system for an infrared PLIF experiment. Fluorescence yield is determined by the competition between V-V transfer (with CO or N_2) and fluorescence at 4.7 μm.

Initial validation efforts have focused on CO due to its straightforward spectroscopy and energy transfer mechanisms. Fig. 4 shows the dominant energy transfer processes for CO-air mixtures with 2ν excitation at 2.35 μm and collection of fluorescence at 4.7 μm. This scheme has been used to visualize CO-air mixing at room temperature, demonstrating CO detectivity below 1%. Future work will seek to refine the current technique, as well as to investigate extensions to polyatomic molecules such as CO_2. These larger molecules, while more complicated to model, offer opportunities for higher signal levels due to stronger emission.

PLIF of Acetone for Temperature and Multiparameter Imaging

Acetone has proven effective as a tracer species for PLIF imaging, yielding large signal intensities with simple implementation. Since the fluorescence yield of acetone is limited by intersystem crossing, the strong compositional effects that arise through collisional electronic quenching in other diatomic tracers (*e.g.*, OH, NO) are avoided. However, there remain significant dependences of fluorescence on temperature and excitation wavelength, and weaker dependences on pressure and composition. Experimental measurements and modeling efforts aimed at characterizing these effects have led to new strategies for temperature imaging which offer important advantages relative to other schemes. At the same time, improved understanding of acetone photophysics has enabled quantitative imaging of concentration in non-isothermal flows. Simultaneous information on temperature and additional flow quantities is provided by multiparameter imaging methods that exploit interline-transfer CCD camera technology.

Acetone PLIF temperature imaging techniques have now been validated in a variety of flows. Single-excitation-wavelength temperature imaging, applicable when pressure and acetone seeding are uniform, provides single-shot temperature sensitivity as good as several degrees Kelvin with minimal experimental complexity, while a dual-wavelength approach is useful where acetone number density varies across a flowfield. We have implemented the dual-wavelength concept using an interline-transfer CCD camera to simultaneously image both temperature and mole fraction in an unsteady, laminar (Re = 370) acetone/air jet flowing over a 300°C cylinder (Fig. 5) and mixing with ambient air. By allowing two images to be acquired onto the same CCD array within 1-2 microseconds of each other, the interline-transfer camera makes possible straightforward multiparameter imaging. Applications include the measurement of temperature and mixture fraction in combustion chambers and evaporating fuel sprays. In flows in which uniform acetone seeding is possible, temperature and pressure can be measured simultaneously.

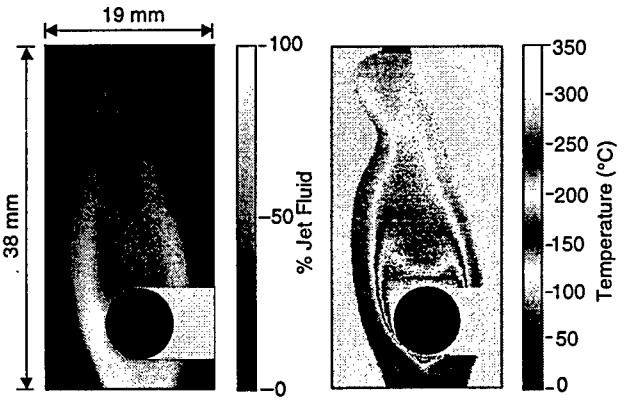

Fig. 5. Mixture fraction (left) and temperature (right) imaged in an unsteady, laminar (Re = 370) jet of acetone-seeded air over a heated cylinder (coming out of the paper). Excitation (left to right) was with a laser sheet at 248 nm (105 mJ) followed 2 μs later by a laser sheet at 308 nm (95 mJ).

CW Multiplexed Diode Laser Ring-Down Spectroscopy

A new diagnostic strategy for sensitive measurements of species concentrations has been developed based on continuous-wave (cw) cavity ring-down spectroscopy techniques using multiplexed diode lasers. Figure 6 shows the experimental schematic used. A pair of narrow-bandwidth diode (InGaAsP) lasers operating near 1.4 μm were multiplexed into a single path using fiber-optic components and injected into a stable optical cavity. The cavity consisted of an aluminum cylinder with high-reflectivity mirrors. One of the mirrors was mounted on a piezo-electric transducer to dither the cavity length. Acousto-optic modulators were used to interrupt the individual beam intensities in the cavity after sufficient buildup was achieved. The fraction of the transmitted multiplexed beam intensity leaving the cavity through the out-coupling mirror was directed onto a diffraction grating which spatially separated (de-multiplexed) the constituent wavelengths. Fast photodetectors were used to record the ring-down intensities of the individual beams. Ring-down time was determined from the transient decay of light by fitting the time-dependent intensity to a single exponential. Absorption measurements were determined from the difference of ring-down times with and without gas in the cell. For the present work, the diode lasers were tuned over overtone and combination vibrational bands of H_2O, isopropyl alcohol, and methanol to record high resolution absorption spectra of each species in the cell. The minimum detectable absorption corresponded to a measurement sensitivity of 7 ppb for H_2O, 60 ppb for isopropyl alcohol and 60 ppb for methanol.

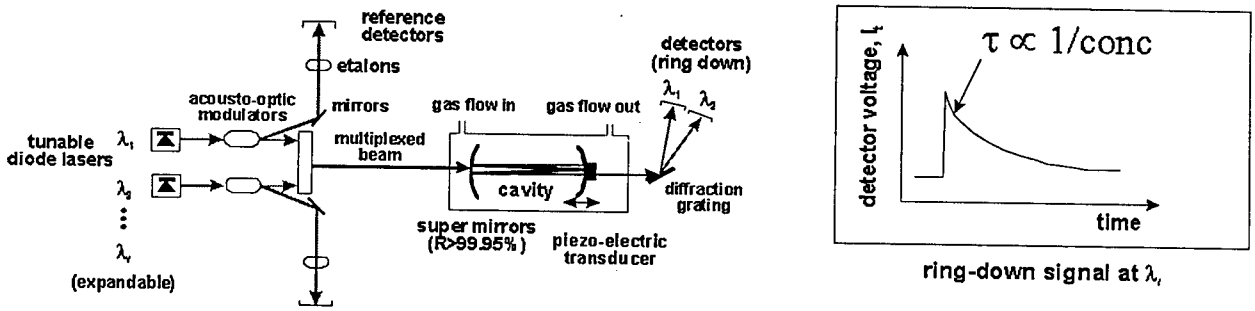

Fig. 6. (Left) Experimental schematic used for cavity ring-down measurements of multiple species in mixtures using multiplexed diode lasers. (Right) Example cavity ring-down voltage signal recorded in the cell. Species concentration is determined from the measured cavity decay time.

PUBLICATIONS/PRESENTATIONS:

1. V. Nagali and R.K. Hanson, "Design of a diode-laser sensor to monitor water vapor in high-pressure combustion gases," Appl. Optics, **36**,. 9518 (1997).
2. S.D. Wehe, D.S. Baer and, R.K. Hanson, "Tunable Diode-Laser Absorption Measurements of Temperature, Velocity, and H_2O in Hypervelocity Flows", AIAA-97-3267, 33rd Joint Propulsion Conference and Exhibit, July 6-9, 1997, Seattle, WA.
3. M.C. Thurber, F. Grisch, and R.K. Hanson, "Temperature Imaging with Single- and Dual-Wavelength Acetone Planar Laser-Induced Fluorescence," Opt. Lett. **22**, 251-253 (1997).
4. M.C. Thurber, F. Grisch, B.J. Kirby, M. Votsmeier, and R.K. Hanson, "Measurements and Modeling of Acetone Laser-Induced Fluorescence with Implications for Temperature Imaging Diagnostics," Appl. Optics, in press.
5. B.J. Kirby and R.K. Hanson, "Infrared PLIF Imaging of Gaseous Flows," AIAA Paper 98-0306 (1998).
6. R.M. Mihalcea, D.S. Baer and R.K. Hanson, "Diode-Laser Sensor for Measurements of CO, CO_2 and CH_4 in Combustion Flows," Appl. Optics **36**, 8745-8752 (1997).
7. R.K. Hanson, "Advanced Laser-Based Diagnostics for Shock Tube/Tunnel Flows," plenary paper, 21st Int'l. Symp. on Shock Tubes and Waves, July 20-25, 1997, Australia.
8. V. Nagali, S.I. Chou, D.S. Baer and R.K. Hanson, "Diode-Laser Measurements of Temperature-Dependent Collision Widths of H_2O Transitions in the 1.4 μm Region," J. Quant. Spectrosc. Radiat. Transfer, **57**, 795-809 (1997).

RESONANT HOLOGRAPHIC INTERFEROMETRY, AN INNOVATIVE TECHNIQUE FOR COMBUSTION DIAGNOSTICS

ARO CONTRACT NO. DAAL03-92-C-0019

Peter A. DeBarber, Ph.D.
Michael S. Brown, Ph.D.
Neal J. Brock

METROLASER, INC.
18010 SKYPARK CIRCLE #100
IRVINE, CA 92614-6428

This report summarizes our progress in the area of resonant holographic interferometry (RHI) during the last year. As described in previous reports, RHI is a nonintrusive optical technique combining the multi-dimensional imaging capability of holography, the phase sensitive detection of interferometry, and the species specificity of spectroscopy to make quantitative measurements of species concentration, temperature, velocity, pressure, mixing and other thermophysical quantities. Quantitative diagnostics such as RHI are needed to gain an understanding of the physics and chemistry of the combustion processes. Understanding these processes will enable more efficient combustors to be designed which will benefit both the military and commercial sectors.

Progress was made in establishing RHI as a quantitative technique and in improving our understanding of RHI in strongly absorbing media. Quantitative RHI measurements of sodium concentration in a static pathlength cell were made. The measurement data is currently being analyzed and compared to absorption measurement data obtained simultaneously. The data is also being compared to the results predicted by our RHI model. Progress was made in automating the process of converting RHI interferograms to concentration data. Phase Shift Interferometry was used to compute the wrapped phase map of the RHI interferograms. Phase unwrapping algorithms and other software were then applied to obtain concentration information. Modifications to the RHI model have been made to improve its prediction capability for strongly absorbing media.

Quantitative RHI Measurements - A static pathlength cell was constructed with a pathlength variation along its height dimension. The cell was evacuated and a small amount of sodium was placed inside. A tube furnace was constructed for the pathlength cell to precisely control the cell temperature and consequently the sodium vapor pressure. Sodium vapor pressure is a strong function of temperature, therefore the temperature of the pathlength cell must be uniform and known accurately in order to make accurate determinations of the sodium concentration. For example, at a temperature of 240C, an

uncertainty of one degree results in a 10% uncertainty in sodium concentration. Accordingly, the tube furnace was constructed 600 cm long with sealed window plates on each end and was wrapped in 7 cm of insulation to reduce thermal gradients (see Figure 1). Five thermocouples were evenly placed along the interior length of the furnace to record the oven and cell temperature.

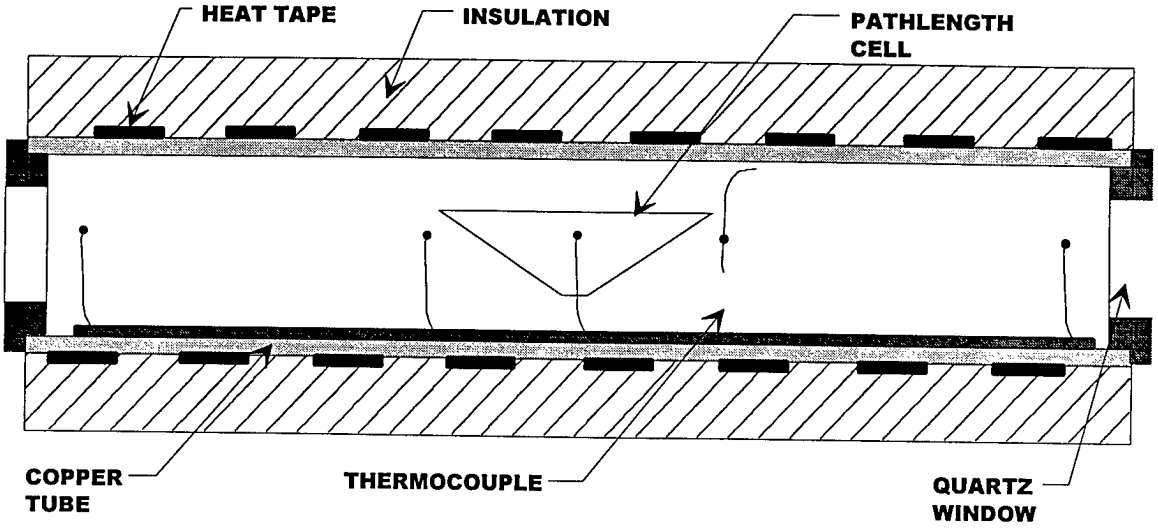

Figure 1. Cross-section of tube furnace with pathlength cell.

A two reference beam RHI system previously developed under this research program was set up in the laboratory of Professor Derek Dunn-Rankin located at the University of California, Irvine. Phase Shift Interferometry (PSI) data reduction was facilitated by the use of a Correcting Holographic Optical Element (CHOE) as described in previous reports. The imaged view of the sodium pathlength cell is diagrammed in Figure 2.

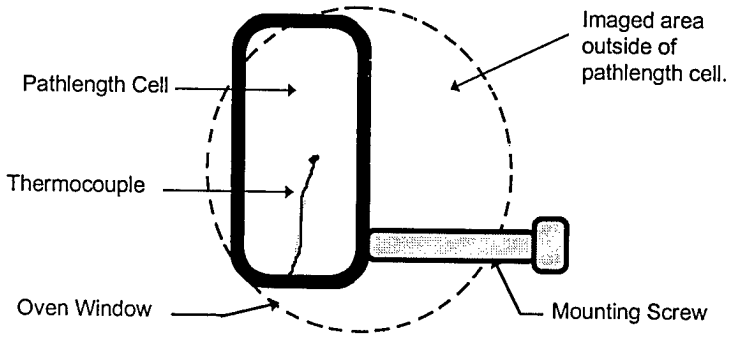

Figure 2. Imaged view of pathlength cell in oven.

RHI data for five different sodium concentrations were recorded using the RHI holocamera. Prior to acquiring the data, careful absorption point measurements were made to determine the recording laser energy necessary to minimize sodium saturation effects. These measurements revealed the need to reduce our hologram size in order to achieve adequate exposure of the film without saturating the sodium. For each RHI data point a corresponding absorption point measurement was made and the temperature at five points along the oven interior was recorded. The absorption data provided a separate method for measuring the sodium concentration as well as detecting saturation. The

temperature data provided a means to calculate the sodium concentration based on its vapor pressure. Thus two separate methods for determining the sodium concentration in the pathlength cell could be compared to the RHI measurements.

Data Conversion - A method was developed for converting the raw RHI interferograms into concentration data. A Correcting Holographic Optical Element facilitated the use of the Phase Shift Interferometry (PSI) data reduction technique. Four phase-shifted interferograms were acquired similar to the interferogram shown in Figure 3a. Several horizontal tilt fringes were added to help visualize the sodium density gradient in the cell. A shift between the fringes inside and outside the cell indicates the presence of sodium. The fringe shift can be seen to increase from bottom to top in Figure 3a as expected due to the increase in pathlength from bottom to top. MetroLaser PSI software was used to produce the wrapped phase map shown in Figure 3b. Phase unwrapping algorithms were then applied to calculate the unwrapped phase map shown in Figure 3c. The unwrapped phase map is a 16-bit grayscale image of the resonant phase shift superimposed with the tilt phase shift. The tilt phase shift is the phase shift added by the presence of the horizontal fringes. The tilt phase shift is removed by subtracting the slope of the grayscale variation outside the pathlength cell from the slope of the grayscale variation inside the cell. The resulting image will then show a grayscale variation inside the cell due only to the resonant species. No grayscale variation should be present outside of the cell since there is no sodium there. When the tilt phase shift is removed the resulting grayscale variation due to the sodium is such a small fraction of the 16 bit image that it is difficult to reproduce with a laser printer. Therefore, an example of the tilt corrected image is not shown.

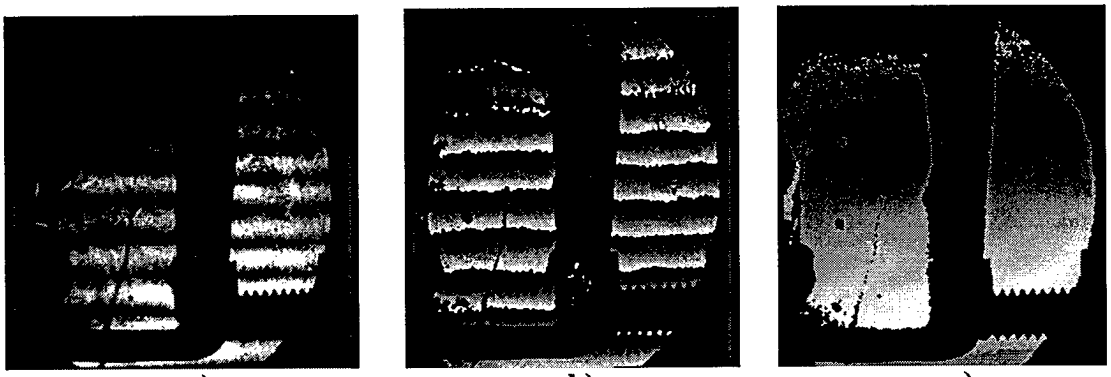

a) b) c)

Figure 3. a) Raw RHI interferogram of sodium in pathlength cell. b) Wrapped phase map of RHI interferogram produced by PSI software. c) Unwrapped phase map.

A method was developed for converting the 16 bit grayscale image into concentration data. First the image is converted to an ASCII file so that the pixel data can be imported to a graphing program. Then columns of pixels from inside and outside the cell are averaged independently and plotted. The results for the RHI data shown in Figure 3 are shown in Figure 4. The slope corresponds to the sodium concentration variation with cell height.

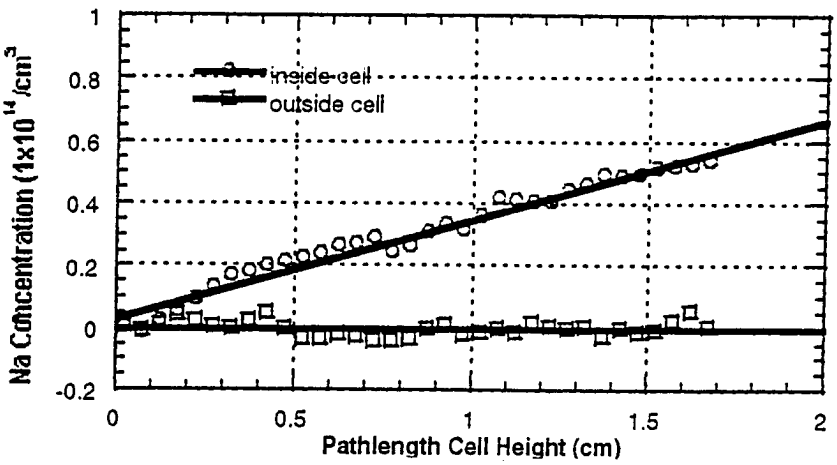

Figure 4. Plot of sodium concentration variation inside the pathlength cell.

Improvements to RHI model - In examining RHI measurements to date and comparing them with model predictions, we have found that the model often under predicts the amount of fringe shift actually seen, particularly for the case of a strongly absorbing target species. Progress was made understanding this discrepancy by considering more sophisticated model approaches. To date, we have largely made use of the standard expressions for the absorption coefficient and refractive index. These expressions are derived for an incoherent collection of simple "dipole oscillators" undergoing steady state excitation by an electric field. The absorption coefficient and refractive index are then found to be the imaginary and real parts of the complex susceptibility. Separation into imaginary and real parts for this model is facilitated by assuming that the refractive index is essentially one. For cases of optically thick media this assumption is not always valid. We therefore have also made use of the expressions for the absorption coefficient and refractive index that are found when the above assumption is not invoked. However, we find that this refinement of the model does not significantly improve the agreement between prediction and measurement.

We believe that further analysis of the Na data will require modeling of pulse propagation effects. In short, for strong coupling between the incident beam and the target species (as is the case for our Na measurements) the instantaneous complex refractive index becomes a function of time and varies with the amplitude of the incident electric field envelope. The total electric field traveling through the test region is a sum of the incident field and the fields re-radiated by the excited Na atoms. One consequence of the time-dependent refractive index is the simultaneous time dependence of the re-radiated fields which in turn alter the pulse shape of the total electric field traveling through the test region. The phase of the total electric field changes as well in a fashion more complicated than that predicted by the simple model that assumes weakly driven oscillators. Fortunately, for species with weak incident beam coupling, such as OH, the simple model more accurately predicts fringe shift and there is no need to consider pulse propagation affects.

NUMERICAL MODELLING OF TWO-PHASE NOZZLE FLOWS

ARO Grant No. DAAH04-94-G-0328

Principal Investigator: D.Foster, J.Martin, M.Corradini, P.Farrell, J.Ghandhi, R.Reitz, C.Rutland

Engine Research Center, Univ. of Wisconsin, 1500 Engineering Dr, Madison WI 53711

Summary: Injector nozzle flows are of interest in diesel combustion engines; i.e., under high pressure conditions. This paper presents current models and results for two-phase nozzle flows under subcooled and superheated conditions. Our approach is a multi-dimensional numerical model of the nozzle with boundary-fitted coordinates and a thermal non-equilibrium model between the liquid and vapor. Results predict the extent of vaporization spatially and temporally for conditions useful in spray analyses.

Authors: M. Corradini, D. Schmidt

Introduction

The study of hot liquid and cold liquid flows through nozzles have been typically carried out independently of each other. The nozzle discharge of hot liquids has been studied by aerospace, chemical and nuclear engineers interested in process engineering and associated loss prevention safety. In contrast cold liquid discharge has been of interest to mechanical engineers who wish to understand a variety of applications, such as high pressure fuel injector nozzles and high speed liquid cutting jets. The former processes involves flashing and boiling of the liquid, while the latter might involve cavitation. Logically, there are similarities between the physics involved and our work addresses these issues and provides some physical insight into the phenomena. This is of particular interest in current diesel engine injection systems where cavitation may have a distinct impact on spray behavior.

Hydrodynamics determine the flow of cold liquid through the nozzle, subject to the constraints imposed by the thermodynamics of the fluid. As the liquid temperature increases, thermodynamics as well as the kinetics of nucleation and boiling assume a larger role in the physical processes. Consider the idealized nozzle geometry depicted in Figure 1. In this conceptual picture we have the nozzle length to be a few nozzle diameters long; i.e., $L/D \sim 2 - 10$. This is important in our applications since we do not consider an orifice or nearly that geometry ($L/D < 1$), since the nozzle will not behave as an orifice and any associated 'hydraulic flip' phenomena is minimized; i.e., this implies that the downstream fluid does not flow upstream to the nozzle entrance. In this geometry, nozzle flow is driven by the high pressure upstream reservoir and accelerated through the nozzle geometry. If the liquid is highly subcooled relative to the exit pressure conditions, cavitation may occur at the nozzle entrance as the velocity increases (Kato et al, 1994; Nurick, 1976), dramatically affecting the discharge flowrate. As the liquid increases in temperature, mass transfer can affect this behavior with vapor nucleation and flashing.

This paper describes our development of a multi-dimensional model for flashing nozzle flow. Past attempts to model cavitation numerically can also be applied to a hot fluid. For example, Chen and Heister (1995) developed a cavitation model based on an assumed relation for interphase mass transfer. The relationship was similar to a relaxation rate equation. This relaxation rate approach seems workable, but the specific physics need to be grounded in observed data on nucleation and flashing flow.

Model Development

A multi-dimensional numerical model of nozzle flow was constructed in order to include the effects of multiphase flow under a range of liquid temperatures and pressures including non-equilibrium effects. Recognizing the similarity to liquid flows with cavitation, we have adapted a cavitation model to predict the behavior of the liquid (Schmidt, 1997). The equations for conservation of mass and momentum were solved using a second order spatial differencing and third order Runge-Kutta time stepping. This assumes that the multiphase fluid is homogeneous; i.e., both phases flow with equal velocities and pressures. The equations are transformed to a computational grid and solved in finite difference form. To avoid density oscillations, the shock capturing scheme of Zijlema (1996) was used in the continuity equation and the density constitutive equation. A mass correction was employed when the density fell below a lower bound and this resulted in relative mass error of much less than 1%. The pressure is solved for iteratively using a bi-conjugate gradient solver with Jacobi preconditioning. Fourth order numerical viscosity was added to the momentum equation to help ensure stability. For the inlet and the outlet boundary conditions the pressure field is fixed and the velocity is calculated. An incompressible flow solution through the nozzle was used as an initial condition. The equations are typically solved on a computational grid that is less than 100 by 50, transformed to rectangular coordinates (Figure 1). To avoid a singularity in the mapping from the physical to the boundary fitted coordinates, the corner of the nozzle is rounded to a radius of 1/40 of the nozzle radius.

The conservation of energy equation assumes the flow is frictionless and adiabatic. These assumptions lead to a condition of constant stagnation enthalpy for the fluid. At this stage the model is an homogeneous equilibrium formulation. However, it is known that at modest subcoolings (cavitation numbers between 0 and 1), the effects of nonequilibrium vapor nucleation and condensation become important. Thus, our approach is to introduce a non-equilibrium quality and relate it to the actual thermodynamic equilibrium quality with a Homogeneous Relaxation Model similar in concept to that recently suggested by Downar-Zapolski (1996). The local quality is defined as

$$Dx / Dt = - (x - \underline{x}) / \Theta \qquad (1)$$

where x is the local quality, $\underline{x}$ is the thermodynamic equilibrium quality, and Θ is the local relaxation time, which the authors correlated to density and pressure. We formulate this non-equilibrium equation of state in terms of the local density and local pressure and then use their correlation for Θ, given by

$$\Theta = \Theta_0 \, \varepsilon^{-0.5} \, \psi^{-1.75} \qquad (2)$$

where ε is the local void fraction and ψ is the absolute value of the ratio of the difference of the inlet saturation pressure to the local pressure divided by the difference in the critical pressure to the inlet saturation pressure. The experimental data base is from flashing liquid flows and thus may be in error for condensation. However, in this region where the cavitation number is below 1, our experience indicates that the vaporization rate is more crucial than condensation. At higher values of the cavitation number (1 to 2), equilibrium behavior once again seems to be a good assumption again.

Current Results and Observations

In order to assess the model behavior, the experiments of Mironov (1987) and Reitz (1990) were modelled using this two-dimensional model. The mass flow data of Mironov are a test of the model under certain subcooled conditions, while the data from Reitz are a good test under the conditions of

flashing flow. This can be a significant improvement over an analytical model or a one-dimensional model; in addition, the two-dimensional formulation allows for prediction of local vapor void, pressure and velocity information. The results are shown in Figures 2 and 3. All the results are nondimensional using three scales; the upstream pressure, the saturated liquid density and the nozzle diameter. Actual thermodynamic properties are from a pure hydrocarbon simulant for diesel fuel. The simulations were performed until a steady-state flow was achieved (up to a nondimensional time of 50). The velocity normal to the exit and the density at the exit were integrated to predict the mass flow and coefficient of discharge. The coefficient of discharge was plotted in Figure 2 along with the data of Mironov (1987) for a nozzle of L/D of 4.0. The model does quite well compared to the data at higher values of the cavitation number. At lower values the 12% deviation may be due in part to the fact that the nozzle grid had a slightly rounded corner whereas the experimental nozzle was described as a sharp leading edge. This model is also capable of simulating a flashing flow as Figure 3 indicates compared to Reitz's data. The geometry was similar and the test involved holding the upstream and downstream pressures constant while increasing the water temperature; i.e. the associated saturation pressure. Reitz noted the flowrate gradually decreases until a threshold where it fell to almost zero. An analytical model like Nurick's (1976) cannot even predict the qualitative behavior observed. Our model does show the observed behavior and identifies the threshold at which the flow markedly decreases. The model indicates that this change occurs at $0.4 < K < 0.5$ due to the movement of the choke plane from the nozzle entrance to its exit as flashing occurs. Although these results are encouraging, they are limited. This model must be compared further to near saturated and subcooled nozzle flows for more fluids.

References

Y. Chen, S.D.Heister, "Two-Phase Modeling of Cavitated Flows," Computers and Fluids, V24, No 7, p799 (1995).

P. Downar-Zapolski, Z.Bilicki, L.Bolle, J.Franco, "The Non-Equilibrium Relaxation Model for One-Dimensional Flashing Liquid Flow," Int'l Jnl of Multiphase Flow, V22, No3, p473 (1996).

H.Kato, H.Kayano, Y.Kageyama, "A Consideration of Thermal Effect on Cavitation Bubble Growth," Cavitation and Multiphase Flow, ASME FED V194 (1994).

Y.V.Mironov, N.S.Razina, "Supersonic Effects with Subcooled Water Flowing Through Cylindrical Nozzles with a Sharp Inlet Edge," Thermal Engineering, V34, No 10 (1987).

W.H.Nurick, "Orifice Cavitation and Its Effects on Spray Mixing," Jnl of Fluids Engineering, V98, p681 (1976).

R.D.Reitz, "A Photographic Study of Flash-Boiling Atomization," Aerosol Science and Technology, V12, p561 (1990).

D.Schmidt, A Model for High Speed Cavitating Nozzle Flows, PhD Thesis, Univ of Wisconsin (1997).

M.Zijlema, "On the Construction of a Third-Order Accurate Monotone Convection Scheme with Application to Turbulent Flows in General Domains," Int. Jnl for Numerical Methods in Fluids, V22, p619 (1996).

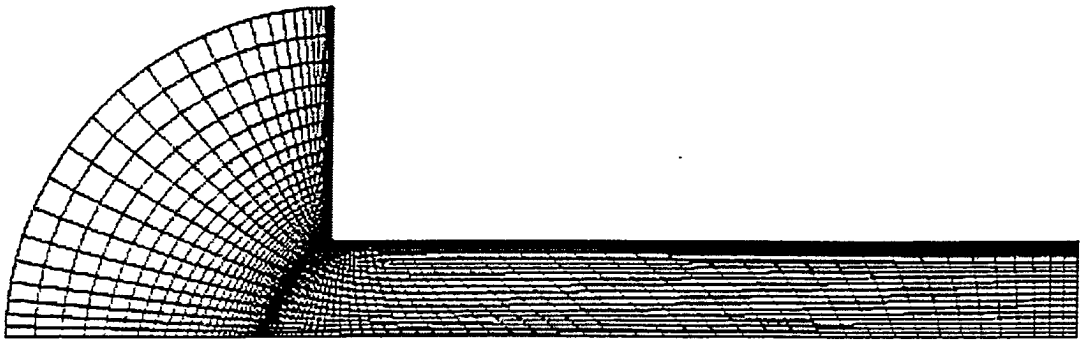

Fig. 1 Computational grid. The left boundary is the inlet, the right boundary is the exit. The lower boundary is a line of axisymmetry and the upper boundary is the nozzle wall.

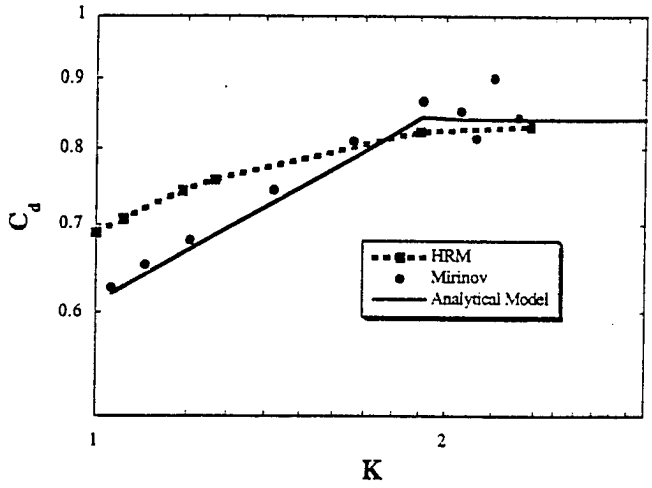

Fig. 2 Comparison of numerical results with the experimental data of Mironov and the predictions of the analytical cavitation model.

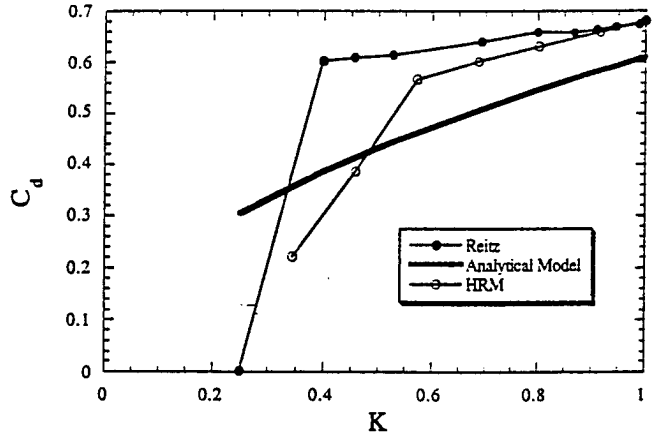

Fig. 3 Comparison of coefficient of discharge predictions to experimental data under superheated conditions. The point at which Reitz could no longer measure mass flow is plotted as zero discharge.

FLUORESCENT DIAGNOSTICS AND FUNDAMENTAL APPROACHES TO DROPLET, SPRAY, ENGINE, AND AERODYNAMIC BEHAVIOR

U.S. ARO Grant DAAG55-97-1-0265

Principal Investigator:

Lynn A. Melton
Department of Chemistry
University of Texas at Dallas
Richardson, TX 75083-0688

Co-Principal Investigator:

John H. Stufflebeam
United Technologies Research Center
East Hartford, CT 06108

SUMMARY/OVERVIEW:

Both UT-Dallas (UTD) and United Technologies Research Center (UTRC) have initiated experiments to investigate the shear field in liquid fuel sheets, ligaments and droplets by non-intrusive, optical techniques. The program at UTD emphasizes the development of fluorescent dopants whose fluorescence changes in response to shear within the liquid; these diagnostics should be appropriate for PLIF measurements. The program at UTRC utilizes birefringence, induced by liquid strain rate, on fuels seeded with specially formulated liquid crystal mixtures. Fringe patterns produced by interference of the light beams enable quantitative measures of the strain rate; these diagnostics should be appropriate for line-of-sight measurements. The data obtained with these shear diagnostics should provide information that is applicable to physics-based modeling efforts of primary atomization processes.

TECHNICAL DISCUSSION

Understanding the formation, heating and evaporation of fuel sprays is important for the design of gas turbine combustors and diesel engines. Currently droplet formation is empirically modeled (i.e. Rosin-Rammler distribution); physics-based models would provide more accurate predictions of combustor performance. Droplet size and trajectory initial conditions are determined by primary atomization processes, i.e., liquid sheet breakup into ligaments, which subsequently form droplets, and yet, the primary atomization process has not received adequate attention in experiments and modeling. Knowledge of the intensity and distribution of shear stress and strain rate in the liquid ligament is critical. The shear drives strain patterns that lead to breakup, which, in turn, influences convective thermal processes in the spray. These

mechanisms effect overall spray properties such as penetration, droplet size distribution, vaporization, and combustion performance relating to emissions (NOx) and efficiency.

AT UTRC

Phototelasticity is used extensively to measure the strain field of two dimensional solid objects by sensing the birefringence of orthogonally polarized light beams. Stress present in a normally isotropic medium causes the formation of a unique optic axis parallel to the direction of applied stress. Wavefronts that are propagated perpendicular to this optic axis are polarized into orthogonal waves with their planes of vibration parallel and perpendicular to the direction of stress. The stress produces an anisotropy in the index of refraction (birefringence) for the two polarizations and thus a relative retardation or phase shift between the waves. The retardation is proportional to the stress, cumulative over the optical path.

$$r = C \cdot (P - Q) \cdot d$$

where r is the retardation between polarizations; C, the stress-optical coefficient of the medium; P and Q, the principal stresses in the medium, and d is the thickness of the sample. If the two waves are recombined to a single polarization upon exiting the sample, interference will be produced and can be quantitatively recorded as a fringe pattern similar to an interferogram. The intensity of light is given by:

$$I = a^2 \cdot \sin^2(2 \cdot \alpha) \cdot \sin^2 \frac{\pi \cdot r}{\lambda}$$

a^2 is the intensity of the incident polarized beam, α is the angle between the incident polarization and the axis of the principle stress and λ is the wavelength of incident light

Normal liquid fuels do not have birefringent properties but the class of compounds known as liquid crystals do exhibit polarization effects when subjected to changes in their environment. The major use of these compounds has been in the field of thermometry. However, they are also sensitive to changes in shear stress, and this property has been exploited to indicate boundary layer transition on aerodynamic surfaces. By using them as additives to the liquid fuel, an *in situ* strain transducer is produced. Special formulations have been developed that show sensitivity to shear and are independent of temperature variations. Liquid crystals are composed of long, rod-like molecules that change their orientation upon exposure to shear stress, the reorientation produces a birefringence which can be visualized with polarization sensitive optics as described above. Liquid crystals dispersed in a liquid fuel will provide sensors of the shear stress in their local region, and the anisotropic refractive index will be monitored with imaging equipment.

Photoelastic experiments are underway at UTRC. An apparatus was configured that demonstrated the desired interference effects (fringes) from a solid sample under strain, then the

apparatus was reconfigured to study liquid fuel samples (Figure 1). Liquid crystal formulations were acquired from Hallcrest, Inc. The samples (BN/R50C, CN/R3 and CN/R7) are all shear sensitive (temperature insensitive), unencapsulated formulations, chosen to cover a wide viscosity range. Experiments are in progress to determine the optimum concentration of liquid crystals for solutions in various solvents, including decane and hexane, and to quantify the photoelastic properties of the medium.

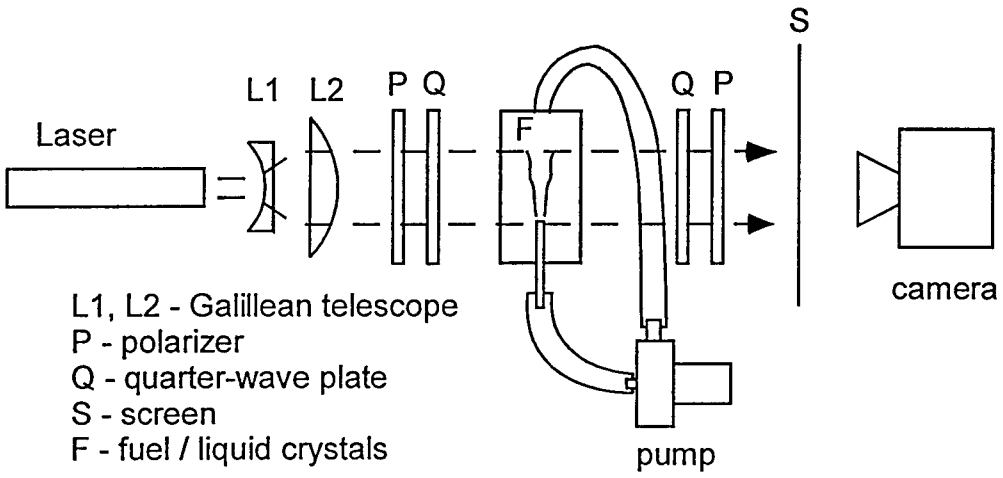

Figure 1.

AT UTD

A commercial viscometer which measures viscosity at specified shear rates of 1-1500 cm^{-1} has been modified to accept a fiber optic coupling to the SPEX spectrofluorimeter, and thus fluorescence spectra as can be measured as a function of shear rate.

The search for effective fluorescent shear sensing molecules has now identified two classes of molecular targets: (1) direct shear sensors, i.e., molecules whose fluorescence (intensity, spectra, polarization, etc.) is affected by shear in the fuel, and (2), indirect shear sensors, i.e., molecules whose fluorescence is affected by the change in conformation of a shear-sensitive (polymeric?) additive to the fuel. The direct strategy is simpler in concept, more difficult to achieve, and less likely to yield sensors which affect the fuel atomization process; the indirect strategy is more complex in concept, more likely to yield near term sensors, and more likely to yield dopant systems which affect the atomization process. Experiments are currently underway involving preliminary tests of both direct and indirect shear sensors.

A collaborative project with Ford Motor Company has come to fruition in the past year. Fluorescent diagnostics which can be use to measure the thickness of a film of (automotive) fuel on a cylinder wall, under combustion conditions, have been developed. These diagnostics, based on cyclohexanone or methylcyclopentanone, are (1) coevaporative with a realistic, simulated

gasoline, (2) virtually unaffected by oxygen quenching, and (3) virtually unaffected by changes in liquid phase temperature. Calibration procedures have been developed, and PLIF images of the time-dependent thickness of a simulated fuel spray onto a heated steel plate have been obtained. The basic calibration procedure involves capturing PLIF images with a CCD camera as a function of the amount of the liquid mixture on the surface of a (heatable) metal disk (a 1" diameter, 0.8" deep, cylindrical hole was cut into a 1.5" dia.aluminum cylinder). The amount of liquid is determined by weight; the disk sits on a (computer readable) top loading balance. In the first calibration method, liquid is pipetted onto the disk, and the PLIF images are captured as a function of increasing liquid film thickness. In the second calibration method, the disk is heated, the full aliquot of liquid is pipetted onto the disk, and PLIF images are obtained at several seconds intervals as the liquid evaporates. The decreasing amount of liquid (and thus the decreasing liquid film thickness) is determined as a function of time from the computer readout of the balance. Figure 2 shows the combined results of the two calibration methods (the two different sets of data were not scaled to match). At present, the diagnostic system gives linear behavior for fuel films thicknesses up to 1.4 mm, which should meet the requirements for automotive diagnostics.

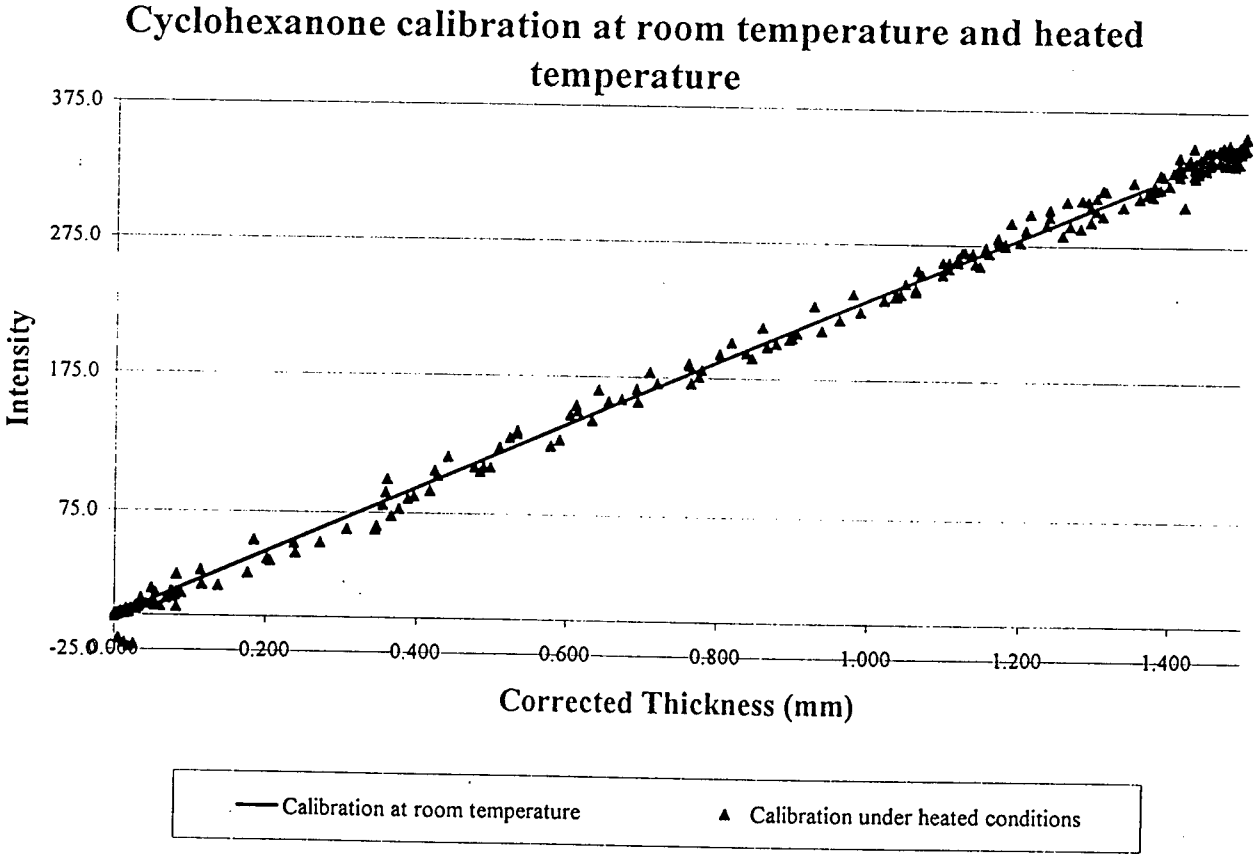

Figure 2

THE EVAPORATION OF LIQUID DROPLETS IN HIGHLY TURBULENT GAS STREAMS

ARO Grant No. 34199-EG

Principal Investigator: Richard D. Gould

Dept. of Mechanical and Aerospace Engineering
North Carolina State University
Raleigh, NC 27695-7910

SUMMARY/OVERVIEW

Experimental measurements show that relatively mild gas phase turbulence can increase the heat/mass transfer rates from liquid droplets by as much as *30 - 50%* when compared to laminar flow evaporation rates at the same droplet Reynolds number based on mean upstream velocity. Thus, the objective of this research program is to better understand the physical processes governing the heat/mass transfer around single liquid droplets in turbulent air flow. One result of this effort is a heat/mass transfer correlation as a function of droplet Reynolds number, Prandtl number and gas phase turbulence intensity. The goals during this project period were to validate this correlation over a wider range of blowing numbers and to gain physical insight into why such mild gas phase turbulence has such a large effect on evaporation rate. Currently, flow visualization studies of the concentration boundary layer around acetone droplets and naphthalene spheres are underway to address this second goal.

TECHNICAL DISCUSSION

As mentioned above, the objective of this research program is to gain a physical understanding of the heat/mass transfer process for turbulent gas phase flow around single liquid droplets. Over the past three years experimental measurements made in the well controlled and characterized turbulent air flow in the test section shown in Figure 1 indicate that the evaporation rate is function of gas phase turbulence parameters in addition to droplet Reynolds and Prandtl number. Droplet diameter, mean air velocity and air temperature were varied independently to determine their effects on droplet evaporation rate. The measurements indicate that relatively mild gas phase turbulence (≈ 5 - *10%* turbulence intensity) can increase the heat/mass transfer rates from liquid droplets by as much as *30 - 50%* when compared to laminar flow evaporation rates at the same droplet Reynolds number based on mean upstream velocity. A heat transfer correlation which accounts for gas phase turbulence level was developed,

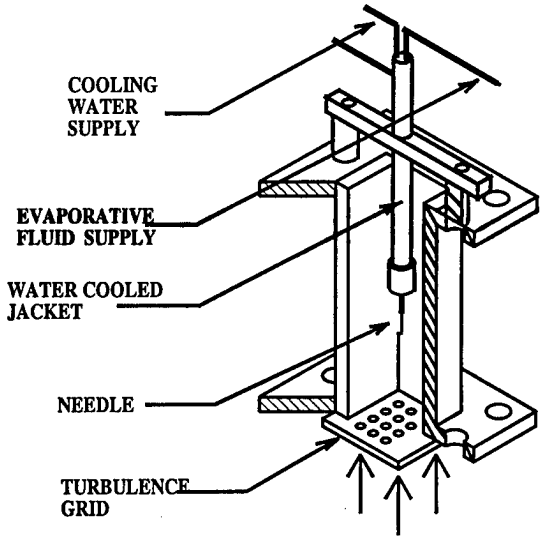

Figure 1. The wind tunnel test-section

$$Nu_f (1+B_H)^{0.7} = 2 + 0.58\,\mathrm{Re}_{\mathrm{mod}}^{1/2}\,\mathrm{Pr}_f^{1/3}\left[1+0.07TI^{0.843}\right] \qquad (1)$$

for the ranges, $50 < Re_{mod} < 1500$, $0.7 < Pr_{mix,f} < 1.0$, $0 < B_H < 0.14$, $0 < TI < 12\%$. This correlation degenerates to existing published laminar flow correlations with excellent agreement when no gas phase turbulence is present. Here B_H is the mass transfer number (or B number)

based on enthalpy. Water, methanol, ethanol, acetone, hexane and heptane liquid droplets were used in generating this correlation (Yearling (1995), Jobin (1997)). Water, methanol, ethanol and acetone have since been discarded as evaporating liquids due to, low B number for water, water vapor absorption of the alcohols and the low surface temperature of acetone droplets which may lead to water vapor condensation (dew point –5 C) on the droplet surface. Wind tunnel air humidity measurements are now made prior to each evaporation rate measurement and test conditions are set so that water vapor condensation does not occur.

A new focus was initiated recently to access whether high surface blowing (i.e. high B number) isolates the droplet from the free stream gas phase turbulence. Some earlier measurements (Jobin, (1997)) seem to indicate that high blowing negates the augmentation due to gas phase turbulence. Unfortunately, heated air is required to attain high B numbers and the calibration of the hot wire anemometer (used to measure mean velocity, and thus Reynolds number) becomes suspect in heated air. At this point the data suggesting this phenomena are somewhat inconsistent and thus need further validation, but it does seems physically plausible that high surface blowing would isolate the droplet surface from the free stream turbulence. Further studies are continuing to investigate whether high blowing does isolate the droplet.

A number of changes were made to the experimental apparatus during the past year in an effort to improve accuracy. Originally, hot wire anemometry was used to characterize the gas phase turbulence to which the droplet is exposed. Presently, a fiber optic probe based single component laser Doppler velocimeter (LDV) is being used to characterize the gas phase turbulence in the test section. Now no calibration is necessary and the turbulence in high temperature air can be measured non-intrusively. In addition, a completely redesigned syringe pump using a precision micrometer barrel as its basis is used to supply fluid to the liquid droplets in balance to that which evaporates such that the droplet retains the same diameter while measurements are made. The goal of these changes is to limit the experimental uncertainty to ±10%. Recent measurements using this redesigned facility for suspended heptane droplets are shown in Figures 2 and 3 below.

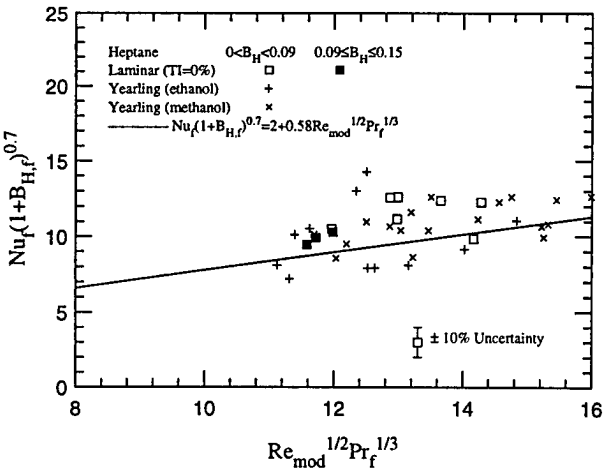

Figure 2. Laminar flow measurements

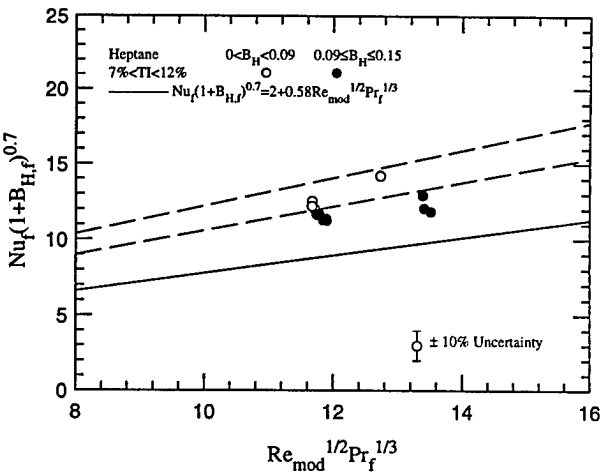

Figure 3. Turbulent flow measurements

The square symbols shown in Figure 2 denote measurements made in laminar flow using the LDV system and the redesigned syringe pump over two blowing number ranges. Also included in this figure are the data of Yearling (1995), using ethanol and methanol droplets, and the correlation (solid line) for droplet evaporation in laminar flow by Renksizbulut and Yuen (1983). The data are consistent which suggests that the new system is operating correctly. Figure 3 shows recent measurements in turbulent flow (7% < TI < 12%) over two blowing number ranges. The lower and upper dashed lines represent the correlation given by Eq. (1) for a turbulence intensity of 7 and 12%, respectively. The low blowing cases (opened circles) are bounded by these dashed lines indicating reasonable agreement with the previous measurements, which were used to construct this correlation. The high blowing cases (solid circles) show slightly lower evaporation rate than the low blowing cases at the same flow conditions indicating that blowing may indeed

isolate the droplet from the freestream turbulence. Clearly the evaporation rate is still larger than for the laminar flow case, so blowing does not completely isolate the droplet from the freestream turbulence.

An ASSERT project was recently initiated to address the second goal of this research program; gaining physical insight into why such mild gas phase turbulence has such a large effect on evaporation rate. Here, planar laser induced fluorescence (PLIF) measurements were made to obtain qualitative concentration measurements of the gaseous boundary layer surrounding the droplet. A schematic diagram of the PLIF setup is shown in Figure 4. The beam waist at the droplet position is approximately 16.5 μm with this system. Both acetone droplets and naphthalene spheres (as model evaporating "droplets") were used. Naphthalene was chosen because naphthalene fluoresces when irradiated with ultraviolet laser radiation and because it sublimes at atmospheric pressure and room temperature. In addition, unlike with acetone droplets, the use of naphthalene mitigates large fluorescence signals from the liquid phase and also the lensing effect due to the gas-liquid interface. This study was undertaken so that the shape and structure the gas phase acetone and naphthalene concentration boundary layer could be determined. Figure 5 shows a series of 3 naphthalene PLIF images made in both laminar and turbulent air at 77 C. Low pass filtering was applied to these images to smooth the intensity distribution prior to assigning contour levels. Note that the left images (laminar air case) show very similar concentration boundary layer structure at the three different time instances. However, the right images (turbulent air case) show that the concentration boundary layer thickness on the wake side of the sphere varies significantly at the three different time instances. This suggests that the increased evaporation rate for the turbulent gas phase case may be due to an oscillating concentration boundary layer in the separation region (i.e. wake) behind the sphere. More PLIF measurements are being made to substantiate this claim. Unfortunately, it is difficult to increase the B number of naphthalene beyond the value given in Figure 5 since naphthalene melts at 80.5 C. Acetone droplets will be used to study the high blowing number case.

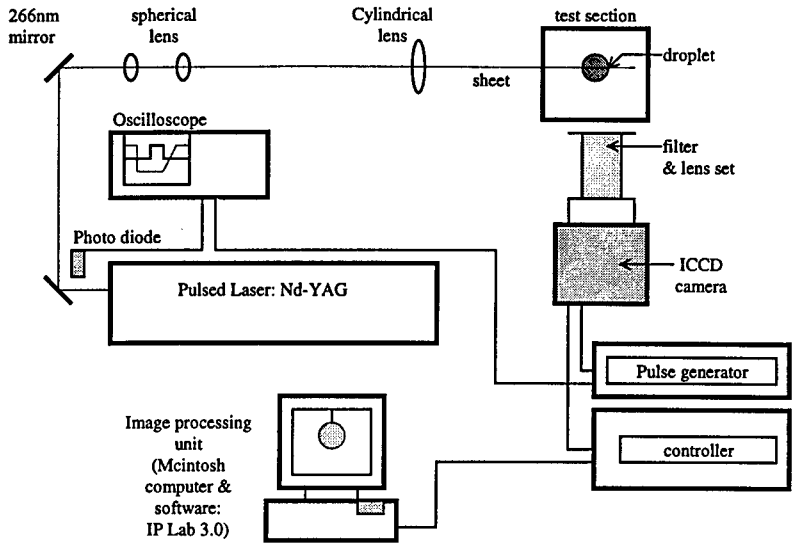

Figure 4. PLIF schematic

In conclusion, many improvements to the experimental apparatus and the experimental methodology were made during this project period. The range of blowing number was extended and the issue of whether surface blowing isolates the evaporating droplet from the gas phase turbulence was raised. Finally, flow visualization studies have been initiated with the goal of understanding why evaporation rate is augmented by the gas phase turbulence.

References

Todd Jobin, 1997, " Convective Heat and Mass Transfer from Evaporating Liquid Droplets in Turbulent Air Flow," MSME Dissertation, North Carolina State University, July.

Renksizbulut, M., and Yuen, M.C., 1983, "Experimental Study of Droplet Evaporation in a High-Temperature Air Stream," *J. of Heat Transfer*, **105**, pp. 384-388.

Paul Yearling, 1995, "Experimental Determination of Convective Heat and Mass Transfer Rates from Single Evaporating Liquid Droplets in a Turbulent Air Flow," PhD Dissertation, North Carolina State University, August.

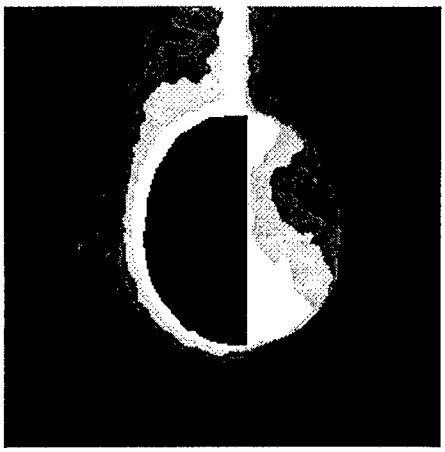

NL77_01

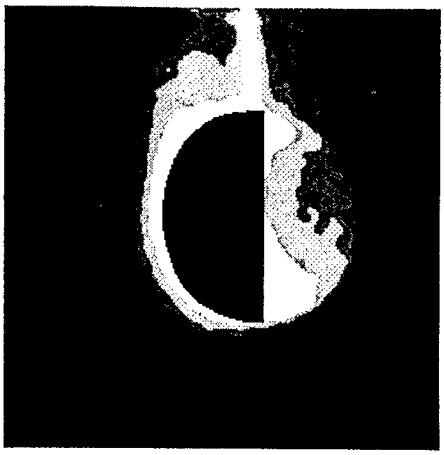

NT77_02

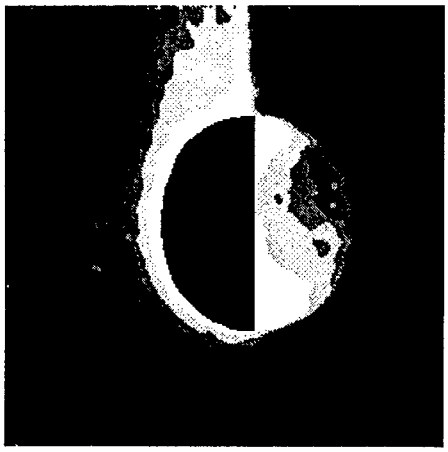

NL77_04

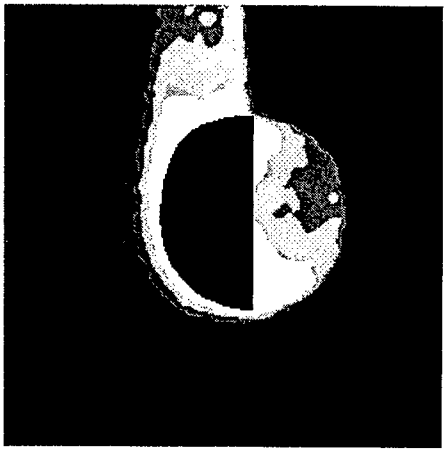

NT77_04

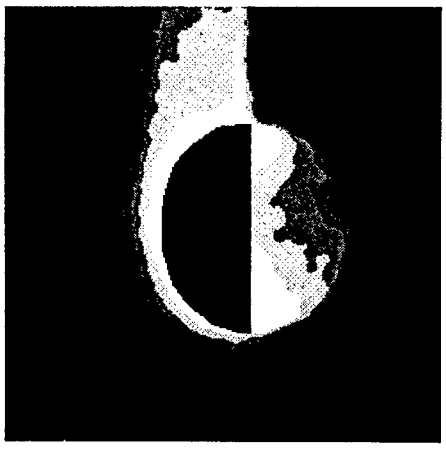

NL77_05

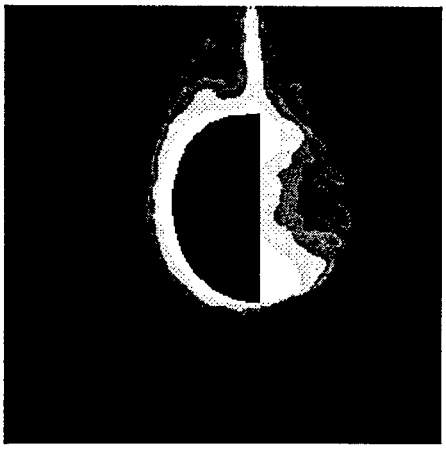

NT77_05

(a) Low turbulence (TI ~ 0.6%)

(b) High turbulence (TI ~6.5%)

Figure 5. PLIF image of naphthalene droplet (Filtered)
(Air temperature ~ 77C, B number ~ 0.0098)

THE EFFECT OF TURBULENCE ON DROPLET DRAG, DISPERSION, VAPORIZATION AND SECONDARY BREAKUP IN DIESEL FUEL SPRAYS

(ARO Grant No. DAAH04-95-0116)

Principal Investigator: Domenic A. Santavicca

Department of Mechanical Engineering
Penn State University
University Park, PA 16802

SUMMARY/OVERVIEW

Secondary droplet breakup is an important phenomenon in diesel fuel sprays, affecting the droplet size distribution and, as a result, the overall combustion process. Secondary breakup correlations used in current spray combustion models are based on results obtained in laminar flows, and thus do not accurately predict the effect of secondary breakup. An experimental investigation was undertaken to study the breakup of methanol and tetradecane droplets by inertial forces in 5 atm flowfields with relative turbulence intensities, I, of 3%, 30%, and 45%. The results indicate that breakup occurs at lower mean flow velocities as I increases. Analysis of the results indicates that the combination of the bulk velocity, and the fluctuating velocities of eddies with scales on the order of the initial droplet diameter, may be responsible for breakup in turbulent flowfields.

TECHNICAL DISCUSSION

Droplet breakup has a critical role in liquid-fuel combustion, where the efficiency and stability of the engine can depend in large part upon the atomization of the fuel [1]. Increasing the rate of breakup and decreasing the size of daughter droplets allows more rapid evaporation of the fuel, promoting more uniform chamber temperatures and reduced pollutant emissions [2, 3], since larger, "rogue" droplets, burning in isolated environments beyond the designated combustion zone, can be eliminated.

The conventional criterion for establishing the tendency of a droplet to break in an inertially-dominated (i.e., $Re=\rho_c V_{rel} D/\mu_c \geq 100$) flowfield is the Weber number, describing the ratio of the flow aerodynamic forces to the droplet surface forces:

$$We = \frac{\rho_c V_{rel}^2 D}{\sigma} \tag{1}$$

The breakup of liquid droplets in gaseous laminar flowfields has been investigated extensively [e.g., 1, 4, 5]. The lowest Weber numbers at which breakup typically occurs are in the range $11 \leq We \leq 14$, where $We_{crit} \approx 11$ corresponds to the first instances of breakup among a group of droplets, and $We_{crit} \approx 14$ corresponds to the case where 100% of the droplets experience breakup. At these Weber numbers, the droplet first flattens into a disk, followed by the stretching of the center of the droplet into a thin film, which bursts into numerous small daughters, along with several larger daughters formed by the toroidal rim. This has been termed bag breakup.

The breakup of liquid droplets in gaseous turbulent flowfields has not been addressed in the literature. Most of the turbulent breakup investigations to date have involved two liquids in stirred mixing vessels, turbulent pipe flow, or free jets, with low relative turbulence intensities, typically $5\% < I = v'/\overline{V}_c < 20\%$. Results have generally been reported in terms of apparatus-specific, empirical equations for final droplet distributions. However, it can be discerned that a mechanism fundamentally different from that causing bag breakup occurs. Droplets are deformed into what Hinze [6] termed a "bulgy" appearance, eventually breaking into several, similarly-sized daughters.

EXPERIMENTAL METHOD

Methanol and tetradecane droplets were introduced, via an aerodynamic droplet generator [7], into a 5 atm air crossflow in a 1.27 cm wide x 1.90 cm high test section. A laminar flowfield with a flat velocity profile was obtained using a combination of tightly-packed spheres and 100 mesh screens upstream of the test chamber. Hot-wire anemometry was used to confirm that spatial variations in the velocities experienced by the fuel droplets were

within ± 5% of the mean. To obtain high levels (I=45%) of homogeneous turbulence, a slot plate developed by Videto and Santavicca [8] was used. To obtain lower (I=30%) levels of turbulence, two 30 mesh screens were added downstream. Laser velocimetry was used to determine the turbulence levels, and confirm that spatial variations in the mean velocity were within ± 10% of the mean.

A Pulnix CCD video camera was used to record the effects of the various flow conditions on the droplets, which were backlit by a strobe. The critical Weber number was assigned at the flowrate where approximately 5% of the droplets experienced breakup.

EXPERIMENTAL RESULTS

In this section, the results have been correlated with the Weber number based on the average flow (continuous-phase) velocity, i.e.,

$$We\left\langle V_{c,mean}\right\rangle = \frac{\rho_c \overline{V}_c^2 D}{\sigma} \tag{2}$$

In these experiments, $V_c \gg V_d$. The mean velocity was used to emphasize the effects of turbulence on the change in flowrate required to affect the droplets. Values of σ at 1 atm were used in lieu of available data at 5 atm.

In the laminar flowfield, approximately 5% of the 370 μm methanol droplets shattered at $We_{crit} = 11$, and by We = 15 all of the droplets were broken. The predominant mechanism was via the bag form, with a few instances (≈ 1% of those experiencing breakup) of simple division into two drops. The final droplet distribution for the majority of the droplets consisted of several large ($\approx 0.5D_{init}$) daughters from the toroidal rim, and numerous small daughters ($\approx 0.1D_{init}$) from the bag. These results are in accord with those of previous investigations [e.g., 1, 4, 5] and provided quantitative proof that the experiment was operating as expected.

In the highly turbulent (I=45%) flowfield, initial breakup occurred at $We_{crit} = 3$, and at We = 18 (the experimental limit), approximately 75% of the 385 μm methanol droplets were shattered. The predominant mechanism was bulgy, splitting into 2 to 3 similarly-sized daughters at the lower Weber numbers, increasing to on the order of 10 daughters at higher Weber numbers. Typical daughter diameters ranged from about one-third to two-thirds the initial droplet diameter. Isolated instances of bag breakup were also observed.

Both bag and bulgy breakup were observed for 375 μm methanol droplets in the I=30% flowfield. Initial breakup was predominantly bulgy, beginning at $We_{crit} = 4$, which usually resulted in 2 or 3 daughters. As the velocity increased, the number of daughters resulting from bulgy breakup increased, but so did the instances of bag breakup. For $We \geq 11$, breakup was equally probable in either form. At We = 18 (the experimental limit), approximately 75% of the droplets were observed to shatter.

The experimental results of the tetradecane droplets were similar to those of methanol, except that they occurred at higher Weber numbers. Breakup in the laminar flowfield was predominantly via the bag mechanism, but began at $We_{crit} = 14$ and ended with 100% of the 355 μm droplets breaking up by We = 20. While not as dramatic, the critical Weber numbers for the turbulent experiments were also slightly higher than in the methanol cases. Specifically, for 310 μm droplets in the I=30% flowfield, $We_{crit} = 6$, and for 350 μm droplets in the I=45% flowfield, $We_{crit} = 4$.

To determine whether the disparate critical Weber numbers were a consequence of the 5 atm flowfield pressure, methanol and tetradecane droplets were introduced into a 1 atm laminar flow. These tests resulted in $We_{crit} = 11$ for both fuels. It is therefore hypothesized that the elevated Weber numbers required to disrupt tetradecane droplets in 5 atm flowfields may be influenced by the fuel's relatively low critical pressure (15.5 atm), compared to methanol (79.0 atm).

The uncertainty in the critical Weber numbers (based on mean velocity) is estimated to be 26% for the laminar breakup experiments and 43% for the turbulent breakup experiments. The larger uncertainties present in the turbulent breakup experiments arise from the greater spatial variations in the mean velocities and the higher uncertainties associated with the laser velocimetry measurements, compared to the hot-wire anemometry system used to characterize the laminar flowfield.

ANALYSIS OF RESULTS

In laminar flows, it has been shown that aerodynamic forces at least 11 times the surface forces are required for bag breakup. The existence of bag breakup in the I=30% turbulent flowfield, at lower Weber numbers (based on mean velocity), raises the issue as to which turbulent scales might be responsible for the increased aerodynamic

forces necessary for this mechanism. If a Weber number, redefined in terms of eddy velocities, can be found that predicts a ratio of 11, this would be a strong indication that the droplets experiencing bag breakup are subjected to forces carried by the corresponding turbulent scales.

It can be further postulated that those same scales also affect droplets in the I=45% flowfield. Redefining the Weber number in the same way would thus be an indication of the magnitude of the transient aerodynamic forces necessary to disrupt the droplet in a manner leading to bulgy breakup.

One alternate definition of the Weber number was proposed by Hinze [6], assuming that only eddies with scales similar to the droplet diameter effect breakup

$$We\langle v_D \rangle = \frac{\rho_c \overline{v_D^2} D}{\sigma} \tag{3}$$

where $\overline{v_D^2}$ = the average value across the entire flowfield of the squares of velocity differences over a distance D (herein termed the D-scales).

Davies [9] used the fluctuating velocities at the largest turbulent scales to calculate the relevant inertial forces for droplet breakup in liquid flowfields, such that

$$We\langle v' \rangle = \frac{\rho_c (v')^2 D}{\sigma} \tag{4}$$

Equations (3) and (4) inherently assume that the droplet has been entrained into the bulk flow, so that only the dynamic pressure differences imposed by turbulent eddies affect droplet deformation and breakup. This scenario is most applicable when droplets with low inertia (e.g., small diameters, low densities) are injected into a flowfield where the drag forces are high (e.g., large drag coefficients, high flow velocities, liquid continuous phases).

For droplets injected into a gaseous flowfield, the relaxation time, during which the droplet is subjected to the bulk and fluctuating velocities of the flow, may be comparable to the characteristic breakup times. Conjecturing that the maximum total velocities in the D-scales are responsible for breakup, a Weber number can be formulated as

$$We\langle V_{c,max}, D-eddies \rangle = \frac{\rho_c (\overline{V}_c + 3v_D)^2 D}{\sigma} \tag{5}$$

where v_D is simply the square root of $\overline{v_D^2}$, and the factor of three is intended to account for the statistical maximum of a probability curve comprising all values of the D-scale velocities. The parameter v_D can be viewed as analogous to the fluctuation velocity associated with the large scales, v', but comprising only the eddies with lengths akin to the droplet diameter. As such, v_D is meaningful as the standard deviation of a probability curve comprising all of the D-scale eddy velocities in a given flowfield.

Similarly, a Weber number can be defined in terms of the maximum total velocities in the largest turbulent scales

$$We\langle V_{c,max}, 1-eddies \rangle = \frac{\rho_c (\overline{V}_c + 3v')^2 D}{\sigma} \tag{6}$$

Equations (5) and (6) would be expected to be relevant in conditions where droplet entrainment times are comparable to those required for deformation and breakup. In these circumstances, it can be postulated that the first droplets observed to break are those injected into a turbulent eddy traveling in the same direction as the bulk flow of the continuous phase.

To explore how instances of bag breakup, known to occur in laminar flows for We = 11 (methanol) and 14 (tetradecane), were observed in the I=30% flowfields at much lower mean flowrates, the alternate definitions of Weber number were compared.

Fromthis comparison, it is apparent that the corrected We_{crit} correspond to Weber numbers well less than one, if definitions using solely the fluctuating velocities of either the large-eddy scales or D-scales are used. It can therefore be concluded that the droplets in the present experiments are experiencing aerodynamic forces greater than those available from the fluctuating velocities alone.

Calculations based on the maximum velocities in the turbulent flowfields result in higher ratios of aerodynamic-to-surface forces. For the I=30% flowfields, the corrected We_{crit} correspond to Weber numbers, as defined by Eqn. (5), of 10.5 for methanol and 13.5 for tetradecane. These values are in agreement with those required for breakup in laminar flows. This explains the instances of bag breakup observed in the I=30% flowfield, and strongly suggests that the maximum velocities imparted by the combination of the mean flow and D-eddies are those experienced by the droplets.

It can be postulated that these same scales also affect droplets in the I=45% flowfield. This corresponds to Weber numbers of 11 and 13 for methanol and tetradecane, which suggests that the magnitudes of the aerodynamic forces necessary to disrupt droplets via the bag and bulgy mechanisms may be similar, and that other factors (e.g., timescales) may determine the form of breakup.

CONCLUSIONS

The experimental data and subsequent analyses have yielded a number of important conclusions regarding the breakup of 300 $\mu m \leq D \leq 400$ μm droplets in turbulent flowfields, at somewhat elevated (5 atm) pressures:

1. For methanol droplets, the critical conditions for initial breakup, based on mean velocity, decrease from $We_{crit} = 11$ in laminar flow to 4 in a moderately turbulent (I=30%) flowfield, and to 3 for a highly turbulent (I=45%) flowfield.

2. For tetradecane droplets, the critical Weber numbers are approximately 30% higher than those observed for methanol. Specifically We_{crit} decreases from 14 in a laminar flow to 6 in the moderately turbulent flowfield and 4 in the highly turbulent flowfield.

3. For both the methanol and tetradecane experiments, the mechanism of breakup was predominantly bag for the laminar flowfield, a mixture of bag and bulgy in the I=30% flowfield, and predominantly bulgy when I=45%.

4. For both methanol and tetradecane, breakup in turbulent flowfields began with simple droplet splitting at We_{crit}, with the number of daughters increasing to on the order of 10 at higher Weber numbers. Daughters resulting from bulgy breakup typically ranged in size from about $0.3D_{init}$ to $0.6D_{init}$.

5. At the experimental limits of the velocity, 100% breakup had not been achieved in either turbulent flowfield. Specifically, for methanol at We_{max} (based on mean velocity) of 18, approximately 75% of the droplets experienced breakup. Tetradecane at $We_{max} = 13$ experienced less than 50% breakup.

6. A number of characteristic scales were examined to investigate the nature of breakup in the present experiments. Evidence suggests that the sum of the mean (bulk) velocity and maximum D-scale eddy velocity imparts the aerodynamic forces primarily responsible for droplet breakup in turbulent flows.

REFERENCES

1. Hsiang, L.-P., and Faeth, G. M., (1995) "Drop Deformation and Breakup Due to Shock Wave and Steady Disturbances," *Intl. Journal of Multiphase Flow* **21**, no. 4, pp. 545-560.
2. Faeth. G. M. (1983) "Evaporation and Combustion of Sprays," *Prog. Energy Combust. Sci.* **9**, pp. 1-76.
3. Mulholland, J. A., et al. (1991) "Trajectory and Incineration of Rogue Droplets in a Turbulent Diffusion Flame," *Comb. and Flame* **86**, p. 297.
4. Wierzba, A. (1990) "Deformation and Breakup of Liquid Drops in a Gas Stream at Nearly Critical Weber Numbers," *Expmts. in Fluids* **9**, pp. 59-64.
5. Krzeczkowski, S. A. (1980) "Measurement of Liquid Droplet Disintegration Mechanisms," *Intl. Journal of Multiphase Flow* **6**, pp. 227-239.
6. Hinze, J. O. (1955) "Fundamentals of the Hydrodynamic Mechanism of Splitting in Dispersion Processes," *AIChE Journal* **1**, no. 3, pp. 289-295.
7. Green, G. J., et al., (1989) "Aerodynamic Device for Generating Monodisperse Fuel Droplets," Paper No. ECS CI 89-96, Fall Mtg. ESS/CI.
8. Videto, B. D., and Santavicca, D. A. (1990) "A Turbulent Flow System for Studying Turbulent Combustion Processes," *Comb. Sci. and Tech.* **76**, pp. 159-164.
9. Davies, J. T. (1987) "A Physical Interpretation of Drop Sizes in Homogenizers and Agitated Tanks, Including the Dispersion of Viscous Oils," *Chem Eng Sci* **42**, no. 7, pp. 1671-1676.

PARTICLE DISPERSION IN A TURBULENT SPRAY

AFOSR Grant F49620-95-1-0276

Annual Report: 8/1/97 - 7/31/98

Principal Investigators: Ian M. Kennedy and Wolfgang Kollmann

University of California Davis, CA 95616.

SUMMARY

Droplet Lasing Spectroscopy was applied successfully to measurements of vaporization rates of droplets in non reacting and in burning droplet streams. The results represented a significant extension of the lasing principle to more realistic spray conditions. The sensitivity of the method to variations in temperature and changes in refractive index was examined and shown to be negligible for likely conditions in a spray. Instantaneous vaporization rates were measured in a burning droplet stream where the technique was found to yield accurate data. An new, efficient numerical scheme for the Large Eddy Simulation of two phase round jets was developed and implemented with considerable success. A model for the dispersed phase was improved.

TECHNICAL DISCUSSION

Experiments

A piezo electric droplet generator was used to inject single droplets along the centerline of the spray. Water was used to form the spray; ethanol doped with Rhodamine 590 at concentrations of approximately $1x10^{-4}$ to $1x10^{-3}$ M was used to form the droplets injected by the piezo electric droplet generator. Ethanol was used for the tagged droplet so that the vaporization rate was measurable in the near field of the jet where the vaporization was expected to be small as a result of small relative velocities between the droplets and the gas flow. All measurements were made at room temperature.

A 10 mm by 1 mm laser sheet of 532 nm radiation from a Nd:YAG laser was directed through the centerline of the jet, perpendicular to the flow direction, one diameter from the nozzle exit. The spray was run continuously at a mass loading of 20 percent. As a dye-doped droplet left the nozzle, the laser was fired. The ensuing lasing emission from the droplet was imaged with a magnification of 1/5.4 via a 50 mm lens onto the 30 micron slit of an Acton SP-150 imaging spectrograph. The focal length of the spectrograph was 150 mm. A 1200 l/mm grating was used to demonstrate the technique. A Princeton Instruments, cooled, 16 bit, 512x512 CCD camera was attached to the spectrograph.

The droplet diameter could be obtained from the emission spectrum and was dependent only on the geometry and the index of refraction as seen in Equation (1)

$$D = 2R = \frac{\lambda_n \lambda_{n+1}}{\Delta\lambda\pi} \frac{\tan^{-1}[m^2 - 1]^{1/2}}{[m^2 - 1]^{1/2}} \qquad (1)$$

where n and n+1 represent consecutive peaks in the lasing spectrum, m is the index of refraction and R is the radius of the droplet. The droplet size had no dependence on intensity as long as the peaks in the spectrum could be resolved. However, the particular approximation of Equation (1) was only valid when the droplets were round. Asphericity

was not an issue in the present experiment because the Weber numbers of the droplets were very small. The lasing was significantly red shifted from the Mie scattering which permitted detection against a strong background from the spray. It was also fortunate that the SRS (Stimulated Raman Scattering), which all of the droplets in the spray could exhibit, was separated significantly in wavelength (about 50 nm) from the lasing emission. The combined effects of optical filtering and the use of an imaging spectrograph permit sizing of *only* the droplet that contained the laser dye.

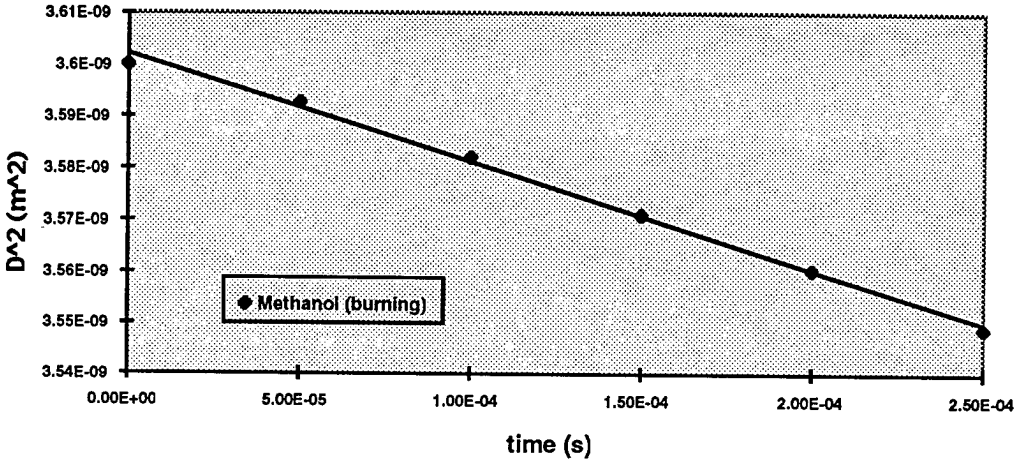

Figure 1 Burning methanol droplet showing diameter squared versus time

The error was linear in droplet diameter and the total error, including both the error from the peak spacing measurement and the error inherent in Equation (1), could be represented as:

$$\%\,Error = (0.1063x10^{6})D + 1 \qquad (2)$$

Equation (2) provided a convenient way of estimating error. It should be noted that the error was quantifiable and known, in contrast to other methods of droplet sizing. Errors due to temperature and water content were found to be insignificant.

Vaporization Rate

As shown in the previous section, the spacing of droplet lasing peaks was sensitive to micron scale changes in droplet size. In order to measure the instantaneous vaporization rate, a more sensitive measurement was needed. As a droplet changed size, by as little as a few nanometers, the morphology dependent resonances change position. The peak spacing stays about the same but the individual resonances shift to shorter wavelengths as the diameter decreases. The shift can be related to the change in radius by:

$$\frac{\Delta\lambda_{shift}}{\lambda_{n}} = \frac{\Delta R}{R} \qquad (3)$$

Therefore, by collecting two consecutive spectra from the same droplet and measuring the shift in the spectra, the change in radius can be found. The evaporation constant can be found by knowing the time between the laser pulses.

To demonstrate this measurement, a dye-doped ethanol droplet was injected at room temperature along the centerline of the water spray. Two laser pulses from the Nd:YAG laser were separated by 100 ms. Emissions from one dye-doped droplet were imaged onto the entrance slit of the imaging spectrograph. The peaks were blue shifted 0.3 nm as a result of droplet vaporization. An evaporation constant of 4×10^{-8} m^2/s $\pm$ 1.3×10^{-8} m^2/s was deduced from this shift in the spectrum.

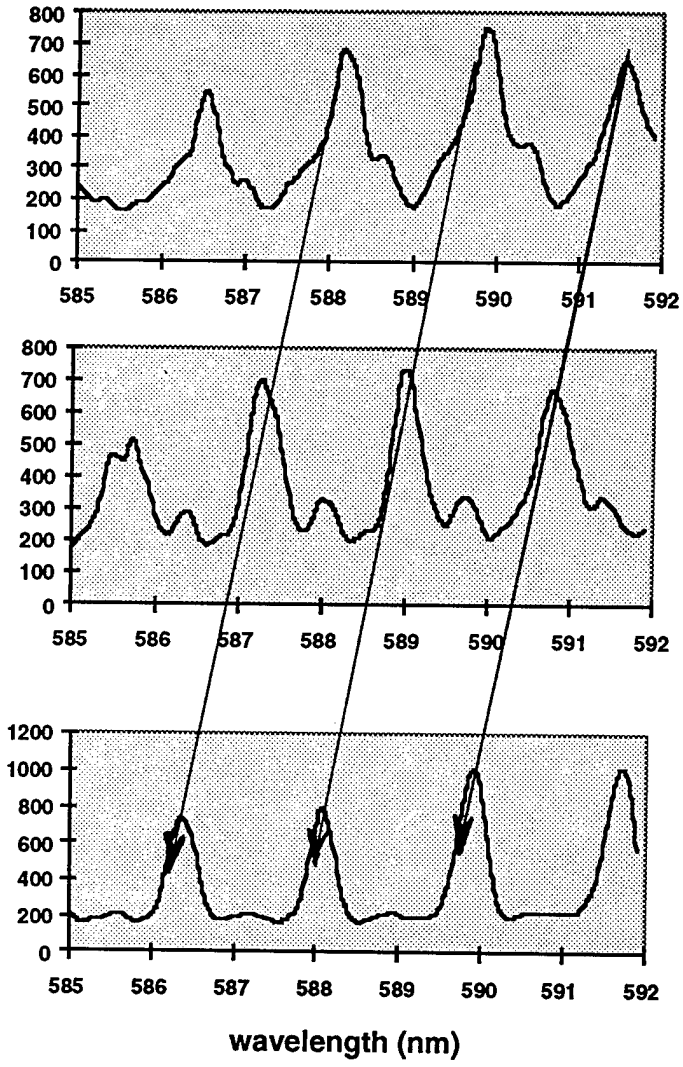

Fig.2 Spectra from three consecutive burning methanol droplets to show shift in peaks

Estimation of Temperature Rise Due to Laser Excitation

It was important to estimate the amount of heating due to laser excitation. Heating by the incident light may have an impact on the vaporization rate measured by the technique. The estimated temperature rise due to laser heating was approximately 0.74 K. This was very small and should have no significant effect on the droplet vaporization rate. The measured vaporization rates were compared to D^2 law predictions with good agreement. The results of this study will appear in Applied Optics.

Burning Droplets

Following the success with the application of the lasing method to an isothermal flow, attention was given to the application of DLS to burning droplets. A TSI Model 3450 vibrating orifice aerosol generator was employed to form a linear droplet stream.

To the best of our knowledge, lasing spectra from *burning* droplets have *not* been reported previously; our observations were unique. The lasing measurements were taken approximately 12 mm from the point of ignition except for the pentane/ethanol mixture where they were made at 10 mm. At approximately 15 mm from the point of ignition, the pentane/ethanol stream became unstable. Hence, the measurements were made far from this region. The burning rate constants found were 1.62×10^{-7}, 2.08×10^{-7}, and 7.28×10^{-7} m^2 s^{-1} for ethanol, methanol, and the pentane/ethanol mixture respectively. The D^2 law behavior of burning methanol droplets in a linear stream

is illustrated in Fig. 1. Typical corresponding spectra for 3 consecutive methanol droplets are shown in Fig. 2. The blue shift in peaks with decreasing droplet diameter is very evident. The quality and hence accuracy of the spectra are excellent. The pentane/ethanol burning rate compared very well to the measurements of Silverman and Dunn-Rankin in hexane with a range of droplet spacings. The results of this study were presented at the WSS meeting of the Combustion Institute, Spring 1998 and have been submitted to Combustion and Flame.

Computational Research

Navier-Stokes solver for the continuous phase

The Navier-Stokes solver for incompressible fluids requires a Poisson solver, which is one of the important features determining the performance of the solver. The Poisson equations for the complex-valued streamfunctions and the pressure modes are solved using one of two methods:

(1) LU-decomposition combined with deferred corrections to reduce the bandwidth of the coefficient matrix. The deferred corrections method for the 4th and higher order schemes is designed as iteration $\mathbf{X}^{n+1}=\mathbf{X}^n+\mathbf{M}^{-1}\mathbf{Q}^n$ where $\mathbf{Q}^n$ is the residual $\mathbf{Q}^n = \mathbf{R}-\mathbf{A}\mathbf{X}^n$. The original system is given by $\mathbf{AX} = \mathbf{R}$, where $\mathbf{A}$ and $\mathbf{R}$ are the coefficient matrix and the right side vector generated by the higher order finite difference schemes for the respective Poisson equations. The coefficient matrix $\mathbf{M}$ is constructed by using the second order discretization for the direction determining the bandwidth and the higher order schemes for the other direction. The convergence of this method is rapid; typically five to ten iterations are sufficient to drive the error to machine accuracy.

(2) Full Multi-Grid (FMG) method adapted for higher order finite-difference schemes. Several mesh levels are used in a W-cycle iteration starting with the solution on the coarsest mesh which is the LU decomposition method used in the first approach. Prolongation and restriction operators constructed for the Poisson equations in transformed coordinates and a red-black Gauss-Seidel smoothing method are used to compute the solution at all mesh levels. This method achieves better accuracy than method (1) in less CPU-time and requires significantly less memory.

PLES model for the particulate phase

During the previous contract period, an LES model for the particles (PLES) was developed and implemented into the LES code for the spatially developing turbulent round jet. The PLES model treats spherical subdomains $D_i(t)$ of the flow field with constant radius R containing $N_i(t)$ particles as an entity (called blobs), that is governed by dynamic equations for position and velocity similar to an individual particle. These equations contain additional terms representing the effect of particle motion inside the blob and the particles leaving and entering it.

The evolution of a blob $D_i(t)$ is determined by its centre location $\underline{X}'_i(t)$, the centre velocity $\underline{v}'_i(t)$ and the number of particles $N_i(t)$ in the blob. The velocity of a blob $D_i(t)$ changes with time according to $d\underline{v}'_i=\underline{P}_i dt+d\underline{Q}_i+ d\underline{S}_i+d\{d^2\underline{Y}/dt^2\}$ The forces acting on a blob are: $\underline{P}_i(t)$ is the particle force based on the centroid properties, $\underline{Q}_i(t)$ the difference between the average acceleration and $\underline{P}_i(t)$. The third contribution is due to the motion of particles through the spherical blob boundary and the motion of particles inside the blob. Closure models have been developed for $\underline{Q}_i$, $\underline{S}_i$ and $\underline{Y}$ based on integrated white-noise processes, which can be simulated using stochastic differential equations of the Ornstein-Uhlenbeck type.

NONLINEAR DISTORTION AND DISINTEGRATION OF LIQUID SHEETS FOR PRESSURE ATOMIZATION SYSTEMS

ARO Grant/Contract No. DAAH-04-96-1-0055

PRINCIPAL INVESTIGATOR:

W.A. Sirignano

Department of Mechanical and Aerospace Engineering
University of California
Irvine, CA 92717

SUMMARY/OVERVIEW:

A robust but simplified approach has been developed to analyze oscillatory nonlinear motion and disintegration of thin injected liquid sheets. The reduced-dimension approach has been employed on planar two- and three-dimensional and axisymmetric annular liquid sheet motion for both dilational and sinuous wave distortions. Both spatially periodic and spatially developing sheet motions have been considered. The method succesfully predicts temporal and spatial variations of velocity, pressure, sheet thickness, and sheet displacement; the location of sheet tearing (point of zero thickness) and the values of critical Weber numbers where bifurcations of the solution occur are predicted. Both dispersive and non-dispersive nonlinear wave motions have been predicted.

AUTHORS

W.A. Sirignano C. Mehring I. Kim

TECHNICAL DISCUSSION

The distortion and disintegration of thin liquid sheets are important in many engineering applications [1, 2]. The interesting examples include the instability and breakup of annular liquid sheets which are encountered in spray combustion and spray drying and which have recently gained interest in connection with the formation of spherical shells as closed chemical reactors in the combustion of toxic wastes [3]. The governing nonlinear equations describe the general case of an annular axisymmetric disturbed sheet which also includes the planar configuration as a limiting case.

Considered are both infinitely and semi-infinitely long, thin sheets of liquid, with disturbance wavelengths in the streamwise or axial direction which are much larger than the sheet thickness. Two-dimensional, axisymmetric, and three-dimensional disturbances are considered. The dynamics of the surrounding gas are neglected. Namely, the density of the gas on the outer periphery of the annular sheet is assumed to be negligible compared to the liquid density; however for the inner gas core, a constant gas pressure is assumed in order to stabilize the undisturbed annular sheet configuration. Viscosity is neglected for both the gas and the liquid.

The continuity and momentum equations are simplified by the integration of each term in the equations across the thin liquid sheets. This manipulation reduces the dimensionality of the problem. That is, a three-dimensional motion is reduced to a two-dimensional unsteady problem and a two-dimensional planar or axisymmetric motion is reduced to a one-dimensional unsteady problem. Details on the analytical method can be found in references [4]-[8].

Dilational and sinuous modes have been studied via both nonlinear and linear analyses. Spatially periodic motion is examined in the infinitely long case, while spatially developing waves are allowed in the semi-infinite case. The semi-infinite case better simulates the practical case with a nozzle. Only the results of calculations for a few configurations can be discussed in this short report. See references [4]-[8] for a more complete discussion. The linear and nonlinear results were consistent; sinuous waves were non-dispersive while dilational waves were dispersive with wave speed decreasing as wavelength increased. The nonlinear dilational waves were symmetric but the nonlinear sinuous waves coupled with dilational oscillations and were not antisymmetric like the linear case.

In order to benchmark the accuracy of the proposed reduced dimension approach, nonlinear one-dimensional results for planar sheets have been compared to fully two-dimensional nonlinear computations using the discrete vortex-method approach described in [9].

Consider first the sinuous two-dimensional case. Nonlinear effects cause a considerable distortion of an initially sinusoidal wave. The transverse oscillation of the sheet is accompanied by an increase in the maximum disturbance amplitude of the wave together with an accumulation of fluid in the maximum deflection region of the sheet, which then results in a more sawtooth-like sheet configuration rather than a sinuousoidal one. The nonlinear coupling between the sinuous and dilational modes causes variations in the sheet thickness with wavelengths about one-half of that for the initially imposed antisymmetric disturbance. This sheet thinning can occur at the location of maximum slope or it might occur at points located near the maximum deflection region. Nonlinear numerical results were also obtained for the annular sheet configuration. Figure 1 shows one of the computed nonlinear results and illustrates the capillary instability as it might be encountered for the case of an antisymmetrically disturbed annular liquid sheet. It is qualitatively similar to the planar results.

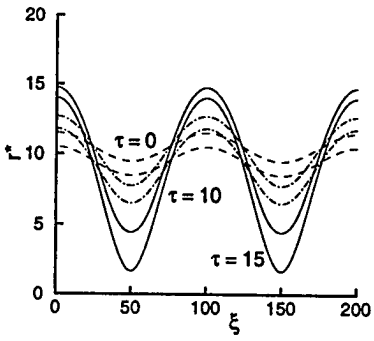

Figure 1: Nonlinear evolution of initially antisymmetrically disturbed annular liquid sheet.

Figure 2 compares nonlinear numerical and linear analytical results for a planar case with high forcing amplitude of the transverse sheet velocity v at the nozzle exit. The forcing amplitude of the sheet centerline location Y at $x^* = 0$ was assumed to be zero. The Weber number in this case was 1000 and the nondimensional time period of the harmonic forcing was $T = 25$. Comparison between the linear limit-cycle solution and the nonlinear transient solution in Figure 2 shows that nonlinear effects become important as the disturbance amplitude of the sheet grows in the downstream direction. In the nonlinear case, the sheet takes a more sawtooth-like shape with fluid agglomerating in its edges. For the semi-infinite case, this phenomenon was also observed experimentally by Asare, Takahashi and Hoffman [10]. Furthermore, and similar to the observation made already in [6], Figure 2 shows increased sheet thinning and eventually sheet pinch-off at points interspaced by half a wavelength and located close to the maximum deflection region of the sheet. Finally, the characteristic beat behavior identified in the linear analysis remains also a characteristic in the nonlinear case. For small beat amplitudes, linear and nonlinear results agree very well in the disturbed flow regions. An experimental observation of the prescribed beat behavior was made by Hashimoto and Suzuki [11] for rather small beat amplitudes. The variation in amplitude due to the long wavelength envelope often results in

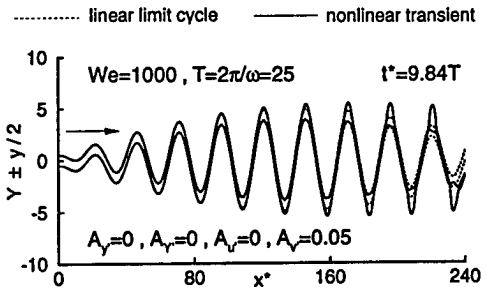

Figure 2: Linear and nonlinear distortion of semi-infinite planar liquid sheet with transverse forcing at $x^* = 0$.

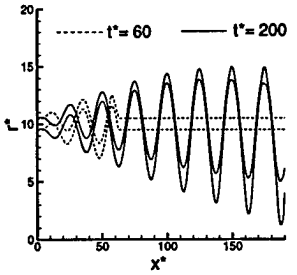

Figure 3: Nonlinear distortion of semi-infinite annular liquid sheet with antisymmetric forcing at $x^* = 0$. $(A_{\overline{r}^*} = 0, A_{\overline{v_r}^*} = 0.05, We = 1/(2\varepsilon^2) = 1000, T = 25)$.

a local zero thickness (or tearing) of the sheet.

Comparison between the planar case and the axisymetric annular case for semi-infinitely long sheets shows that, similar to the infinite case, the sheet might collapse due to the action of the sheet curvature perpendicular to the main flow direction, i.e. the circumferential direction. See Figures 2 and 3. This instability can be used to generate closed spherical shells bounded by the nozzle wall and the annular sheet up to the point of collapse.

Consider now three-dimensional symmetric motion on a sheet without any mean curvature. The mean flow is in the x-direction. Figure 4 displays $\tilde{z}$ versus X in the plane $Y = 0$ for $0 \leq \tau \leq 3T$

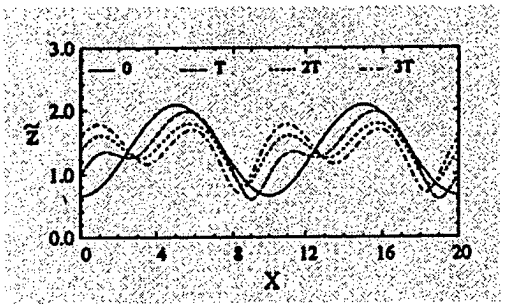

Figure 4: $\tilde{z}$ versus X in the plane $Y = 0$ for $0 \leq \tau \leq 3T$.

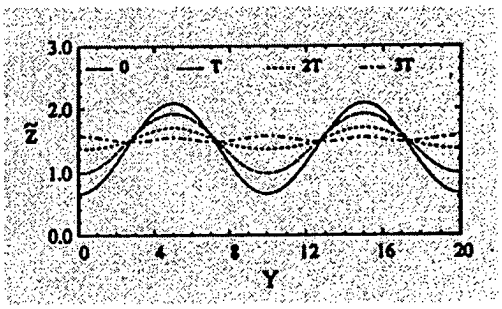

Figure 5: $\tilde{z}$ versus Y in the plane $X = 0$ for $0 \leq \tau \leq 3T$.

where the period $T = 6.4$. The initially sinusoidal disturbance propagates in the $X-$direction with large deformation compared with the case for lower amplitudes during $0 \leq \tau \leq T$. As more time elapses, two higher harminic waves are generated during $T \leq \tau \leq 3T$. However, these higher harmonic waves degenerate into the initial wave during $3T \leq \tau \leq 6T$. Results for $\tau > 6T$ indicate that this process is repeated in a cycle.

Figure 5 describes $\tilde{z}$ versus Y in the plane $X = 0$ with the same parameters as in Figure 4. Intitially the sinusoidal disturbance oscillates standing in the Y-direction during $0 \leq \tau \leq T$. As more time elapses, the standing wave is nearly flat during $T \leq \tau \leq 3T$, while Figure 4 shows that two higher harmonic waves are generated in the $X-$direction during that time. However, the nearly flat wave bounces into a wave with finite amplitude during $3T \leq \tau \leq 6T$, whereby the two higher harmonic waves degenerate into the initial wave in the $X-$direction during that time. Results for $\tau > 6T$ indicate that this process is repeated in a cycle. This periodic exchange of energy between the transverse oscillations and the streamwise oscillations does not occur when the two wave numbers are disparate.

In summary, a reduced dimension approach has been formulated reducing the complexity of the numerical solution. The nonlinear results for both sinuous and dilational oscillations agree well with complete multidimensional calculations. Qualitative agreement with experiments is also found. Two-dimensional, axisymmetric annular, and three-dimensional nonlinear motions have been studied both for spatially periodic and spatially developing cases. The distortion of the sheet including the point in space and time of sheet break-up can be predicted. Dispersive and non-dispersive nonlinear wave motions have been identified. Critical Weber number values where bifurcations occur in the solution have been identified. Future studies will address conical sheets, effects of high pressure, and viscous effects.

References

[1] LEFEBVRE, A. H. 1989 *Atomization and Sprays.* Hemisphere Pub. Corp.

[2] MASTERS, K. 1985 *Spray drying handbook, 4th ed.* Wiley & Sons.

[3] RAMOS, J. I. 1995 On the growth of underpressurized annular liquid jets. *Appl. Math. Modelling,* vol. 19, pp. 13–25.

[4] SIRIGNANO, W. A. & MEHRING, C. 1996 Nonlinear two-dimensional symmetric travelling wave distortion of a thin liquid sheet. In *Dynamics of Exothermicity,* special honorific volume for A. K. Oppenheim. *Comb. Sci. and Techn.* book series (ed. J. Ray Bowen). Gordon & Breach.

[5] MEHRING, C. & SIRIGNANO, W. A. 1998 (a) Nonlinear capillary wave distortion and disintegration of thin planar liquid sheets. *J. Fluid Mech.*, submitted for review.

[6] MEHRING, C. & SIRIGNANO, W. A. 1998 (b) Nonlinear distortion of infinitely long thin planar and annular liquid sheets. *Proc. 11th Ann. Conf. Liquid Atom. Spray Sys.*, in press. ILASS, North and South America.

[7] MEHRING, C. & SIRIGNANO, W. A. 1998 (c) Nonlinear distortion of semi-infinitely long thin planar and annular liquid sheets. *Proc. 11th Ann. Conf. Liquid Atom. Spray Sys.*, in press. ILASS, North and South America.

[8] KIM, I. & SIRIGNANO, W. A. 1998 Three-dimensional symmetric distortion of thin liquid sheets. *Proc. 11th Ann. Conf. Liquid Atom. Spray Sys.*, in press. ILASS, North and South America.

[9] RANGEL, R. H. & SIRIGNANO, W. A. 1991 The linear and nonlinear shear instability of a fluid sheet. *Phys. Fluids A*, vol. 3, no. 10, 2392–2400.

[10] ASARE, H. R., TAKAHASHI, R. K. & HOFFMAN, M. A. 1981 Liquid sheet jet experiments: comparison with linear theory. *Trans. ASME, J. Fluids Eng.*, vol. 103, no. 4, pp. 595-604.

[11] HASHIMOTO, H. & SUZUKI T. 1991 Experimental and theoretical study of fine interfacial waves on thin liquid sheet. *JSME Int. J., Ser. II*, vol. 34, no. 3, pp. 277–283.

SECONDARY BREAKUP AND TURBULENCE INTERACTIONS OF DROPS

(AFOSR Grant No. F49260-95-I-0364)

Principal Investigator: G.M. Faeth

Department of Aerospace Engineering
The University of Michigan
3000 François-Xavier Bagnoud Bldg.
Ann Arbor, Michigan 48109-2140, U.S.A.

SUMMARY/OVERVIEW:

Turbulence interactions and secondary breakup of drops are being studied because these are important but poorly understood processes of dense sprays. Work on turbulence interactions of drops emphasizes turbulence generation caused by fast moving drops in sprays. Present experiments show that continuous phase properties consist of contributions due to both particle wakes and interwake turbulence and that the particle wake disturbances correspond to the laminar-like turbulent wakes observed for moderate Reynolds number spheres in turbulent environments .

Secondary breakup is important in sprays because drops formed by primary breakup are intrinsically unstable to secondary breakup. Past work has resolved the outcomes of secondary breakup when effects of liquid viscosity are small but has also shown that secondary breakup should be treated as a rate process, rather than by jump conditions, in many instances. Thus, current work is using pulsed holography to resolve secondary breakup properties as a function of time during shear, bag and multimode breakup processes for conditions where effects of liquid viscosity are small, i.e., Ohnesorge numbers less than unity.

TECHNICAL DISCUSSION:

Introduction. Past work has demonstrated the importance of turbulence generation and secondary breakup in sprays (Faeth 1996; Ruff and Faeth 1995; Tseng et al. 1996); therefore, these phenomena are being studied as discussed in the following:

Turbulence Generation. Turbulence generation by drops controls the turbulence properties of dense sprays (Faeth 1996; Ruff and Faeth 1995; Tseng et al. 1996). Drop generated turbulence differs from conventional turbulence because it is truly stationary while involving randomly-arriving velocity disturbances due to drop wakes. Past work based on stochastic analysis assuming that flow properties resulted entirely from particle wakes helped explain some properties of these flows but was not complete due to lack of information about particle wakes at intermediate Reynolds numbers in turbulent environments and problems of measurements in dense particle-laden flows (Parthasarathy and Faeth 1990; Mizukami et al. 1992). Subsequently, Wu and Faeth (1993,1994,1995) developed information about particle wakes at intermediate Reynolds numbers in turbulent environments while a counterflow particle upflowing-air wind tunnel has been assembled to resolve experimental problems of dense particle-laden flows. Dispersed- and continuous-phase mean and fluctuating velocities are being observed with this arrangement using phase-discriminating laser velocimetry (Chen and Faeth 1998a,b).

Initial measurements are emphasizing the properties of particle wake disturbances and the contribution of these disturbances to overall continuous-phase turbulence

properties. Typical examples of these results are illustrated in Fig. 1, where streamwise and crosstream gas velocities are plotted as a function of time for 0.5 mm diameter particles at near terminal velocity conditions and high and low particle loadings. As expected, the streamwise velocities exhibit large negative spikes, whose frequency increases with particle loading, which is characteristic of particle wake disturbances; in addition, crosstream velocities exhibit no wake disturbances which is also expected for the present nearly vertical particle trajectories at this particle Reynolds number (Chen and Faeth 1998a,b).

High resolution streamwise velocity measurements in particle wakes are plotted as a function of time in Fig. 2. Corresponding predictions for laminar-like turbulent wakes, drawn from Wu and Faeth (1994,1995) are also shown on the plot. Predictions and measurements are seen to be in excellent agreement which supports the use of the properties of laminar-like turbulent wakes to estimate and interpret effects of wake disturbances during turbulence generation in dispersed flows.

More insight about the relative contributions of wake and interwake turbulence properties on the total properties of homogeneous dispersed flows dominated by turbulence generation can be obtained from the probability density functions (PDF) of velocity fluctuations . Typical results along these lines are illustrated in Fig. 3 for 0.5 mm diameter particles at low and high particle loadings specified by low and high values of the dimensionless dissipation factor, D. PDF's are illustrated on these plots for streamwise and crosstream velocities, along with fits of the measurements. The results are independent of the particle fluxes with PDF(v) nicely fitted by a Gaussian function but PDF(u) exhibits greater kurtosis and skewness than a Gaussian function. This behavior follows directly from the presence of the negative velocity spikes due to particles wakes. Thus, both wake disturbances and interwake turbulence contribute to the overall apparent turbulence properties of the present flows which helps explain past problems of explaining flow properties based on contributions from each region alone (Mizukami et al. 1992; Chen and Faeth 1998a,b).

Stochastic simulations accounting for the random distributions of particles in space and the laminar-like turbulent wake disturbances of each particle are illustrated in Fig. 4. This figure shows the regions of wake disturbances over a typical crossection of the flow at a high particle loading for 0.5 mm diameter particles (taking the radius of the wake region as twice its characteristic half radius at each distance from the particle and the maximum wake length to the point where the mean velocity defect is less than 10% of the ambient rms turbulence level). These results show that the wake-containing region is sparse (yielding a wake volume fraction of roughly 1/150 for the condition pictured in Fig. 4) which agrees with the limited time intervals of wake spikes seen in Fig. 1. Nevertheless, the large velocity disturbances of the wake region, compared to the interwake turbulence region, still implies a significant contribution of wake disturbances to apparent overall turbulence generation properties.

Current work is considering conditional measurements of continuous-phase properties along with stochastic analysis to model overall flow properties, in an effort to quantify the contributions to the flow from wake disturbances and interwake turbulence.

Secondary Drop Breakup. Past studies have shown that drops produced by primary breakup are unstable for secondary breakup and have established drop size and velocity distributions as jump conditions after secondary breakup (Faeth 1996). Thus, current work is emphasizing the properties of secondary breakup as a rate process for small Ohnesorge number conditions where effects of liquid viscosity are small. This has involved consideration of the behavior of shear, bag and multimode breakup, in turn, see Chen et al. (1997) and Chou and Faeth (1998) for more details about these results.

Work during the past year has emphasized determination of drop size and velocity distributions and the rate of generation of dispersed liquid, as a function of time during bag

breakup. The pure bag breakup regime is rather narrow, consisting of a Weber number range of 13-20. In this regime, three kinds of drops are produced, bag drops, basal ring drops and node drops on the basal ring with each group being relatively monodisperse. The velocity of the parent drop as a function of time is illustrated in Fig. 5, the measurements agree quite well with predictions based on simplified analysis. The bag drops form first and accelerate rapidly due to their small size; this accounts for spreading of drops from the bag breakup process as illustrated in Fig. 6. This spreading and the extended time required for complete breakup motivate current interest in the temporal properties of secondary breakup.

Current work is considering the multimode breakup regime which begins by the appearance of a plume drop at the middle of the bag. The growth of this drop, its merging with node drops in the basal ring, the development of a plume behind the plume drop due to collapse of a portion of the bag and gradual disappearance of the bag, with increasing Weber number, explain the evolution from bag to shear breakup and the rich variety of phenomena of the multimode breakup regime. Subsequent work will concentrate on large Ohnesorge number behavior where liquid viscosity becomes important and only shear breakup is observed.

REFERENCES

Chen, J.-H. and Faeth, G.M. (1998a) 37th Aero. Sci. Meeting, submitted.

Chen, J.-H. and Faeth, G.M. (1998b) AIAA Paper No. 98-0240.

Chou, W.-H. and Faeth, G.M. (1998) Int. J. Multiphase Flow, in press.

Chou, W.-H., Hsiang, L.-P. and Faeth, G.M. (1997) Int. J. Multiphase Flow, 23, 651-669.

Faeth, G.M. (1996) 26th Symp. (Intl.) on Comb., The Combustion Institute, Pittsburgh, 1593-1612.

Mizukami, M., Parthasarathy, R.N. and Faeth, G.M. (1992) Int. J. Multiphase Flow, 18, 397-412.

Parthasarathy, R.N. and Faeth, G.M. (1990) J. Fluid Mech., 220, 485-537.

Ruff, G.A. and Faeth, G.M. (1995) Prog. Astro. Aero., 166, 263-296.

Tseng, L.-K., Ruff, G.A., Wu, P.-K. and Faeth, G.M. (1996) Prog. Astro. Aero., 171, 3-30.

Wu, J.-S. and Faeth, G.M. (1993) AIAA J., 31, 1448-1455.

Wu, J.-S. and Faeth, G.M. (1994) AIAA J., 32, 535-541.

Wu, J.-S. and Faeth, G.M. (1995) AIAA J., 33, 171-173

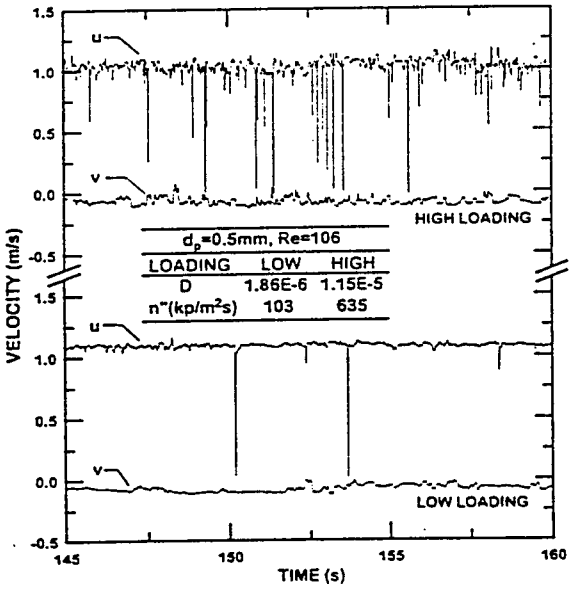

Fig. 1 Streamwise and crosstream velocities as a function of time for high and low particle loadings and 0.5 mm diameter particles.

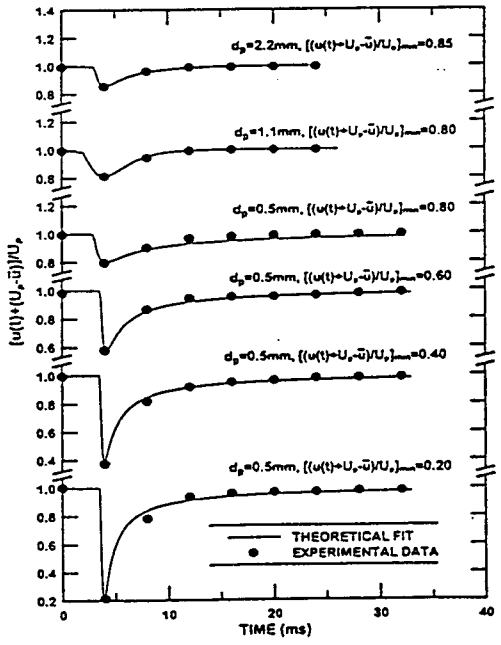

Fig. 2 Measured and predicted streamwise velocities in particle wakes as a function of time for various minimum relative wake velocities.

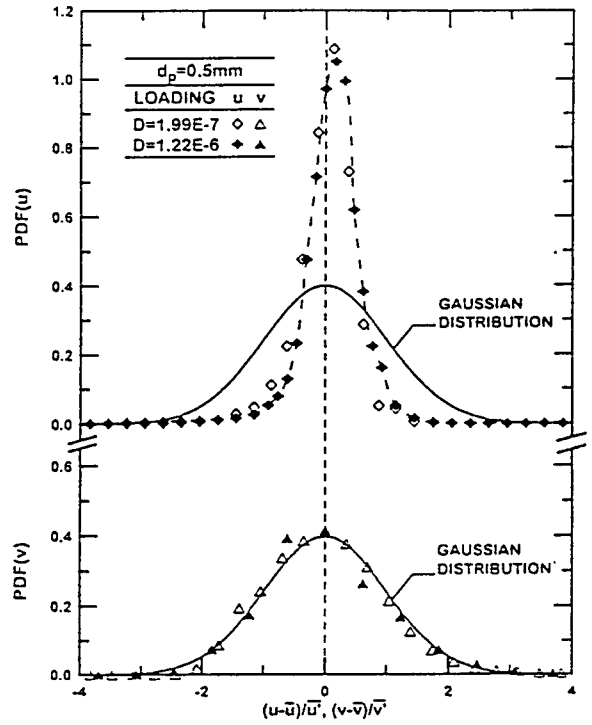

Fig. 3 Streamwise and crosstream PDF's of gas velocities at low and high particle loadings for 0.5 mm diameter particles.

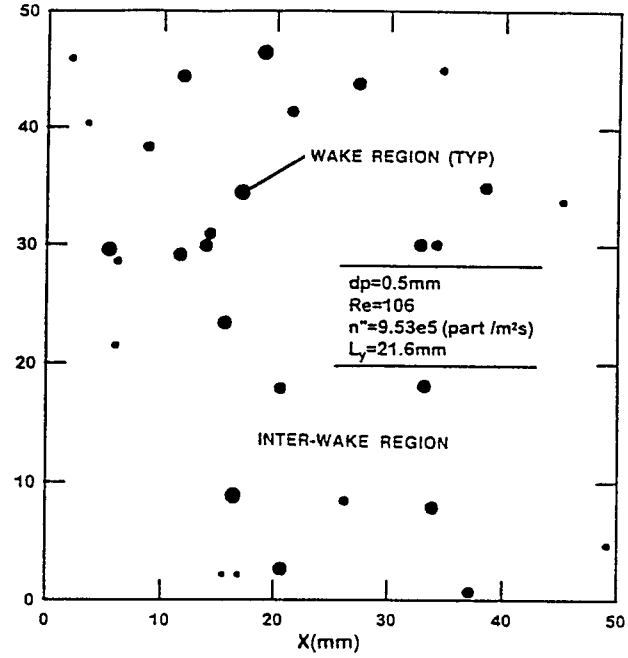

Fig. 4 Stochastic simulation of particle wake crossections for a high particle loading and 0.5 mm diameter particles.

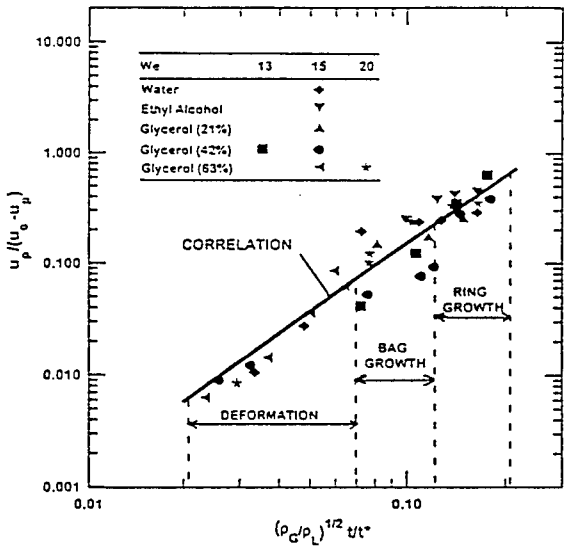

Fig. 5 Measured and predicted parent drop velocities as a function of time during bag breakup.

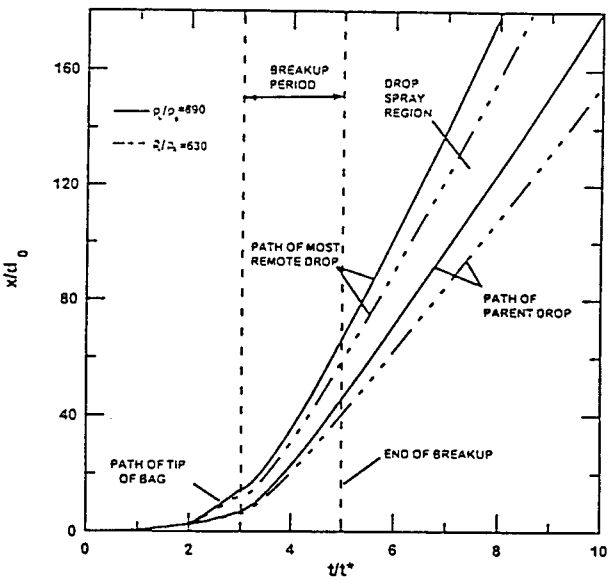

Fig. 6 Growth of the spray-containing region during bag breakup.

COMPUTATIONAL INVESTIGATION OF ATOMIZATION

(AFOSR-contract FA9620-96-1-0356)

Grétar Tryggvason
Department of Mechanical Engineering and Applied Mechanics
The University of Michigan
Ann Arbor, MI 48109-2121

SUMMARY/OVERVIEW:

Atomization of liquid fuels is studied by numerical simulations. The Navier-Stokes equations are solved by a finite difference/front tracking technique that allows resolution of inertial and viscous forces as well as the inclusion of surface tension at the deformable boundary between the fuel and the air. The main part of the study focuses on the secondary breakup of drops, but the primary breakup of jets is also being examined. The focus is on those aspects of the breakup that are difficult to address experimentally, such as the behavior at high pressures and temperatures.

TECHNICAL DISCUSSION

Numerical simulations of the deformations and breakup of drops are being done, for both shock generated disturbances as well as gradual disturbances, where inertial and viscous effects for both the drop and the ambient gas as well as surface tension effects are fully accounted for. The simulations will help determine where in parameter space the various breakup modes take place, how long breakup takes, and what the resulting drop size distribution is. The goal of the investigation is to provide results that extend and complement experimental investigations, and lead to better engineering models of drops in sprays.

These computations are made possible by a recently developed numerical technique that has been used already for a number of multifluid problems. The method incorporates an explicit tracking of the drop surface with a finite difference method for the full Navier-Stokes equations for the drop and the ambient gas. Arbitrary differences in density and viscosity are possible, large surface deformations are allowed and surface tension is fully accounted for. For problems with mass and heat transfer, conservation equations for mass and energy are solved also. The technique has been used for two-dimensional, axisymmetric, and fully three-dimensional problems and validated extensively by comparisons with analytical solutions for simple cases, other numerical studies, grid refinement, and experiments. To allow the examination of three-dimensional situations where there is a wide range of scales, a new three-dimensional code that allows grid points to be clustered in certain regions is being developed.

To examine the breakup of drops as the density difference becomes smaller, we have conducted extensive axisymmetric simulation of four systems: Impulsive and gradual disturbances for two different density ratios (1.15 and 10). At low density ratios, the density disappears as an independent control parameter and we have shown that the low density results apply to density ratios as high as two if we rescale time using the Boussinesq approximation. In addition to full simulations where the Navier-Stokes equations are solved, a few inviscid simulations have also been done for the small density ratio case to isolate the effect of viscosity.

The breakup of the drops is governed by four nondimensional numbers. In addition to the density and viscosity ratio, the ratio of inertia to surface tension is described by an Eötvos number for gradual disturbances and a Weber number for impulsive acceleration. The effect of viscosity is described by the Ohnsorge number (the ratio of the viscous force to the surface tension). Our

simulations have now resulted in a fairly complete picture of the evolution at small density ratios. For small Eotvos and Weber numbers the drops remain spherical in all cases, independently of the Ohnsorge number and density and viscosity ratio. If the Ohnsorge number is low, the deformations of the drop depend only on the Eotvos/Weber number (and the density ratio). As the Eotvos/Weber number is increased, the drops deform into a disk-like shape due to high pressure at the fore and aft stagnation points and low pressure around the equator. For gradual disturbances this results in a steady state motion where the work done by the constant acceleration is dissipated by the drag on the drop, but for impulsive acceleration the drop oscillates. Increasing the Eotvos/Weber number further results in a continuing deformation where most of the drop fluid ends up in a taurus connected by a thin film. For moderate Eotvos/Weber numbers, the initial momentum of the drops is relatively low and once the taurus is formed, the rim moves faster than the film for drops with gradual disturbances. The film "bulges" back and experimentally is seen that this bag eventually breaks. The simulations have shown that the bag break-up mode is a viscous phenomenon, due to flow separation at the rim of the drops and the formation of a wake, and therefore not seen in inviscid computation. For drops subject to an impulsive acceleration, the formation of a backward facing bag is only seen for the higher density ratios. Bag breakup requires a driving force that acts stronger on the drop than on the surrounding fluid and for impulsively accelerated drops this driving force is the fluid inertia. As the density difference becomes small, the difference between the drop and the fluid inertia vanishes and the low density ratio drops simply stop and surface tension pulls them back into a spherical shape. Experimentally, bag breakup is commonly observed, but the density ratio is larger than simulated here. Increasing the Eotvos or the Weber further, results in a different mode of breakup that also depends on the density ratio. For low density ratios, the fluid initially still ends up in the rim of the drop, but the initial momentum is now sufficiently large that the ambient fluid moves the film faster than the taurus, leading to a bag that extends forward of the drop. For higher density ratios, not all the fluid moves to the rim resulting in a taurus connected to the rest of the drop by a thin sheet. As this sheet is pulled from the drop, the fluid is drained from the drop. As the driving force is increased the size of the rim is reduced and for very high Eotvos/Weber numbers, small drops are pulled from the rim. Examination of the dynamic of the vorticity generated at the drop surface and the effect of surface tension and a large density difference have been used to explain some of the different trends observed. The vortex dynamics suggests that the shear breakup mode where fluid is stripped from the rim of the drop by an essentially inviscid effects. Simulations show, for example that unlike the bag breakup case, separation does generally not take place. We have, however, not yet done inviscid simulations for large density ratios to confirm that this is the case. In the transition between a bag breakup mode and shear breakup, we have found drops that oscillate in a chaotic manner. Such transition phenomena have been seen experimentally for higher density ratios.

In addition to the Ohnsorge number effect, where the boundary between breakup modes is shifted to higher Eotvos/Weber numbers as viscous effects become more important, the fluid and drop viscosity can change the drop shape during breakup if the Ohnsorge number is high enough. High viscosities can, for example lead to skirted drops at low density ratios, where thin fluid skirts are pulled from the rim of the fluid, in a way similar to the shear breakup seen for higher density ratios.

Figure 1 shows the breakup of several impulsively accelerated drops for a density ratio of ten and different Weber numbers. Other parameters are given in the figure. Each column is a different case and the initial spherical drop is shown at the top of each column. Notice that the nondimensional times have been selected differently for each sequence. Initially, when the drop has been given a velocity relative to the surrounding fluid, it becomes flatter. For low Weber numbers the drops do not break up, but as the Weber number is increased, they start to oscillate and the amplitude of the oscillations increases, eventually leading to bag breakup. At even higher Weber number, shear breakup takes place and for an infinitely high Weber number (zero surface tension) small drops are torn from the edge of the drop. While the resolution is not sufficient to fully resolve these drops, the evolution is similar to what is observed experimentally.

The simulations have been used to generate "break-up" maps for low density ratios and it is found that the general character of those maps agrees with what has been found experimentally at larger density ratios. At low Ohnsorge numbers the transition between the various modes depends only on the density ratio and the Eotvos number, but a high Ohnsorge number will move the transition to a higher Eotvos number. However, there are some fundamental differences like the absence of a bag breakup for low density impulsive drops.

In the present simulations, the actual breakup of the drops has not been followed. While it is relatively simple to allow interfaces to break, the length scales involved are too small to resolve in a simulation that also follows the rest of the drop. While the current methodology has been used to follow the draining of a thin film to the point when it breaks, in simulations of colliding drops, we believe that it is more practical to model the actual breakup separately. We are currently developing techniques to estimate the distribution of drop sizes after breakup based on local applications of the conservation of mass and surface tension energy. The drop size distribution is nearly always bimodal for small density ratios, with small drops coming from the bag and the rest of the drop forming larger drops. It is, however, already clear that in situations where secondary breakup takes place, the smallest drop sizes are not generally obtained by making the primary drops as small as possible. Since larger primary drops can result in smaller drop sizes after secondary breakup, it is possible that there is an optimum size of the primary drops for a given acceleration.

A three-dimensional code designed to allow us to look at a "pie-slice" of a nearly axisymmetric flows and refine the grid in regions of interest has recently been completed. The code is currently being used to simulate breakup of jets, following an initial two-dimensional study done during the first year. The two-dimensional simulations showed that surface tension suppresses the rollup seen for a shear boundary between miscible fluids of similar density and leads to fingers of interpenetrating fluids. For small density differences the evolution is symmetric with respect to the light and the heavy fluid, but for larger density ratios the fold consisting of a heavy fluid becomes smaller and at later time the evolution becomes similar to a breaking wave with heavy fluid being stripped from the crest. Even in two-dimensions the folds can break up into drops. The three-dimensional simulations show that the "folds" are unstable in two ways. If the evolution is essentially two-dimensional, then fluid cylinders perpendicular to the shear are generated and drops are formed when these cylinders breakup by a Rayleigh Instability. If three-dimensional disturbances are strong, the initial "folds" develop into long fingers parallel to the shear and drops are formed by "end-pinch" instability of these fingers. Similar fingers are seen in the "fiber" breakup modes of jets. This evolution has also been seen recently in numerical studies by other investigators.

Three-dimensional simulations of drops in shear flows have also been started. For bubbles it has been shown that deformation have a major influence on the lift force, including changing its sign for relatively modest deformation. The simulations, as well as a number of two-dimensional ones, done to establish the necessary resolution, have shown that this is true for drops as well—as expected. We are currently examining the effects of the various parameters, including those imposed by the numerical setup, and trying to parameterize the lift force so that it can be used in simulations using point particles.

During the next year, the focus of the investigation will be three fold:

- Further quantification of the results obtained so far, including estimated of drop sizes and the time it takes a drop to disintegrate and the completion of papers describing the axisymmetric drop break-up and the break-up of a two-dimensional interface.
- Three-dimensional aspects of both the drops and the jets breakup, again, focusing on the ultimate size of the drops after breakup.
- The motion of drops and their interaction with the flow, including quantification of the dependency of lift on drop deformation.

Evolution of impulsively started drops: ρ_d/ρ_c 10, Re_d 212, Re_d 1931

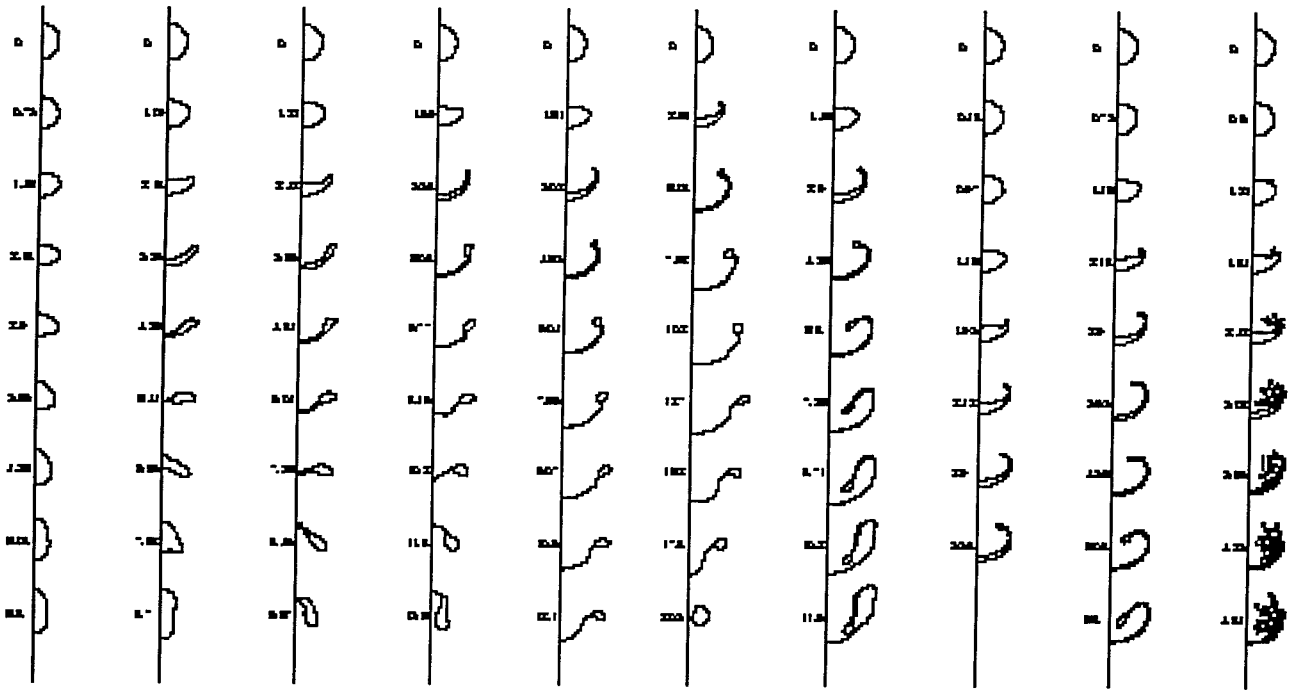

$Ut/r_e = 4.7$ $Ut/r_e = 12.5$ $Ut/r_e = 18.7$ $Ut/r_e = 28.1$ $Ut/r_e = 47.2$ $Ut/r_e = 68.8$ $Ut/r_e = 86.1$ $Ut/r_e = 2\cdot.8$ $Ut/r_e = 91.5$ $Ut/r_e = \infty$

MOLECULAR DYNAMICS INVESTIGATION OF SUPERCRITICAL FUELS

AFOSR Grant No. F49620-97-1-0128

M. M. Micci and L. N. Long

Department. of Aerospace Engineering
The Pennsylvania State University
University Park, PA 16802

SUMMARY/OVERVIEW:
Molecular dynamics (MD) implemented on parallel processors is being used to model supercritical fuel phenomena occurring in combustion devices. The coefficients of viscosity and thermal conductivity and equation of state of hydrocarbons at high pressures and temperatures are being obtained via MD and both agree with and extend NIST values. Three-dimensional supercritical oxygen and ethylene droplet vaporization into gaseous oxygen, helium and hydrogen using two-site Lennard-Jones potentials for the oxygen has been modeled and both the disappearance of surface tension above the critical point and the modification of the critical point for a binary mixture have been observed. Methods for scaling the computations to larger physical sizes are being investigated.

TECHNICAL DISCUSSION:

Transport Properties and Equation of State. Molecular dynamics is being used to calculate the coefficients of viscosity and thermal conductivity and equation of state of hydrocarbons at high (supercritical) pressures and temperatures. The transport coefficients are obtained through the appropriate autocorrelation function and the fluid pressure for a given temperature and density is calculated from the virial coefficients (1). Figures 1 and 2 compare the calculated coefficients of viscosity and thermal conductivity for ethylene at 15 Mpa and a range of temperatures with NIST provided values. The calculated values agree with the NIST values and extend the trends to higher temperatures where NIST data is not available. Figure 3 compares MD calculated pressures with experimental data. Agreement is good except at the highest density.

Submicron Droplet Evaporation. Liquid oxygen has been modeled evaporating into gaseous oxygen, helium and hydrogen using up to 45,000 molecules at gas temperatures up to 300 K and gas pressures up to 20 Mpa. For liquid oxygen evaporating into gaseous oxygen under subcritical conditions the droplet remains spherical due to surface tension until complete evaporation. Above the critical point surface tension quickly disappears and the droplet becomes convoluted with segments breaking offbefore evaporation is complete. A critical point which is a function of the mixture composition has been observed in the MD simulations of liquid oxygen evaporating into gaseous helium or hydrogen. Environment pressures much higher than the critical pressure of oxygen were required to produce the change in droplet behavior described above. A helium pressure of 20 Mpa was not sufficient to produce supercritical evaporation behavior. For hydrogen environments, a pressure of 7.5 Mpa still resulted in subcritical evaporation while a pressure of 20 Mpa did result in the disappearance of surface tension and supercritical evaporation behavior. Fig 4, with a hydrogen environment at 300 K and 4 Mpa, shows the surface tension and droplet sphericity remaining throughout the evaporation. The disappearance of both surface tension and a spherical droplet geometry for supercritical conditions is evident in Figure 5 where the environment is at 300 K and 20 Mpa.

Micron Droplet Evaporation. Although previous studies where the number of atoms was varied over one and a half orders of magnitude showed that the simulated evaporation behavior remained the same (2), computational capability currently does not permit the simulation of micron size droplets on the atomic level. Two methods for scaling soft sphere molecules interacting via a Lennard-Jones 12-6 potential are being examined. The first method, proposed by Greenspan (3), matches total system mass and energy. Thus particle mass and the Lennard-Jones parameters ε and σ are scaled, respectively, by $m_s = \frac{N}{N_s} m$, $\varepsilon_s = \frac{N}{N_s} \varepsilon$ and $\sigma_s = \sqrt[3]{\frac{N}{N_s}} \sigma$, where N is the number of particles and the subscript s denotes the scaled quantities. The second method, proposed by Long and Micci (4), matches a characteristic temperature and density, defined by $T^* = \frac{kT}{\varepsilon}$ and $\rho^* = nm\sigma^3$, where the superscript asterix denotes a characteristic variable. This results in scaling σ the same way as Greenspan but keeping ε and particle mass constant. Fig 6 compares the two scaling methods to an unscaled simulation of supercritical oxygen droplet evaporation for a scaling factor of 10 to 1. Both methods match the unscaled evaporation rate within the statistical uncertainty resulting from the small scaled system sizes. Fig 7 shows the supercritical evaporation of a micron LOX

droplet obtained with the second method and a scaling factor of a million to one. The number of droplet molecules raised to the two thirds power is proportional to the surface area, thus a D^2 versus time evaporation behavior would be a straight line. It can be seen that the droplet follows the D^2 law for a large part of its evaporation.

References

1. Nwobi, O. C., Long, L. N. and Micci, M. M., "Molecular Dynamics Studies of Transport Properties and Equation of State of Supercritical Fluids". Scheduled for publication in *Journal of Thermophysics and Heat Transfer.*
2. Kaltz, T. L., Long, L. N., Micci, M. M. and Little, J. K., Supercritical Vaporization of Liquid Oxygen Droplets Using Molecular Dynamics. Scheduled for publication in *Combustion Science and Technology.*
3. Greenspan, D., *Particle Modeling*, Birkhauser, Boston, 1997.
4. Long, L. N., Micci, M. M. & Wong, B. C., "Molecular Dynamics Simulations of Droplet Evaporation", AIAA Paper 94-2907, 30th Joint Propulsion Conference, Indianapolis, IN, June 1994.

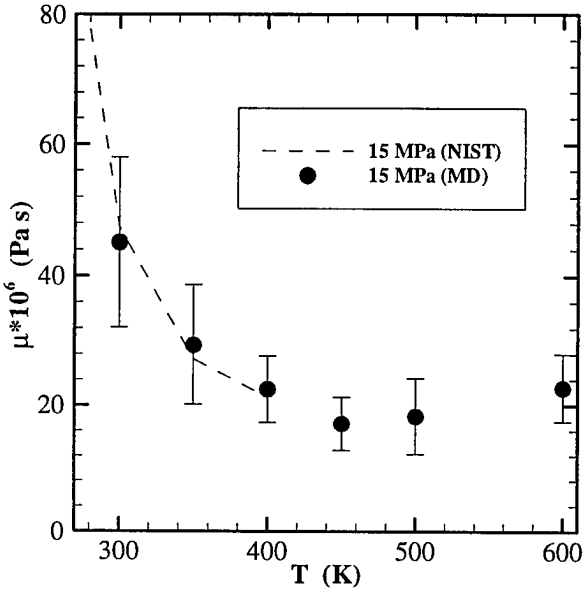

Figure 1. Ethylene shear viscosity as a function of temperature comparing MD and NIST calculated values at a pressure of 15 MPa.

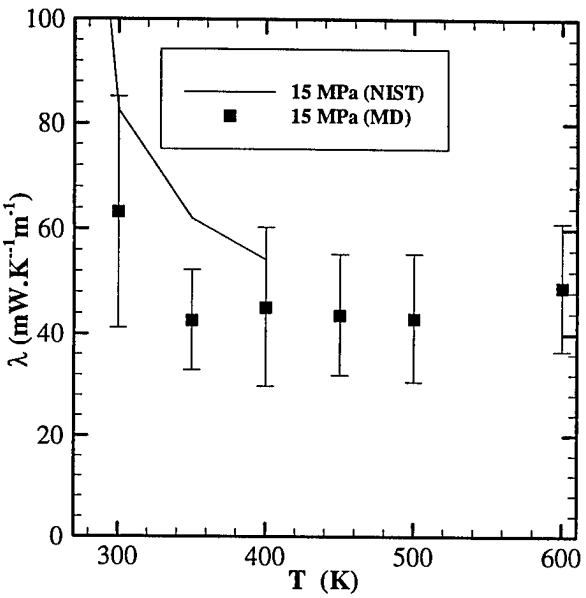

Figure 2. Ethylene thermal conductivity as a function of temperature comparing MD and NIST calculated values at a pressure of 15 MPa.

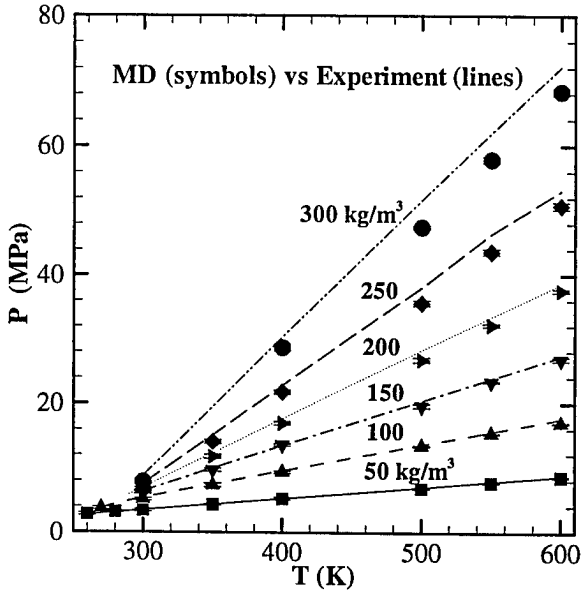

Figure 3. Ethylene pressure as a function of temperature for various densities comparing MD and experimental values.

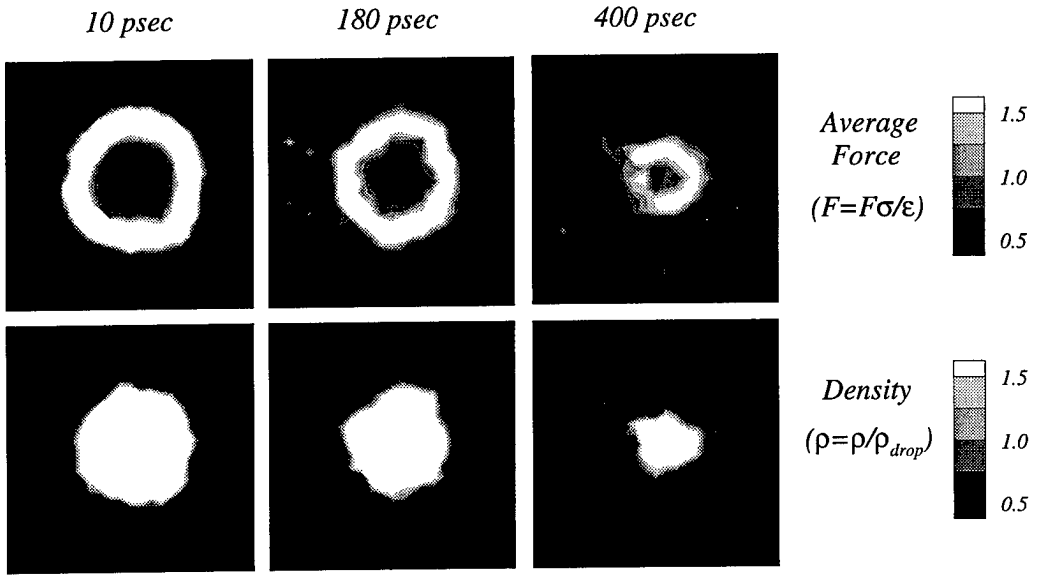

Figure 4. Contour plots of average force and density at 10, 180, and 400 picoseconds of simulation time for a LOX droplet in hydrogen at 300 K and 4 MPa. The average force is an indication of the surface tension experienced by the droplet. The density is non-dimensionalized so the droplet surface density is equal to one.

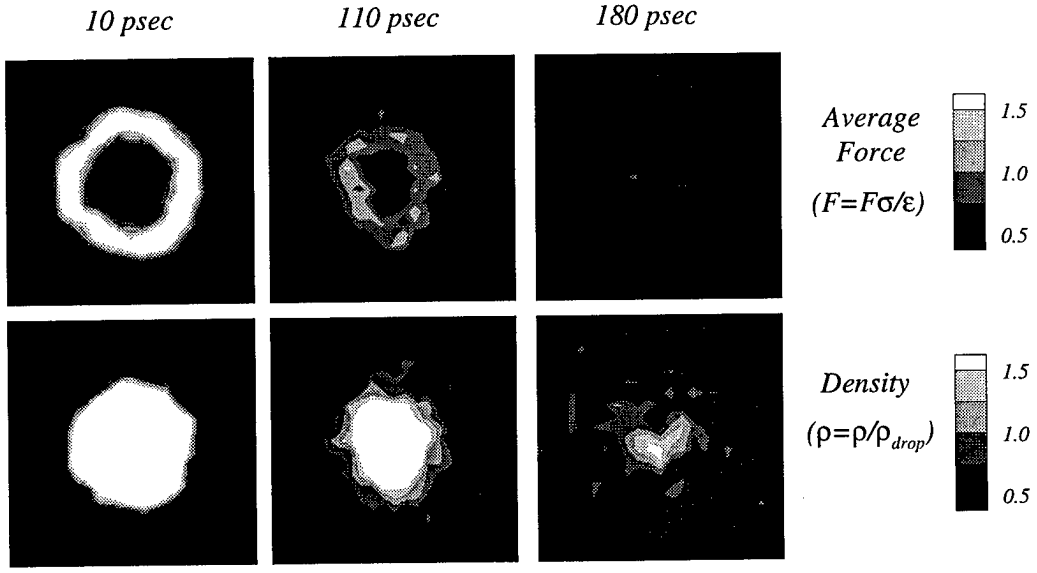

Figure 5. Contour plots of average force and density at 10, 110, and 180 picoseconds of simulation time for a LOX droplet in hydrogen at 300 K and 20 MPa. The average force is an indication of the surface tension experienced by the droplet. The density is non-dimensionalized so the droplet surface density is equal to one.

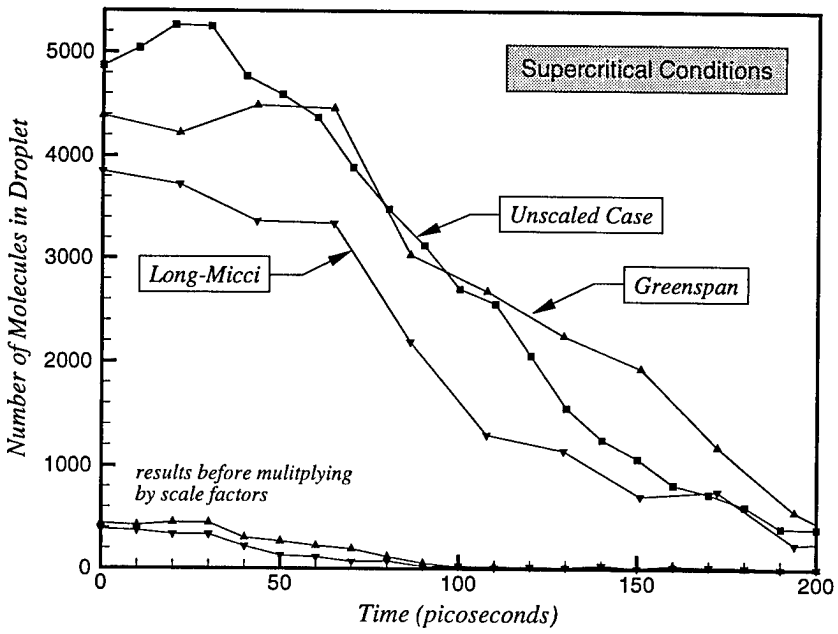

Figure 6. Comparison of evaporation rates between the two scaling methods for a supercritical case. The environment is at 200 K and 12.5 MPa. The ratio of real to scaled particles is 10 to 1.

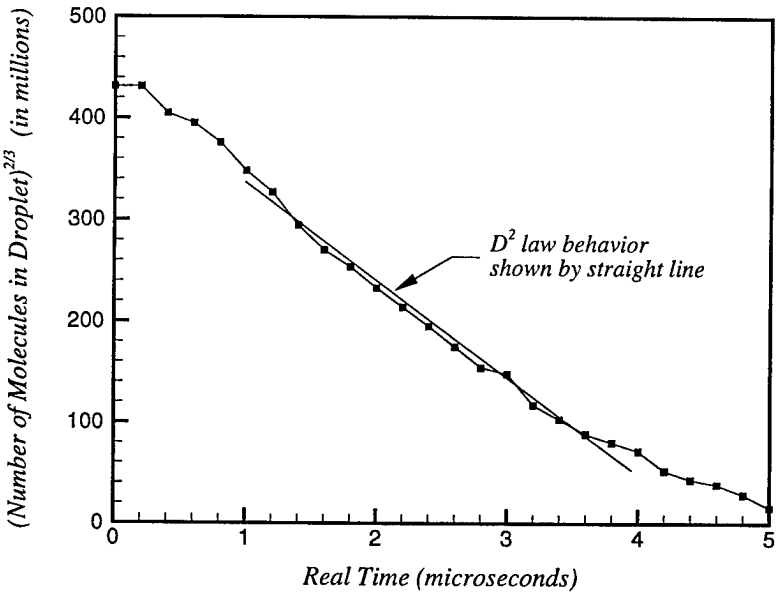

Figure 7. Comparison of micron droplet evaporation rate with D^2 law behavior. The straight line is not the slope predicted from the D^2 law, but is simply to illustrate the portion of the curve to be compared.

TITLE: STUDY OF THE SUB- AND SUPERCRITICAL BEHAVIOR OF FUEL DROPLETS AND JETS

(AFOSR Grant/Contract No. F49620-98-1-0373)

Principal Investigators: Yaw D. Yeboah and Tiejun Bai

Department of Engineering
Clark Atlanta University
223 James P. Brawley Dr.
Atlanta, GA 30314

SUMMARY/OVERVIEW:

The project is focused on experimental research into the sub- and supercritical behavior of fuel droplets and jets. Suspended, free-dropping hydrocarbon fuel droplets and jets will be studied in an experimental facility which provides a controllable high pressure and temperature environment. Besides pressure and temperature measurement, high speed images of the droplets and jets will be taken for quantitative analysis of the gasification rate and other properties. Particle Image Velocimetry or Laser Doppler Velocimetry will be used to characterize the convective environments. The study is expected to produce significant amount of experimental data and information that will enhance the understanding of the basic phenomenon of fuel droplet/jets gasification and combustion. Since little data is available in supercritical pressure and temperature regime, the experimental data and information are much needed for numerical model development and validation.

TECHNICAL DISCUSSION

For decades droplet combustion has been an active area of research because of its importance in liquid fuel combustion applications and the difficulties involved in research on this topic, both experimentally and theoretically. The research conducted in the past mainly focused on the droplet gasification and combustion at normal environment where both the ambient temperature and pressure were below critical conditions. Little work has been done in the area of supercritical droplet gasification and combustion. As a result, the basic behavior of droplets in supercitical pressure and temperature environments is still not fully understood. Furthermore, majority, if not all, of the previous experimental studies have been confined to nonconvective or naturally convective conditions. Under these conditions, heat and mass transfer between the droplet and the environment are limited to diffusion only, which is no where close to the real situation in many applications.

The most recent and detailed work in the area of supercritical droplet combustion with convective environment was conducted by Litchford et al., using a suspended droplet in a pressurized chamber. In their experiments, a preheated jet that came from an electric heater was used to ignite the suspended droplet. Images and temperature history were recorded to analyze the droplet gasification and combustion characteristics.

This project started in April 1998. Initial work has focused on the modification of an existing droplet experimental setup which was built with funding from other sources. This droplet experimental setup consists of a liquid pressurizing and transfer system, a high pressure/temperature chamber, a droplet generator, an ignitor, and a measurement system. The setup provides a quiescent environment with pressure ranges covering both subcritical and supercritical conditions for many hydrocarbon fuels. However, the facility lacks the capability of providing a convective flow and changing ambient temperature. Using the existing facility, Clark Atlanta University has conducted experiments on hexane fuel droplet gasification and combustion under various pressures but room temperature and quiescent environment. In order to conduct fuel droplet and jet combustion tests under supercritical pressure with variable ambient temperature and possibly convective flow, the experimental setup needs to be modified. The current design is to add an electrical heater in the fuel feeding line and the ambient gas feeding line. In addition, the droplet generator will also need to be modified to provide the capability of forming fuel jets. In this presentation, the existing experimental setup, its planned modification, and the experimental plan will be discussed in detail. The modification of the experimental setup will be completed in August and experiments will begin in September.

In summary, this study is expected to produce significant amount of experimental data and information that will enhance the understanding of the basic phenomenon of fuel droplet/jets gasification and combustion. Since little data is available under supercritical pressure and temperature regimes, the experimental data and information produced in this project will provide the much-needed experimental evidence for numerical model development and validation.

THE CHEMISTRY CONTROLLING IGNITION OF HYDROCARBONS AND THEIR MIXTURES AT HIGH PRESSURE

Contract No's. DAAG55-98-1-0286 and DAAG55-97-1-0196
Reference No's. 37699-EG and 36910-EG-AAS

N.P. Cernansky and D.L. Miller

Department of Mechanical Engineering and Mechanics
Drexel University, Philadelphia, PA 19104

SUMMARY/OVERVIEW

A research program to investigate the high pressure oxidation and ignition characteristics of hydrocarbon fuels has continued, and includes efforts under an associated AASERT Award. The objectives of this program are to develop the kinetic and mechanistic information in the low and intermediate temperature regimes (650-1000 K) and at elevated pressures (up to 20 atm) which will be useful to understand the oxidation of pure hydrocarbons, determine the synergistic and antagonistic effects for multicomponent mixtures of full boiling range fuel components, and formulate hypotheses on ignition mechanisms. Efforts are directed towards experimental investigation of the oxidation of pure hydrocarbons and hydrocarbon blends, prediction and validation of mechanisms relevant to preignition chemistry of hydrocarbons and hydrocarbon mixtures, and development of in situ measurement techniques using degenerate four-wave mixing (DFWM) and Cavity Ringdown Laser Absorption Spectroscopy (CRLAS). The on-going experimental studies are providing new diagnostic tools and detailed species measurements during hydrocarbon oxidation for use in the development and validation of autoignition models incorporating chemistry from the low temperature and negative temperature coefficient regime. Interpretation of the experimental results and development of appropriate chemical kinetic models are being accomplished as a combination of in-house work and collaborative work with other researchers. These efforts are expected to culminate in a better understanding of the preignition chemistry of hydrocarbons and hydrocarbon mixtures.

I. EXPERIMENTAL AND MECHANISTIC STUDIES IN THE PRESSURIZED FLOW REACTOR (PFR)

Facility -- Over the past few years the pressurized flow reactor at Drexel University has been upgraded with the addition of a second stage air heater in order to cover the full range of low and intermediate temperatures. The reactor can now reach temperatures in excess of 1000 K (the previous limitation was 850 K). The reproducibility of the facility after modification was confirmed by conducting a reactivity mapping experiment using n-pentane as fuel. The reactivity map matched previous results very well and day-to-day variation is within 5%.

Neopentane Oxidation -- As part of our recent efforts, experiments investigating the oxidation of neopentane in the well characterized thermal and fluid environment of our pressurized flow reactor (PFR) have been completed. Specifically, an investigation of neopentane oxidation has identified a negative temperature coefficient (NTC) regime for neopentane (Figure 1). Under dilute and lean conditions (75% unreactive nitrogen, $\phi = 0.3$), the NTC of neopentane starts at 712 K and ends at 790 K. For comparison, the reactivity map of n-pentane is also plotted. Major

intermediate products, such as formaldehyde, isobutene, 3,3-dimethyloxitane, acetone, carbon monoxide, carbon dioxide, etc., from neopentane oxidation were measured using our Fourier Transform Infrared Spectroscopy facility and non-dispersive infrared analyzers (Figure 2). Because of the structure of neopentane, the traditional theory explaining NTC of hydrocarbons is not applicable. It is well accepted that NTC behavior occurs at temperatures when reactions forming conjugate alkenes become dominant. However, for neopentane, no such conjugate alkene exists. Based on the experimental results, we found the formation of isobutene and 3,3-dimethyloxetane increase as temperature increases in the NTC region while the formation of other species decreases. The reactions leading to isobutene and 3,3-dimethyloxetane are believed to be correlated to this NTC behavior. In order to improve current hydrocarbon oxidation mechanisms in the low and intermediate temperature regions and at elevated pressure, we are collaborating with Lawrence Livermore National Laboratory (LLNL) to test and refine the current detailed model of neopentane oxidation. This effort involves the reevaluation of the relevant thermochemistry and kinetics and comparison of model simulations with our experimental species evolution profiles. The results from this study will contribute to our better understanding of hydrocarbon oxidation mechanisms.

High Boiling Point Fuels -- In related research work, we continued our examination of the preignition reactivity of high boiling point fuels. We generated detailed reactivity maps for several industry standard fuels (ISF's) in our pressurized flow reactor. The fuels examined in our work include RFA, RFB, 87 PRF, 92 PRF, a standard Ford test fuel, Indolene, and a simplified fuel mixture of aromatic, olefinic and saturated hydrocarbons (92 RON MIX). The negative temperature coefficient regimes of all these fuels have been mapped and accurately match our engine data for similar fuels (Figure 3). It was seen in these results that the surrogate mixture matches the reactivity and the start of NTC behavior of the ISF'S quite well. Using the FTIR, we have initiated "group species analysis" which is a semi-quantitative method for analyzing the reaction progress involving measurement and calibration of the characteristic spectroscopic features produced by the hydrocarbon classes such as alkanes, alkenes, aromatics, and aldehydes. Preliminary results show great promise for using group analysis as a means of comparing the reaction pathways for all of the PRF's, ISF's and RON blends. A detailed intermediate and product analysis can be carried out for the surrogate mixture for further development of a chemical model.

II. LASER DIAGNOSTIC ACTIVITIES

For the past three years, we have been developing new sensitive techniques for measuring highly reactive radicals in-situ in combustion processes. We have had great success in a collaborative effort with the David Rakestraw group at Sandia National Laboratory (Livermore CA) measuring several radical polyatomic species in high temperature / low pressure laminar flat flames using Cavity Ringdown Laser Absorption Spectroscopy (CRLAS). This was the first reported measurement of a combustion-generated polyatomic radical using infrared-CRLAS, CH_3 radical at 3.3 μm, and of HCO at 614 nm in a fuel rich flame (Figures 4 and 5).

The motivation for measuring these unstable radical species is to assist in determining the mechanisms which govern the combustion of PRF's and ISF's at high pressures. It is very difficult to sort out the mechanism of these complex fuels without tracing some of the important radical species. One of the most important radicals governing the NTC region at high pressures and moderately low temperatures is the hydroperoxy radical HO_2. HO_2 was not studied in the previous flat-flame work because chemical kinetic models predicted that not enough was formed to yield a detectable CRLAS signal. More recently, we have begun investigating the feasibility of measuring radicals such as HO_2, OH, CH_3 and HCO in our pressurized flow reactor. Since the pressure is much higher and the temperature is considerably lower than the flat-flame, there should be more HO_2 present. Figure 6 shows the effect of pressure on the predicted cavity

ringdown signal with an inlet temperature of 650 K. These results indicate that HO_2, OH and HCO are all detectable at pressures above 6 atm. We plan to measure the CRLAS spectrum of these radicals using a supersonic jet expansion to both cool the molecules and reduce the pressure. Both of these effects enhance the CRLAS signal.

III. CURRENT AND FUTURE WORK

Currently, we are simulating our neopentane experimental results in collaboration with LLNL. A neopentane oxidation mechanism in the low and intermediate temperature regions and at elevated pressures will be refined. Analysis of our data from high boiling point fuels is underway. In the future, we will extend our study to examine the preignition chemistry of hydrocarbon mixtures and full boiling range fuels at pressures encountered in practical combustion devices. Specifically, we will first use our pressurized flow reactor to explore the preignition oxidation chemistry of larger, fuel-type hydrocarbons, which include C6s, C7s, C8s, reference fuels, and higher hydrocarbons. Then, we will investigate the reaction of two, three, and four component hydrocarbon mixtures and industry standard fuels in order to further develop the concept of surrogates which reproduce the ignition behavior of these fuels. In conjunction with this experimental program, we will develop chemical kinetic models in collaboration with LLNL. In this phase we will examine the ability of candidate mechanisms to simulate our experimental results. A comparison between the experiments and the simulation will be used to improve the detailed models. In addition, newly developed laser diagnostics will be incorporated into our experimental facility to allow measurement of more species and radical concentrations.

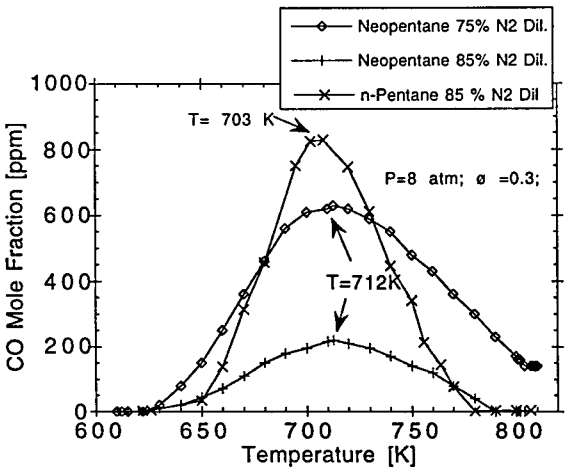

Figure 1. Reactivity maps for neopentane at two different N_2 dilutions and for n-pentane.

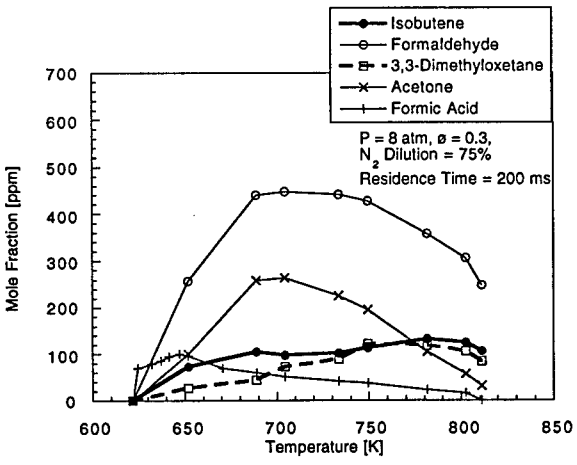

Figure 2. Major products formed during the reactivity mapping of neopentane.

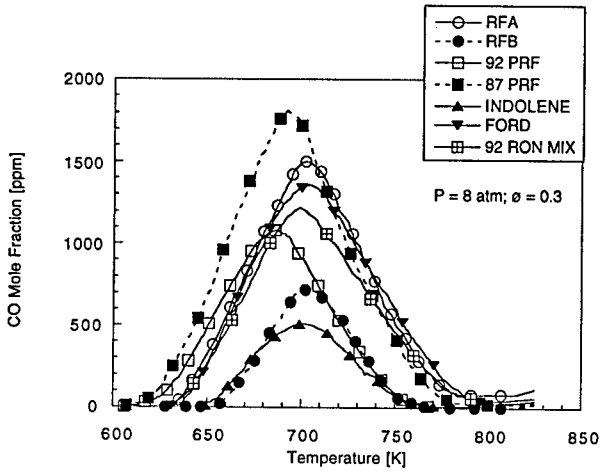

Figure 3. Reactivity mapping of industry standard fuels, primary reference fuel blends, Indolene, standard Ford test fuel, and 92 RON MIX, a mixture of aromatic, olefinic and saturated hydrocarbons blended to match the overall compositions of the ISF's.

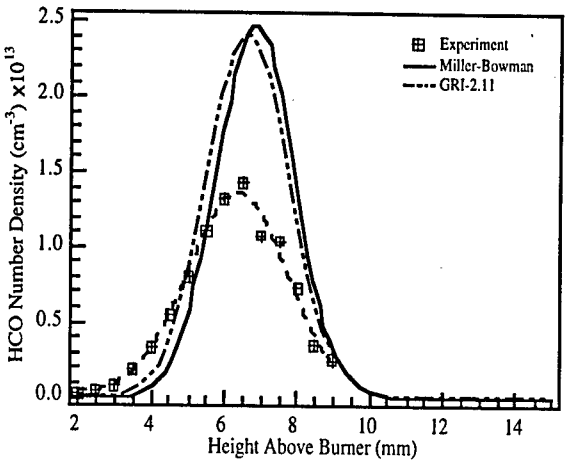

Figure 4. Comparison of experimental HCO concentrations with model predictions in stoichiometric, 37.5 torr, $CH_4/O_2/N_2$ flat flames.

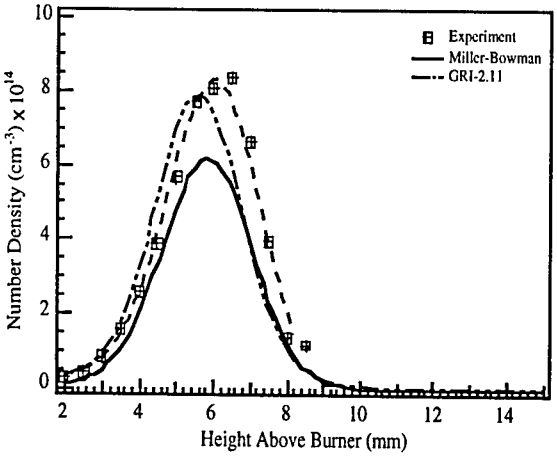

Figure 5. Comparison of experimental CH_3 concentrations with model predictions in stoichiometric, 37.5 torr, $CH_4/O_2/N_2$ flat flames.

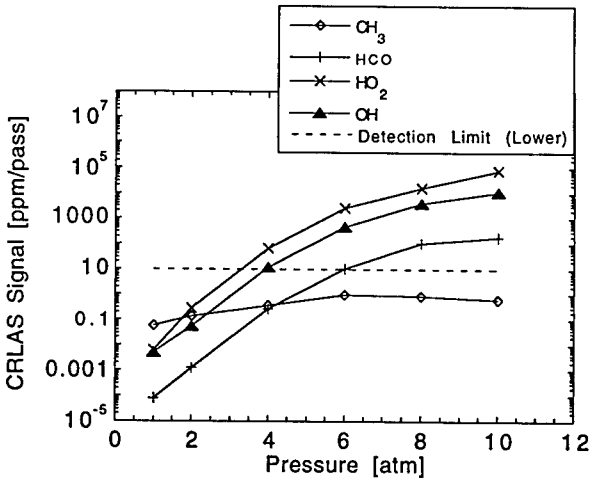

Figure 6. CRLAS signal as a function of pressure. All radicals except CH_3 are detectable using CRLAS at pressures above 8 atm.

CHEMICAL KINETICS AND AERODYNAMICS OF IGNITION

(ARO Grant No. DAAG55-97-0315)

Principal Investigator: Chung K. Law

Department of Mechanical and Aerospace Engineering
Princeton University, Princeton, NJ 08544

SUMMARY/OVERVIEW

This program investigates ignition in convective-diffusive systems with the goal of improving the understanding of the complex interactions between convective-diffusive transport, turbulence, and chemical reactions involved in the ignition event in Diesel engines. These interactions are studied experimentally and computationally by using the counterflow configuration where a heated air jet is opposed by a cold fuel jet. Two major research thrusts were undertaken, namely studies on effects of NO addition on the ignition of hydrogen and hydrocarbons, and the role of turbulence on hydrogen ignition. Concerning the former, earlier studies have indicated that NO can significantly enhance the ignition event in a homogenous system, but the effects in a diffusive inhomogenous system, as found in engines, have not been determined. We have demonstrated that the homogenous ignition results are largely carried over, at least qualitatively, to the nonpremixed system. Concerning the latter, we have demonstrated that, under most conditions the high rates of reaction in the hydrogen system determine that the system behaves in a quasi-steady manner and the ignition event is not significantly altered by the presence of turbulence. However, for very lean mixtures turbulence was able to alternately ignite and extinguish the flow.

TECHNICAL DISCUSSION

1. Ignition Enhancement of Hydrogen through NO Addition

Combustion in practical engines generates significant amounts of NO_x. It is therefore of importance to assess the effects of NO on the ignition and burning processes, especially recognizing that numerous studies in homogenous systems have shown that NO can vigorously accelerate the oxidation process of hydrogen, carbon monoxide, and hydrocarbons. Since Diesel engines rely upon autoignition to initiate the combustion process, it is of interest to determine whether NO plays a similarly important role in nonpremixed systems and thereby can significantly alter the engine performance. To this end, experiments were conducted with pure hydrogen flowing against hot air doped with varying amounts of NO. Numerical calculations were also performed to aid in understanding the chemistry involved in these systems. The results are shown in Fig. 1, which plots the variation of the ignition temperature as a function of NO concentration in air. The experimental results are in symbols while lines represent modeling results obtained at 1 atm.

Firstly, as expected, addition of NO, even at a very low concentration (250 ppm), exerts a strong catalytic effect on the system and reduces the ignition temperature of hydrogen. This effect is due to the fact that NO catalytically transforms the normally chain terminating HO_2 radical into chain propagating OH radicals. Secondly, as observed for homogeneous ignition, it appears that there exists an optimal NO concentration beyond which the ignition temperature actually increases with increasing NO concentration. This indicates that at a certain concentration level, NO starts to act as an inhibitor to the oxidation process. Under these conditions, recombination reactions between NO and the radicals H, O, and OH act as a radical

sink, leading to a rise in the ignition temperature. Thirdly, in the range of this study, it is found that with increasing pressure, the magnitude of the catalytic effect increases and the optimal concentration slightly decreases. The increase of the catalytic effect with pressure is due to the pressure sensitive reaction producing HO_2. With more HO_2 present, the catalytic reactions are favored. Similarly, the recombination reactions responsible for ignition inhibition are pressure dependent. As these reactions become faster at higher pressures, their effect is felt sooner and the minimum point moves to lower NO concentrations

Another series of experiments were conducted with 30% hydrogen mixed with nitrogen to assess the effects of NO on reduced hydrogen concentrations. In these experiments, shown in Fig. 3, high levels of NO addition again have a pronounced inhibiting effect below 2 atm such that the ignition temperatures are significantly higher than the pure air case. At 2 atm, the ignition temperature obtained at the same NO concentration is similar to that of pure air. For pressures above 2 atm, one can observe a rapid increase in the ignition temperature beyond the optimal NO concentration. Beyond this rapid increase, the inhibiting effect of NO is less pronounced with further increase. These trends are explained by the fact that decreasing H_2 decreases the amount of HO_2 and therefore lowers the catalytic NO effect. On the other hand, the radical recombination reactions are not significantly affected by the H_2 concentration, hence shifting the overall balance in favor of inhibition.

2. Effect of NO Addition on Hydrocarbon Ignition

To assess the effects of NO addition on the hydrocarbons, ignition experiments were conducted on methane, ethane, propane, and iso-butane. Just as for hydrogen, the ignition temperatures of all hydrocarbons decrease with the presence of NO in air. This decrease is accentuated by increasing pressure and depends on the specific hydrocarbons. From the results shown in Fig. 3 for one atmosphere, it can be seen that, among these fuels, methane has the highest sensitivity to NO in air followed by hydrogen. Propane also has a high sensitivity. Comparatively, ethane and iso-butane are less sensitive. The ignition temperature reduction can again be explained as a catalytic transformation of the low temperature terminating species (RO_2) into chain propagating species.

Contrary to the hydrogen case where there exists a clear optimal NO concentration for all experiments performed above 1 atm, hydrocarbon fuels are more complex. For example Fig. 4 shows that a clear minimum does not always exist for ethane. When present, the NO concentration at which the lowest ignition temperature is achieved again depends on the nature of the fuels and pressure. Typically, for hydrocarbons, the minimum point is achieved at 0.5% of NO in air at 1 atm as compared to 0.1% of NO in air for hydrogen. With increasing pressure, the minimum point shifts toward lower NO concentration, which is similar to the hydrogen case.

3. Turbulent Ignition of Hydrogen at High and Low Fuel Concentrations

Ignition in many practical devices and phenomena occur in turbulent, diffusive environments. The present study extends our previous investigations on *laminar* hydrogen ignition in convective-diffusive systems to *turbulent* flows. Since turbulence can be visualized as a cascade of eddies which impose a wide range of time and length scales on the laminar flow, randomness associated with turbulence results in a distribution of instantaneous strain rates about a mean turbulent strain rate at a given point in the flow. Turbulent ignition was investigated over a range of bulk strain rates and turbulent intensities for both high and low hydrogen concentrations. High fuel concentrations were represented by 20% hydrogen in nitrogen. Under the flow conditions examined, no apparent effect of turbulence on ignition temperature was observed, and the data was scattered about the calculated laminar ignition

temperatures (Fig. 5). This was consistent with the insensitivity to flow conditions previously observed in laminar systems due to the high rates of reaction relative to transport.

Experiments with low fuel concentrations exhibited two modes of ignition, which are shown in Fig. 6. Sudden ignition, identical to laminar ignition, was found at the higher fuel concentrations. Intermittent ignition, seen at lower fuel concentrations, was characterized by a range of temperatures where the flame repeatedly ignited and extinguished with the duration and frequency of the ignited flame depending on the hot air temperature. This range of temperatures straddled the laminar ignition temperature at a similar bulk strain rate. The onset of the intermittent ignition mode was shifted to higher fuel concentrations and the width of the intermittent band, for a fixed fuel concentration, increased as the turbulence intensity increased as shown in Fig. 7. A shift to higher temperatures was observed when the mean strain rate was increased, while the intermittent ignition band width and the fuel concentration at the onset of intermittent ignition were increased slightly.

The large turbulent timescale, relative to the other timescales in the problem, means that the system is expected to exhibit a quasi-steady response, allowing steady-state laminar ignition results to be applied to understand the response of the kernel to the fluctuating net strain rate. Such calculations show that the hysteresis between ignition and extinction is lower in the intermittent ignition cases than the sudden ignition cases. As a result, turbulent fluctuations in the strain rate can alternately ignite and extinguish the system until the temperature is sufficiently high for the extinction strain rate to remain above the maximum strain rate excursion. Nevertheless, *ignition* events are still determined by the condition that the minimum strain rate fluctuation is below the ignition strain rate.

MAJOR PUBLICATIONS

[1] "Ignition of counterflowing methane versus heated air under reduced and elevated pressures," by C.G. Fotache, T.G. Kreutz and C.K. Law, *Combust. Flame* 108:442-470 (1997).

[2] "Ignition of hydrogen-enriched methane by heated air," by C.G. Fotache, T.G. Kreutz and C.K. Law, *Combust. Flame* 110:429-440 (1997).

[3] "Theory of radical-induced ignition of counterflowing hydrogen versus oxygen at high temperatures," by B.T. Helenbrook, H.G. Im and C.K. Law, *Combust. Flame* 112:242-252 (1998).

[4] "Mild oxidation regimes and multiple criticality in nonpremixed hydrogen/air counterflow," by C.G. Fotache, C.J. Sung, C.J. Sun and C.K. Law, *Combust. Flame* 112:457-471 (1998).

[5] "Ignition in nonpremixed counterflowing air versus heated air: computational study with skeletal and reduced chemistry," by T.G. Kreutz and C.K. Law, *Combust. Flame*, in press.

[6] "Ignition of oscillating counterflowing nonpremixed hydrogen against heated air," by C.J. Sung and C.K. Law, *Combust. Sci. Technol.*, in press.

[7] "An experimental study of hydrocarbon ignition in convective-diffusive systems under variable pressures: ethane, propane, n-butane, and isobutane," by C.G. Fotache, H. Wang and C.K. Law, *Combust. Flame*, submitted.

[8] "Turbulent ignition of nonpremixed hydrogen by heated counterflowing atmospheric air," by J.D. Blouch, C.J. Sung, C.G. Fotache and C.K. Law, *Twenty-Seventh Symposium (International) on Combustion*, The Combustion Institute, Pittsburgh, PA, in press.

[9] "Effects of NO on the ignition of hydrogen by heated counterflowing air," by Y. Tan, C.G. Fotache and C.K. Law, submitted.

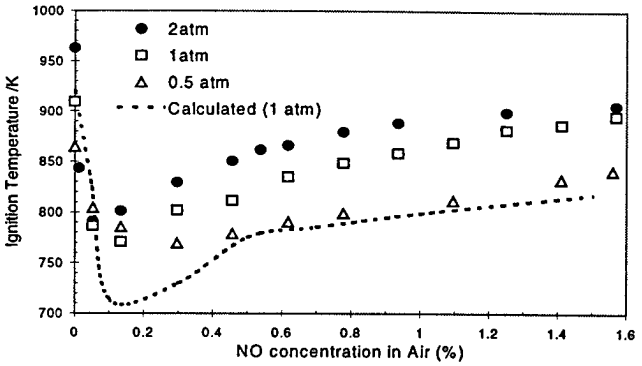

Figure 1: Ignition of pure H_2 vs. NO doped air

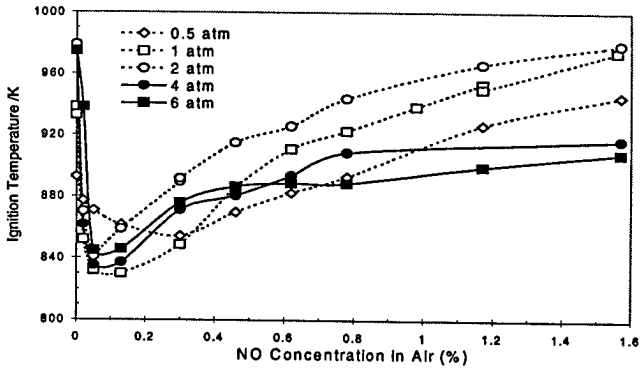

Figure 2: Ignition of 30%H_2/70% N_2 vs. NO doped air.

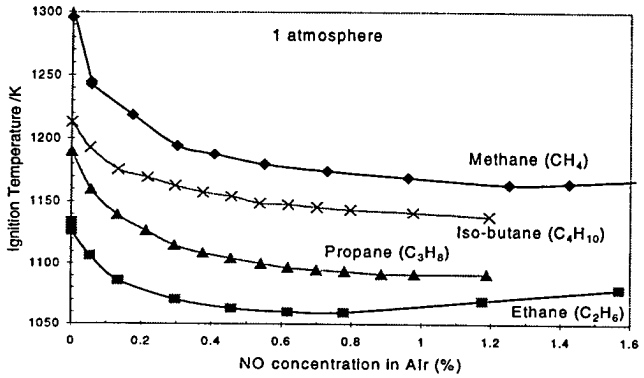

Figure 3: Effect of NO addition to air on hydrocarbon ignition temperatures.

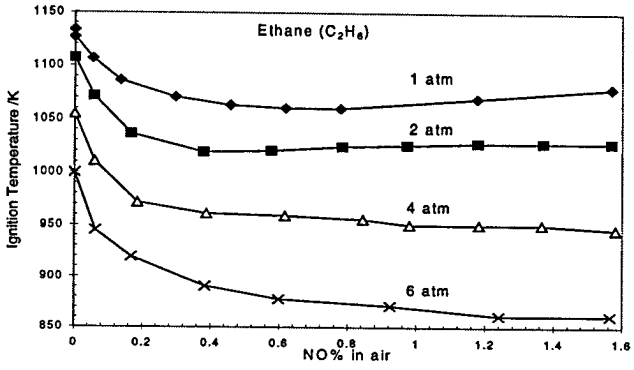

Figure 4: Effect of pressure on sensitivity to NO addition.

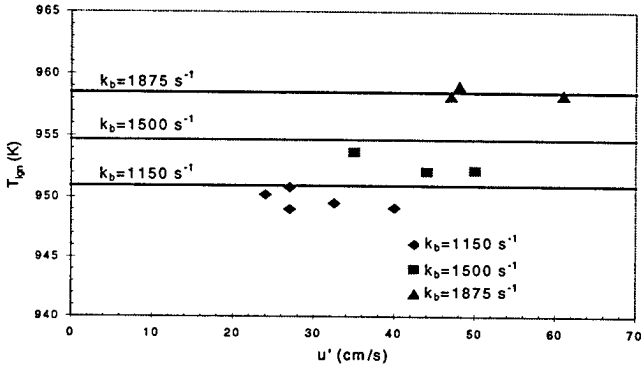

Figure 5: Ignition temperature as a function of turbulent intensity for 20% H_2/80% N_2.

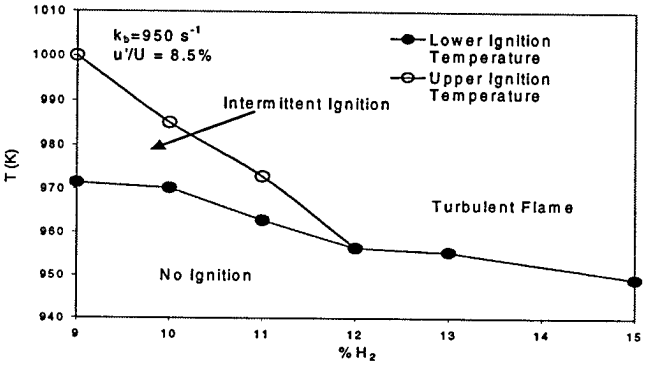

Figure 6: Intermittent ignition behavior.

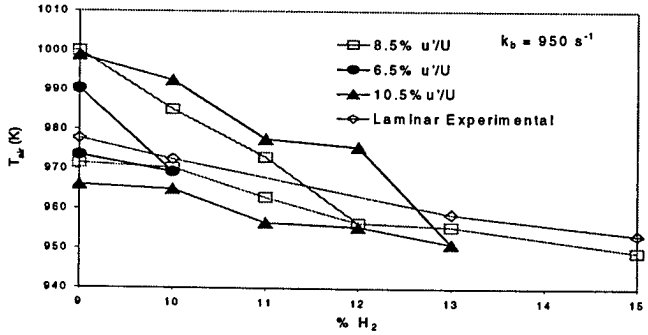

Figure 7: Effect of turbulent intensity on intermittent ignition.

ADVANCED SUPERCRITICAL FUELS

AFOSR Task # 93WL002

Principal Investigators: Tim Edwards, Jim Gord, Mel Roquemore

Air Force Research Laboratory
AFRL/PRSF Bldg 490
1790 Loop Rd N
Wright Patterson AFB, OH 45433-7103

SUMMARY/OVERVIEW:

Increases in aircraft and engine performance are increasing the heat load being transferred into an aircraft's primary coolant--the fuel. This research is aimed at understanding the limitations of operation of fuel heated to 480 C (900 F) and beyond. Important issues are expected to be thermal stability, heat transfer/flow instabilities, and injection/combustion properties.

TECHNICAL DISCUSSION

Fuel thermal stability is one of the major barriers to the use of high temperature fuels. Thermal stability in this context refers to the tendency of a fuel to form deposits on fuel systems surfaces, filters, and controls. As shown in Figure 1, deposits can be formed by two major mechanisms, thermal-oxidative and pyrolytic [1]. Current fuels are subject only to thermal-oxidative fouling, since the current fuel temperature limits range from 325 F (JP-8) to 550 F (JP-7). At AFRL, experimental and modeling efforts in the last year have focussed on unraveling the complex oxidative and deposition processes in multicomponent fuels such as JP-7 and JP-8 [1-23]. JP-8 contains hundreds of hydrocarbons, with small amounts of heteroatomic species. Although the concentration of minor species is small, the impact can be large. Oxidative deposition rates are typically less than 1 ppm, which may seem small, but can severely impact small fuel system passages and controls in a matter of hours. An additive package developed under the JP-8+100 program has demonstrated a significant reduction in deposition from JP-8 fuels, but the further improvements needed for operation under supercritical conditions (>750 F) will require a better understanding of the oxidation and deposition chemistry [2]. As shown in Figure 2, the oxidative reactions are fairly complex and interlinked [3]. Attempts to reduce deposition through modifications to these chemical pathways have been hampered in JP-8 fuels by the huge variety of chemical species present in this distillate fuel [3-5]. Modeling efforts have been fairly successful at reproducing JP-8 oxidation and deposition behavior with 10-20 reactions [6-12]. A difficulty has been reproducing the wide variation in JP-8 deposition behavior that can occur within the JP-8 specification. Deposition levels can vary by an order of magnitude or more for specification JP-8's, and are a complex function of flow rate, dissolved oxygen levels, recirculation, and additives [1-23]. One explanation can be seen in Table 1, which shows the variation in sulfur levels and other properties in JP-8 fuels purchased by DOD in FY97

[24]. If one wants to predict the deposition behavior of a given JP-8 fuel, then the sulfur level of the fuel as purchased is a key model input (as a minimum).

Fuel pyrolytic deposition mechanisms are easily as complicated as oxidative mechanisms [1]. Efforts in the past year have focussed on understanding fuel condensation reactions in pyrolyzing fuels [25-27], and examining pyrolysis-suppressing additive mechanisms in fuels [28]. As the understanding of these processes improves, they are being added to models used to simulate fuel system components [29]. AFOSR-funded research at Princeton has demonstrated the close ties between fuel structure and condensation behavior [37]. Studies of the influence of heat flux, residence time, and fuel system configuration on deposition continue [30,31], with applications to gas turbines and hypersonics [32]. In situ diagnostics continue to be investigated to assess the physics and chemistry of the deposition processes under high temperature and pressure conditions [33-36]. In-situ Raman studies can track the formation of olefins and aromatics, as well as the supercritical nature of the fuel during pyrolysis; fluorescence can track changes in polarity [36]. Changes in C-H and C-C Raman signals with pressures through supercritical have been demonstrated for hexane [36]. In-situ diagnostic probing of catalytic fuel cracking has been demonstrated in another AFOSR-funded effort at Worcester Polytechnic Institute [38].

Table 1 – FY97 JP-8 analyses, weighted average of shipments totaling $7X10^8$ gal [24]

	Specification	Mean	Range
Total sulfur, wt%	0.3	0.047	0-0.3
Aromatics, vol %	25	18.8	6.0-24.6
H_2 content, wt %	13.5	13.7	13.4-14.3

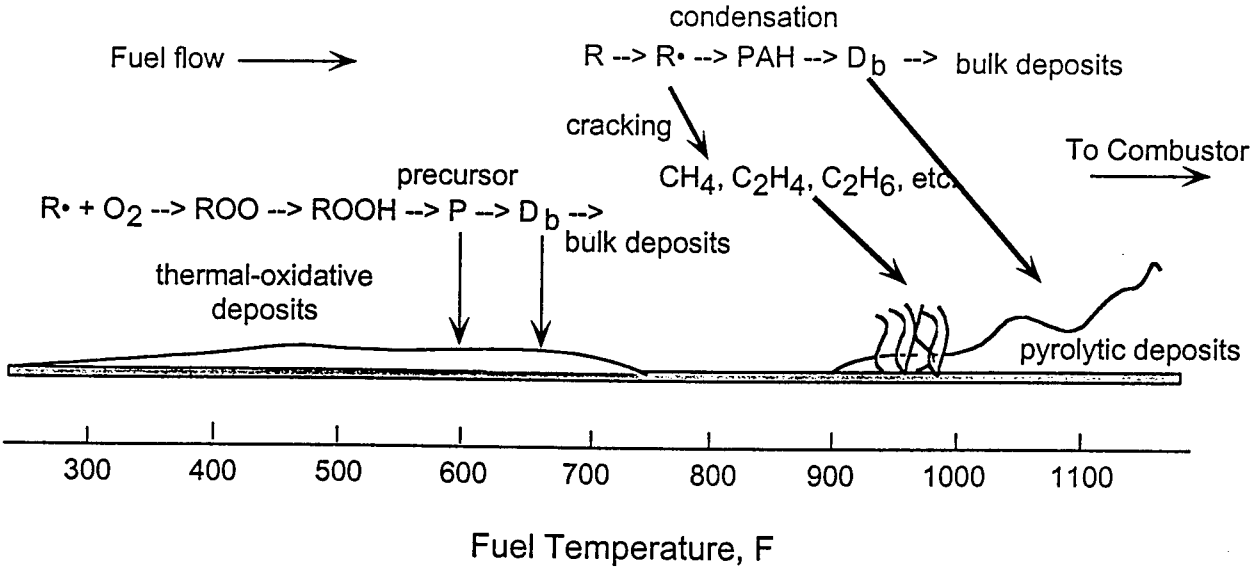

Figure 1. Fuel deposition regimes as a function of temperature.

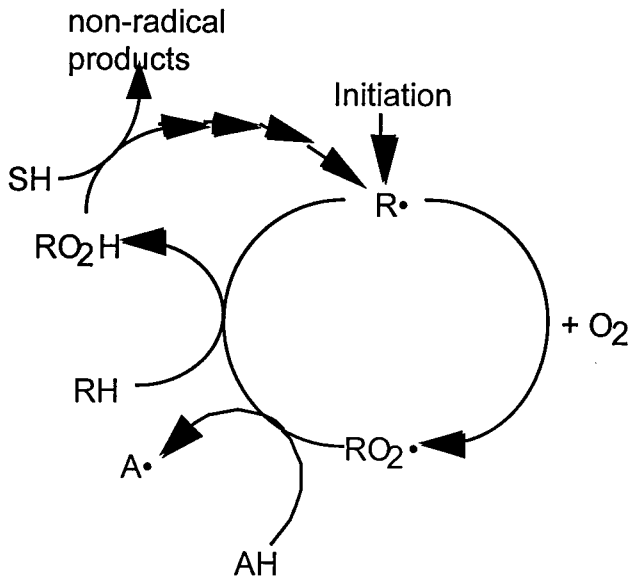

Figure 2. Fuel oxidation pathways. SH=fuel sulfur compounds, RH=fuel hydrocarbons, AH=fuel anti-oxidants. The sulfur-containing "non-radical products" are the precursors to deposit formation.

REFERENCES

[1]. Edwards, T., Atria, J. V., "Thermal Stability of High Temperature Fuels," ASME 97-GT-143, ASME Turbo Expo, June 1997.

[2]. Edwards, T., "Prospects for JP-8+225, A Stepping Stone to JP-900," AIAA Paper 98-3532, July 1998.

[3]. Zabarnick, S., Mick, M. S., "Studies of Hydroperoxide Decomposing Species for Inhibiting Oxidation in Jet Fuels," paper to be presented at ACS National Meeting, Petroleum Chemistry Division, Boston, MA, August 1998.

[4]. Zabarnick, S., Mick, M. S., Striebich, R. C., Grinstead, R. R., Heneghan, S. P., "Studies of Silylating Agents as Thermal-Oxidative Jet Fuel Additives," ACS Fuel Chemistry Division Preprints, Vol. 43 (1), pp. 64-68, 1998.

[5]. Beaver, B., DeMunshi, R., Heneghan, S. P., Whitacre, S. D., "Model Studies Directed at the Development of New Thermal Oxidative Stability Enhancing Additives for Future Jet Fuels," Energy & Fuels, Vol. 11, pp. 396-401, 1997.

[6]. Ervin, J. S., Zabarnick, S., "Computational Fluid Dynamics Simulation of Jet Fuel Oxidation Incorporating Pseudo-Detailed Chemical Kinetics," Energy and Fuels, Vol. 12, pp. 344-352, 1998.

[7]. Ervin, J. S., Zabarnick, S., "Numerical Simulation of Jet Fuel Oxidation & Fluid Dynamics," Proceedings of 6th (Int'l) Conference on Stability & Handling of Liquid Fuels, Vol. 1, pp. 385-402, DOE CONF-971014, Feb. 1998.

[8]. Zabarnick, S., "Pseudo-Detailed Chemical Kinetic Modeling of Antioxidant Chemistry for Jet Fuel Applications," Energy and Fuels, in press (1998).

[9]. Katta, V. R., Jones, E. G., Roquemore, W. M., "Modeling of Deposition Process in Liquid Fuels," AIAA 97-3040, July 1997.

[10]. S. Zabarnick, "Chemical Kinetic Modeling of Antioxidant Chemistry for Jet Fuel Applications," Energy & Fuels, submitted for publication.

[11]. Ervin, J. S., Zabarnick, S., " Modeling of Fuel Oxidation Using a Pseudo-detailed Chemical Kinetic Model," Energy & Fuels, submitted for publication.

[12]. Ervin, J. S., Heneghan, S. P., "The Meaning of Activation Energy and Reaction Order in Autocorrelating Systems," ASME Journal of Engineering for Gas Turbines and Power, in press (1998).
[13]. Jones, E. G., Balster, L. M., "Impact of Additives on the Autoxidation of a Thermally Stable Aviation Fuels," Energy and Fuels, Vol. 11, pp. 610-614, 1997.
[14]. Jones, E. G., Balster, W. J., Balster, L. M., "Aviation Fuel Recirculation and Surface Fouling," Energy and Fuels, Vol. 11(6), pp. 1303-1308, 1997.
[15]. Pickard, J. M., Jones, E. G., "Catalysis of Jet A Fuel Autoxidation by Fe2O3," Energy and Fuels, Vol. 11(6), pp. 1232-1236, 1997.
[16]. Jones, E. G., Balster, L. M., "Autoxidation of Diluted Aviation Fuels," ACS Fuel Chemistry Division Preprints, Vol. 43 (1), pp. 44-48, 1998.
[17]. Balster, L. M., Jones, E. G., "Autoxidation of Aviation Fuel Blends," ACS Fuel Chemistry Division Preprints, Vol. 43 (1), pp. 49-52, 1998.
[18]. Jones, E. G., Balster, W. J., Balster, L. M., "Evaluation of the Effectiveness of a Metal Deactivator and Other Additives in Reducing Insolubles in Aviation Fuels," ASME Journal of Engineering for Gas Turbines and Power, Vol. 119, to be published (Oct 97).
[19]. Balster, W. J., Jones, E. G., "Effects of Temperature on Formation of Insolubles in Aviation Fuels," ASME 97-GT-218, ASME Turbo Expo, June 1997; to be published in ASME Journal of Engineering for Gas Turbines and Power.
[20]. Jones, E. G., Pickard, J. M., "Liquid-Phase Oxidation Kinetics of Aviation Fuels," ACS Fuel Chemistry Division Preprints, Vol. 43 (1), pp. 53-59, 1998.
[21]. Ervin, J. S., Williams, T. F., Heneghan, S. P., Zabarnick, S., "The Effects of Dissolved Oxygen Concentration, Fractional Oxygen Consumption, and Additives on JP-8 Thermal Stability," ASME Journal of Engineering for Gas Turbines and Power, Vol. 119, pp. 822-829, 1997.
[22]. Zabarnick, S., Whitacre, S. D., Mick, M. S., Ervin, J. S., "Studies of Jet Fuel Oxidation Using Oxygen Monitoring and Chemical Kinetic Modeling," Proceedings of 6th (Int'l) Conference on Stability & Handling of Liquid Fuels, Vol. 1, pp. 363-383, DOE CONF-971014, Feb. 1998.
[23]. Zabarnick, S., Whitacre, S. D., "Aspects of Jet Fuel Oxidation," ASME Journal of Engineering for Gas Turbines and Power, in press (1998) (ASME 97-GT-219).
[24]. Liberio, P., personal communication 4/98, FY97 data from DFSC JP-8 database.
[25]. Striebich, R. C., Rubey, W. A., "High Pressure, High Temperature Pyrolysis Reactions in the Condensed Phase with In-Line Chemical Analysis," paper to be presented at ACS National Meeting, Petroleum Chemistry Division, Boston, MA, August 1998.
[26]. Maurice, L. Q., Edwards, T., "Formation Pathways for Aromatic Species in Pyrolytic Endothermic Fuel Processes," 1997 JANNAF Combustion/JSM Meeting, West Palm Beach, FL, Oct. 1997.
[27]. Maurice, L. Q., Striebich, R., Edwards, T., "Formation of Cyclic Compounds in the Fuel Systems of Hydrocarbon High Speed Vehicles," AIAA Paper 98-3534, July 1998.
[28]. Minus, D. K., Corporan, E., "Deposition Effects of Radical Stabilizing Additives in JP-8 Fuel," paper to be presented at ACS National Meeting, Petroleum Chemistry Division, Boston, MA, August 1998.
[29]. Sheu, J.-C., Jones, E. G., Katta, V., "Thermal Cracking and Fouling of Norpar-13 Fuel Under Near-Critical and Supercritical Conditions," AIAA Paper 98-3758, July 1998.
[30]. Ervin, J.S., Williams, T., and Hartman, G., "Flowing Studies of Jet Fuel at Supercritical Conditions," ASME Session 22, Paper No. 98-3760.
[31]. Linne, D. L., Meyer, M. L., Edwards, T., Eitman, D. A., "Evaluation of Heat Transfer and Thermal Stability of Supercritical JP-7 Fuel," AIAA Paper 97-3041, July 1997.
[32]. Edwards, T., Maurice, L. Q., "HyTech Fuels/Fuel System Research," AIAA Paper 98-1562, April 1998.
[33]. Vilimpoc, V., Sarka, B., "Application of Photon-Correlation Spectroscopy and Quartz-Crystal Microbalance to the Study of Thermally Stressed Jet Fuel," Industrial and Engineering Chemistry Research, Vol 36, pp. 451-457, 1997.
[34]. Bunker, C. E., Rollins, H. W., Gord, J. R., Sun, Y.-P., "Efficient Photodimerization Reaction of Anthracene in Supercritical Carbon Dioxide," Journal of Organic Chemistry, Vol. 62, pp. 7324-7329, 1997.
[35]. Bunker, C. E., Sun, Y.-P., Gord, J. R., "Time-Resolved Studies of Fluorescence Quenching in Supercritical Carbon Dioxide: System Dependence in the Enhancement of Bimolecular Reaction Rates at Near-Critical Densities," Journal Physical Chemistry A, Vol. 101, pp. 9923-9239, 1997.
[36]. Bunker, C. E., Gord, J. R., Grinstead, K. D., "Spectroscopic Investigations of High-Temperature, High-Pressure Model Aviation Fuels," paper to be presented at ACS National Meeting, Petroleum Chemistry Division, Boston, MA, August 1998.
[37]. Stewart, J., Brezinsky, K., Glassman, I., "Supercritical Methylcyclohexane Pyrolysis: A Flow Reactor Study," paper to be presented at ACS National Meeting, Petroleum Chemistry Division, Boston, MA, August 1998.

[38]. Moser, W. R., Suer, M., Dardas, Z., Ma, Y. H., "Mechanisms of the Catalytic Cracking of Heptane Under Supercritical Fluid Conditions," paper to be presented at ACS National Meeting, Petroleum Chemistry Division, Boston, MA, August 1998.

FUELS COMBUSTION RESEARCH

(AFOSR GRANT F49620-98-1-0134)

Principal Investigator: I. Glassman
Department of Mechanical and Aerospace Engineering
Princeton University
Princeton, NJ 08544

A. Summary

Progress has continued in the investigation of the thermal and combustion characteristics of fuels at conditions of special interest to the Air Force. Recent efforts have concentrated on the characteristics of endothermic fuels necessary as coolants in next generation aircraft and fuel fouling under sub- and super-critical conditions.

B. Technical Discussion

Various hydrocarbon fuels, which can be classified as undergoing endothermic pyrolysis, are being considered for next generation aircraft of interest to the Air Force. Methycyclohexane, a prototype endothermic fuel, was the focus of the study reported last year (1,2,3). Currently reported are experiments and models for the possible candidate endothermic fuels - decalin, tetralin and n-decane. In particular, their pyrolysis characteristics under sub- and super-critical conditions were studied to determine whether their chemistry would lead to particulate formation (fouling) in fuel lines. Since they must eventually go under combustion in the engine, their gas phase reaction kinetics has been under investigation as well. Progress has been extensive and is detailed in the following paragraphs.

The supercritical decalin, tetralin, and decane pyrolysis mechanisms were investigated as a function of temperature and pressure in the high pressure plug flow reaction described in detail in previous reports. In addition, mixtures of 90% (molar) decalin with 10% decane and 90% tetralin with 10% decane were examined over a range of temperatures at a constant pressure of 3.13 MPa. Temperatures examined in each set of experiments ranged from around 700 K to 810 K. Typical pressures ranged from 0.2 to 10.0 MPa. Since the density of the reacting stream varied with temperature, pressure, and conversion, the residence time in the reactor varied.

Supercritical decalin pyrolysis was examined over a temperature range of 730 to 810 K at a pressure of 4.14 MPa. The major products of supercritical decalin pyrolysis at 810 K and a residence time of 62 seconds, listed in order of decreasing molar yield included: methane, propane, ethane, propene, ethene, butene, butane, methylhexahydroindane, and indene. The yield of products increased exponentially as temperature increased, as expected when Arrhenius kinetics predominate. A global activation energy, assuming pseudo first order reaction, of 276 ±/-10 kcal/mole (Fig. 1) was determined for decalin decay from 729 to 815 K at 4.14 MPa. A pre-exponential was found to be $10^{15.8\pm1.5}$. This analysis did not differentiate between the cis and the trans decalin isomers but considered their sum. The pseudo first order assumption was verified in a second set of experiments which examined decalin decomposition over a range of pressures at a constant temperature of 761 K. A global reaction order of 0.98 was determined, supporting the global pseudo first-order assumption.

Supercritical tetralin pyrolysis over a range of temperatures from 702 K to 802 K at 4.77 MPa was also examined. At 802 K and a residence time of 79 sec., major products listed in order of decreasing yield included: naphthalene, methylindane, ethane, methane, ethene, phenylbutane, propane, propene, phenylpropane, ethylbenzene, and toluene. A pseudo first order global activation energy for tetralin pyrolysis was determined to be 273 kJ/mole, with a pre-exponential of $10^{15.9\pm1.5}$. A global reaction order of 1.01 was determined from experiments where pressure was varied at a constant temperature.

As well, in order to assess the potential application of tetralin and decalin as H-donors, supercritical pyrolysis of mixtures of 10% decane in 90% decalin and 90% tetralin (molar percent) were also examined. These experiments were conducted over a temperature range of 700 to 800 K at a pressure of 3.13 MPa. An Arrhenius plot illustrating decane decomposition in three different media is shown in Fig. 2. As Fig. 2 illustrates, pure decane decomposition has the highest decay rate observed in this temperature range. Although it has the highest activation energy, its pre-exponential factor is much greater than that found in either of the mixtures.

More recent gas phase decalin pyrolysis results (4) are reported in Fig. 3. The major pyrolysis products found included large amounts of methane, alkene (ethene, propene, butadiene) and the aromatics benzene and toluene. Major products of supercritical decalin pyrolysis at 730-810 K and 4.14 MPa included similar light alkenes (ethene, propene, butadiene) as well as some benzene and toluene, especially at higher temperatures. However, the lower temperature supercritical pyrolysis also included an abundance of light alkanes, methylhexahydroindane, indene, indane, methylenecylohexene, and cyclohexadiene, species not found in the one atmosphere higher temperature gas phase studies.

In the same temperature range as this investigation (770 K) and at one bar, Ondruschka et al. (5) investigated gas phase decalin pyrolysis using laser powered homogeneous pyrolysis and a quartz flow reactor. At

770 K, they found an abundance of methane, ethane, ethene, propane, propene, butene, butadiene, cyclical C_5 products, benzene, and methylenecyclohexene. Again, the major light olefins and alkanes observed in their work were consistent with the results discussed here. Although considerable similarity was found between the results of this study and that conducted by Ondruschka et al. At 770 K, a striking contrast between the one bar and the supercritical study is found in the prevalence of methylhexahydroindane at supercritical conditions, a major product not found by Ondruschka et al., and in the relatively low yields of methylenecyclohexene in the supercritical pyrolysis. The differences in product distribution between the two studies conducted at the same temperature but different pressures indicated that the major reaction mechanisms of decalin pyrolysis may exhibit some pressure or concentration dependence.

Prior to a discussion of possible explanations for the pressure dependence of these reaction mechanisms, it is useful to consider in detail what the possible reaction pathways for some of the major products are. As shown in pathways I to III of Fig. 4, methylhexahydroindane formation is initiated by H-abstraction from any of the decalin C-H bonds. A subsequent β-scission creates a cyclohexane structure with two side chains, one olefinic, and one radical. The two side chains link by radical site addition to the double bond and, with H transfer from a neighboring molecule, methylhexahydroindane is formed. Representative β-scission pathways for alkene formation are illustrated in pathways IV and V. Methylenecylohexene formation as proposed by Ondruschka, et al. (5) is illustrated in pathway VI. Pathway VI is initially identical to pathway II. However, immediately after the β-scission, instead of the two side chains joining as in pathway II, a 1,5 H transfer which takes advantage of the mobility of the radical side chain shifts the radical site to the other ring. Subsequent β-scission results in methylenecyclohexene.

These mechanistic pathways are revealing as to how the pressure dependence of some of the dominant decomposition pathways may be occurring. Mechanistic pressure dependence was investigated in greater detail in a second set of experiments which examined decalin pyrolysis at a constant temperature of 761 K and a range of pressures (0.3 to 8.6 MPa). The mole fraction yields of methylhexahydroindane over yields of methylenecyclohexene as pressure was found to be varied at a constant temperature of 761K. Clearly, methylenecyclohexene formation is favored at low pressure while methylhexahydroindane formation is favored at high pressures. Because these products appear to be formed from the same or similar intermediates (pathways I-III and VI), a favorable concentration dependence for the ring contraction of pathways I-III over the 1,5 H isomerization of pathway VI and other alternatives to ring contraction may explain this trend. One explanation may be caging effects, as has been proposed in a related study (6).

In the earlier study of supercritical methylcyclohexane pyrolysis (6), it was postulated that the production of methylcyclopentane structures resulted from ring condensation (C_6 to C_5) from a cyclohexeneyl radical, similar to the methylhexahydroindane formation mechanism proposed here. It was suggested that ring condensation may be influenced by a physical cage of molecules surrounding the C_6 radical, a consequence of the very high concentration environment associated with supercritical fluids or liquids. The cage promotes the formation of a more compact structure, a C_5 ring, and discourages the radical from opening up to form a larger, linear structure -- such as the large radical intermediate of pathway VI of Fig. 4. Thus, caging effects promoting the ring contraction of pathways I-III and discouraging the formation of the large intermediate of pathway VI may be responsible for increasing yields of methylhexahydroindane and decreasing yields of methylenecyclohexene with increasing pressure.

In addition to being used for development of possible reaction mechanisms, the data from this set of experiments were also used to measure global kinetic parameters. The measured global activation energy of 276 kJ/mole and global pre-exponential of $10^{15.8}$ sec^{-1} show good agreement with those found in supercritical decalin pyrolysis studies at similar temperatures and pressures. For the program's one atmosphere gas-phase studies (7), a global activation energy of 217 kJ/mole and $A=10^{11.4}$ were determined. The much lower EA in this work is thought to result from a more fully developed radical pool in the higher temperature gas phase study. A more fully developed radical pool could suggest greater participation of the very low activation energy radical abstraction reactions (typically around 10-30 kJ/mole) in the global fuel decay scheme and less participation of the higher activation energy C-C homolysis reactions (typically around 350 kJ/mole). The combination of these factors would tend to reduce EA_{global}.

Tetralin pyrolysis has been examined by many investigators for a variety of applications. Poutsma (8) has reviewed many of these mechanistic studies of gas, liquid, and supercritical tetralin pyrolysis in the 650 to 1000 K range. Based on his review, expected major products of supercritical tetralin pyrolysis are methylindane, naphthalene, and butylbenzene. The major products of tetralin pyrolysis found in the current investigation over a temperature range of 702 to 802 K at a pressure of 4.77 MPa are in excellent agreement with those expected.

Just as supercritical decalin pyrolysis differs mechanistically from gas phase decalin pyrolysis, Poutsma (8) argues that in a similar temperature range, supercritical and liquid tetralin pyrolysis appear to follow a different mechanistic pathway than does gas phase tetralin pyrolysis. For supercritical tetralin near 720 K and 4 to 10 MPa, similar to the conditions of this investigation, Poutsma argues that ring contraction (methylindane formation) dominates over dehydrogenation (naphthalene formation) and hydrogenolysis (butylbenzene formation); in contrast, Poutsma states that gaseous tetralin pyrolysis in the same temperature range appears to be dominated by dehydrogenation, then ring contraction, and finally C_2 loss to form benzocyclobutene.

To further detail the effects of pressure on C_6-C_5 ring contraction in tetralin pyrolysis as well as other effects, a second set of experiments examined tetralin pyrolysis at a constant temperature of 761 K and a range of pressures from 1.8 to 9.9 MPa. The variation of methylindane yield with pressure was very similar to that of methylhexahydroindane in the decalin pyrolysis. Like methylhexahydroindane, methylindane formation was heavily favored at higher pressures. As discussed below, the favorable tetralin ring contraction in a supercritical or liquid

environment noted by other authors and found experimentally in this investigation is consistent with a reaction mechanism incorporating caging effects to be reported.

The experimental evidence gathered for supercritical tetralin pyrolysis suggest a global activation energy of 273 kJ/mole and global pre-exponential of $10^{15.1}$ sec.$^{-1}$ and compare well with the measured global decomposition parameters found for decalin, 276 kJ/mole and $10^{15.8}$ sec.$^{-1}$. This result suggests that structural similarities between decalin and tetralin in the chemically active portions of the molecules may translate into some similarity in terms of reactivity.

Decane pyrolysis is mechanistically well understood. It is examined here to explore the potential application of decalin and tetralin as hydrogen donors to inhibit some pathways of pyrolytic decomposition and to afford the fuel greater thermal stability. These types of molecules can easily donate hydrogen to an unstable radical to terminate a chain or to discourage the formation of unsaturated hydrocarbons, which can lead to solid formation.

For supercritical pyrolysis of neat decane, major products were completely in accord with traditional pathways associated with conventional gas phase alkane pyrolysis. Radical β-scission forms 1-alkenes and smaller radicals. Smaller radicals may stabilize through an H-transfer reaction or an addition reaction to form an alkane. They also may isomerize (for example, the 1,5 H-shift isomerization), or undergo additional scission reactions to ultimately form an abundance of ethene and methane.

However, in striking contrast to conventional gas phase hydrocarbon pyrolysis which is dominated by the formation of light olefins, under supercritical conditions a much greater yield of alkanes is found along with reduced yields of ethene and 1-olefins. This observation is consistent with the fact that the ratio of the rates of H-abstraction to β-scission, normally much less than one, increases by a factor of around 50 over atmospheric pyrolysis at the same temperature due to the high concentrations of the supercritical fluid (at 4.5 MPa). For example, using representative rates of scission and abstraction from Allara and Shaw (1980), at 750 K and one atmosphere, $k_{abstraction}[RH]/k_{scission}=0.04$. However, at 750 K and 4.5 MPa, supercritical conditions, $k_{abstraction}[RH]/k_{scission}=1.7$. Thus, the comparatively high yields of alkanes in the supercritical state is entirely due to higher [RH].

Global kinetic parameters describing pure decane pyrolysis were found to be EA = 269 kJ/mole with an A factor of 1015.1 sec-1. This global activation energy is slightly below the activation energies of decalin or tetralin, 276 kJ/mole and 273 kJ/mole. This difference, in conjunction with a pre-exponential which was nearly equal in all cases (equal within the experimental uncertainty), suggests that decane is not quite as thermally stable as is decalin or tetralin under these conditions.

Finally, it appears that the addition of tetralin or decalin to decane resulted in a slight improvement in the thermal stability of decane, consistent with the results found by Song et al. (9) who examined the stability of n-tetradecane with tetralin as an H-donor additive. Experiments conducted with mixtures of 10% decane in 90% decalin or 90% tetralin revealed that decane in the mixtures had conversions greater than a few percent at slightly higher temperatures than did neat decane. For example, a 30 percent conversion is reached at temperature of 770 for the neat fuel but is not reached until temperatures above 790 K in the decane/H-donor blend (Fig. 3). This result is also illustrated in the Arrhenius plot of Fig. 2. Rates of global decane decomposition were higher for neat decane than for decane in decalin or tetralin. Rates of decane decomposition in the two mixtures were nearly equal within the given experimental uncertainty.

C. References

1. Glassman, I., Abstract, "Fuels Combustion Research", Air Force Office of Scientific Research Contractors' Meeting, Cleveland, OH, 1997.
2. Stewart, J., Brezinsky, K., and Glassman, I., "Pyrolytic Formation of Polycyclic Aromatic Hydrocarbons in Supercritical Methycyclohexane", Eastern States Section/The Combustion Institute Technical Meeting, 1995.
3. Zeppieri, S., Brezinsky, K., and Glassman, I., "Pyrolysis Studies of Methylcyclohexane and Oxidation Studies of Methylcyclohexane/Toluene Blends", Combust. Flame, 108, 266 (1997).
4. Stewart, J., Brezinsky, K., and Glassman, I., "Pressure and Temperature Effects of Supercritical Decalin Pyrolysis", Eastern States Section/The Combustion Institute Technical Meeting, 1997.
5. Ondruschka, B., Zimmermann, G., and Remmler, M., J. of Analyt. And Appl. Pyrolysis, 18, 19 (1990).
6. Davis, G., M.S.E. Thesis, Dept. of Mech. And Aero. Eng'g., Princeton University, Princeton, NJ (1994).
7. Zeppieri, S., Brezinsky, K., and Glassman, I., "Atmospheric Pyrolysis and Oxidation Studies of Decalin", Eastern States Section/The Combustion Institute Technical Meeting, 1997.
8. Pontsma, M.L., Energy and Fuels, 4, 113 (1990).
9. Song, C., Wei-Chuan, L., and Schobert, H., Ind. Eng. Chem. Res., 33, 548 (1994).

Figure Captions

Fig. 1 Global decomposition kinetic parameters for supercritical decalin, tetralin, and decane decomposition.

Fig. 2 Global decomposition kinetic parameters for supercritical neat decane, 10% decane in 90% decalin (molar), and 10% decane in 90% tetralin. Uncertainty in analyzing very low conversions at lower temperatures contributed to experimental noise. Decane is slightly more stable with the H-donors decalin and tetralin than neat.

Fig. 3 Arrhenius plot of overall decalin pyrolysis

Fig. 4 Possible mechanisms of the formation of some of the major products of decalin decomposition including methylhexahydroindane formation, representative β-scission pathways of alkene formation, and methylenecyclohexene formation.

Fuel	Act. Energy (kJ/mole)	Pre-Exp. (1/sec)	R^2
Decalin	276 +/- 10	$10^{15.8 +/- 1.5}$	0.97
Tetralin	273 +/- 10	$10^{15.1 +/- 1.5}$	0.92
Decane	269 +/- 10	$10^{15.9 +/- 1.5}$	0.98

Fig. 1

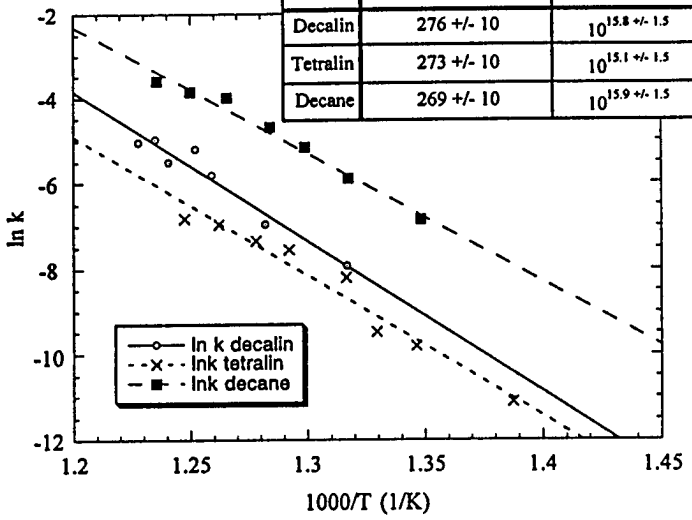

Fuel	Act. Energy (kJ/mole)	Pre-Exp. (1/sec)	R2
Decane	269 +/- 10	$10^{15.9 +/- 1.5}$	0.98
Decane in Decalin	252 +/- 10	$10^{14.3 +/- 1.5}$	0.92
Decane in Tetralin	261 +/- 10	$10^{14.7 +/- 1.5}$	0.93

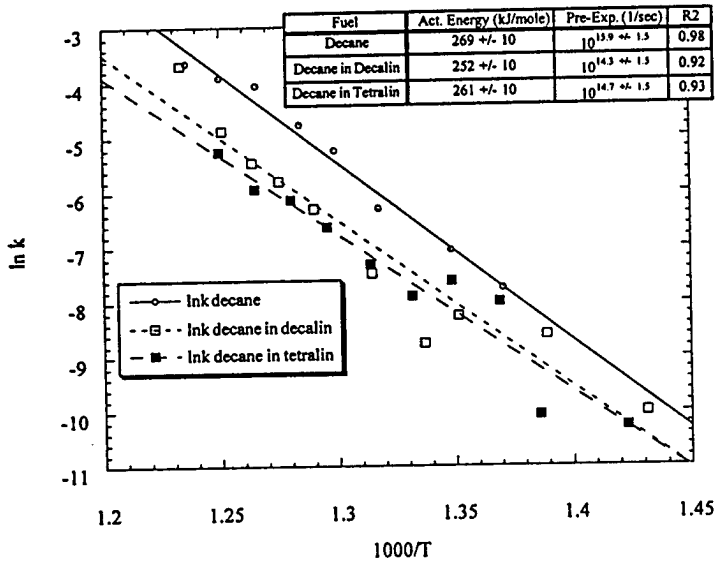

Fig. 2

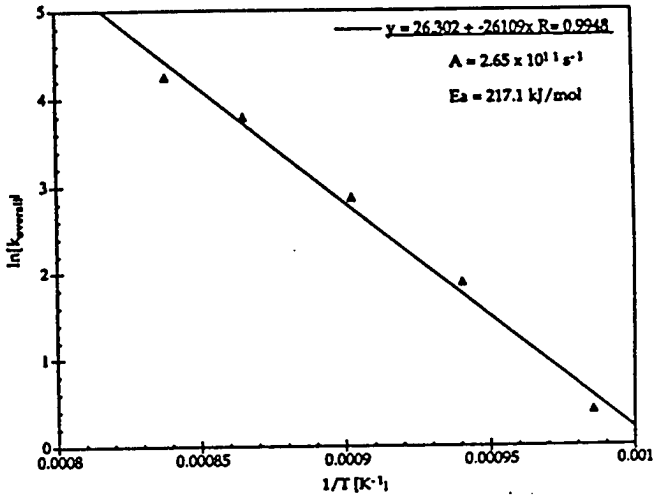

Fig. 3

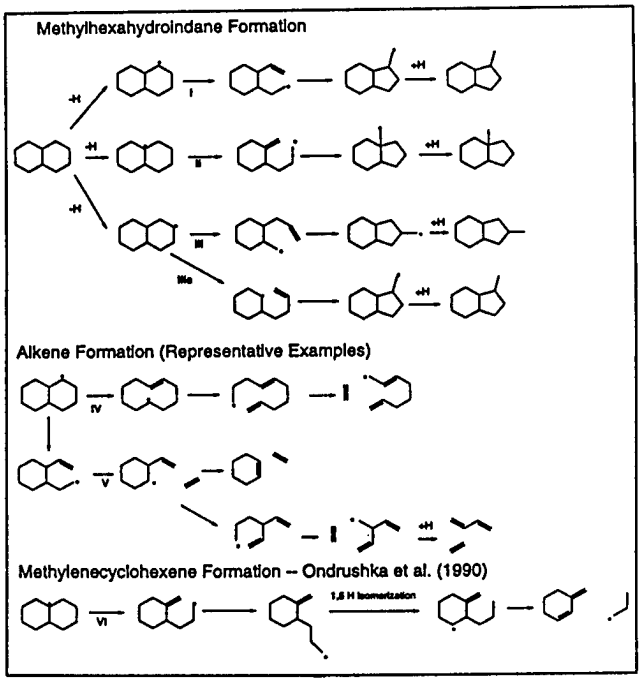

Fig. 4

THEORETICAL AND COMPUTATIONAL STUDIES OF NUCLEATION IN SUPERCRITICAL FUELS

(AFOSR GRANT F49620-96-1-0169)
Principal Investigator: Pablo G. Debenedetti

Department of Chemical Engineering
Princeton University
Princeton, NJ 08544-5263

SUMMARY/OVERVIEW

The objective of this research is to improve the basic understanding of how thermodynamics and nucleation kinetics influence the deposit of pyrolytic products from supercritical fuels. We investigate the precipitation of picene from supercritical methylcyclohexane under both thermodynamic and kinetic control. The kinetic calculations are useful for identifying operating conditions that minimize deposit formation. We also model the time evolution of single organic droplets exposed to an excess of miscible supercritical fluid, the typical configuration used in the supercritical anti-solvent (SAS) process for the production of microparticulate polymeric powders. Finally, we compute the particle size distribution during the adiabatic expansion of a supercritical fluid containing dissolved solutes, accounting for nucleation, condensation, and coagulation.

TECHNICAL DISCUSSION

The Statistical Associating Fluid Theory (SAFT) was used to model the fluid-phase equilibrium of picene in methylcyclohexane (Huang and Radosz, 1990). An expression based on classical nucleation theory with due account for fluid-phase nonideality was used to calculate the deposition rate of picene from methylcyclohexane (Debenedetti, 1990). Steady, one-dimensional, friction-driven, adiabatic expansions were described by coupling mass, momentum, and energy balances with the SAFT equation of state (Lele and Shine, 1992).

Figures 1 and 2 contrast predictions for thermodynamically and kinetically-controlled precipitation of picene from supercritical methylcyclohexane solutions during partial adiabatic expansion while flowing through cylindrical tubes. Figure 1 illustrates the effects of varying inlet temperature and pressure of methylcyclohexane solutions. The assumption of instantaneous precipitation (thermodynamic control) always leads to substantial accumulation of solid-phase picene. The kinetic calculation, however, suggests that to minimize deposits along fuel transfer lines it is advantageous to operate with low inlet temperatures and high inlet pressures. Figure 2 depicts the effects of varying inlet pressure and transfer line length. Longer transfer lines give rise to larger fuel expansions,

which result in greater solute precipitation. Results which account for nucleation kinetics indicate that there exists a critical length for each inlet pressure above which deposit formation occurs suddenly and rapidly approaches the limit of instantaneous precipitation. Higher inlet pressures enable longer transfer lines before the burst of nucleation occurs.

The supercritical antisolvent (SAS) process has been used in several experimental studies for the precipitation of polymers with interesting morphologies (Yeo *et al.*, 1993) and biologically active protein particles (Winters *et al.*, 1996). However, the complex interaction of jet hydrodynamics, phase behavior, and mass transfer that governs the process has not been investigated theoretically. Theoretical work on fuel droplet combustion (Hsieh *et al.*, 1991; Jia and Gogos, 1993) was used as a basis for developing a model which predicts the evolution in time of a single droplet of an organic solvent exposed to an excess of miscible supercritical fluid. Mass transfer occurs in two directions: from the solvent droplet into the supercritical fluid and from the supercritical fluid into the droplet.

Figure 3A shows the effect of pressure on the initial interfacial molar flux for several isotherms. The temperatures and pressures shown are typical for SAS operation. It can be seen that the initial molar flux is always into the droplet. Each isotherm passes through a minimum, which corresponds to the pressure for maximum droplet swelling. The sensitivity to pressure is greater near the critical temperature of the supercritical fluid. Figure 3B shows the change in the droplet radius as a function of time. Droplet lifetimes are characterized by rapid diffusion of supercritical fluid into the droplet, followed by gradual shrinking as the organic solvent diffuses into the excess supercritical fluid. These results suggest that the model can be used to gain insight into the relationship between operating conditions (temperature, pressure, droplet size) and droplet behavior as a function of time.

We have developed an aerosol dynamics code that tracks the evolution of the particle size distribution during steady, one-dimensional expansion of a supercritical fluid containing dissolved solutes. The calculation takes into account fluid-phase nonideality, nucleation, condensation, and inter-particle coagulation. Figure 4 shows the evolution of the particle size distribution during a friction-driven adiabatic expansion. This is the first time that this type of calculation has been implemented to study particle formation in supercritical fluids.

REFERENCES

Debenedetti, P. G. 1990. AIChE J. **36:** 1289

Hsieh, K. C., Shuen, J. S., Yang, V. 1991. Combust. Sci. Tech. **76:** 111.

Huang, S. H., Radosz, M. 1990. Ind. Eng. Chem. Res. **29:** 2284.

Jia, H., Gogos, G. 1993. Int. J. Heat Mass Transf. **36:** 4419.

Lele, A., Shine, A. D. 1992. AIChE J. **38:** 742.

Winters, M. A., Knutson, B. L., Debenedetti, P. G., Sparks, H. G., Przybycien, T. M., Stevenson, C. L., Prestrelski, S. J. 1996. J. Pharm. Sci. **85:** 586.

Yeo, S. D., Debenedetti, P. G., Radosz, M., Schmidt, H. W. 1993. Macromolecules. **26:** 6207.

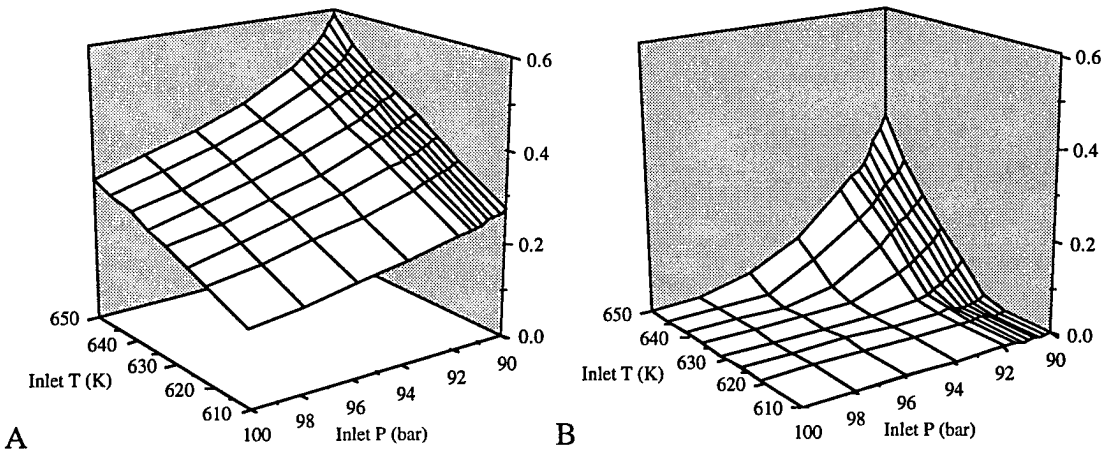

Figure 1: (A) Instantaneous and (B) kinetically-constrained precipitation of picene from adiabatically-expanding supercritical methylcyclohexane flowing through a cylindrical tube [length (L) = 0.40 m, diameter (D) = 2.0 mm]. The vertical axis gives the cumulative amount precipitated as a fraction of the total inlet flow. The assumption of instantaneous precipitation always leads to a substantial accumulation of solid-phase picene. The more realistic, kinetically-controlled calculations show that it is possible to suppress precipitation by operating at low enough inlet temperatures and high enough inlet pressures.

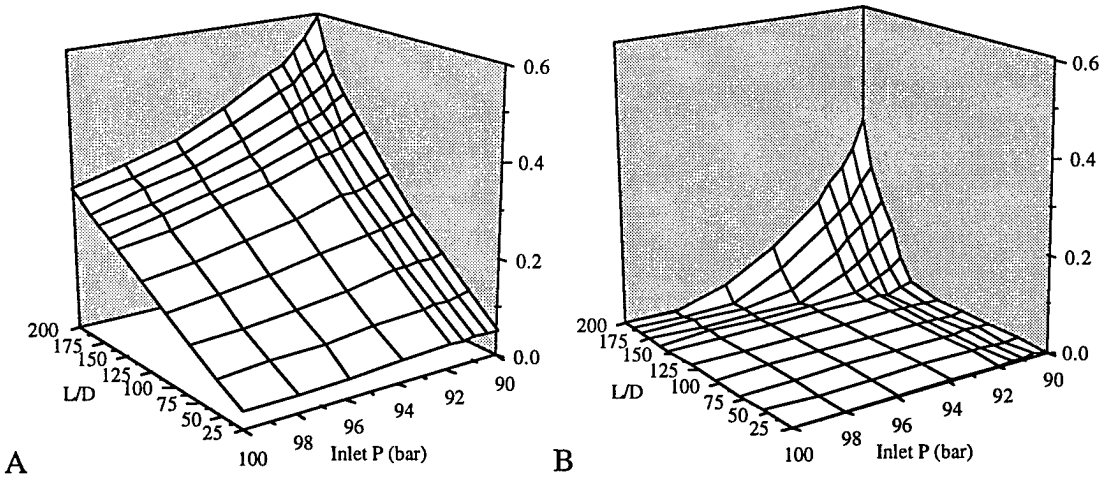

Figure 2: (A) Instantaneous and (B) kinetically-constrained precipitation of picene from adiabatically-expanding supercritical methylcyclohexane flowing through a cylindrical tubing [length (L) = 0.05 to 0.40 m, diameter (D) = 2.0 mm]. Same vertical scale as in Figure 1. Inlet temperature maintained at 650 K. There is a critical length for each inlet pressure at which accumulation rapidly increases, approaching the limit of instantaneous precipitation.

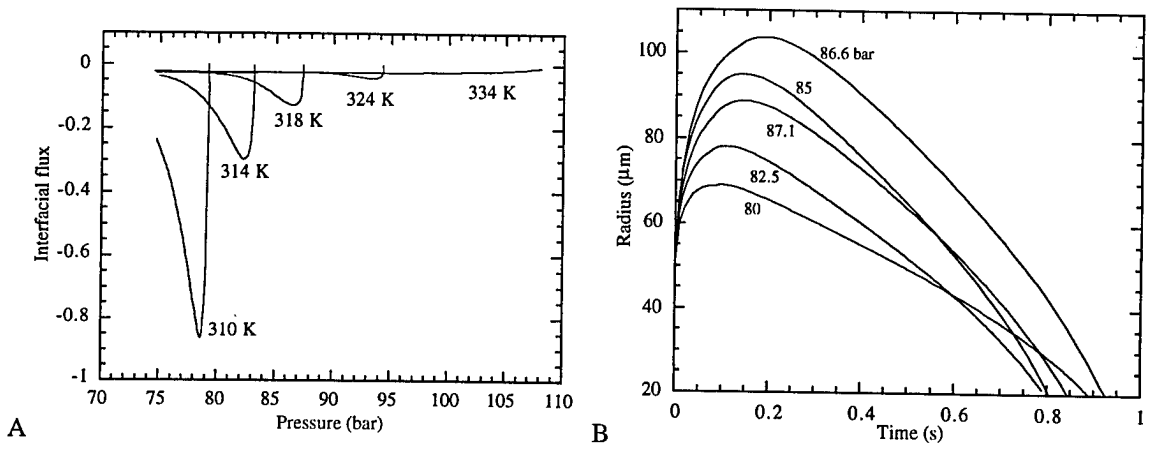

Figure 3: (A) Effect of temperature and pressure on the initial interfacial molar flux for toluene droplets exposed to an excess of supercritical carbon dioxide. Negative values indicate net flux into droplet. The molar flux has been scaled with $[4000 \cdot \rho^* \cdot D^* / r_o]$ where ρ^* and D^* are, respectively, the saturated molar density and diffusivity of the liquid phase, and r_o is the initial droplet radius. (B) Evolution of toluene droplet radius at 318 K and different carbon dioxide pressures.

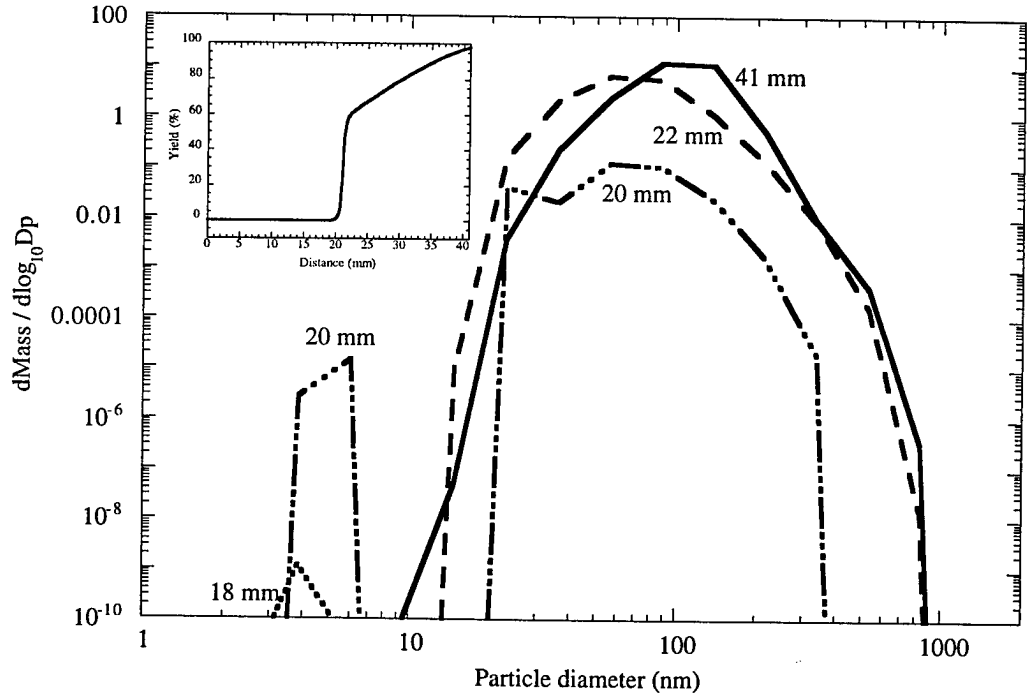

Figure 4: Evolution of the particle size distribution for phenanthrene precipitating from supercritical carbon dioxide expanding in a (50 micron x 41 mm) capillary. Inlet conditions: 200 bar and 325K. The inset shows the total precipitated mass, expressed as a percentage of the total amount of solute present initially, along the capillary's axis.

EXPERIMENTAL STUDIES ON SUPERCRITICAL FLOWS

(AFOSR Contract F49620-97-C-0002)

Principal Investigator: Gregory W. Faris

SRI International
Molecular Physics Laboratory
Menlo Park, California 94025

SUMMARY/OVERVIEW

We are using stimulated scattering (stimulated Rayleigh, Brillouin, and Raman scattering) to study supercritical fluids. New diagnostics are needed in the supercritical regime because low pressure diagnostics do not work well. From our measurements we can determine thermal, compressional, and compositional properties of supercritical fuels. These techniques should improve our knowledge of fluid properties in the supercritical state.

TECHNICAL DISCUSSION

Objectives

The objectives of this research are to develop stimulated scattering as a diagnostic for supercritical fluids, and use this technique to improve our understanding of fluids in the supercritical state.

The study of supercritical fluids and flows requires new diagnostic techniques. Currently available techniques such as laser-induced fluorescence (LIF) and coherent anti-Stokes Raman scattering (CARS) are complicated by increased molecular interactions, leading to stronger quenching, larger absorption and refractive index, and incomplete understanding of the influence of local conditions on spectroscopic parameters such as linewidths, nonresonant background contributions, and quenching rates. We believe that stimulated scattering techniques hold great promise for studying supercritical fluids.

Stimulated Scattering

Rayleigh, Brillouin, and Raman scattering occur commonly as spontaneous scattering. These scattering processes arise from natural oscillation modes of materials and can be used to determine the physical parameters responsible for those oscillations. When these collective modes are excited with a powerful laser, the mode oscillations can be driven so hard that they grow exponentially. In this case, the oscillations cause stimulated scattering. The dominant advantage of stimulated scattering is that the scattered signal can be made arbitrarily large; otherwise, these processes produce extremely weak signals. By using a probe to measure the induced amplification, we can obtain very good quantitative results. This technique is distinct from the stimulated scattering that builds up from noise, in which case quantification is very difficult.

The large signals from stimulated scattering are particularly helpful for investigating Rayleigh and Brillouin scattering, where the weak signals available from spontaneous scattering are difficult to discriminate from background excitation light. Other advantages of stimulated scattering include exceptional temporal resolution, and improved spectral resolution and signal-to-noise ratio. Furthermore, the use of two laser beams allows spatial registration and point measurement of local conditions.

With a single detection system, all three processes—Rayleigh, Brillouin, and Raman—can be measured. These processes together provide measurements of a wide range of material properties. Rayleigh scattering provides information on thermal properties, Brillouin scattering on compressional or elastic properties, and Raman scattering on chemical and compositional properties, density, and temperature. While spontaneous Brillouin[1] and Raman[2,3,4] scattering have been applied to supercritical fluids, the use of stimulated scattering for supercritical fluids is new.

Experiment

The first phase of our work is directed primarily at measurements of the properties of bulk supercritical materials in static or flowing cells. This work will allow measurements of the physical properties of supercritical fuels, including compressibility, speed of sound, thermal diffusivity, and chemical composition, density, and temperature. This phase is significant, because current work on supercritical fuels is limited to measurements performed after returning the fuels to ambient conditions, rather than in the supercritical state. With experience gained from measurements on uniform supercritical fluids, we expect that we will then be able to apply these techniques to supercritical mixing and combustion.

Stimulated scattering measurements are performed by producing strong scattering interactions using a pump laser and then probing the scattering using a second probe laser. The experimental arrangement for this type of measurement is shown in Figure 1. The pump laser sets up an electric polarization oscillating at the characteristic frequency of a scattering mode of the material. For strong laser driving, this polarization acts as a driving force, leading to amplification of both the material oscillation and a scattered optical wave. The optical amplification is detected as a gain or loss on the probe beam. Spatial resolution is determined by the overlap volume of the pump and probe beams.

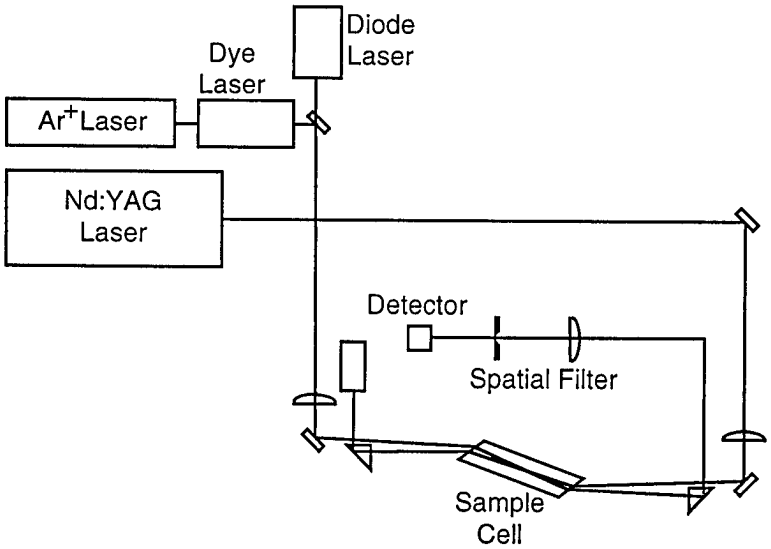

Figure 1. Experimental arrangement for stimulate scattering measurements.

As a pump laser for our stimulated scattering measurements we use an injection-seeded Nd:YAG laser. This laser has been modified previously allowing production of linewidths down to 20 MHz.[5] This narrow linewidth is possible through generation of long pulse lengths produced through lowered oscillator gain and pulse lengthening in the amplifier. Narrow linewidths for the pump laser are important for resolving Brillouin features which can be as narrow as 13 MHz.[6] The injection-seeded Nd:YAG laser has not been operated in a narrowband for several years, and required replacement of several optics and complete realignment. The laser is now operating very well.

Because stimulated scattering measurements are nonresonant, they can be performed at any wavelength for which the medium is transparent. Much of our previous measurements were performed at 532 nm.[7,8] The pump beam was the second harmonic of an injection-seeded Nd:YAG laser. The probe beam was produced with a cw dye laser pumped by an argon ion laser. Recent advances in diode laser technology allow use of a tunable diode laser as the probe laser. In this case, the fundamental of the Nd:YAG laser is used as the pump laser and measurements are performed at 1.064 μm.

The wavelengths of 532 nm and 1.064 μm each have their relative advantages. The fundamental wavelength has lower absorption for some of the samples we wish to study, such as thermally stressed jet fuel.[9] While this capability is desirable, it is not essential to our studies. Use of a diode laser probe beam also avoids the large operating costs for the argon laser as well as reduces the amount of time required for keeping the argon and dye lasers in good operation. On the other hand, operation at the second harmonic provides larger gain coefficients for stimulated scattering. For example, for Brillouin scattering, the gain coefficient should be about four times larger at 532 nm than at 1.064 μm.

We plan to perform most of our measurements at 1.06 μm, using the Nd:YAG laser fundamental as the pump radiation and a diode laser as the probe laser. We originally proposed to modify a high power tunable diode laser from SDL for these measurements. This laser can provide up to 0.5 W, but is not narrow band. Given the amount of effort required to convert this laser to narrowband operation, we have chosen to use a lower power diode laser from Environmental Optical Sensors, Inc. that already operates narrowband. Although there are potential complication involved with scatter pump light when using a lower power probe laser, these are expected to be less involved than converting the high power laser to narrowband operation.

Scattered pump light can appear to be a spurious gain signal on the probe laser. Significant discrimination against the scattered pump beam is achieved by spatial filtering of the probe beam prior to detection. However, as the power of the diode laser is low, other means of reducing scattered pump light may be necessary. Cell design can reduce this scattered light as described below. Another approach is to amplify the diode laser using either an anti-reflection coated laser diode or a fiber amplifier similar to the Yb-doped fiber lasers which have recently become available. A third approach is to use frequency modulation (fm) techniques to discriminate against the pump light. Our diode laser has a bias tee to allow use of high frequency modulation for fm detection.

A sample cell has been constructed that has a length longer than the overlap between the pump and probe lasers. This removes the scattered pump light from the line of sight along the probe beam. For a given probe power, the scattered pump light places a limit on the minimum size of the stimulated gain signal. The cell has Brewster angle windows to further reduce scattered light.

Environmental Optical Sensors Inc. (EOSI) produces a tunable diode laser with single mode operation tunable over 30 to 40 nm around 1.064 μm with close to 10 mW of power. A laser was purchased from EOSI to perform our measurements. Although EOSI had supplied lasers at this wavelength in the past, they have had a number of difficulties in supplying our laser. Shipment of the laser was delayed due to difficulties in applying the anti-reflection coating required for single mode operation of this laser. When the laser was shipped, it died within the first two weeks. A second laser was sent, which also died prematurely. The EOSI has supplied three lasers at this wavelength to other researchers this year, so we are confident that they can ultimately provide us with a laser. However, as of this date we do not have a functioning laser at 1.064 μm.

The rest of the experimental apparatus for 1.064 μm stimulated scattering measurements is in place, including the pump laser, detection electronics, and full integration of the tunable diode laser driver to a computer data acquisition package. The diode laser module has been interfaced to a PC-compatible computer to allow automated measurement of stimulated scattering spectra. Before the first laser died, we tested the laser amplitude noise and found it to

be within an acceptable range for our measurements. Excessive laser amplitude noise would prevent measurements of small gain signals. We are ready to take data for the 1.064 scattering measurements as soon as the laser arrives.

We have demonstrated that the cell and pump laser are easily capable of generating stimulated scattering signals by producing stimulated Brillouin scattering from dichloroethane without a probe beam. In this case, the stimulated scattering builds up from a single photon spontaneously scattered by the sample. This requires gains of exp(30) or more, or much more than that required for our stimulated scattering measurements.

Because we do not currently have an operating laser diode for the probe laser, we have set up additional lasers to operate at 532 nm. We have borrowed an Ar^+ laser and cw ring dye laser for this purpose. These lasers are now incorporated into our experiment and we are aligning them to perform stimulated scattering experiments. Switching between 532 nm and 1.064μm operation is performed by inserting or removing the doubling crystal in the Nd:YAG laser.

REFERENCES

1. R. W. Gammon, H. L. Swinney, and H. Z. Cummins, Phys. Rev. Let **19**, 1467 (1967).

2. M. S. Brown and R. R. Steeper, "CO_2-Based Thermometry of Supercritical Water Oxidation," Appl. Spectroscopy **45**, 1733 (1991).

3. W. Kohl, H. A. Lindner, and E. U. Frank, "Raman Spectra of Water to 400°C and 3000 Bar," Ber. Bunsenges. Phys. Chem. **95**, 1586 (1991).

4. R. D. Woodward and D. G. Talley, "Raman Imaging of Transcritical Cryogenic Propellants," 34 Aerospace Sciences Meeting & Exhibit, Reno, NV, AIAA paper 96-0468 (1996).

5. G. W. Faris, M. J. Dyer, and W. K. Bischel, "Laser Linewidth Narrowing Induced by Amplifier Gain Saturation," Opt. Lett. **19**, 1529-1531 (1994).

6. G. W. Faris, L. E. Jusinski, and A. P. Hickman, "High Resolution Stimulated Brillouin Gain Spectroscopy in Glasses and Crystals," J. Opt. Soc. Am. B **10**, 587-599 (1993).

7 G. W. Faris, L. E. Jusinski, M. J. Dyer, W. K. Bischel, and A. P. Hickman, "High-Resolution Brillouin Gain Spectroscopy of Glasses and Crystals," Opt. Lett. **15**, 703 (1990).

8. G. W. Faris, M. J. Dyer, and A. P. Hickman, "Transient Effects on Stimulated Brillouin Scattering," Opt. Lett. **17**, 1049 (1992).

9. G. W. Faris, "Experimental Studies on Supercritical Flows," in ARO/AFOSR Contractors Meeting in Chemical Propulsion, Ohio Aerospace Institute, June 17-19 1997, pp. 112-115.

Phenomenological Soot Model to Predict Particle Size, Number Density and Total Soot Mass

ARO Grant No. DAAH04-94-G-0328

Principal Investigators: Engine Research Center

Mike Corradini, Pat Farrell, Dave Foster, Jaal Ghandhi,
Jay Martin, John Moskwa, Rolf Reitz and Chris Rutland

University of Wisconsin Engine Research Center

1500 Engineering Drive

Madison WI 53706

SUMMARY/OVERVIEW:

AUTHORS: Andrei Kazakov, David Foster

The phenomenological soot model developed at the Engine Research Center of the University of Wisconsin as been fully implemented into the Center's version of KIVA. The program has been run and evaluated against the experimental measurements from many different engines in the laboratory. Of particular note is the encouraging comparison between the predictions of the simulation and the temporally and spatially resolved, in-cylinder measurements of the volume fraction, number density and mean particle size of an operating Cummins NH diesel engine.

TECHNICAL DISCUSSION:

The chemistry of soot formation has been the subject of extensive research for many years. At this time there seems to be general agreement among researchers in the field as to the phenomenological steps involved in the sooting process. These steps, which form the basis of a phenomenological model, are shown conceptually in Figure 1. Under conditions of fuel pyrolysis the fuel molecule fragments into smaller molecules, which in the figure are classified as precursors and growth species. The precursors then combine to form polycyclic aromatic hydrocarbons (PAH's) which continue to grow until the inception of an initial soot particle. These initial particles are on the order of 2 nm in diameter. The incipient particles grow through gas phase reactions with growth species, agglomeration and coagulation to become "mature" soot particles that are on the order of

50 nm in diameter. The mature particles may also stick together after collision to form long chain structures. A phenomenological soot model, based on the processes depicted in Figure 1, has been developed at the Engine Research Center[1]. The model which represents the processes of precursor formation, growth species formation, gas phase species oxidation, particle inception, particle growth and oxidation has been evaluated against fundamental flame data published in the literature and good agreement between the predictions and experiments were obtained. Last year the model was fully implemented as a sub-grid scale model into the ERC version of KIVA.

Implementation of this sub-model involves the addition of nine rate equations used in the tracking of four quantities, soot number density, precursor radical density, growth species density and soot volume fraction. Use of this sub-model makes it possible to predict not only the soot mass but also the mean size. Furthermore, if a size distribution is assumed, log-normal for example, one could also assess the size distribution. It may even be possible to assess the deposition of SOF through the deposition of precursors directly onto the particle.

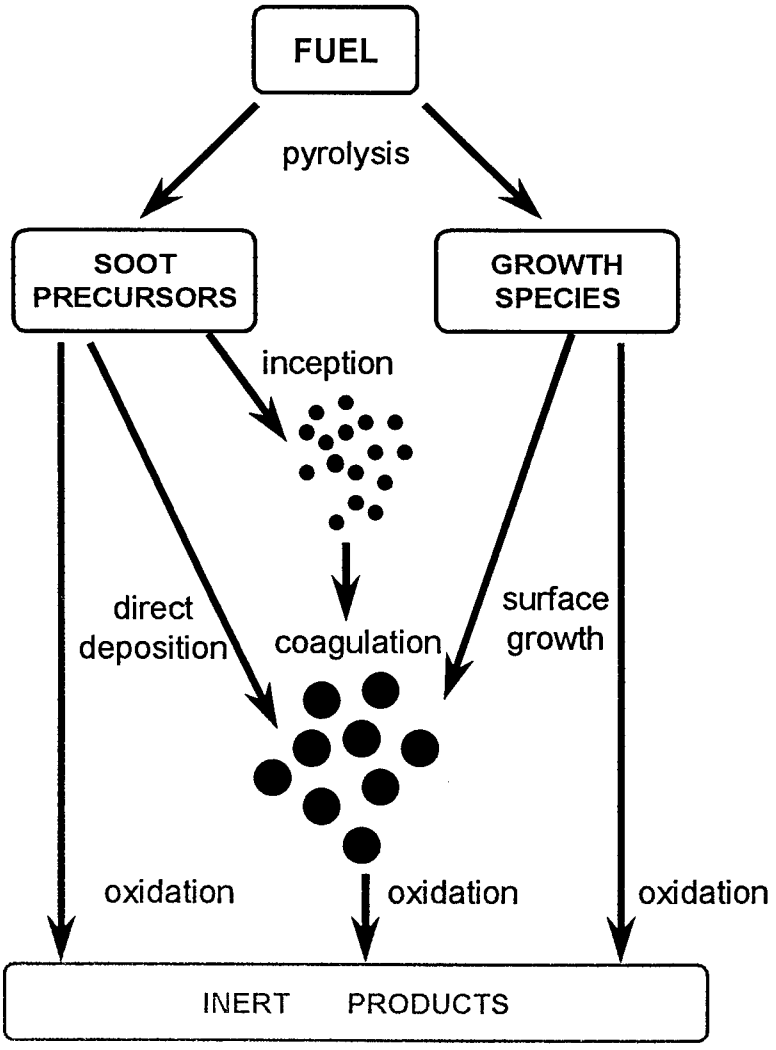

Figure 1, Schematic of the phenomenological steps of the sooting process

The model was compared to engine out particulate data for a range of engines, the Caterpillar 3401, the Cummins NH, the Cummins N14 and the TACOM/Labeco engines in our laboratory. The comparison is excellent. In addition comparisons between the model predictions and detailed in-cylinder data was made. The most significant results were the comparison between the predictions of the model and the in-cylinder data of Tree [2,3]. Figures 2 and 3 show the in-cylinder measurement location and the comparisons of measured and predicted values of soot volume fraction, particle number density and mean particle diameter for a Cummins NH heavy duty engine. Dale Tree during his Ph.D. work at the ERC made the measurements [4]. The location of the measurements is shown in the schematic at the top of the Figure 2. Two different theoretical analyses were performed on the data, so the volume fraction, number density and mean diameter were assessed two different ways, as shown in the Figure 3. As determined by Tree during his experiments, the signal to noise and repeatability of the data was such that only the crank angle interval from approximately 5 crank angles before top dead center (-5 ATDC) to 16 crank angles after top dead center (ATDC) yielded reliable information. In viewing the figures one should restrict their comparisons between the model and experiments to this region. The comparison between the predictions and measurements is very encouraging. The most notable difference between the measurements and predictions is the mean particle size. The prediction sizes are significantly smaller than the measured sizes. This is not altogether unexpected as the measurements relied on a scattering and extinction technique, which is sensitive to the diameter to the sixth power, so a bias to larger sizes is expected.

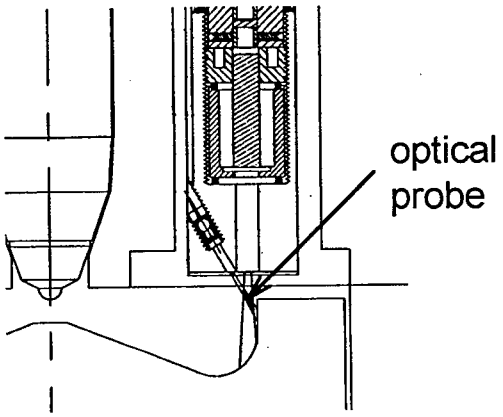

Figure 2 Schematic of in-cylinder measurement location for soot volume fraction, number density and mean particle diameter in a Cummins NH research engine

Also shown in Figure 3 are planar slices showing the predicted locations of the soot cloud at different crank angles. Comparing these predicted locations to the experimental measurement location, viewing area, shown in Figure 2 yields additional insight into behavior observed experimentally.

Additional comparisons between the predicted two-color temperature and KL factor for a Cummins N14 have also been completed with very encouraging results.

REFERENCES:

1. Fusco, A., Knox-Kelecy, A.L. and Foster D.E., "Application of a Phenomenological Soot Model to Diesel Engine Combustion," COMODIA 94, Proceeding of the Third International Symposium on DIAGNOSTICS AND MODELING OF COMBUSTION IN INTERNAL COMBUSTION ENGINES, July 11-14, 1994, Yokohama, Japan
2. Tree, D., R. and Foster, D. E., "Optical Soot Particle Size and Number Density Measurements in a Direct Injection Diesel Engine," Comb. Sci. and Tech., 1994, Vol 95, pp313-331
3. Tree D. R, and Foster, D. E., "Optical Measurements of Soot Particle, Number Density, and Temperature in a Direct Injection Diesel Engine as a Function of Speed and Load," SAE 940270, *Transactions*

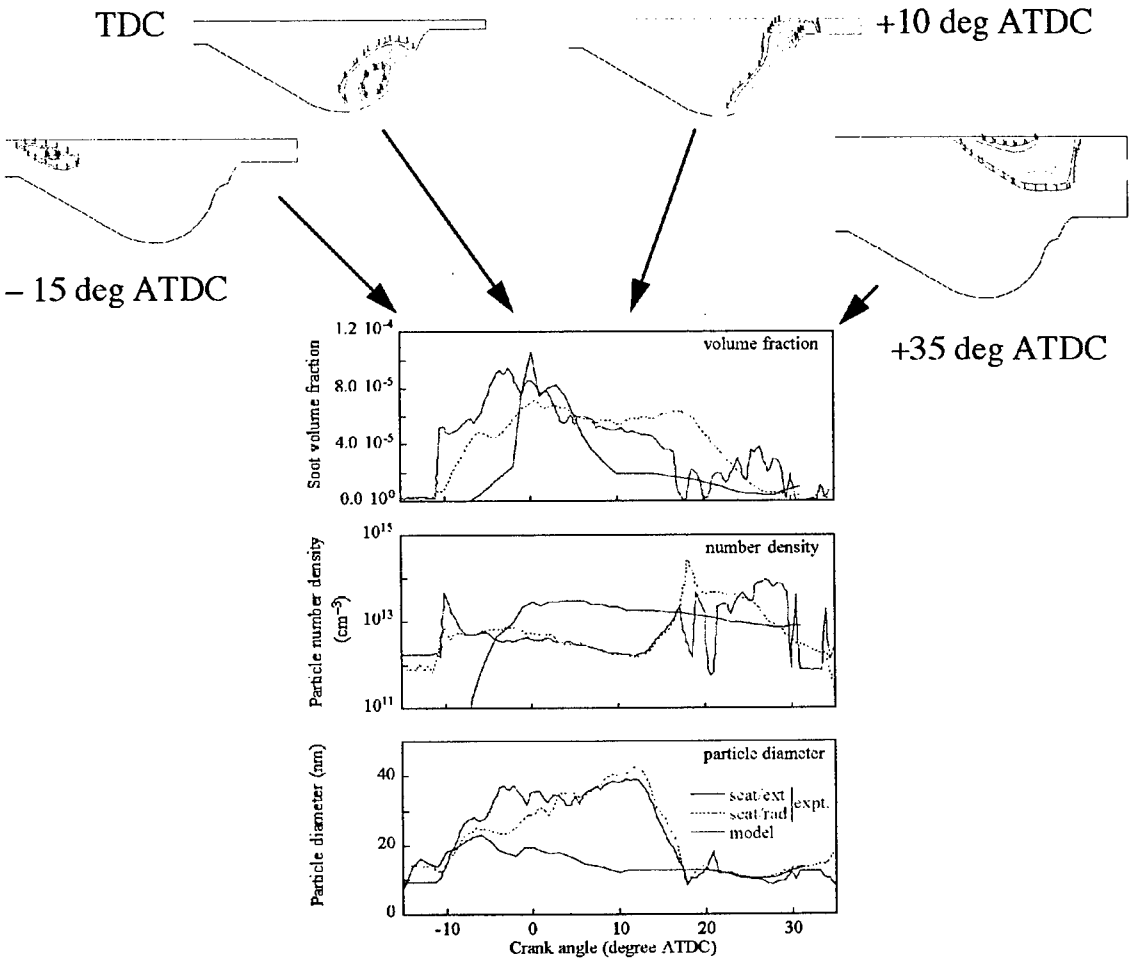

Figure 3, Comparison of predicted and measured in-cylinder soot number density, volume fraction and size for a crank angle range of 5 degrees before top dead center to 15 degrees after top dead center.

TRANSPORT AND INTERFACIAL PHENOMENA IN MULTIPHASE COMBUSTION SYSTEMS

AFOSR Grant No. 97-1-0266
Principal Investigator: **Daniel E. Rosner** ‡

Yale University, Department of Chemical Engineering
High Temperature Chemical Reaction Engineering Laboratory
New Haven, CT 06520-8286, USA

SUMMARY / OVERVIEW

The performance of aircraft gas turbine engines under sooting conditions and/or ramjets burning slurry fuels (leading to oxide aerosols and deposits), depends upon the formation and transport of small particles of complex morphology, often in highly non-isothermal combustion gas boundary layers (BLs). Aggregate formation / transport are also important in chemical reactors used to synthesize/process aerospace materials, including turbine blade coatings, optical waveguides, ceramic precursor powders,...)(Rosner,1997). Accordingly, this research is directed toward providing chemical propulsion system engineers with rational new predictive techniques to deal with *particle formation-transport-deposition phenomena*, accounting for significant non-spherical particle morphology effects. An interactive experimental/theoretical approach is being used to gain an understanding of performance-limiting mass/energy transfer-phenomena at or near interfaces. This includes the development and exploitation of laboratory burners and new diagnostic/characterization techniques (Figs. 1,2). Resulting experimental data, together with the predictions of asymptotic theories (Figs. 3,4), are then used to propose and verify rational engineering correlations for future design/optimization.

TECHNICAL DISCUSSION / RECENT RESEARCH PROGRESS‡

Most results obtained under Grant AFOSR 97-1-0266 during the period: 9/1/97-6/98 can be divided into the subsections below:

1. EXTENDED THEORY / IMPLEMENTATION OF LASER-INDUCED INCANDESCENCE (LII)

Light emission from aerosol particles heated by a laser pulse has been used to infer instantaneous mean particle diameter, local soot volume fractions, and even *particle size distributions* (see. eg. Roth and Filippov, 1996) under suitable conditions. The latter possibility is associated with the quantitative interpretation of particle cooling curves,exploiting the particle size dependence of cooling by carrier-gas impingement and particle evaporation. The energy transfer model of Roth and Filippov (1996) has recently been augmented to account for significant changes of polyatomic gas thermophysical properties at high temperatures (Filippov and Rosner,1998). In our current work, a detailed LII analysis is applied to size primary soot particles in an atmospheric pressure laminar ethylene/air diffusion flame. To guide future development of the *in situ* LII technique, results for the inferred distribution of spherule sizes are being compared TEM analysis of thermophoretically (TP-) sampled particles from the same flame. The burner investigated was a 4 mm diam. axisymmetric fuel jet surrounded by coflowing air. A second harmonic of Nd:YAG laser (532 nm) pulses was directed at different positions along the jet centerline. The LII signal was collected perpendicular to the laser axis using a flat-convex lens focused onto a photomultiplier slit. A fast pre-amplifier transformed the signals, which were then registered by a computer. Digitized signals were processed later for reconstruction of the spherule particle size distribution using the theory outlined in Filippov and Roth(1996). Actual laser pulse temporal shapes were used in the signal processing. Soot particle samples were thermophoretically extracted at corresponding positions in the flame and digitally analyzed using high-resolution TEM pictures*. Preliminary size distribution comparisons between LII and TP/TEM methods show encouraging agreement. For example, the continuous normalized distribution function in Fig.1 corresponds to LII-inferred spherule sizes at 2.2 cm above the burner, while the similarly normalized curve passing through the squares is based on statistical analysis of the TEM images for TP-sampled soot particles near this point. Both methods indicate *ca.* 20 nm. diam. soot spherules at this location. The broader LII-inferred curve is probably due to the width of the laser beam (about 1.2 mm) used in these preliminary experiments and the substantial spatial variation of soot spherule sizes near this measurement point. Higher resolution experiments employing narrower pin-holed laser beams are under way, along with extensions of the theory to also permit LII inferences of soot *aggregate* sizes in high pressure flames.

---

† AFOSR Contractors' Mtg : Propulsion/Airbreathing Combustion, 29 June-1 July 1998, Long Beach CA

‡ For research collaborators consult **REFERENCES**

**Thermophoretic sampling /TEM image analysis* (Dobbins and Megaridis, 1987, Rosner *et.al.* 1991, Koylu *et. al.* 1995) is now widely used in laboratory research on sooting flames, mainly to obtain *size* and aggregate *morphology*. Recent extensions which now include local, absolute *soot volume fraction* measurements are discussed in Parts 2,4.

2. THERMOPHORESIS-BASED SOOT DIAGNOSTIC METHODS: THERMOPHORETIC SAMPLING PARTICLE DIAGNOSTIC (TSPD) AND THERMOCOUPLE PARTICLE DENSITOMETRY (TPD)

Two thermophoresis-based methods for measuring absolute local *soot volume fractions*, ϕ_p in flames have now been successfully implemented (in both co-flow and counterflow laminar diffusion flames). The first, called *Thermocouple Particle Densitometry* (TPD)(McEnally *et.al.*(1997)), exploits the laws governing thermocouple response to *thermophoretic soot deposition*, as first suggested by Eisner and Rosner (1985). The second, which we call *Thermophoretic Sampling Particle Diagnostic* (TSPD) (Koylu, *et.al.* (1997)) is an extension of TEM-based thermophoretic sampling to also obtain absolute, local soot volume fractions, again making use of the laws governing *thermophoretic soot deposition* (*eg.*, Rosner *et..al.*(1991,1992)). This latter method has the important attribute of also providing required details of *aggregated soot morphology* (*eg.*, spherule diameters, fractal dimension and aggregate size distribution) difficult to reliably extract from non-intrusive laser light scattering (LLS-) or extinction (LLE-)measurements. Both thermophoresis-based methods are independent of (often unknown) soot optical properties, unbiased with respect to soot morphology and size distribution, and yield spatially resolved ϕ_p values directly even at low soot concentrations (below 0.1 ppm). Accordingly, they are especially applicable to spatially non-uniform and/or lightly sooting laminar steady flames. Of course, neither technique is "instantaneous" or "non-intrusive". In experimental tests TPD- and TSPD-soot volume fractions were systematically larger than de-convoluted LLE- results in the lowest portion of an C_2H_4 co-flowing difffusion flame (and throughout a CH_4 flame), evidently due to the deposition of visible-light-transparent particles, now known to be present in such flames. This implies that TSPD and TPD can prove valuable in future studies of the significance of these LLE-"invisible" soot precursors. They will also help us develop/calibrate the promising *in situ* LII technique (Section 1) and apply equally well to inorganic systems (see Section 4).

Because suspended particles experience appreciable thermophoresis in combustion gases, this phenomenon is frequently considered an obstacle to making accurate gas velocity measurements in flames. However, we have shown that thermophoretic phenomena can actually be exploited to obtain the important gas velocity passing through a thin gaseous diffusion flame. This is because suspended particles passing through a diffusion flame sheet experience an appreciable "jump" in thermophoretic velocity (see, eg., Gomez and Rosner, 1993). Since particle mass is conserved across such a sheet, and the gas velocity and temperatures are locally continuous, there must be a corresponding (negative) jump in the particle volume fraction, often easily measured (*eg.*, using laser extinction or light scattering methods; see Fig. 2). On this basis we have derived a potentially useful equation which allows calculation of the *gas velocity* normal to a diffusion flame sheet from measured values of the local temperatures and "soot" volume fractions. Only the local thermophoretic diffusivity, written $(\alpha_T D)_p$, needs to be estimated, but this is now known to be confined to rather narrow limits which are remarkably insensitive to particle size, morphology and chemical composition (Rosner *et.al.*,1991,1998). We illustrate this general method (which might be called: *thermophoretic velocimetry* (TPV)) for the particular case of a laminar methane/oxygen counterflow diffusion flame far from extinction, through which small alumina aggregates (mobility diameter of *ca.* 50 nm and present with a volume fraction of only *ca.* 0.1 ppm; Xing *et.al.*,1997)) pass. On this basis it is possible to calculate the corresponding particle velocities and the decisive heating and cooling rates (O(33,000 K/s)) experienced by these alumina particles in the immediate vicinity of the flame (Xing, *et al.*, 1997). The method should apply equally well to carbonaceous soot in ordinary hydrocarbon/air diffusion flames, but only in those cases where the soot is able to pass through the flame and local oxidation due to flame-produced OH is negligible (see, *eg.*, McEnally *et.al.*, 1997). Other necessary conditions for the validity of this method have been spelled out and quantified, and we are currently investigating other applications of potential interest.

3. TRANSPORT PROPERTIES OF FLAME-GENERATED AGGREGATES AT HIGH PRESSURES

Our recent research on transport theory underlying thermophoretic soot sampling from atmospheric pressure hydrocarbon/air flames (Rosner *et al.*, 1991, Rosner and Khalil,1998), and the morphology of suspended soot particles (Koylu *et al.*, 1995; Brasil *et.al.*,1998), has led us to rather startling conclusions about the effects of aggregation on thermophoretic transport at very high pressures of chemical propulsion interest. Without exception, all recent studies of soot thermophoresis in non-isothermal combustion products (flame structures or thermal boundary layers near cooled containment surfaces) have made use of the estimate that the thermophoretic diffusivity of soot aggregates in atmospheric pressure flames is not very different from the *free-molecule* kinetic theory prediction (0.5385 ν_g) for individual soot spherules, independent of their high intrinsic thermal conductivity. In Fig. 3, which presents our recent results for the normalized thermophoretic deposition rate from a coagulation-aged population of spherical particles (Rosner and Khalil,1998), this corresponds to the large Knudsen number -asymptote $\bar{R}$=1. However, in the highest pressure laboratory studies of flame-generated soot (up to *ca.* 50 atm.) Knudsen numbers based on average aggregate mobility diameter are as small as 0.1, even corresponding to Knudsen numbers, Kn1, based on (primary) spherule diameter, of order unity. While a comprehensive theory for *aggregate* thermophoresis as a function of these Knudsen numbers is not yet available, a rational estimate can be obtained by imagining that an aggregate behaves like a homogeneous sphere with an effective mobility diameter about equal to the gyration diameter but with an *effective thermal conductivity* equal to that expected for the 'granular medium' (of spherules) existing at the gyration radius (for some details, see Tandon and Rosner, 1995). Results of this plausible model indicate that the thermophoretic deposition rates of aggregates of even conductive materials

like carbonaceous soot, for which kp/kg ≈1000 in *ca.* 1200K combustion products, will remain high at *all* Knudsen numbers due to the poor *effective thermal conductivity* of such aggregates. Conversely, the spherules themselves, typically about 30 nm in diameter, will exhibit dramatically *reduced* thermophoretic diffusivities at very high pressures---say, over 50 atm. Thus, while our aggregate thermophoretic diffusivity estimates are provisional, our two principal conclusions (Rosner *et.al.*,1998), expected to be 'robust', are:

C1 Actual soot *aggregate* deposition rates at very high pressures are now expected be perceptibly (but not appreciably) *higher* than the "reference" rates formally expected using the *free-molecule* isolated sphere thermophoretic diffusivity

C2 If soot aggregates could be prevented from forming, or broken up prior to thermophoretic deposition, then appreciable deposition rate *reductions* could be realized at very high pressures due to their high intrinsic (spherule) thermal conductivity.

This behavior is depicted in Fig. 4, showing the predicted pressure dependence of the corresponding soot deposition rates for turbulent jet impingement on a cooled solid surface in the absence of shear-removal. Incidentally, an interesting experimental corollary of our present findings is that, in contrast to the fortunate situation at 1 atm.(Rosner *et.al.*,1991), thermophoretic sampling at very high pressures *would* be 'biased' (*against* small aggregates and isolated spherules).

4. LIGHT-SCATTERING MEASUREMENTS OF MORPHOLOGICALLY EVOLVING FLAME-GENERATED NANO-AGGREGATES

As part of our program of examining aggregate morphology effects on laser-based soot diagnostic techniques, aluminum oxide aerosol produced in a laminar, atmospheric pressure counterflow nonpremixed methane flame have also been investigated extensively using *in-situ* laser light-scattering (LLS) techniques in combination with better-established thermophoretic sampling/TEM methods. These flame-synthesized nano-particles, here present at local volume fractions less than 0.3 ppm, apparently underwent morphological changes due to formation (from TMA precursor), aggregation, and sintering processes in the *ca.* 3.3×10^4 K/s heating environment near the *ca.* 2300K temperature flame (Xing, *et.al.*,1997). To characterize this particulate morphological evolution, multi-angular LLS measurements were made/interpreted based on the Rayleigh-Debye-Gans scattering theory for fractal aggregates of low spectral absorptivity*. The optically determined fractal dimension, D_f, aggregate size distribution, mean radius of gyration and local particle volume fraction were found to be generally consistent with our independent *ex-situ* thermophoretic sampling/TEM experiments (see Section 2). The optically inferred fractal dimension increased from the cluster-cluster value: 1.60 to 1.84 with axial position, indicating a morphological evolution of alumina aggregates due to finite-rate, spatially resolved high-temperature sintering. An extension of the thermophoretic sampling method (McEnally *et.al.*,1997; Koylu *et.al.*,1997) was successfully applied for the first time to inorganic (here oxide) particles (see,also, Fig.2). Local particle volume fractions inferred from the LLS technique generally agreed with this *ex-situ* technique, supporting our analysis of both sets of measurements. The LLS-methods and results presented here are expected to open the door to more complete analyses of nano-aggregate coagulation and sintering kinetics in such flame environments, and ultimately improve the modeling of more complex (*eg.*, turbulent, high pressure) combustion systems involving particle formation and morphological change.

CONCLUSIONS, FUTURE RESEARCH

The ability to reliably predict the local concentration, sizes, transport properties and stability of *aggregated* flame-generated *particles* (carbonaceous soot, B_2O_3, Al_2O_3, ...)† in high pressure, high temperature environments is important for many technologies relevant to the U.S.A.F., especially jet engine combustor design. Indeed, realistic soot morphology is not yet even a part of chemically complex sooting *laminar* flame models, and the computational methods used to include coagulation dynamics (*eg.*, "moment" methods) donot lend themselves to this next step. Also, some properties needed to correctly interpret the results of recently introduced laser diagnostics applied in research on soot formation/suppression at high pressures (*eg.*, laser-induced incandescence (LII)) are not yet available. In this AFOSR program considerable experimental and theoretical progress along these lines has been made/reported and this research is now being extended . These experimental techniques, together with closely coupled theoretical calculations of particle birth/dynamics in counterflow diffusion flames and mixing/boundary layers, are leading to a valuable understanding of combustion-generated ultra-fine particles, including their coagulation and deposition dynamics.

---

*'Young' carbonaceous soot also has low absorptivity in the visible wave-length interval (see Section 2)

†Finely divided boron- and aluminum-based fuel additives for performance enhancement lead to non-carbonaceous "soots" in many air-breathing and rocket combustor situations. Moreover, trace inorganics in petroleum-based fuels, or in the air breathed for combustion likewise lead to submicron inorganic aerosols affecting system performance. In this AFOSR program we have shown that soot aggregates from a wide variety of organic and inorganic combustion systems exhibit interesting and mechanistically significant *morphological* similarities (Rosner (1996), Koylu *et.al.*,1995, Xing *et.al.*,1996, 1997)

REFERENCES

Brasil, A. M., Farias, T.L., Koylu, U.O., Carvalho, M.G., and Rosner, D.E.(1998), " A Recipe for Image Characterization of Fractal-Like Aggregates", prepared for *J. Aerosol Sci.*

Dobbins, R. and Megaridis, C.(1987), "Morphology of Flame-Generated Soot as Determined by Thermophoretic Sampling", *Langmuir* **3** 254-259

Eisner, A.D. and Rosner, D.E., "Experimental Studies of Soot Particle Thermophoresis in Non-isothermal Combustion Gases Using Thermocouple Response Techniques", *Comb & Flame* **61** 153-166 (1985)

Farias, T.L., Koylu, U.O., and Carvalho, M.G., "Effects of Polydispersity of Aggregates and Primary Particles on Radiative Properties of Simulated Soot", *J. Quant. Sprectroscop. Radiat. Transfer* **55** (3) 357-371 (1996)

Filippov, A.V, and Rosner, D.E.,(1998)."Energy Transfer Between an Aerosol Particle and Gas at High Temperature Ratios in the Knudsen Transition Regime",*Int. J. Heat Mass Transfer*, (submitted, May)

Filippov, A.V., Rosner, D.E, Xing, Y., Long, M. and Schaeffer, A.(1998),"Comparison Between Detailed LII Method and TEM Analysis for Ultrafine Soot Particles in Flames", *27th Combustion Symposium*, Boulder CO; Poster W5G05

Garcia-Ybarra, P. and Rosner, D.E.(1989),"Thermophoretic Properties of Non-spherical Particles and Large Molecules", *AIChE J.* **35** (1) 139-147

Gomez, A., and Rosner, D.E., "Thermophoretic Effects on Particles in Counterflow Laminar Diffusion Flames", *Comb Sci. and Tech.* **89**, 335-362 (1993).

Koylu, U., Xing, Y., and Rosner, D.E., "Fractal Morphology Analysis of Combustion-Generated Aggregates Using Angular Light Scattering and Electron Microscope Images", *Langmuir* (ACS) **11** (12) 4848-4854 (1995)

Koylu, U., McEnally, C., Rosner, D.E. and Pfefferle, L, "Simultaneous Measurements of Soot Volume Fraction and Particle Size/Microstructure in Flames Using a Thermophoretic Sampling Technique", *Comb & Flame* **110,** 494-507 (1997)

Mackowski, D.W., Tassopoulos, M. and Rosner, D.E., "Effect of Radiative Heat Transfer on the Coagulation Dynamics of Combustion-Generated Particles", *Aerosol Sci. Technol (AAAR)* **20**, 83-99 (1994).

McEnally, C.S., Koylu, U.O., Pfefferle, L.D. and Rosner, D.E., "Soot Volume Fraction and Temperature Measurements in Laminar Non-Premixed Flames Using Thermocouples", *Comb & Flame* **109,** 701-720(1997)

Neimark, A.V., Koylu, U.O. and Rosner, D.E., "Extended Characterization of Combustion-Generated Aggregates: Self-Affinity and Lacunarities", *J. Colloid Interface Sci.* **180**, 590-597 (1996)

Rosner, D.(1997),"Combustion for Chemical Synthesis and Materials Processing", *Chem. Eng. Educ.*(ASEE), 34, 228-235

Rosner, D.E. and Khalil, Y.F.(1998) ,"Particle Morphology and Knudsen Transition Effects on Thermophoretically Dominated Mass Deposition Rates From 'Coagulation-Aged' Populations", *J. Aerosol Sci.*(submitted April)

Rosner, D.E., Farias, T., Brasil, A.M., and Carvalho, M.G.(1998),"Soot Morphology and High Pressure Effects on Thermophoretically Dominated Deposition Rates", *27th Combustion Symposium*, Boulder CO; Poster W5G11

Rosner, D.E., Mackowski, D.W and Garcia-Ybarra, P., "Size and Structure-Insensitivity of the Thermophoretic Transport of Aggregated 'Soot' Particles in Gases", *Comb. Sci & Technology* **80** (1-3), 87-101 (1991).

Rosner, D.E., Mackowski, D.W, Tassopoulos, M., Castillo, J.L., and Garcia-Ybarra, P., "Effects of Heat Transfer on the Dynamics and Transport of Small Particles in Gases", *I&EC-Research (ACS)* **31** (3), 760-769 (1992).

Rosner, D.E., **Transport Processes in Chemically Reacting Flow Systems**, Butterworth-Heinemann (Stoneham MA), 3d Printing (1990) sold out; for 4th printing contact author directly; 2d ed. in prep.

Rosner, D.E. and Tandon, P., "Prediction and Correlation of Accessible Area of Large Multi-Particle Aggregates", *AIChE J.* **40** (7) 1167-1182 (1994)

Rosner, D.E. and Tassopoulos, M.,"Deposition Rates from 'Polydispersed' Particle Populations of Arbitrary Spread", *AIChE J.* 35 (9) 1497-1508 (1989)

Rosner, D.E., Tandon, P., Konstandopoulos, A. and Tassopoulos, M.(1994),"Prediction/Correlation of Particle Deposition Rates From Dilute Polydispersed Flowing Suspensions and the Microstructure/Properties of Resulting Deposits", Proc. **1st Int. Particle Technology Forum** (AIChE, IChE), Vol.2, pp. 374-381

Rosner, D.E., and Papadopoulos, D., "Jump, Slip, and Creep Boundary Conditions at Non-Equilibrium Gas/Solid Interfaces", *I&EC-Research (ACS)* **35** (9), 3210-3222 (1996).

Roth, P. and Filippov, A.V.(1996), "In Situ Ultra-fine Particle Sizing by a Combination of Pulsed Laser Heat-up and Particle Thermal Emission",*J. Aerosol Sci.*, **27** 95-104

Tandon, P., and Rosner, D.E., "Translational Brownian Diffusion Coefficient of Large (Multi-particle) Suspended Aggregates", *Ind Eng Chem-Res* (ACS) **34** 3265-3277(1995)

Tandon, P., and Rosner, D.E.(1998), "Monte-Carlo Simulation of of Fractal Particle Aggregation and Restructuring", *J. Colloid Int. Sci* (in press)

Tandon, P., and Rosner, D.E., "Sintering Kinetics and Transport Property Evolution of Large Multi-Particle Aggregates", *Chem. Eng. Communic.* (S.K. Friedlander issue), **151**, 147-168 (1996)

Xing, Y., Koylu, U.O., and Rosner, D.E., a) "Synthesis and Restructuring of Inorganic Nano-particles Particles in Counterflow Diffusion Flames",*Comb & Flame* **107**, 85-102(1996); also: b) Paper #88d , Vol. V, *5th World Congress ChE* (June 1996), pp. 43-48 and c) PhD Dissertation (Y. Xing), Yale Univ. Dept. Chem Engineering(1997)

Xing, Y., Rosner, D.E., Koylu, U.O. and Tandon, P., "Morphological Evolution of Oxide Nano-particles in Laminar Counterflow Diffusion Flames---Measurements and Modelling", *AIChE J.* **43** (11A) 2641-2649 (1997)

Xing, Y.,Koylu, U.O.and Rosner, D.E. (1998)"*In Situ* Light Scattering Measurements on Morphologically Evolving Flame-Synthesized Oxide Nano-Aggregates" *J. Optics*(submitted May)

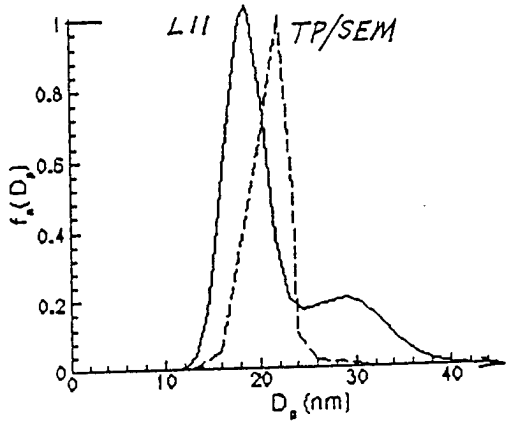

Fig. 1. Preliminary comparison of inferred soot spherule size distribution functions in a 1 atm laminar diffusion flame: LII *vs.* TP/TEM (after Filippov *et al.*(1998))

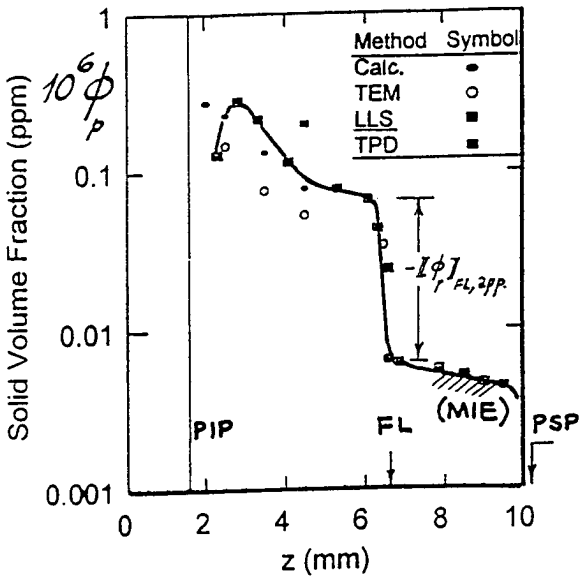

Fig. 2. Observed particle volume fraction drop across a diffusion flame "sheet" as basis for "thermophoretic velocimetry" (after Xing, Y. *et al.* (1997,1998) and Rosner (1998), in prep.)

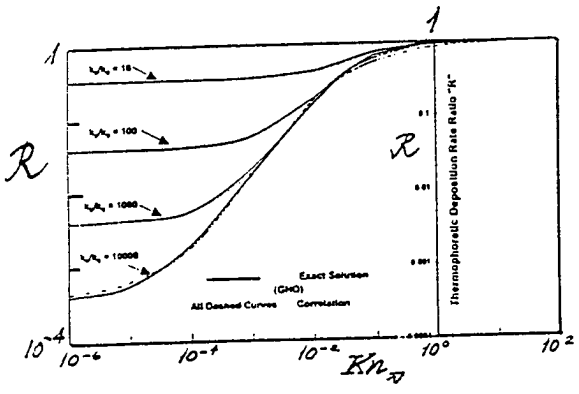

Fig. 3. Normalized thermophoretic mass deposition rates from a 'coagulation-aged' population of spherical particles; Dependence on Knudsen number (based on mean size) and intrinsic thermal conductivity ratio (after Rosner and Khalil, 1998)

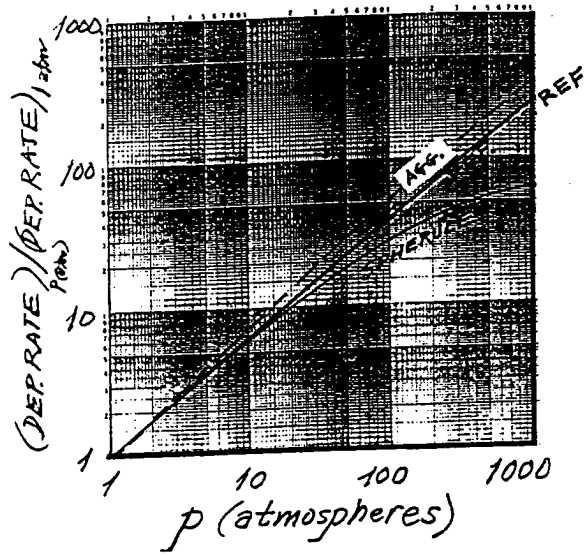

Fig. 4 Predicted dependence of soot deposition rate on pressure for turbulent jet impingement; Cases shown (see Section 3): Aggregates, Isolated Spherules, and 'Reference rate' (formally based on free-molecule limit thermophoretic diffusivity) (Rosner *et.al,* 1998; Rosner and Khalil,1998)

SOOT EVOLUTION AND CONTROL

ARO Grant DAAH04-95-1-0429

Principal Investigator Prof. R. A. Dobbins

Division of Engineering
Brown University
Providence, RI 02912

Summary/Overview:

This research seeks further understanding of particle formation in combustion devices burning hydrocarbon fuels. The study has focused on the formation of precursor particles -- the predecessor stage to carbonaceous aggregates that are the final end product. The composition of the precursor particles has been explored using the laser microscope mass spectroscopy (LMMS), and it is found to contain many polycyclic aromatic hydrocarbons (PAHs) ranging in mass from 202 to 448 amu. The intervention of particle formation prior to the onset of the carbonization process that forms the less reactive soot aggregates offers a candidate control strategy.

TECHNICAL DISCUSSION:

1. Deuterated Fuel Studies

The use of LMMS has provided mass spectra that implicate a key role of PAHs in soot formation. However, mass spectroscopy in general yields accurate mass data of the chemical species yet only ambiguous information on chemical formula. For example, a given mass M of a PAH of generalized formula C_xH_y can also correspond to the hydrogen-poor compound $C_{x+1}H_{y-12}$, , or the hydrogen-rich compound $C_{x-1}H_{y+12}$ because all three of these species possess the essentially identical mass, M=12x+y. This limitation of mass spectroscopy is the subject of commentary in the literature of PAHs formed in flames. The ambiguity is eliminated by the substitution, where possible, of a deuterated hydrocarbon fuel to produce C_xD_y compounds whose masses are *incrementally* shifted by +y, +y-12, and by +y+12 mass units, respectively, in the above instances. To implement this test, five liters of deuterated ethene C_2D_4 were obtained from a commercial laboratory though a competitive grant program. Particle samples were taken from a diffusion flame burning this fuel at heights corresponding to the those known to contain precursor particles in the normal flame. The LMMS analysis of the particles from the deuterated flame are listed in Table I below along with the compounds of corresponding species from the normal fuel. A mass increase of +y units between the PAHs and the polycyclic aromatic deuterocarbons (PADs) proves the values of x and y have been properly identified, and the chemical formula of each C_xH_y PAH compound has been unambiguously ascertained.

The Stein Fahr [1] analysis of the chemical stability of C_xH_y compounds for even x and y, and related comments of others [2,3] lead to the general conclusion that the most compact or pericondensed PAHs containing only hexagonal rings, i.e., compact benzenoid PAHs, are the most chemically stable. Examination of the structure of the first several coronene molecules, which strictly fulfill the property of compactness, lead to their representation as $x=6i^2$, $y=6i$ for

integer values of i≥2. Elimination of i in favor of x and y yields the expression for the $y_c^2=6x$ as the locus of the most stable PAHs, the stabilomer line. This line can be used to extend the stabilomer grid to arbitrarily large values of carbon number x. A graph of y versus x for a given PAH displays its proximity to the most compact or stable molecular configuration and separates molecular species according to H richer or poorer than for the most compact C_xH_y species.

Figure 1 shows the theoretical stabilomer data of Stein and Fahr [1, 1985] along with the earlier LMMS experimental data by Mauney et al. [4, 1984] showing the many individual PAHs singled out in these studies. The Mauney data is for soot from the kerogen in a subterranean shale oil retort, and it is formed through long exposures to moderate temperatures that allow time for the achievement of thermodynamic equilibrium. The agreement between the theoretical and experimental data and the stabilomer line reinforces the stabilomer concept.

The PAHs that have been identified in past studies of the residue found on soot particles from diverse fuels (wood biomass, vehicle exhaust, crude oil, diesel particulate and kerogen) are shown in Figure 2. The PAH residual products lie near the stabilomer line for all carbon numbers x. We conclude that the stabilomer line represents, for diverse fuels, the general pathway by which flame generated PAHs grow until the carbonization process that is favored by high temperatures intervenes to convert them into carbonaceous fractal aggregates.

2. Dark Field TEM Studies

To make more clear the relationship between the precursor particles and the carbonaceous aggregates, we have conducted dark field TEM (DFTEM) studies of the evolving particles in the ethene diffusion flame. Vander Wal [5] has shown the presence of crystallinity in precursor particles and has provided important insight into the evolution of these particles. While bright field TEM work takes advantage of automatic timing for film exposures, DFTEM procedures involve trial and error exposures of the photographic media both in the electron microscope and in the enlargement process. Crystallinity is revealed by DFTEM when the Bragg condition is fulfilled by successive atomic layer planes, and bright domains within the particle boundaries become apparent. Studies of carbon blacks post treated at high temperatures have appeared in the literature, and they display the predominance of bright domains on the edges of the particles that are associated with concentric edge layer planes. This pattern is also seen in the DFTEM images of precursor particles sampled from the ethene diffusion flame obtained in our laboratory by Dr. Huxiong Chen. These micrographs were made using the (002) reflection of the electron beam diffraction pattern. An important observation is that *even the small precursor particles display weak bright domains* in DFTEM that become enhanced as the particles grow toward the aggregate stage. The growth of these spots displays the continuity of the development of the liquid-like precursor particles into the solid carbonaceous spherules. These small particles have been shown to contain planar PAH molecules whose alignment into parallel planes during the carbonization process is the likely source of Bragg reflections. (DKTEM positive prints, which do not copy well, will be shown). DKTEM images were also obtained of the soot released by the ethene smoking flame, and they show similar patterns of bright domains to those formed by the particles sampled from within the flame. Unfortunately the sample size, approximately 10^{-15} g, yielded by thermophoretic sampling is too small to permit crystallographic analysis of the particles in the nonsmoking ethene diffusion flame.

3. X-ray Diffraction Studies

Larger samples, about 0.1 g, of soot are necessary to perform X-ray diffraction analysis of the development of crystallinity and the determination of the crystal lattice parameters using the standard methods[6]. X-ray spectra of carbonaceous materials can interpreted assuming a

hexagonal unit cell of dimensions (a,a,c). Large samples of carbonaceous soot were obtained by increasing the ethene volume flow rate to 4.9 mL/s in the standard burner to produce a smoke emitting flame from which soot samples were collected. A Siemens Model 5000 Diffractometer was used to obtain the X-ray spectrum. The angular position of the (002) reflection revealed an interplanar spacing of c/2=0.377 nm which is higher than the 0.335 nm value for highly crystalline graphite as expected. The (100) reflection gives a=0.263 nm which corresponds to a C-C bond length of 0.114 nm. This line width indicates a planar crystalline dimension of 1.9 nm. Statistical symmetry the c direction would imply that the basal plane paracrystalline layer contains roughly 100 carbon atoms - comparable in planar extent to the c-c-coronene molecule, $C_{96}H_{24}$, although lacking its circular symmetry. DFTEM micrographs also have been obtained of particles sampled from the smoking flame, and they too show the bright domains produced by the Bragg reflections discussed above.

4. Control of soot Formation

The intervention of PAH and soot formation in combustion sources through the oxidation of the precursor gases and precursor particles prior to the formation of carbonaceous aggregates is a clearly an advantageous particle control strategy. This method is successfully applied in steady flow commercial equipment [7,8] and in the laboratory diffusion burners by using highly dilute fuel mixtures to produce blue, carbon free flames [9]. Unfortunately, such flames cannot be ignited without the use of a temporarily applied, near stoichiometric mixture in which carbonaceous soot is formed. For this reason this method of intervention of particle formation is more difficult to apply in reciprocating engines that involve repetitive ignition cycles. Two measures that work toward particle suppression from engines are exhaust gas recirculation (EGR) and charge stratification. EGR moderates combustion temperatures to slow carbonization. Charge stratification provides rich fuel regions to facilitate ignition even with overall lean mixtures, and can reduce the impingement of fuel on the cooler cylinder walls. Even though these measures may be only partially successful, they can contribute to the control of particle emissions and reduce the penalties associated with the installation of particle traps and oxidation catalytic converters [10].

References

1. Stein, S. E., and Fahr, A., J. Phys. Chem. 89, 3714 (1985).
2. Bachmann, H., et al., *Twenty-sixth Symposium (International) on Combustion*, p2259 (1996).
3. Siegmann, K., et al., Combust. Sci. and Technol. 109, 165 (1995).
4. Mauney, T., et al., Science of the Total Environment, 36, 215 (1984).
5. Vander Wal, R. L., Combust. Sci. and Technol. 126, 333 (1997).
6. Klug, H. P. and Alexander, L. E.,., *X-Ray Diffraction Procedures For Polycrystalline and Amorphous Materials*, J. Wiley and Sons, 2nd Edition, 1954.
7. Viessmann Werke GmbH & Co., 35107 Allendorf/Eder, Germany.
8. Hofbauer, P. and Bornschscheuer, W., "Rotex Burner Sets Standards in Low Emission Combustion", Report on *Oil Heat National Technology Conference and Workshop*, Brookhaven National Laboratory, Upton NY (1995).
9. Dobbins, R. A., Combust. Sci. and Technol. 121, 103 (1996).
10. Johnson, J. H., et al., *A review of Diesel Particulate Control Strategy and Emission Effects-The Horning Memorial Award Lecture*, SAE Technical Paper Series 940233, 1994.

TABLE I. NORMAL AND DEUTERATED PAH PAIRS

Precursor particles sampled from C_2H_4 and C_2D_4 diffusion flames
Major species in bold type

x/y	C_xH_y PAHs M (amu)	Count Frt* (%)	C_xD_y PADs M (amu)	Count Frt** (%)
16/10	**202**	**8.31**	**212**	**13.8**
18/10	226	2.62	236	0.57
18/12	228	5.39	240	2.76
19/11	239	5.69	250	4.49
20/10	250	4.27	260	0.75
20/12	**252**	**26.2**	**264**	**12.8**
21/11	263	4.78	274	5.17
21/12	264	4.94	276	3.55
22/10	274	1.34	284	1.43
22/12	**276**	**19.2**	**288**	**23.1**
24/12	**300**	**5.86**	**312**	**10.8**
24/14	302	3.90	316	0.50
26/12	324	0.74	336	1.28
26/14	326	2.76	340	3.48
28/14	350	1.95	364	6.19
30/14	374	1.36	388	6.68
32/14	398	0.50	412	2.14
38/16	472	0.22	488	0.43

* Based on 44 spectra

** Based on 18 spectra

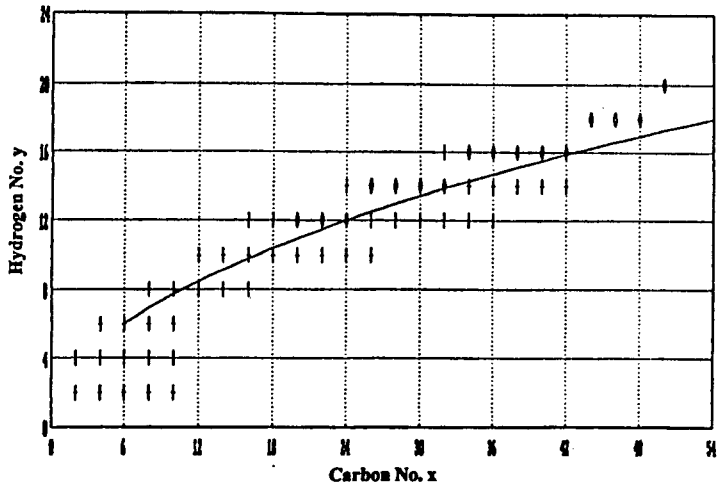

Fig. 1. Stabilomer Plot Showing the 1984 Experimental Data Mauney et al.(0) and the 1985 Theory of Theory and Fahr (+). The solid line, $y_c^2 = 6x$, describes the most compact PAHs.

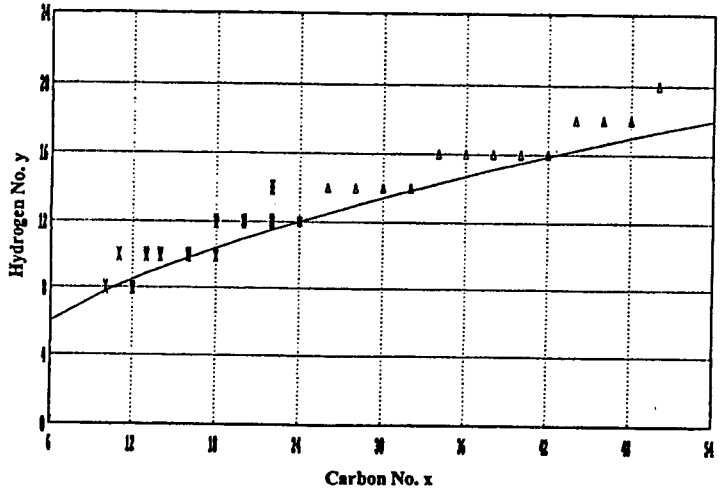

Fig. 2. Stabilomer Plot Showing PAHs Detected on Soot from a Wide Range of Fuels - Wood Biomass (×), Vehicles (0), Crude Oil (+), Diesel fuel (V), and Kerogen (Δ).The solid line is $y_c^2 = 6x$.

SOOT, TEMPERATURE AND OH MEASUREMENTS IN AN UNSTEADY COUNTER-FLOW DIFFUSION FLAME

(ARO Grant/Contractor No. DAAH04-95-1-0230)

Principle Investigator: William Roberts

Dept. Of Mechanical and Aerospace Engineering
Box 7910
North Carolina State University
Raleigh, NC 27695-7910

SUMMARY/OVERVIEW:

Previous studies have shown that laminar counterflow diffusion flames exposed to steady rates of strain exhibit many of the essential features of turbulent diffusion flamelets. However, all real turbulent flames are subjected to unsteady rates of strain due to the inherent unsteadiness of the flow field. These unsteady strain rates may have a great impact on the fluid mechanic-chemical kinetic interaction and, therefore, may effect the reaction zone temperature and formation of soot. The goal of this project is to quantify the effect of unsteady strain on the temperature, OH mole fraction, and the soot formation process using laser based diagnostic techniques.

TECHNICAL DISCUSSION:

A counterflow burner similar to the design of K. Seshadri was modified to allow for the placement of two loudspeakers. The upper section supplies the air flow through a central tube which is 2.5 cm in diameter. This air tube is surrounded by a nitrogen co-flow which prevents entrainment of ambient air into the reaction zone and preheating of the air. The air tube is fed from a plenum which is bounded on the top by a 20 cm loudspeaker. The lower section, the fuel side, is the same as the air side except the fuel tube is surrounded by a water jacket to prevent preheating. This water jacket is surrounded by an annulus and then a second water jacket. Product gases are evacuated from the reaction zone by suction through the annulus between the water jackets and exhausted outside the building. Five 80 mesh screens, separated by 3 mm spacer rings, are stacked at exit of both the fuel and air tubes. These screens create a pressure drop which flattens the exit velocity profiles and breaks up any large scale flow structures. A signal generator and amplifier are used to drive the speakers with a sine wave function, which set up a controlled oscillation in the reactant flow field. Both the amplitude and frequency of the imposed oscillation are varied in this study.

Unsteady Flame Extinction Measurements:

In this work, a two color LDV system, operating in forward scatter collection mode, was used to measure both the instantaneous local strain rate at the flame and the phase of the velocity oscillation as a function of initial (steady) strain rate, oscillation frequency, and amplitude of the unsteady strain rate component in a propane/air flame. The unsteady extinction strain rates were then determined by extrapolating these measurements to the

applied voltage required to extinguish the flame. Measurements were also taken in methane/air and diluted methane (73% N_2/27% CH_4)/air flames for comparison to experimental results reported in the literature.

For the unsteady experiments, both temporal and axial profiles of velocity, at the peak velocity within the oscillation, were measured in the propane/air flame at four frequencies; 25, 50, 100, and 200 Hz, and four initial steady strain rates; 30, 60, 90, and 120 s^{-1}. These profiles were also measured for both diluted and undiluted methane flames at the same four frequencies, but only a single steady strain rate of 90 s^{-1}. These results are shown in Figure 1. Velocity profiles were measured at three other temporal positions within the oscillation for diluted methane and propane flames at an initial strain rate of 90 s^{-1} and oscillation frequency of 100 Hz, and are shown in Figure 2.

The following conclusions can be drawn from these measurements:

1. The actual instantaneous peak strain rate increases linearly with speaker oscillation amplitude.

2. The phase angle of the velocity oscillation was quantified and found to be a function of the axial coordinate, which artificially increases the measured strain rate. The phase angle was not a function of oscillation amplitude or initial strain rate.

3. The weaker diluted methane flame responded in a quasi-steady manner at low frequencies, but departed from this as the frequency was increased beyond 100 Hz, where the flame was able to survive short excursions above the steady strain rate limit. This flame was not subject to flow reversal at any frequency.

4. The pure methane and propane flames, the minimum velocity within the oscillation at extinction was negative. This significantly distorted the flow field and is most likely responsible for extinction at the low frequencies and low initial strain rates, as the peak strain rate was much lower than the steady extinction strain rate. The magnitude of flow reversal at the extinction amplitude decreased with increasing initial strain rate and oscillation frequency, but the propane and methane flames were always subjected to some degree of flow reversal. At the higher frequencies and initial strain rates, the peak instantaneous strain rate was approximately equal to the steady strain rate.

5. For the methane and propane flames, peak instantaneous strain rate does not occur at the maximum velocity within the oscillation, but rather somewhere near zero fluctuation velocity with a negative slope.

Soot Volume Fraction Measurements:

Images of soot volume fraction have been acquired in the unsteady counterflow diffusion flame burner using Laser Induced Incandescence (LII). In the LII technique, soot particles are heated to near vaporization temperatures by a short pulsed Nd:YAG laser beam formed into a sheet and the resulting thermal radiation is collected with an intensified digital camera. The intensity of the thermal emission can be correlated with soot volume fraction. In order to get quantitative measurements, the image intensities require correction and calibration. A well characterized laminar jet diffusion flame (ethylene with air co-flow) was chosen as the calibration source. Laser beam extinction measurements, which provide an integrated line of sight measurement, were also made as a function of height in this flame and compared to those published in the literature. The calibration technique (formulated by Choi and Jensen) uses a double iteration to calculate the calibration factor and corrected

soot volume fraction distribution using a single integrated line of sight laser extinction measurement. The distribution is corrected for laser beam absorption and scattering as well as signal absorption and scattering on its way to the detector. This technique assumes an axisymmetric flame.

LII images were collected at four different steady strain rates. Superimposed on these steady strain rates was an oscillating component of reactant flux, whose frequency and amplitude was varied. Both low and high amplitude oscillations were investigated at each frequency, relative to the extinction amplitude. Soot volume fraction measurements were made at four different frequencies at each of the four steady strain rates. A representative case is shown in Figure 3. To reveal any transient effects of the fluid mechanics on the combustion and soot formation processes, LII images were collected at four different temporal locations through out the oscillation period. These locations corresponded to peak velocity, minimum velocity, and average velocity with both a positive and negative slope. These images show strong transient effects at the lower strain rates with high frequency and amplitudes.

Thermometry:

A second part of this work is the measurement of temperature field as a function of oscillation frequency and amplitude in this flame. These measurements are being made with a two-color PLIF technique. Excitation of isolated transitions in the $A^2\Sigma^+ \leftarrow X^2\Pi(1,0)$ band of OH was accomplished using the frequency doubled output from an Nd:YAG pumped dye laser. PLIF images were recorded by a Princeton Instruments ICCD camera. A PMT was used to measure fluorescence from a porous plug burner to assure proper tuning of the OH fluorescence transition. The signal to background ratio is very low for the propane-air flames due to the broadband fluorescence of polycyclic aromatic hydrocarbons (PAH), soot precursors. The background was averaged, with the dye laser tuned off transition, and subtracted from the OH PLIF images. It was difficult to tune onto the transition in the propane flame due to the high background, thus a methane-air mixture was used in the porous plug burner, providing high signal to background and ensuring proper tuning.

A two-line method was used to determine local temperature from the 2-D fluorescence images through a Boltzmann analysis. In this technique, a scan over multiple transitions is performed and the temperature is determined from taking the ratio of fluorescence images. This method assumes the excited state dynamics, such as Rotational Energy Transfer (RET) rates, Vibrational Energy Transfer (VET) rates, and collisional quenching rates are independent of rotational energy level, and cancel in the ratio. With careful selection of transition pair, this approach can yield good results; however, there are weak rotational level dependencies in these rates. To expand the range of applicability and to increase the level of accuracy, modifications can be made to model rotational level-dependent excited state dynamics. The fluorescence data collected in this study, shown in Figure 4, will be used to calibrate an 8-level dynamic fluorescence model under development. To obtain maximum temperature sensitivity over the expected range of gas temperature, from 1400 K to 2400 K, the $Q_1(5)$ and $Q_1(14)$ branches were used. In addition, the $Q_1(5)$ and $Q_1(14)$ lines are well isolated spectrally. The reaction zone in the counterflow burner is on the order of a few cm, thus, beam absorption and fluorescence trapping were tolerable, permitting the probing of the stronger Q branch.

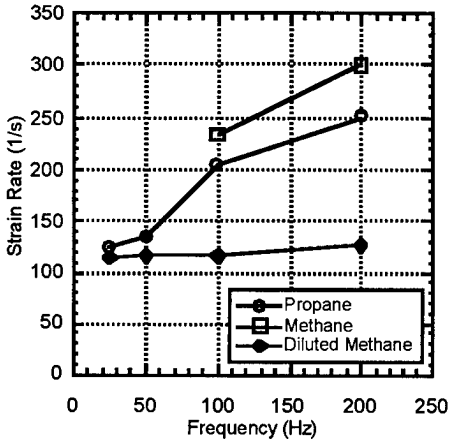

Fig 1 Peak Strain Rate at Quenching

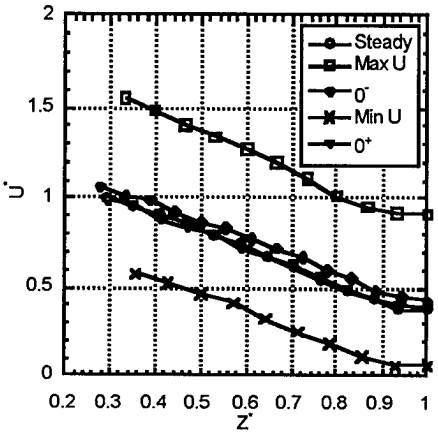

Fig 2 Axial Velocity Profiles as a Function of Oscillation Phase

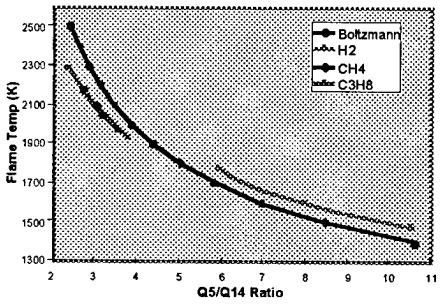

Fig 4 2-Line OH PLIF Thermometry Calibration

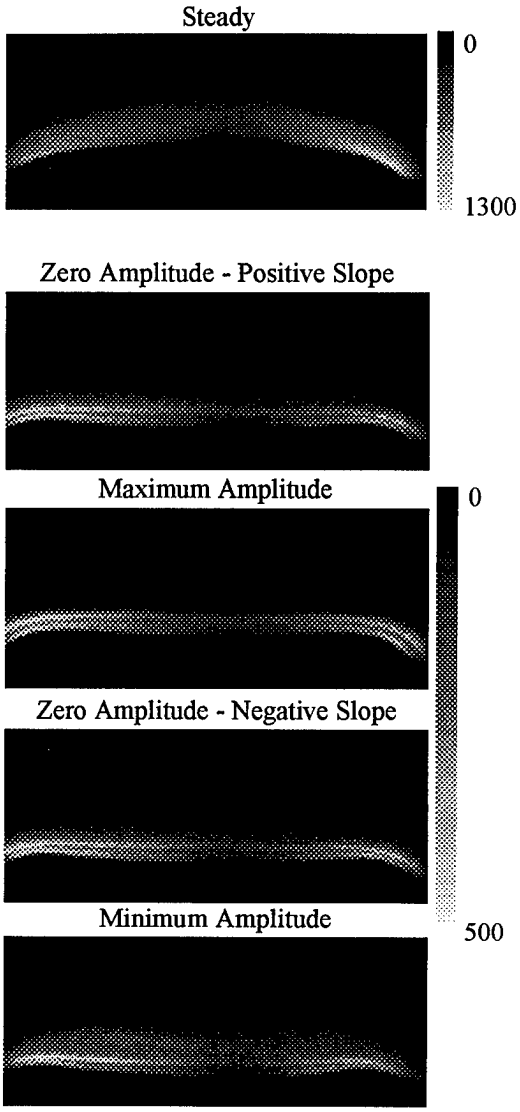

Fig 3 Time Averaged LII for GSR = 15(1/s), f=50Hz, A=50% of extinction.

FUNDAMENTALS OF SOOT FORMATION IN GAS TURBINE COMBUSTORS

AFOSR Contract F49620-98-C-0008

Principal Investigators: M. B. Colket, R. J. Hall, D. Liscinsky and M. Smooke

United Technologies Research Center and Yale University
Silver Lane, E. Hartford, CT 06108 New Haven CT

SUMMARY/OVERVIEW:

The overall objectives of this work are to obtain necessary fundamental data and to enhance and then validate modeling procedures in order to support modeling of soot production in practical gas turbine combustors. Several focused tasks of this effort include (1) extending measurements of surface growth rate constants to high temperatures, characteristic of rich zones in advanced combustors; (2) modeling of steady, laminar diffusion flames with different fuels to assist in validating the models; (3) advancing the modeling capabilities for describing known physical processes involved in soot production, including carbonization, ageing, and aggregate formation to enable more reliable extrapolation of existing models; and (4) modeling of sooting, transient flames to offer some physical understanding of processes controlling soot formation and destruction in turbulent, diffusion flames.

Measurements of Surface Growth Rates at High Temperatures

An important parameter for the prediction of soot production is the surface growth rate. Virtually all fundamental and reliable measurements of this parameter have been obtained over the temperature range of 1500-1950K. Many authors simulate this rate using a rate constant which increases exponentially with temperature (Arrhenius formulation). This assumption is acceptable under standard conditions since soot formation usually occurs in diffusion flames at temperatures below 1800K. Ref 1 and 2 have separately developed temperature-dependent expressions showing a substantial fall-off in the net rate constant for surface growth above about 1850K. These formulations were in part developed based on limited data at elevated temperatures (see Ref 3). Reliable data at temperatures above 2000K is very limited and hence extrapolation of this fall-off trend is highly uncertain. This problem is a concern since for advanced, high performance gas turbine combustors the 'sooting' rich zone will be at temperatures well in excess of 2000K. Hence, there is an obvious weakness in extrapolating existing models to such conditions.

To provide the needed data, a series of fuel-rich, laminar premixed flames are being examined, analogous to several previous studies (see for example, Ref. 4-5). In the present study, we are using a variety of methods to characterize the soot evolution, including laser absorption (with tomography), thermal particle densitometry (TPD), and thermophoretic sampling followed by transmission electron photography. Quartz probes for collection of gas samples (with gas chromatography) and thermocouples are being used to characterize the flame and its structure. At

present, we are validating our methods based on several 'literature' flames and expect to shortly extend these methods to higher temperature conditions.

Modeling of Soot Formation in Diffusion Flames

In addition to work in modeling opposed jet diffusion flames (see Ref. 6-7), significant accomplishments in the modeling of a coflow, laminar diffusion flame model have been achieved. Most studies in which detailed chemical kinetics are coupled with detailed soot models have been focused on one-dimensional problems. Ref. 8 and 9 have modeled laminar jet diffusion flames using monodisperse soot formation models with skeletal reaction mechanisms. In this program, we have incorporated the sectional soot formation and radiation models developed in Ref. 1 and 6 into the laminar, axisymmetric, diffusion flame code (see Ref. 10) for a cylindrical fuel stream surrounded by a coflowing oxidizer jet. This recent work is described in detail in Ref. 11 for an attached methane flame (Ref. 12) and in Ref. 13 for a diluted, lifted ethylene flame. For methane, a modified GRIMech 2.11, with all NO related reactions deleted and some benzene formation and destructions steps added, was used for the computations. The ethylene mechanism was derived from GRIMech, based on comparisons to PSR data and ignition delay times. We have collaborated with colleagues at Yale who have been investigating these flames using a variety of experimental techniques (thermocouples, TPD, quartz probes with on-line mass spectrometry and, in the case of the ethylene study, planar laser imaging using Rayleigh scattering and laser-induced incandescence).

For the attached methane flame, qualitative agreements were good, but several quantitative differences between the model and experiment were apparent. Most of these were attributable to an inability to model accurately the bulk flow features of the flame (particularly flame height was over predicted and peak flame temperatures were under predicted. Given these important differences, the agreement of species concentrations and soot profiles were quite good. However, quantitative comparisons between the measured and predicted soot profiles could not be made (predictions were about a factor of four low). Predicted distributions of particle size as a function of radius is shown in Fig. 1 at a height of 3 cm (approximately one cm below the height at which the peak centerline value is obtained). These distributions can be shown to be representative of the two soot producing regions of the flame. One along the wings (just inside of the flame front) where peak volume fractions are attained and the other along the centerline where much slower growth and particle sizes are observed.

The diluted lifted ethylene flame was selected in order to avoid possible complications of interactions between the burner lip and the flame, a possible source of the above discrepancies. In addition, optical diagnostics were included to add additional information to help resolve any differences between the model and physical probing of the flame. Overall, the agreements between the model and the experiments were extremely good for many features of the flame. Between the three 'solutions' for the ethylene flame (one model and two experiments), usually at least two of the methods agreed well (both spatial distributions and quantitative values). A comparison of the gas sampling and model predictions for benzene is shown in Figs. 2a and b, with identical scales for both contour plots. A limitation in the soot model can be illustrated by examining Fig. 3a, b, and c, which compare contour plots of total soot volume fraction for the model and the two experimental methods. While the maximum values of soot volume are reproduced well, the predicted soot profiles peak in the wing tips, while both experimental methods (TPD and LII) peak along the centerline. A preliminary analysis of this failure in the

model is its inability to reproduce accurately the processes of early PAH formation occurring along the centerline of the burner. Additional work in this area is proceeding as are initial efforts to model the 'Santoro' ethylene diffusion flame.

References

1. M. Colket and R. Hall, Proceedings of the International Workshop on Mechanism and Models of Soot Formation (H. Bockhorn, Ed.), Springer-Verlag, Heidelberg, (1994).
2. P. Markatou, H. Wang, and M. Frenklach, C&F, **93**, 467 (1993).
3. H. Bockhorn, F. Fetting, and H. Wenz, Ber. Bunsenges. Phys. Chem., **87**, 1067 (1983).
4. S. Harris, A. Weiner and R. Blint, C&F 72, 91 (1988). And references contained therein.
5. P. Sunderland and G. Faeth, C&F **105**, 132 (1996).
6. R. Hall, M. Smooke, and M. Colket, in Physical and Chemical Aspects of Combustion, Combustion Science and Technology Book Series (1997).
7. M. Smooke, R. Hall, and M. Colket, "Application of Continuation Methods to Soot Formation in Diffusion Flames," submitted for publication, (1998).
8. C. Kaplan, C. Shaddix and K. Smyth, C&F **106**, 392 (1996).
9. I. Kennedy, D. Rapp, R. Santoro, and C. Yam, C&F **107**, 368 (1996).
10. M. Smooke, Y. Xu, R. Zurn, P. Lin, J. Frank, and M. Long, Twenty-Fourth Symposium (International) on Combustion, The Combustion Institute, Pittsburgh, p. 813, (1992).
11. M. Smooke, C. McEnally, L. Pfefferle, R. Hall, and M. Colket, "Computational and Experimental Study of Soot Formation in a Coflow, Laminar Diffusion Flame", accepted for publication in Combustion and Flame, 1998.
12. C. McEnally, A. Schaffer, M. Long, L. Pfefferle, M. Smooke, M. Colket, and R. Hall, "Computational and Experimental Study of Soot Formation in a Coflow, Laminar Ethylene Diffusion Flame", accepted for oral presentation at the 27th International Symposium on Combustion, Boulder, CO, 1998.

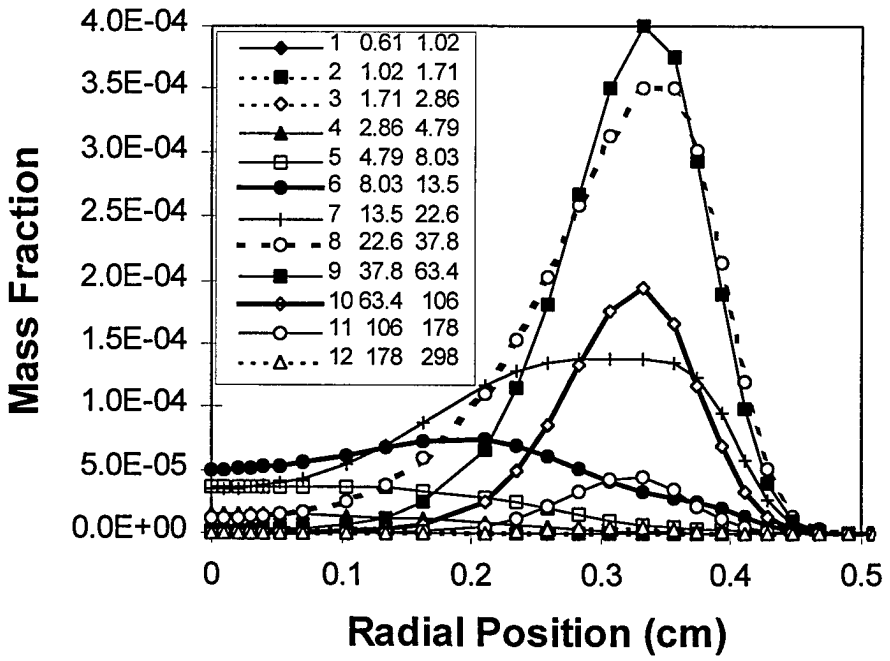

Fig. 1 Contributions of various soot mass classes to the total soot volume fraction as a function of radius at a height of 3 cm. Labels for the mass classes include the minimum and maximum diameters (nm).

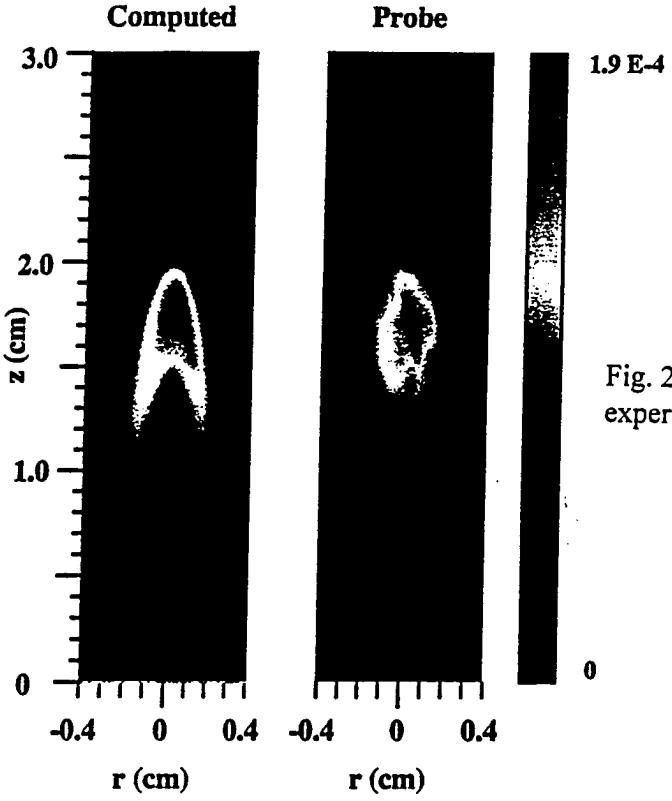

Fig. 2. Comparison between the computed (a) and the experimental (b) benzene mole fraction isopleths.

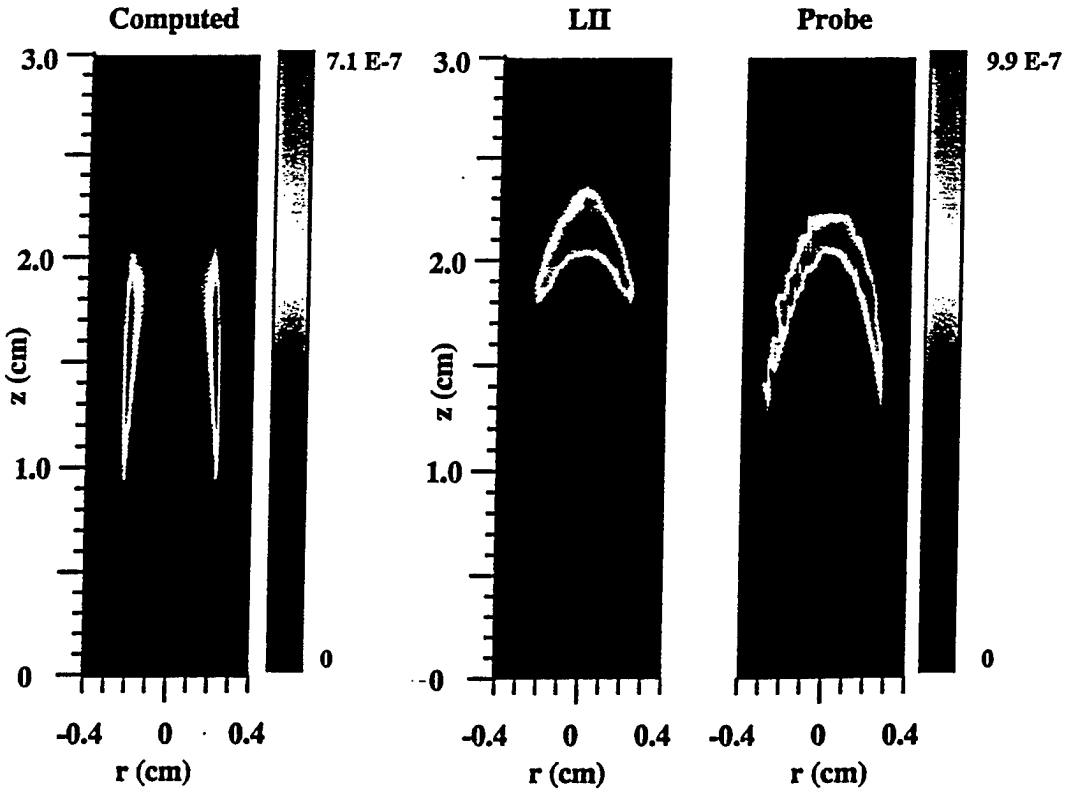

Fig 3. Comparison of the computed (a) and experimental soot volume fraction isopleths. The center figure (b) contains the thermophoretic sampling measurements and the right figure, c, contains the laser-induced incandescense measurements.

SOOT FORMATION IN TURBULENT COMBUSTING FLOWS

(AFOSR Grant/Contract No. F49620-97-1-0094)

Principal Investigator: R. J. Santoro

Propulsion Engineering Research Center
And
Department of Mechanical Engineering
The Pennsylvania State University
University Park, PA 16802-2320

SUMMARY/OVERVIEW

Current interest in high performance, low emissions gas turbine engines by the Air Force underscores the need for research on soot formation processes, since soot formation is directly related to issues involving performance and operability. Although recent research has provided significant advances in terms of understanding the basic mechanism controlling soot formation and destruction, many questions remain. In particular, an understanding of soot formation under high pressure and turbulent flame conditions is lacking. Since gas turbine combustors characteristically involve such flows, it is necessary to address these conditions if further progress is to be made. The current study is specifically directed at providing measurements of soot formation and destruction in atmospheric and high pressure turbulent flames. To date, measurements of the soot volume fraction, temperature and relative OH radical concentrations have been obtained for atmospheric flames over a Reynolds number range of 4000 to 23,000 for ethylene jet flames. These measurements have yielded quantitative information of the quantity of soot formed, the probability density functions for soot volume fraction, relative OH radical concentration, and temperature as well as providing determinations of the evolution of the integral length scales in the flame as a function of flame position and Reynolds number. This data is intended to form the basis for validating models of flame systems representative of gas turbine combustors. Such modeling capability is required to develop the needed insight necessary for implementing advanced design methodologies for future gas turbine combustors.

TECHNICAL DISCUSSION

Studies of soot formation in turbulent diffusion flames under atmospheric and elevated pressure conditions are being conducted to determine the controlling phenomena governing soot inception, growth and oxidation. Ethylene (C_2H_4) has been selected as the fuel and the soot formation process in the turbulent diffusion flames resulting from combustion of the fuel jet issuing into quiescent air is being investigated as a function of Reynolds number. Fuel jets issuing from tubes of 2.18 and 4.12 mm have been studied for Reynolds numbers ranging from 4000 to 23,000. The flame configuration selected closely follows that of Turns and Myhr [1] since a large comparative data base with respect to radiation and NO_x emissions exists for these flames.

Studies have focused on soot volume fraction measurements using laser-induced incandescence (LII), OH radical and polycyclic aromatic hydrocarbon (PAH) measurements using laser-induced fluorescence (LIF) and temperature measurements using Coherent Anti-Stokes Raman Spectroscopy (CARS). The application of the LII technique for soot measurements is noteworthy since it allows quantitative soot volume fraction measurements to be obtained locally. Recent studies of the LII technique have demonstrated that it is capable of quantitative soot volume fraction measurements if an appropriate calibration source is utilized [2-4].

Earlier reports on these current studies have noted that observed instantaneous soot volume fraction may be an order of magnitude larger than the temporally averaged mean value. This fact was attributed to the highly wrinkled structure of the turbulent flames that leads to localized high concentrations of soot particles that when temporally (and consequently spatially) averaged over the

flame result in significantly lower mean values. Furthermore, the results indicated that three distinct zone soot formation/destruction regions exist. The first region is characterized by rapid soot growth in which the soot particles and OH radicals exist in distinctly separate regions of the flame. As the Reynolds number is increased, the soot particle laden region shifts towards the center of the flame. Following this region of growth, which is clearly demarcated by the absence of PAH fluorescence as indicated from the LIF-PAH imaging measurements, a mixing dominated zone is observed that is strongly affected by increases in the Reynolds number. Mixing processes in this region affect the maximum soot volume fraction measured in an individual flame with the soot volume fraction decreasing with increasing Reynolds number. The final region is characterized by an overlapping of the soot particle and OH radical fields that leads to rapid oxidation of the soot. Only the high concentration regions formed lower in the flame survive this region to be emitted from the flame as smoke.

In order to characterize spatial soot formation processes, quantitative analysis for soot volume fraction, OH radical and soot zone thickness variations, probability and integral length scales have been performed. Turbulence is shown to influence the amount of soot formed, but does not affect the characteristic profiles of the soot particle distribution in the flame. The primary effect of the turbulence is to broaden the radial soot concentration profile at a given axial position. Measurements of the soot and OH radical zone thickness show that the soot zone thickness varies linearly in the formation region, while approximately a doubling of thickness of the OH radical zone is evident over the Reynolds number range studied in these flames. Probability density functions for soot, OH radical and PAH indicate that OH radical and PAH are spatially interrelated to soot formation and oxidation processes. The shape of the probability density function for soot particles shows an exponential distribution with highly positive skewness. Based on measurements of species eddy size variations, soot and OH radical length scales show anisotropic patterns with axial preferential orientation in the streamwise direction. These measurements also indicate that the OH radical length scale is the largest and PAH is the smallest among three species at a given axial position.

More detailed information on the length scales is presented by analyzing the axial and radial variations of the eddy size of the soot volume fraction and OH radical fields. A comparison of average eddy sizes was obtained for two different Reynolds numbers, 8000 and 12,000. The average eddy size is defined as half the average integral length scale. Soot eddy size at r/d = 0 and r/d = ± 10 as a function of the axial position is plotted in Figure 1.

The maximum soot eddy size is approximately 7 mm (~3d) with the eddy size at r/d = 0 increasing linearly along the jet axis for both turbulent cases. Eddies at r/d = ± 10 are very asymmetric. Soot eddy size at r/d = ± 10 rapidly grows until reaching the middle flame height, but this increase ceases above the middle of the flame and levels off further downstream. In particular, the effect of turbulence is more pronounced below the middle of the flame In contrast to soot eddy size, OH radical eddy size at r/d = 0 and r/d = ± 10, surprisingly always increases along the flame as illustrated in Figure 2 even though the flame is frequently broken by air entrainment. The maximum OH radical eddy size is observed to be approximately 12 mm (~5d) for the higher Reynolds number flame.

For the soot length scales, at r/d = ± 10 they are seen to increase with axial position throughout the formation region. The increase in length scale ceases in the oxidation region because parcels of air are entrained into the flame boundary and produce high intermittency in the soot particle field and thus, breakdown the soot field structure. Moreover, oxidation due to OH radicals reduces the soot concentrations and, in turn, reduces the size of the eddies already formed. On the other hand, length scales on the axis increase with axial position throughout the flame because of the lower soot intermittency compared to the intermittency off the flame axis. In contrast to the soot, OH radical length scales at r/d = 0 and r/d = ± 10 increase over the entire flame.

An analysis of the radial dependence of eddy sizes for the soot and OH radical fields is shown in Figure 3. Eddy sizes off the jet axis at a given axial position were ratioed by those on the jet axis. There is relatively little radial dependence with increasing Reynolds number for the soot eddy size in the oxidation regions while some variation is observed in the formation region (y/d <120). The observation that the radial eddy size variation for soot particles for both turbulent cases changes little further downstream, implies that the soot eddy is moving off the axis very fast compared to the mixing rate. However, soot eddies in the formation region undergo severe turbulence flow field effects during their

radial movement. With increasing Reynolds number, a weak radial dependence of soot eddy size can be observed. However, a difference exists in the OH radical case such that OH radical eddy sizes off the axis are always larger than those on the axis except near the flame tip. There is a remarkably radial uniformity compared to the average and fluctuations of soot that show large radial dependencies. These radial variations arise from the intermittency of the soot field. As pointed out by Dasch et al. [5], the radial uniformity of soot eddies implies that the soot chemistry in the soot-containing regions is relatively slow compared to the radial mixing.

From the CARS temperature measurement, single-shot temperature spectra obtained show fairly good agreements with theoretical N_2 spectra. A method to obtain the fuel diffusion layer in which average stoichiometric conditions are locally satisfied is suggested by analyzing the correlation between temperature and unburned fuel. In the temperature pdfs, temperature bimodality is observed over all the axial positions and the bimodality width with respect to radial distance increases with increasing Reynolds number. With respect to soot formation, the highest soot formation and the peak mean temperature are observed on the fuel-rich side of the stoichiometric flame location while the peak OH· concentration lies on the fuel-lean side.

REFERENCES

1 Turns, S. R. and Myhr, F. H., "Oxides of Nitrogen Emissions from Turbulent Jet Flames Part I – Fuel Effects and Flame Radiation," *Combustion and Flame*, 87:319-335, 1991.

2 Quay, B., Lee, T-W, Ni, T. and Santoro, R. J., "Spatially Resolved Measurements of Soot Volume Fraction Using Laser-Induced Incandescence," *Combustion and Flame*, 97:384-392, 1994.

3 Ni, T., Pinson, J. A., Gupta, S. and Santoro, R. J., "Two-Dimensional Imaging of Soot Volume Fraction by the Use of Laser-Induced Incandescence," *Applied Optics*, 34, pp. 7083-7091, 1995.

4 Ni, T., Gupta, S., and Santoro, R. J., "Suppression Of Soot Formation In Ethene Laminar Diffusion Flames By Chemical Additives," *Twenty-fifth Symposium (International) on Combustion*, The Combustion Institute, 1994, pp. 585-592.

5 Dasch, C. J. and Heffelfinger, D. M., "Planar Imaging of Soot Formation In Turbulent Ethylene Diffusion Flames: Fluctuations and Integral Scales," *Combustion and Flame*, 85:389-402, 1991.

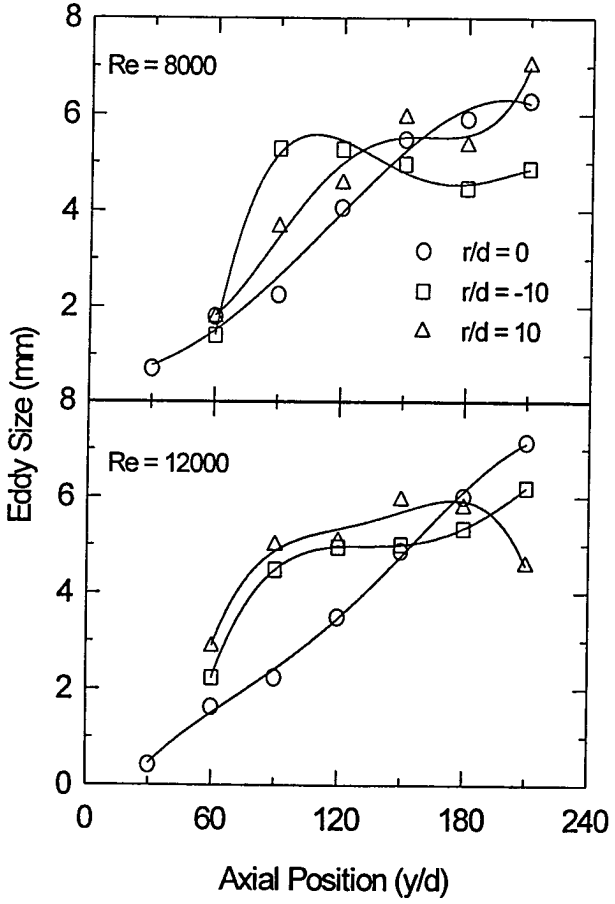

Figure 1. Average soot eddy size as a function of axial position for Re = 8000 and 12000 flames

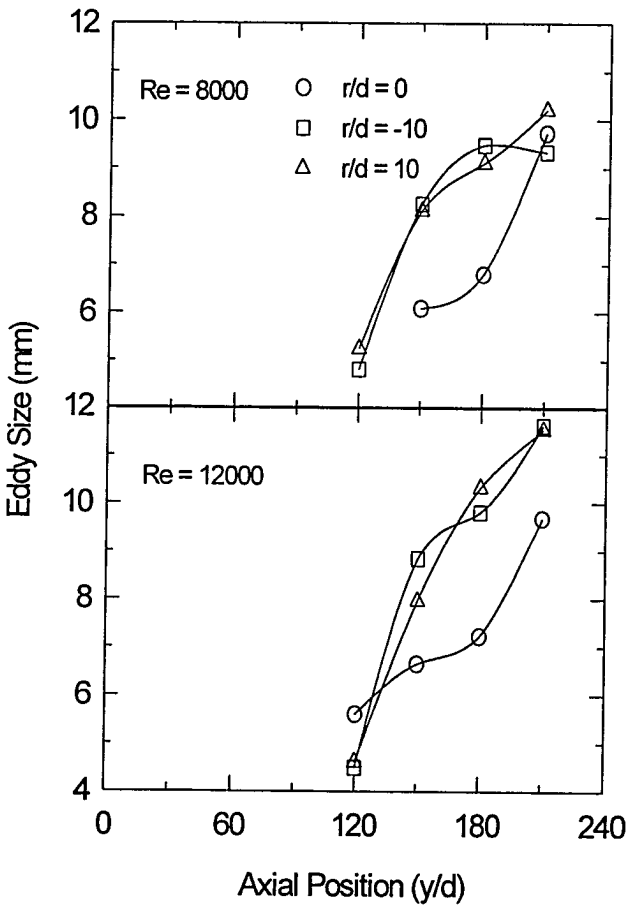

Figure 2. Average OH· eddy size as a function of axial position for Re = 8000 and 12000 flames

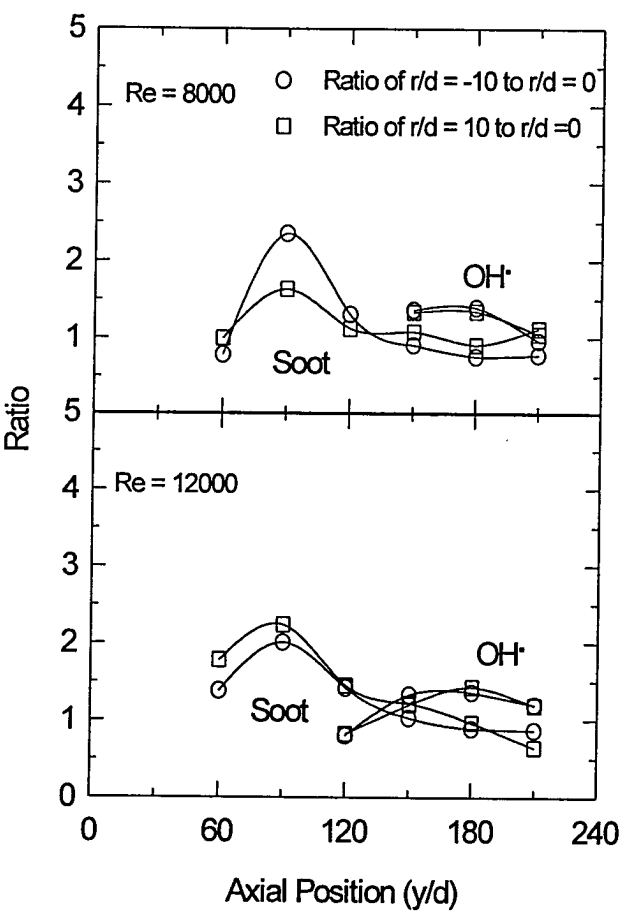

Figure 3. Radial variation of the soot particle and OH· eddy size for Re = 8000 and 12000 flames

ABSTRACTS OF WORK UNITS NOT PRESENTED AT THE MEETING

HIGH RESOLUTION MEASUREMENTS OF SUPERSONIC SHEAR FLOW MIXING AND COMBUSTION

AFOSR Grant No. F49620-98-1-0003

Werner J.A. Dahm and James F. Driscoll

Gas Dynamics Laboratories
Department of Aerospace Engineering
The University of Michigan
Ann Arbor, MI 48109-2118

Summary/Overview

Achieving supersonic mixing and combustion while maintaining acceptable flame stability characteristics and emissions of trace chemical species are key to the development of improved airbreathing propulsion systems. The present investigation contributes to this objective by making high-resolution imaging measurements of the physical structure of supersonic mixing and combustion in a turbulent shear flow. The work consists of two major parts.

The first part is an experimental and theoretical investigation of the outer-scale properties of mixing and combustion in a supersonic shear flow facility. Emphasis is on measuring changes in the large-scale structure and growth rate of a two-dimensional supersonic turbulent shear flow due to compressibility effects, and comparing with results obtained in supersonic mixing layers elsewhere in the AFOSR program. Comparisons with results from mixing layers allow identification of the effects of compressibility that are generic to all supersonic turbulent shear flows. This work also builds on recent advances in understanding density effects due to heat release on the growth rates and other outer-scale properties of turbulent shear flows. Density effects due to compressibility are being analyzed similarly to develop fundamental understanding and predictive modeling capabilities for supersonic turbulent shear flows.

The second major part of this work is investigating the fully-resolved four-dimensional spatio-temporal structure of the fine scales of molecular mixing in subsonic and supersonic turbulent shear flows. A recently-developed measurement system will permit the first-ever simultaneous study of the combined four-dimensional spatial and temporal structure of the conserved scalar field $z(\mathbf{x},t)$, the molecular mixing rate field $\nabla\zeta\cdot\nabla\zeta(\mathbf{x},t)$, and the underlying vorticity and strain rate fields $\omega_i(\mathbf{x},t)$ and $\varepsilon_{ij}(\mathbf{x},t)$ in a gaseous turbulent shear flow. These measurements will permit essential new insights to be gained into the fundamental issues that dominate the coupling between turbulent flow, molecular mixing, and nonequilibrium reaction chemistry in turbulent combustion systems.

Technical Discussion

During the past year we have obtained extensive experimental results for the outer-scale properties and large-scale structure of supersonic turbulent jets operating in the wake mode. Typical results are shown in Figs. 1 and 2. There are indications that the large-scale structure of the flow, which is clearly evident in the further downstream parts of the flow, where the local Mach number is become subsonic, may be suppressed in the upstream portion of the flow. This is being further investigated. However, the local flow width $\delta(x)$ and growth rate $d\delta/dx$ in Figs. 2 and 3 show results consistent with the $(x/\vartheta)^{1/2}$ scaling that is characteristic of the corresponding subsonic flow, even in the upstream parts of the flow. This can be clearly seen in the log-log plots in Fig. 3, where it can be further observed that this conclusion appears to be independent of the choice of flow width definitions.

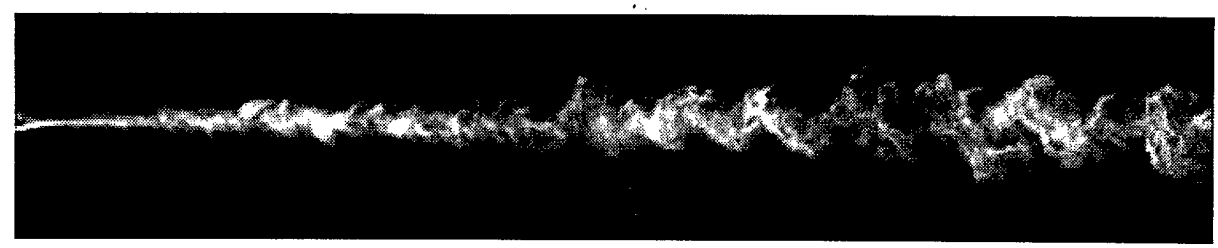

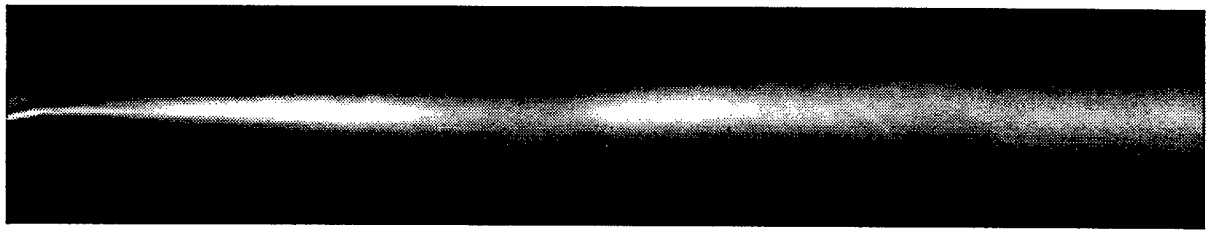

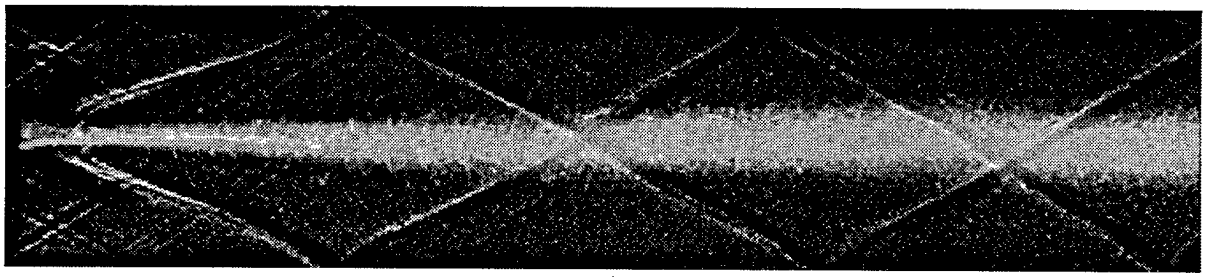

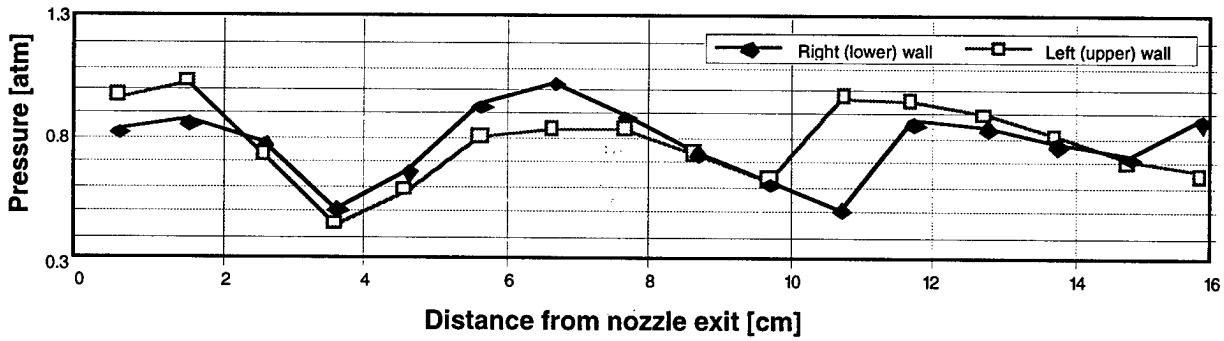

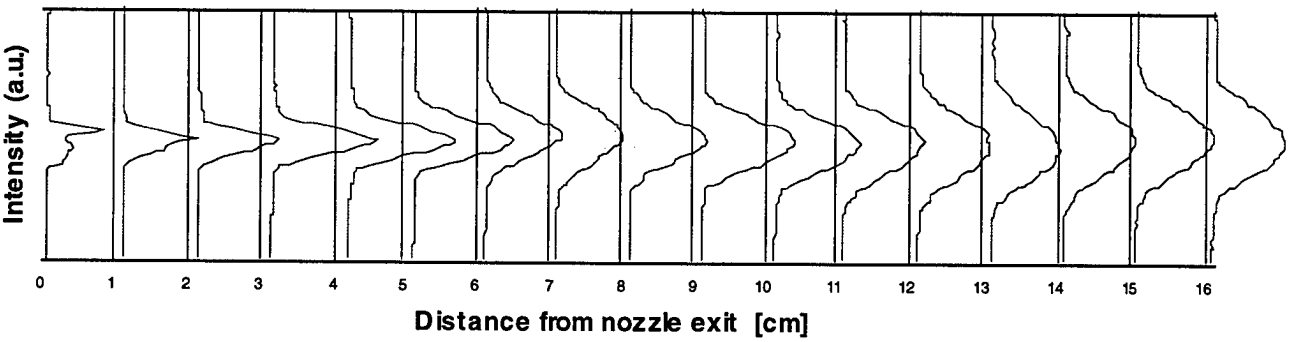

Fig. 1. Typical experimental results for outer-scale properties obtained in the two-dimensional supersonic turbulent shear flow, showing instantaneous mixing regions and large-scale structure as visualized by alcohol fog technique *(top)*, ensemble average *(second)*, with supersonic wave structure superimposed *(third)*, wall static pressure measurements *(fourth)*, and local flow width d(x) as indicated from second panel. See also Fig. 2. Growth rates obtained from bottom panel are shown in Fig. 3.

Several supersonic hydrogen-air flames were imaged in our Supersonic Mixing and Combustion Facility. Acetone PLIF was used to visualize the fuel concentrations in the jet-like flames, and OH PLIF was used to visualize the reaction zones. The supersonic flames that were studied were partially lifted, having a flame base that is stabilized in a recirculation zone behind the bluff-body fuel injector. It was found that the structure of the supersonic flames is closer to that of a partially premixed flame, and is very different from the structure of a conventional attached subsonic jet flame.

The partial premixing of hydrogen and air is enhanced by the extremely strong recirculation zone downstream of the fuel injector, which is driven by the Mach 2.5 airstream. The OH reaction zone structure has the appearance of a tangled web of thin reaction layers for subsonic coflow air; as the coflow air becomes supersonic the layers become thicker and merge, and the instantaneous OH concentrations become spatially diffuse. The increased homogeneity of the OH reaction zone at supersonic conditions is attributed to the intense premixing of fuel and air prior to combustion. Our experimental observations provide strong evidence that the flame is partially premixed, which emphasizes the need to develop new models, especially those that can represent a complex set of reaction layers, some of which are diffusion layers and some partially premixed flames.

We have also initiated an ongoing interaction with researchers at the Air Force's WPAFB in Dayton, OH (T. Jackson, J. Donbar). The first phase of this interaction has been completed; Michigan Ph.D. candidates operated advanced PIV / OH / CH diagnostics at WPAFB to answer fundamental research questions relating to turbulent mixing and reaction. For the first time, the CH and OH reaction zone structure and the hydrodynamic strain rate were measured in an intensely turbulent nonpremixed flame. A regime of combustion was investigated in which the intense turbulence and long residence times provided extremely large degrees of flame wrinkledness and large values of flame surface density. Some partial premixing was observed in certain cases. The relevant nondimensional parameters that characterize this regime of combustion are being deduced from the data.

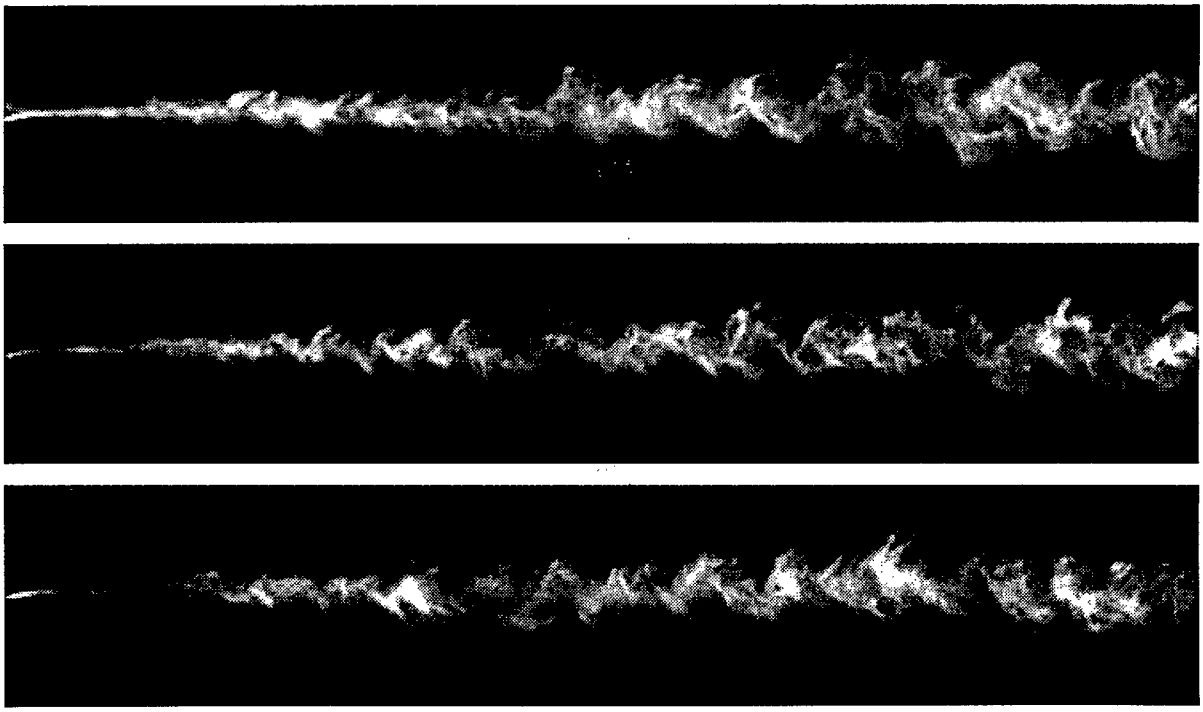

Fig. 2. Typical large-scale structure in the two-dimensional supersonic turbulent shear flow shown in three different realizations, visualized by alcohol fog technique. Note the large-scale structure is clearly evident in the farther downstream regions of the flow, where the local Mach number is subsonic.

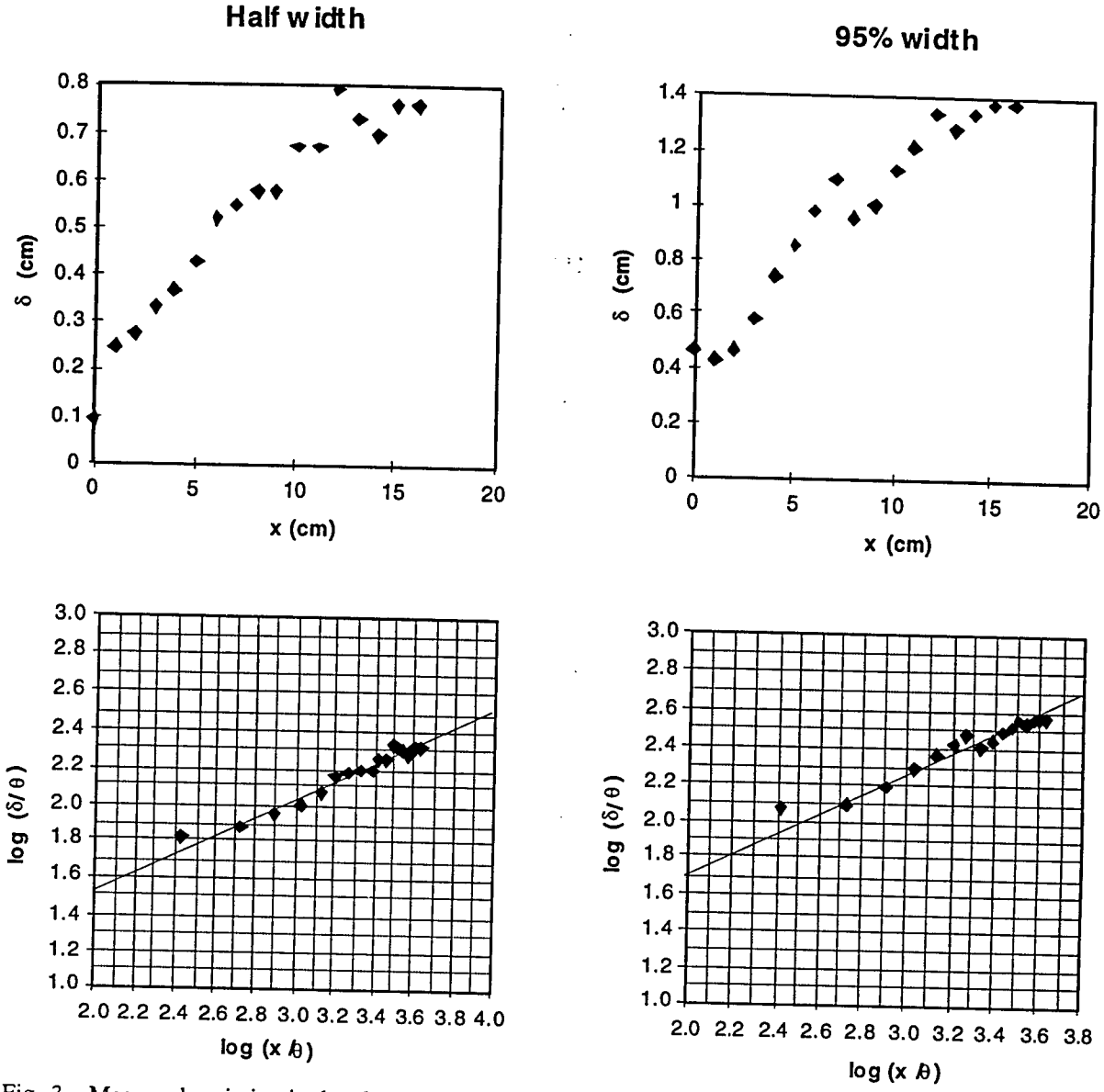

Fig. 3. Measured variation in local outer-scale flow width δ(x) defined by half-width *(left)* and 95% width *(right)* with downstream distance x/ϑ in the two-dimensional supersonic shear flow, shown in linear form *(top)* and logarithmix form *(bottom)*. Note straight line gives $(x/\vartheta)^{1/2}$ power law scaling.

Bryant, R. (1998) Planar Laser Induced Fluorescence Images of Fuel Mixing and the Reaction Zone in a Supersonic Combustor, Ph.D. Thesis, The University of Michigan.

Bryant, R. & Driscoll, J. F. (1997) Acetone Laser Induced Fluorescence for Visualization of Low Pressure, Low Temperature Flows, submitted to *Experiments in Fluids.*

Buch, K.A. and Dahm, W.J.A. (1998) Experimental study of the fine-scale structure of conserved scalar mixing in turbulent flows. Part II. Sc ≈ 1; *J. Fluid Mech.* **364**, 1-29.

Dahm, W.J.A. & Southerland, K.B. (1997) Experimental assessment of Taylor's hypothesis and its applicability to dissipation estimates in turbulent flows. *Phys. Fluids* **9**, 2101-2107.

Donbar, J. (1998) Reaction Zone Structure and Velocity Measurements in Turbulent Nonpremixed Jet Flames, Ph.D. Thesis, The University of Michigan.

Frederiksen, R.D., Dahm, W.J.A. & Dowling, D.R. (1997*a*) Experimental assessment of fractal scale similarity in turbulent flows. Part 2: Higher dimensional intersections and nonfractal inclusions. *J. Fluid Mech.* **338**, 89-126; Part 3: Multifractal scaling. *J. Fluid Mech.* **338**, 127-155; Part 4: Effects of Reynolds and Schmidt numbers. Submitted to *J. Fluid Mech.*

Mixing, chemical reactions, and combustion in subsonic and supersonic turbulent flows

AFOSR Grant F49620-98-1-0052

P. E. Dimotakis and A. Leonard

Graduate Aeronautical Laboratories
California Institute of Technology, Pasadena, CA 91125

Summary/Overview

This effort is focused on fundamental investigations of mixing, chemical-reaction, and combustion processes, in turbulent, subsonic, and supersonic free-shear flows. The program is comprised of an experimental effort; an analytical, modeling, and computational effort; and a diagnostics and data-acquisition-development effort. The computational studies are focused on fundamental issues pertaining to the hydrocarbon-ignition/-combustion and numerical simulation of compressible flows with strong fronts, in both chemically-reacting and nonreacting flows.

Technical discussion

Investigating the effects of various parameters on turbulent-shear-layer mixing and combustion at high Reynolds number, experiments were conducted to explore the influence of inflow conditions. Chemically-reacting, incompressible, shear-layer flows were investigated in the GALCIT Supersonic Shear Layer Facility, at freestream conditions $U_2/U_1 \simeq 0.4$ and $\rho_2/\rho_1 \simeq 1$ and a local Reynolds number, $Re_\delta \equiv \rho \Delta U \delta(x)/\mu \sim 2 \times 10^5$.

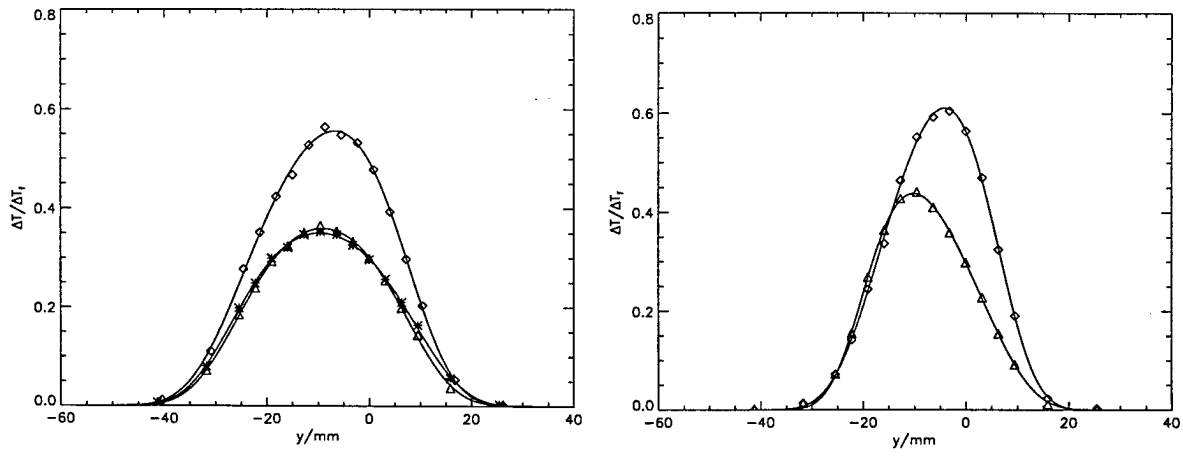

FIG. 1 Normalized temperature-rise data. Left: untripped boundary layers. Right: tripped high-speed boundary layer. Reactant compositions - diamonds: $\phi = 8$; triangles: $\phi = 1/8$; asterisks: $\phi = 1/8$, reduced chemical-kinetic rate.

Chemically-reacting "flip" experiments allow us to deduce the structure and amount of molecular-scale mixing, information unobtainable from direct scalar imaging at such high Reynolds numbers. Two sets of temperature-rise data from such experiments are presented below (Fig. 1). The only difference between these is a 0.8 mm-diameter trip wire on the splitter plate (high-speed side), 50 mm upstream of its trailing edge. The data are measured far downstream, at $x/\theta_1 \simeq 3300$, where x is the streamwise coordinate and θ_1 is the high-speed boundary layer momentum thickness, and at a large value of the pairing parameter,[1] $P \simeq 47$. By these criteria, the flow may be regarded as fully-developed.[2,3] The change in inflow conditions can be seen to have a significant effect on all scales of the flow: the shear-layer growth rate, δ/x, has decreased by 21%; the mixed-fluid fraction (efficiency of molecular-scale mixing), has increased by 11%; and the mixed-fluid composition ratio has decreased by 9%. Additionally, the data indicate a change from a non-marching scalar probability-density function (pdf), to a marching pdf, when the boundary layer was tripped. These observations suggest a shear-layer behavior that depends not only on local-flow properties, but also on upstream conditions, reminiscent of results from low-dimensionality, non-linear (chaotic) systems.[4]

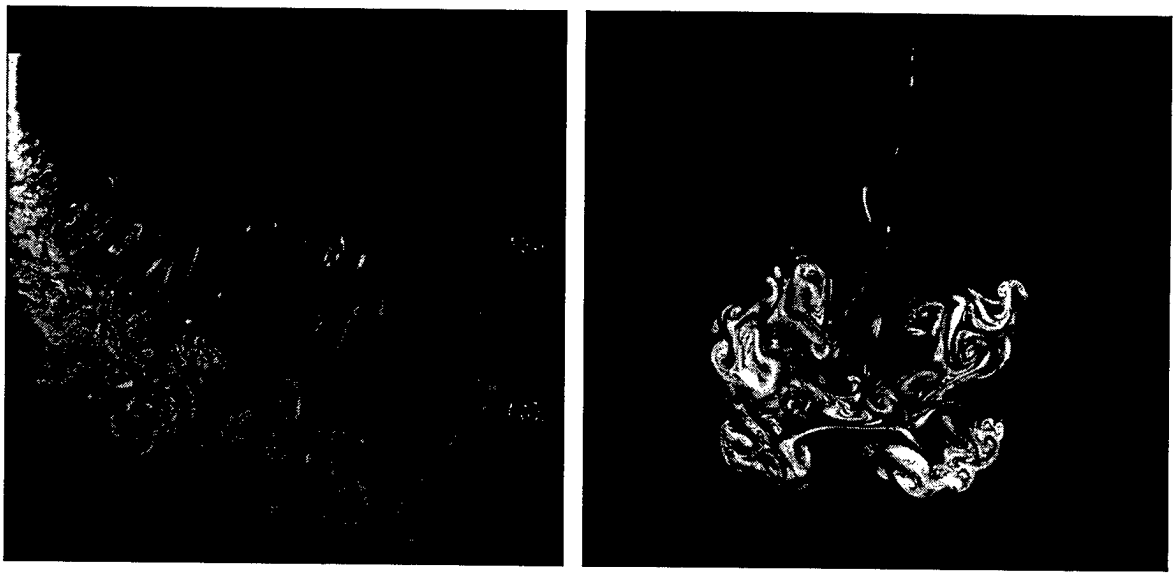

FIG. 2 Transverse jet at $Re_j \simeq 1.0 \times 10^3$ and $U_j/U_\infty \simeq 34$. Left: LIF image in plane parallel to free-stream (log-intensity scale). Right: Slice perpendicular to free-stream.

Experiments on the development and far-field structure of a liquid-phase turbulent jet issuing into a cross-flowing uniform stream were conducted at a jet Reynolds number, $Re_j \equiv U_j d_j/\nu \simeq 1.0 \times 10^3$, for a velocity ratio, $U_j/U_\infty \simeq 34$. Laser-induced fluorescence (LIF) images measured scalar-species concentration in two orthogonal slices of the transverse jet (Fig. 2). The data show wake structures similar to those reported previously,[5] *e.g.*, "fingers" of dyed jet-fluid extending from the tunnel wall to the main body of the jet. These are transported downstream with nearly uniform velocity after being formed near the jet exit.

As part of our investigation of the geometry of scalar isosurfaces in liquid-phase turbulent jets, an analysis of area-perimeter properties of isoscalar "islands" and "lakes" derived from 2-D images of jet-fluid concentration images has been conducted. The images are slices in a plane normal to the jet axis in the far field and correspond to a fluid Schmidt number of $Sc \simeq 2.0 \times 10^3$ and flow Reynolds numbers of $Re \simeq 4.5 \times 10^3$, 9.0×10^3, and 18×10^3.[6,7] For such data, scalar level sets form disjoint "islands" and "lakes", depending on whether the interior is at a lower, or higher, scalar level, respectively. Island/lake statistics, such as size and shape complexity, are important in many contexts: for chemical reactions and combustion in non-premixed hydrocarbon turbulent flames, for example, combustion is largely confined to the instantaneous stoichiometric (isoscalar) surface.[8] In 2-D, such a measure, Ω_2, dubbed *shape complexity*, can be defined as,

$$1 \leq \Omega_2 \equiv \frac{P}{2\,(\pi A)^{1/2}} \leq \infty \ ,$$

with P the perimeter and A an island/lake area, and $(\Omega_2)_{\min} = 1$ attained for a circle. Corresponding extensions can also be made for higher-dimensional embedding spaces.

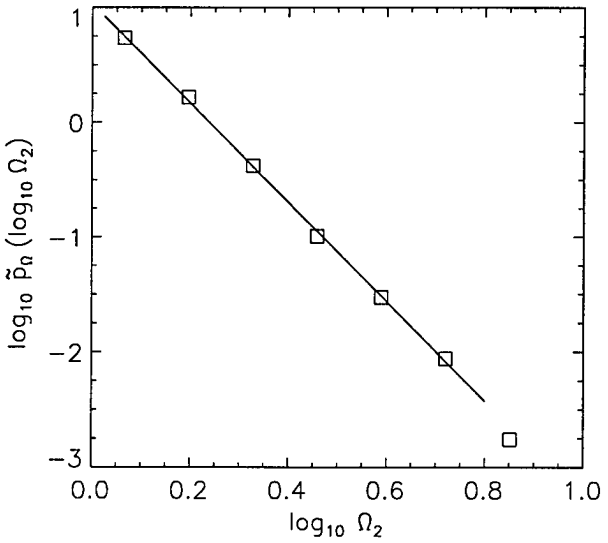

FIG. 3 Shape complexity pdf of islands and lakes. Solid line: power-law fit (in these coordinates).

An analysis of the liquid-phase jet data described above indicates that a power law for over 3 decades in size (6 decades in area), or, equivalently, log-Poisson statistics, provide a good approximation for the pdf of shape complexity in this flow, with similar statistics expected in turbulent flows in general. Such distributions are necessary in modeling burning-time distributions in nonpremixed combustion, for example.[9]

Numerical-simulation investigations were conducted on ignition characteristics of hydrocarbon fuel blends, at conditions relevant to high-Mach-number, air-breathing-propulsion vehicles. A two-point-continuation method was employed, with a detailed description of

molecular transport and chemical kinetics, focusing on the effects of fuel composition, reactant temperature, additives, and imposed strain rate. It captured the entire S-curve that describes the processes of vigorous burning, extinction, and ignition. The results demonstrate that ignition of such fuel blends is dominated by the synergistic behavior of CH_4 and C_2H_4. A fuel temperature $T_{\text{fuel}} = 950\,\text{K}$ was used in the simulations. For low air temperatures, *e.g.*, $T_{\text{air}} \simeq 1050\,\text{K}$, addition of small amounts of CH_4 enhances C_2H_4 ignition, while for $T_{\text{air}} > 1200\,\text{K}$, CH_4 inhibits ignition. The ignition of blends of CH_4 and C_2H_4 was significantly promoted through independent additions of small amounts of H_2, and F_2 with NO. The latter yields F-radicals which effectively consume hydrocarbon molecules.[10]

References

[1] Ho, C.-M., and Huang, L.-S., "Subharmonics and vortex merging in mixing layers," *J. Fluid Mech.* **119**, 443–73 (1982).

[2] Bradshaw, P., "The effect of initial conditions on the development of a free shear layer," *J. Fluid Mech.* **26**(2), 225–236 (1966).

[3] Karasso, P. S., and Mungal, M. G., "Scalar mixing and reaction in plane liquid shear layers," *J. Fluid Mech.* **323**, 23–63 (1996).

[4] Slessor, M. D., Bond, C. L., and Dimotakis, P. E., "Turbulent shear-layer mixing at high Reynolds numbers: effects of inflow conditions," GALCIT Fluid Mechanics Report FM98–1 (1998).

[5] Fric, T. F., and Roshko, A., "Vortical structure in the wake of a transverse jet," *J. Fluid Mech.* **279**, 1–47 (1994).

[6] Catrakis, H. J., and Dimotakis, P. E., "Mixing in turbulent jets: scalar measures and isosurface geometry," *J. Fluid Mech.* **317**, 369–406 (1996).

[7] Dimotakis, P. E., and Catrakis, H. J., "Turbulence, fractals, and mixing," NATO Advanced Studies Institute series, *Mixing: Chaos and Turbulence*, GALCIT Report FM97–1 (1996).

[8] Burke, S. P., and Schumann, T. E. W., "Diffusion Flames," *Ind. Eng. Chem.* **20**, 998 (1928).

[9] Catrakis, H. J., and Dimotakis, P. E., "Shape Complexity in Turbulence," *Phys. Rev. Lett.* **80**, 968–971 (1998).

[10] Egolfopoulos, F. N., and Dimotakis, P. E., "Non-premixed hydrocarbon ignition at high strain rates," *Twenty-Seventh Symposium (International) on Combustion*, Paper 5C11. GALCIT Report FM98–7 (1998).

RAMJET RESEARCH

AFOSR TASK 2308BW

Principal Investigators: Thomas A. Jackson
Mark R. Gruber

Propulsion Sciences and Advanced Concepts Division
Propulsion Directorate
Air Force Research Laboratory
Wright-Patterson AFB OH 45433

SUMMARY OVERVIEW

This research program addresses relevant technical issues associated with the fuel-air mixing processes (liquid, supercritical, and gaseous phase fuels) in subsonic and supersonic flows and the role of turbulent transport on mixing and combustion in ramjet/scramjet combustors. Five sub-areas continue. They are summarized in what follows with only the first outlined in detail. (1) Pressure-sensitive paint was applied to circular and elliptic injector nozzles to assess the effects of the surface pressure field on injector performance. The elliptic nozzle fostered faster lateral spreading of the wake, smaller separated zones, weaker bow shocks, and higher effective back pressures thus explaining the recently observed differences in transverse penetration and mixing of the two jets. (2) An investigation of angled liquid injection for ramjet/scramjet applications using shadowgraph has revealed two regimes describing the breakup of the liquid column: aerodynamic and non-aerodynamic. A column breakup parameter was defined based on the observed breakup characteristics that allowed correct prediction of the column fracture location. (3) Injection and mixing mechanisms in supercritical fuel injection flowfields were studied using Raman scattering. Condensation was a serious problem at low injection temperatures. Mole fraction distributions followed a Gaussian distribution while the temperature field revealed deficits inside the jet plume due to rapid expansion. (4) Nonpremixed turbulent jet flames were investigated using simultaneous CH-fluorescence and particle image velocimetry. Results yield quantitative measurements of strain rate and flame thickness from the base to the tip of the flame. (5) Filter-based diagnostics were developed for measurements of velocity and temperature in three-dimensional, unsteady, turbulent, reacting and non-reacting flows. Both lab- and full-scale experiments were conducted.

The objectives of this work are to study the effects of injector geometry on the near-field development in the flowfield created by sonic transverse injection into a supersonic crossflow. Effective injection into a supersonic flow remains a daunting task in the successful design and implementation of a scramjet-based propulsion system. Transverse fuel injection provides rapid penetration of the fuel into the crossflow and promotes relatively rapid near-field mixing between the fuel and air; however, it suffers from high pressure losses and significant wall heating effects.

It has been recently observed that for the same jet-to-freestream momentum flux ratio, jets issuing from circular and elliptic nozzles have appreciably different transverse penetration and lateral spreading characteristics.[1] Figure 1 shows the penetration correlations resulting from planar laser sheet imaging studies of these two flowfields at a jet-to-freestream momentum flux ratio (J) of 3. The jet issuing from the elliptic injector clearly suffers approximately a 20%

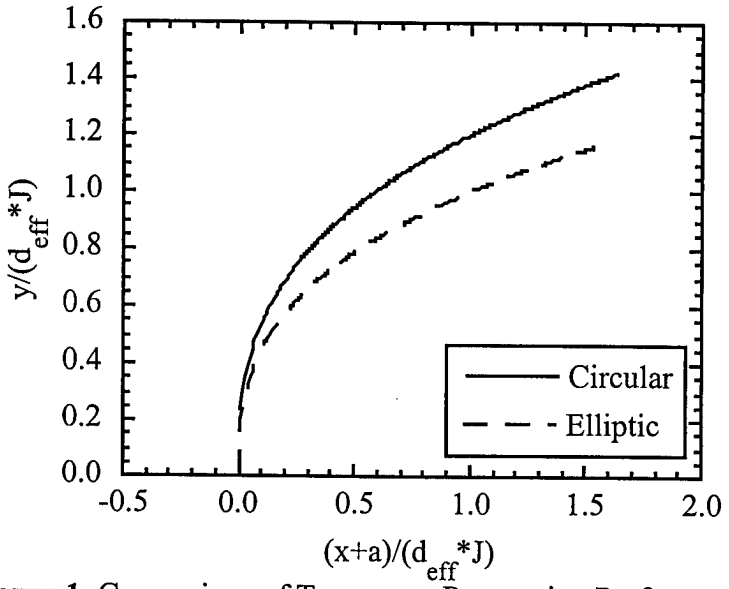

Figure 1 Comparison of Transverse Penetration Performance (J = 3)

reduction in transverse penetration compared to the circular case. Schetz and Billig[2] pointed to the "effective back pressure" as an important indicator of the extent to which the jet penetrates into the crossflow. This pressure, analogous to the back pressure in the case of injection into a quiescent medium,[3] is the average static pressure in the near-field region surrounding the injector orifice. It is expected that, because of the significant change in injector geometry, the wall static pressure fields surrounding the circular and elliptic nozzles are appreciably different. Thus, the effective back pressure may be the key to correlating the observed performance differences in penetration for these two injectors. Presently, the most effective technique for experimentally determining the surface pressure field around such wall-mounted injectors is pressure-sensitive paint (PSP). This technique allows nonintrusive examinations of the wall pressure field with tremendously improved spatial resolution over conventional static pressure taps, and has been selected for use in this work.

Figure 2 presents PSP images from the two injector cases studied. Each image has been properly analyzed to produce quantitative pressure information. As presented, the color scales in the two images correspond to normalized wall static pressure (i.e., p/p). Because of the tremendous improvement in spatial resolution offered by PSP over conventional pressure taps,

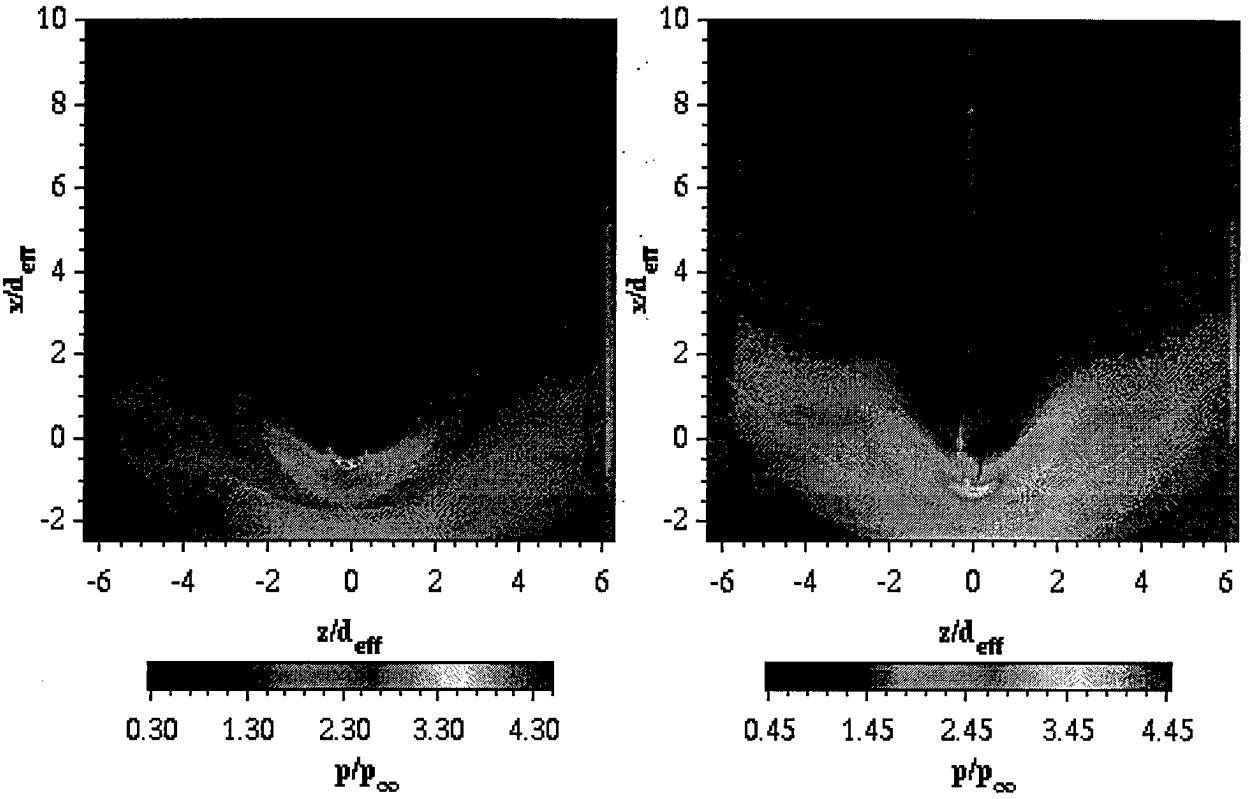

Figure 2 Effects of Injector Geometry (J = 4)

the entire pressure field is well observed (each image contains roughly 180,000 pressure measurements). Although somewhat similar in appearance, important differences may be observed between the two images. The separation region occurring upstream of the injector is much smaller for the elliptic nozzle. Also, the development of the wake region in the elliptic nozzle flowfield is appreciably different compared to the wake of the circular jet. Clearly, it grows in the lateral direction much faster than in the circular case. This is directly a result of the axis-switch which occurs for the elliptic jet. The flow on the injector centerline recompresses faster in the elliptic case. This is thought to be a consequence of how the counter-rotating vortices develop in this flowfield. The vortices entrain more freestream fluid into the wake region resulting in this rapid recompression. The bow shock waves are also observed in the images upstream of the injector nozzles. Further details are found in Gruber et al.[4] Figure 3 shows the results of analyzing the PSP images for effective back pressure. The plot indicates that the effective back pressures in the elliptic injection cases are all between 20-35% higher than their respective circular injection results. Thus, the jet issuing from the elliptic nozzle encounters a relatively higher pressure environment than does the circular jet at the same relative operating conditions. It is therefore reasonable to expect that the elliptic jet will not penetrate as deeply

into the crossflow as the circular jet. This analysis provides strong support for the recently observed differences in performance between these two injectors.[1] It also supports the importance of the effective back pressure concept as it applies to comparisons in transverse penetration performance between injectors of different geometries.

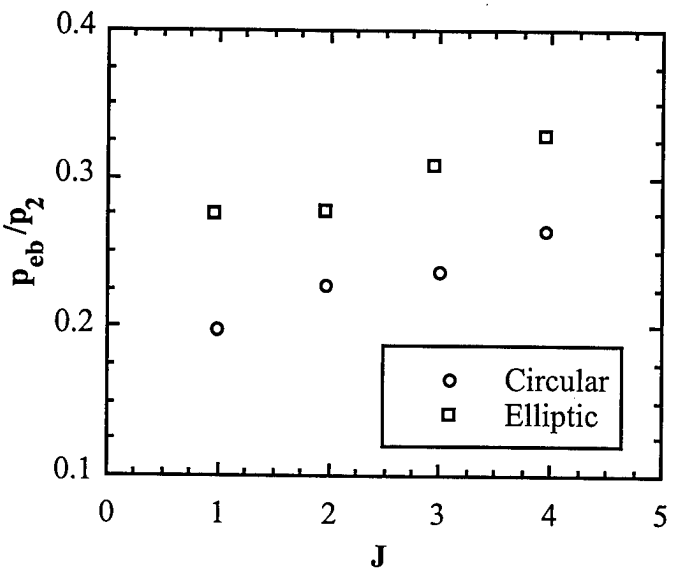

Figure 3 Effects of Injector Geometry on Effective Back Pressure

1. Gruber, M. R., Nejad, A. S., and Dutton, J. C., "An Experimental Investigation of Transverse Injection from Circular and Elliptical Nozzles into a Supersonic Crossflow," Wright Laboratory, WL-TR-96-2102, 1996.
2. Schetz, J. A., and Billig, F. S., "Penetration of Gaseous Jets Injected into a Supersonic Stream," *Journal of Spacecraft and Rockets*, Vol. 3, No. 11, 1966, pp. 1658-1665.
3. Adamson, T. C., and Nicholls, J. A., "On the Structure of Jets from Highly Underexpanded Nozzles into Still Air," *Journal of the Aero/Space Sciences*, Vol. 26, 1959, pp. 16-24.
4. Gruber, M. R., Nejad, A. S., and Goss, L. P. , "Surface Pressure Measurements in Supersonic Transverse Injection Flowfields," AIAA Paper 97-3254, 1997, also submitted to *Journal of Propulsion and Power.*

EVALUATION OF CLOSURE MODELS OF TURBULENT DIFFUSION FLAMES

(AFOSR Grant No. F49620-97-1-0092)

Principal Investigators: George Kosály and James J. Riley

Department of Mechanical Engineering
University of Washington, Seattle, WA, 98195-2600

SUMMARY/OVERVIEW

Current work in large eddy simulations focuses on the validation of the Large-Eddy Flamelet Model via DNS. To validate our DNS computations simulation results were compared to the classical measurements of Comte-Bellot and Corrsin.[1] DNS data have been used to investigate how sensitive the average species mass fractions are to the subgridscale modeling of the dissipation rate and the variance of the mixture fraction. The DNS investigation of differential diffusion effects in turbulent reacting flows demonstrated the importance of the terms related to the conditional fluctuations of the mixture fraction in the modeling of the conditionally averaged mass fractions.

TECHNICAL DISCUSSION

Large-Eddy Simulation of Turbulent Combustion

The Large-Eddy Laminar Flamelet Model (LELFM) for predicting filtered chemical species concentrations in Large-Eddy Simulations (LES) of non-premixed turbulent reacting flows has been demonstrated to be quite accurate for higher Damköhler numbers.[2,3] The model is based on flamelet theory and uses presumed forms for both the dissipation rate and subgrid-scale (SGS) probability density function of a conserved scalar. Inputs to the model are the thermochemistry tables, the filtered scalar, and its SGS variance and filtered dissipation rate.

Current research focuses on (1) evaluating the overall model by comparing simulation results with the laboratory data of Bilger et al.,[4] and on (2) evaluating models for the filtered dissipation rate and SGS variance (the "sub-models") by filtering data from 512^3-point Direct Numerical Simulations (DNS) of a single-step, isothermal reaction developing in the isotropic, incompressible, decaying turbulence field of Comte-Bellot and Corrsin.[1] In order to proceed with the evaluation of the scalar mixing and chemistry data, it is first necessary to demonstrate that the DNS of the velocity field matches the laboratory flow.

In the laboratory experiment, nearly isotropic turbulence decays downstream of a grid of spacing M oriented normal to a uniform, steady flow. Statistical data were collected at downstream locations $x/M = 42$, 98, and 171. The Reynolds number based on the Taylor microscale and the rms velocity at the first station is 71.6. The numerical simulations are performed by a pseudo-spectral code using a 512^3-point periodic domain considered to be moving with the mean flow, and are in dimensional units (centimeters and seconds) with no scaling between the laboratory and simulation parameters. Simulations are initialized to match the laboratory kinetic energy spectrum at $x/M = 42$. In the computer code, Fourier pseudo-spectral methods are used to approximate spatial derivatives, and a second-order Adams-Bashforth scheme with projection is used for time-stepping.

Figure 1 shows that the simulation and laboratory velocity spectra match almost perfectly at $x/M = 98$ and $x/M = 171$. The simulation not only accurately predicts the energy spectra, but other quantities such as the total dissipation rate, the Taylor microscale, λ, and the rms velocity, u_{rms}, the latter two of which are shown in Fig. 2. This is the first simulation of decaying isotropic turbulence verified to be accurate by laboratory data. For an accurate simulation, a much larger computational domain is required than previously thought, with the key criteria being that the kinetic energy transfer spectrum be negligible at the largest length scale in the simulation.

In order to test the LES models for the SGS variance, the filtered dissipation rate, and the average species concentrations, a scalar field consisting of a large blob of fuel was superimposed on the velocity field and allowed to evolve. The DNS scalar fields were then filtered onto a 32^3 point mesh to form simulated LES fields. With this method, the LES model predictions can be compared directly with the exact values from the DNS. Fig. 3 shows the performance of a model for the SGS variance in which it is assumed that

the SGS variance is related to the resolved-scale variance through a coefficient that is a function of time but not of space. The model predicts the correct magnitude, on average, but there is considerable scatter. Fig. 4 shows the results for the average product concentration when the models for the SGS-variance and filtered dissipation rate are used in the LELFM. The line denoted "ee" shows the model prediction when the exact (DNS) values are used for the SGS-variance and filtered dissipation rate; "mm" indicates that sub-models were used for these quantities. Despite the scatter evident in Fig. 3, and comparable errors in models for the filtered dissipation rate, LELFM is quite accurate.

The next steps in this research are: (1) to complete the evaluation of additional models for the SGS-variance and filtered dissipation rate using the existing DNS data, (2) to evaluate results of actual large-eddy simulations of the flow of Comte-Bellot and Corrsin, and (3) to perform a three-way comparison between reacting scalar mixing layer laboratory data of Bilger et al.,[4] a $512 \times 512 \times 1024$-point DNS of a similar flow, and large-eddy simulations of the same flow as the DNS. Several LES of the flow have been completed and the DNS is in progress.

Differentially Diffusing Scalars in Turbulence

Following our earlier work to account of differential diffusion in turbulent mixing,[5] our new work refers to reacting scalars (one-step chemistry scheme) in turbulent flows.[6] The direct numerical simulations refer to isotropic, decaying and incompressible turbulence. Fig. 5 shows the ratio of the average fuel reaction rates with ($\langle\widetilde{w}_F\rangle$) and without ($\langle w_F\rangle$) differential diffusion for identical chemistry rates but different Reynolds numbers, Re. The initial values of Re in the study vary between 33 and 326. The figure demonstrates that, due to the separation of the large and small scales, the influence of differential diffusion decreases with increasing Re-values.

In a recent paper, Pitsch and Peters,[7] used flamelet (FL) arguments to derive a new model that accounts for differential diffusion in reacting turbulence. The model equations refer to the average species mass fractions conditioned on the mixture fraction. (The formalism is set up such that differential diffusion does not act on the conditioning variable.) We have shown that the same model equations can be also derived from the Conditional Moment Closure (CMC) equations[8] by neglecting the terms that account for the conditional fluctuations and refer, therefore, to this model by the acronym CMC-FL. Fig. 6 shows the same ratio as Fig. 1, but instead of using DNS data, the reaction rates have been computed from the CMC-FL model. The comparison shows that CMC-FL does not account for the fundamental tendency that the influence of molecular effects on averages gradually disappears with increasing values of Re. Figs. 5 and 6 show, furthermore, that CMC-FL overestimates the influence of differential diffusion on the reaction rates.

The investigations demonstrate that the key to the modeling of differential diffusion is the modeling of the terms due to the conditional fluctuations. Once these terms have been neglected, differential diffusion scales with the ratio of the diffusion coefficients, as in laminar flow. The proper turbulent scaling is "residing" in the terms that have been neglected in the modeling.

Figure 7 compares the average fuel reaction rate versus time as computed from the DNS data with and without differential diffusion ($\langle\widetilde{w}_F\rangle_{DNS}$, $\langle w_F\rangle_{DNS}$), as computed from CMC-FL ($\langle\widetilde{w}_F\rangle_{CMC-FL}$) and as computed from the CMC equation with the conditional terms the taken into account ($\langle\widetilde{w}_F\rangle_{CMCA}$). The figure demonstrates the key importance of the conditional fluctuations.

Figure 8 shows the DNS data for the average fuel mass fraction conditioned on unity value of the mixture fraction ($\widetilde{Q}_F(\eta = 1, t)$) against time for different Reynolds numbers. (The $\widetilde{Q}_F(\eta = 1, t) = 0$, $\widetilde{Q}_F(\eta = 1, t) = 1$ assumption is an inherent part of the modeling.) The figure demonstrates that this modeling assumption improves with increasing Re values. The curve without differential diffusion, $Q_F(\eta = 1, t)$, is also shown for comparison.

Presently we are working on the modeling of the terms accounting for the conditional fluctuations. We believe that the DNS experiments will enable us to build the new modeling into RANS and LES computations.

---

[1] G. Comte-Bellot and S. Corrsin, "Simple Eulerian time correlation of full and narrow-band velocity signals in grid-generated, 'isotropic' turbulence," J. Fluid Mech. **48**, 273 (1971).

[2] A. W. Cook and J. J. Riley, "Subgrid-scale modeling for turbulent, reacting flows," Combust. Flame **112**, 593 (1997).

[3] A. W. Cook, J. J. Riley, and G. Kosály, "A laminar flamelet approach to subgrid-scale chemistry in turbulent flows," Combust. Flame **109**, 332 (1997).

[4] R. W. Bilger, L. R. Saetran, and L. V. Krishnamoorthy, "Reaction in a scalar mixing layer," J. Fluid Mech. **233**, 211 (1991).

[5] V. Nilsen and G. Kosály, "Differentially diffusing scalars in turbulence," Phys. Fluids **9**, 3386 (1997).

[6] V. Nilsen and G. Kosàly, "Differential diffusion in turbulent reacting flows," Submitted to Combust. Flame (1998).
[7] H. Pitsch and N. Peters, "A consistent flamelet formulation for non-premixed combustion considering differential diffusion effects," Accepted by Combust. Flame (1997).
[8] R. W. Bilger, "Conditional moment closure for turbulent reacting flow," Phys. Fluids A 5, 436 (1993).

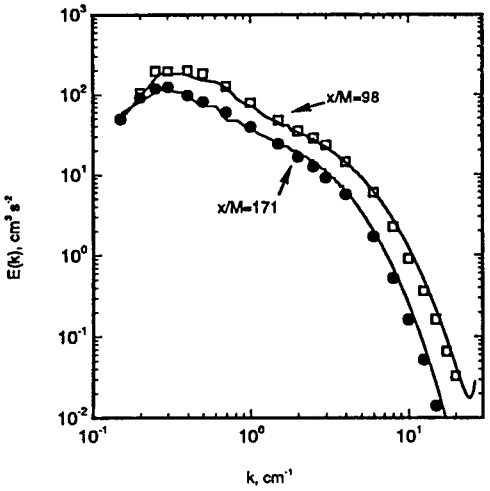

FIG. 1. Kinetic energy spectra for the flow of Comte-Bellot and Corrsin[1]. Symbols are from lab data and lines from a 512^3 DNS. The flow was initialized with the laboratory spectrum at $x/M = 42$

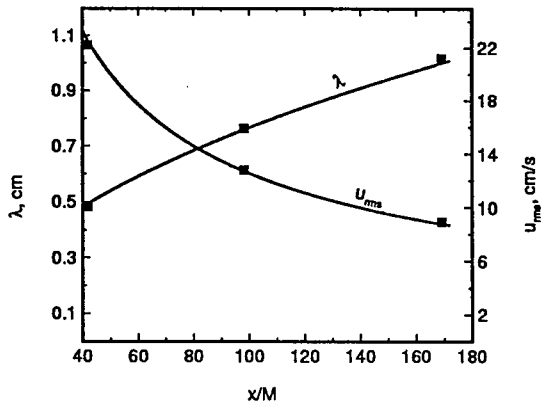

FIG. 2. Taylor length scale, λ, and the rms velocity, u_{rms}, for the flow of Comte-Bellot and Corrsin[1]. Symbols are from lab data and lines from a 512^3 DNS.

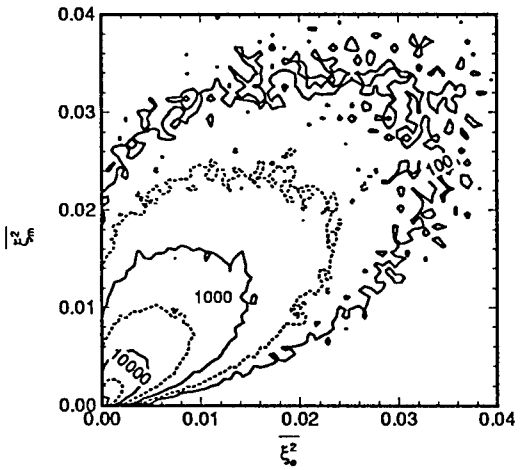

FIG. 3. Joint PDF with the exact SGS variance (from DNS) on the horizontal and a model prediction on the vertical. In this particular model, it is assumed that the SGS-variance can be related to the resolved-scale variance by a coefficient that is a function of time but not of space.

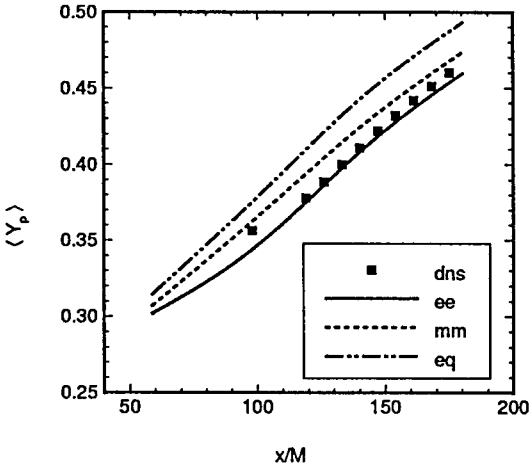

FIG. 4. Spatial average of the filtered product mass fraction from the reaction fuel + oxidizer → product. For curve ee, the exact (from DNS) SGS variance and filtered dissipation rate were used in the LELFM; for curve mm, modeled values were used. eq indicates the equilibrium chemistry limit and dns denotes the DNS results.

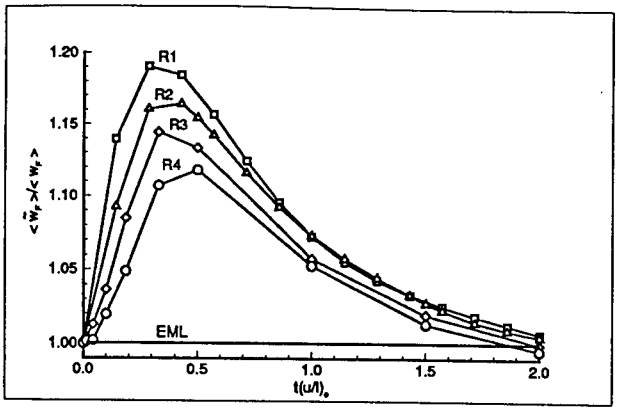

FIG. 5. $\langle \widetilde{w}_F \rangle / \langle w_F \rangle$ versus $t(u'/\ell)_o$ for the R1, R2, R3 and R4 velocity fields ($Da_o \equiv A(\ell/u')_o = 8$, $\mathcal{D}_F/\nu = 2$). The "tilde" indicates the presence of differential diffusion. The absence of the "tilde" signifies that the coefficients of molecular diffusion are identical.

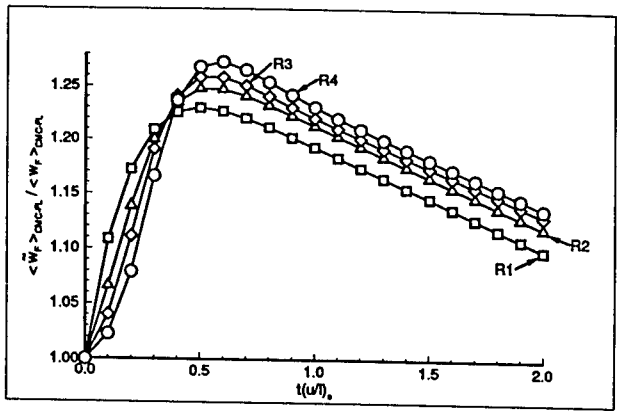

FIG. 6. $\langle \widetilde{w}_F \rangle / \langle w_F \rangle$ versus $t(u'/\ell)_o$ as computed from CMC-FL for the R1 ($-\square-$), R2 ($-\triangle-$), R3 ($-\diamond-$) and R4 ($-\ \bigcirc\ -$) velocity fields ($Da_o = 8$, $\mathcal{D}_F/\nu = 2$).

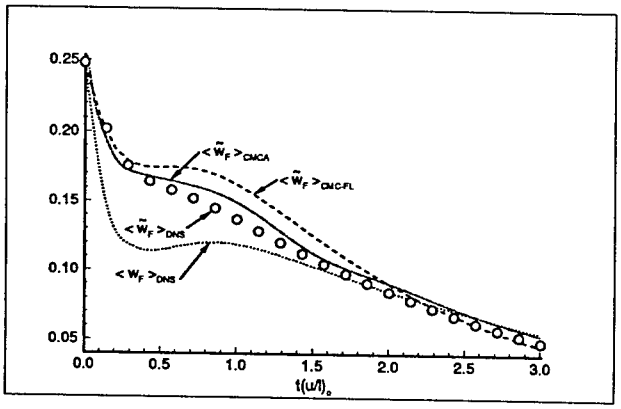

FIG. 7. The average consumption rate of fuel versus $t(u'/\ell)_o$ for the R1 velocity field ($Da_o = 8, \mathcal{D}_F/\nu = 4$). The $- \cdots -$ curve ($\langle \widetilde{w}_F \rangle_{CMCA}$) refers to the solution of Eqs. (5a,b) with the unclosed terms taken from the DNS. Also included is the CMC-FL predictions (dashed curve) and DNS values of $\langle \widetilde{w}_F \rangle$ (circles) as well as $\langle w_F \rangle$ ($\mathcal{D}_F/\nu = 1$) represented by the dotted curve.

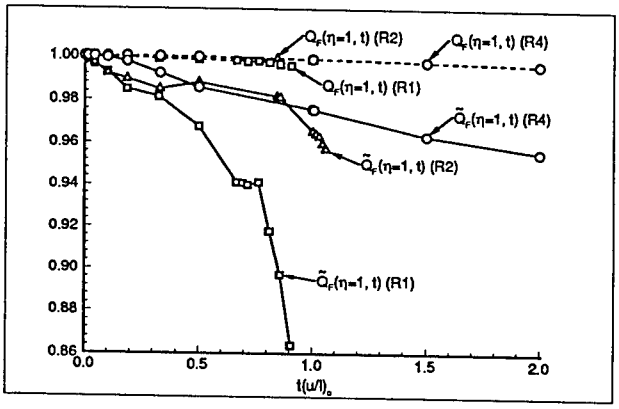

FIG. 8. The average fuel mass fraction conditioned on $Z = 1$ versus $t(u'/\ell)_o$ for the R1 ($-\square-$), R2 ($-\triangle-$) and R4 ($-\ \bigcirc\ -$) velocity fields. The solid and dashed curves refer to the $\mathcal{D}_F = 4\nu$ and $\mathcal{D}_F = \nu$ case, respectively ($Da_o = 8$). Here $Z = 1$ has been assigned to computational grid points if $1 - \Delta Z \leq Z \leq 1$, where $\Delta Z = 1.0 * 10^{-6}$.

STUDIES ON HIGH PRESSURE AND UNSTEADY FLAME PHENOMENA

(AFOSR Grant No. F49620-95-1-0092)

Principal Investigator: Chung K. Law

Department of Mechanical and Aerospace Engineering
Princeton University, Princeton, NJ 08544

SUMMARY/OVERVIEW

The objective of the present program is to study the structure and response of steady and unsteady laminar premixed and nonpremixed flames in reduced and elevated pressure environments through (a) non-intrusive experimentation and (b) computational simulation with detailed and reduced kinetics as well as variable transport properties. During the reporting period progress has been made in the following projects: (1) A computational study of the effects of pulsating instability on the fundamental flammability limit of rich hydrogen/air flames (2) An experimental and kinetic modeling study of propyne oxidation. (3) An experimental and computational study of the kinetics of iso-octane and n-heptane flames. (4) Development of a comprehensive reduced mechanism for methane oxidation.

TECHNICAL DISCUSSION

1. Pulsating Instability in the Fundamental Flammability Limit of Rich Hydrogen/Air Flames

In this study, simulations of a one-dimensional planar hydrogen/air flame with detailed chemistry and transport have shown that pulsating instability develops as the rich flammability limit is approached. The presence of radiative heat loss does not greatly affect the behavior of these oscillations, although it becomes important when the oscillations are strong enough for the heat loss to extinguish the flame during the weakly-burning portion of the oscillating cycle. The flammability limit determined in this manner occurs at a lower equivalence ratio than that corresponding to the extinction turning point of the steady flame. This indicates that oscillation reduces the flammability limit defined for the steady flame.

Figure 1 shows the temporal variation of the maximum flame temperature for various flames with radiative loss. It is seen that while the maximum flame temperature fluctuates, its trough value decreases with increasing frequency, but never crosses the flame temperature of the steady-state turning point flame (970 K). However, at ϕ=7.8, the maximum temperature drops below the steady turning point temperature, and the flame extinguishes. Because of the intrinsic nature of the oscillations studied herein, the period of oscillation is much longer than the corresponding characteristic flame time. In addition, it is seen from Fig. 1 that the frequency of the intrinsic oscillation decreases with increasing equivalence ratio. As a consequence, upon the relatively slow, intrinsic oscillation, the flame cannot recover once its maximum flame temperature drops below that of the steady-state turning point. Therefore pulsating instability reduces the flammability range.

A unified explanation is also put forth concerning the nature of this pulsating instability. Both a Lewis number greater than unity and a large overall activation energy through the competition of the chain-branching and chain-terminating reactions are found to be necessary conditions for oscillations to develop. Figure 2 plots the product $Ze(Le-1)$ as a function of ϕ. It is then clearly seen that, at the onset of oscillation at $\phi\sim7.4$, the Sivashinsky criterion based on constant-density model is satisfied, with $Ze(Le-1)=11.6>4(1+\sqrt{3})\approx11$.

This work is reported in Publication No. 1.

2. Experimental and Kinetic Modeling Study of Propyne Oxidation

Three different oxidation experiments were conducted on the Princeton Turbulent Flow Reactor (lean, stoichiometric, rich), with nitrogen as the diluent. Figure 3 shows the species

profiles for the stoichiometric case only. It is seen that allene is produced in the very early stage of the reaction, followed by CO, acetylene, and methane. In addition, ethylene, benzene, and 1,3-butadiene were also found to have large concentrations, although they are not shown herein.

It is noticed that the model predicts fairly well all the major species profiles, with the exception of ethane. Experimentally, propyne and allene were found to be close to, but not exactly in equilibrium at the later stages of oxidation. According to the model prediction, allene is formed mainly by the direct isomerization of propyne. The departure from equilibrium is due to perturbations from the reaction $pC_3H_4 + H = CH_3 + C_2H_2$ (R1), and $pC_3H_4 + OH = C_3H_3 + H_2O$ causing rapid propyne consumption.

Allene is consumed mainly through H abstraction by OH. Acetylene and the methyl radical are almost entirely formed by reaction (R1). Methane is predominately formed by H abstraction by CH_3 from propyne and allene. Ethylene is formed from $pC_3H_4 + O = C_2H_4 + CO$ and from the chemically activated reaction $aC_3H_4 + O \rightarrow CH_2COCH_2^*$ = cyclopropenone* $\rightarrow C_2H_4 + CO$, where * denotes a vibrationally excited adduct. Benzene concentration is slightly overpredicted by the model and its production is due to the reaction $C_3H_3 + C_3H_3$ = benzene. CO is produced from the formyl radical via thermal decomposition and its reaction with molecular oxygen. The source of the formyl radical is mainly through the reaction $C_3H_3 + O_2 = HCO + CH_2CO$.

Laminar flame speeds for propyne/(18%O_2 in N_2) mixtures were also obtained over the equivalence ratio range of 0.7 to 1.7, at atmospheric pressure and room temperature. Figure 4 presents the linearly- and nonlinearly-extrapolated flame speeds. The present kinetic model predicts reasonably well the shape of the flame speed curve, but it over-predicts the experimental data at lean to stoichiometric equivalence ratios. Based on the model, the consumption of propyne in laminar premixed flame is mainly due to reaction (R1), followed by the isomerization of propyne to allene. Unlike the results obtained in the flow reactor study, propyne and allene concentrations were not close to equilibrium in flames. Based on sensitivity analysis, the flame speed was most influenced by reactions of hydrogen and the C_1 hydrocarbon species. There are only a few reactions of propyne and propargyl which influence flame speed under all stoichiometric conditions. Within the uncertainty limits of the rate constants, it is not possible to bring the predicted flame speeds to a better agreement with the experimental data for the lean to stoichiometric conditions (Fig. 4).

This work is reported in Publication No. 2.

3. Laminar Flame Speeds and Oxidation Kinetics of iso-Octane/Air and n-Heptane/Air Flames

Figures 5 and 6 compare the linearly- and nonlinearly-extrapolated flame speeds for both n-heptane/air and iso-octane/air mixtures respectively. Flame speeds for n-heptane were observed to be greater than those of iso-octane throughout the entire range of equivalence ratios, with the difference being around 4 cm/s for lean mixtures, reaching a maximum of about 5 cm/s for near-stoichiometric mixtures, and decreasing to about 2 cm/s at the very rich conditions.

Figures 5 and 6 also compare the present laminar flame speeds with the Bunsen flame results of Gibbs and Calcote and Heimel and Weast, and with the tube data of Gerstein *et al.*. It is noted that there is substantial disagreement in the flame speed data obtained from these previous experiments. Figures 5 and 6 also show that the previously determined flame speeds can differ quite substantially when compared to the present stretch-compensated flame speed data. Wall effects, including heat loss and radical scavenging, may be one of the reasons which account for the disagreement in flame speed data in the study of Gerstein and co-workers. However, their results are further complicated by the notable influence that stretch coupled with mixture nonequidiffusion has on the measured flame speeds, which is also prevalent in the two Bunsen flame experiments. The two sets of Bunsen flame data are not close and even exhibit opposite trends for n-heptane flame speeds. The technique used by Gibbs and Calcote for the determination of flame speeds was well documented and exhibits tendencies which are supported by flame stretch theory, although the data of Heimel and Weast seem to agree better with the present flame speeds.

Predictions, using a detailed kinetic model based on the works of Held *et al.* and of Curran and Westbrook, agreed quite well with the experimental data, especially for lean mixtures, while yielding somewhat lower values for stoichiometric to rich mixtures. The model accurately predicted the fuel decay profile as well as those of propene and iso-butene, which are the two major intermediates formed initially at flow reactor conditions. The present analysis suggests that the major high temperature reaction pathways proposed by Curran and Westbrook accurately

describe the high temperature oxidation of iso-octane, and indicates that the development of a comprehensive model requires additional studies on the reaction kinetics of propene and iso-butene.

This work is reported in Publication No. 3.

4. An Augmented Reduced Mechanism for Methane Oxidation

Recognizing the anticipated increase in the computational capability in the foreseeable future, the objective of the present study was to develop augmented reduced mechanisms, consisting of ten to twenty lumped reactions and the corresponding number of species, which are suitable for implementation in the computational simulation of complex flame phenomena and practical combustor performance. These augmented reduced mechanisms are simpler than the detailed mechanisms but more complete than the present four- or five-step reduced mechanisms. As such they are expected to be sufficiently comprehensive to describe the various possible combustion phenomena of interest, with extensive thermodynamic parametric variations.

A comprehensive augmented reduced mechanism, consisting of 16 species and 12 lumped reaction steps, has thus been developed for methane oxidation. Subsequently, responses of various combustion phenomena, including perfectly-stirred reactor responses, auto-/shock tube ignition delay times, laminar flame speeds, and ignition-extinction limits of counterflowing system, are computed with detailed and the 12-step augmented reduced mechanisms. Comparison demonstrates good to excellent performance of the reduced mechanism in predicting this wide range of combustion phenomena at various temperatures, pressures, and compositions.

Figure 7 compares the performance of the 4-, 10-, and 12-step mechanisms in predicting the auto-ignition delay times of atmospheric, stoichiometric methane/air mixtures, at various initial temperatures. It is seen that the 4-step mechanism is totally inadequate in predicting the ignition delay. Subsequent relaxation of QSS species leads to significant improvements in the descriptive capability of the corresponding reduced mechanism. The 12-step mechanism substantially reduces the discrepancy.

Figure 8 presents calculated laminar flame speeds over equivalence ratios from 0.7 to 1.3, with pressure ranging from 0.25 to 20 atm. The agreement is generally quite good. For the pressure range of 0.25 to 1 atm, the discrepancy is within 4%. With increasing pressure, however, the performance of the 12-step reduced mechanism improves significantly.

This work is reported in Publication No. 4.

MAJOR PUBLICATIONS (May, 1997 – April, 1998)

1. "Pulsating Instability in Near-Limit Propagation of Rich Hydrogen/Air Flames," by E. W. Christiansen, C. J. Sung, and C. K. Law, *Twenty-Seventh Symposium (International) on Combustion* , in press.
2. "An Experimental and Kinetic Modeling Study of Propyne Oxidation," by S. G. Davis, C. K. Law and H. Wang, *Twenty-Seventh Symposium (International) on Combustion* , in press.
3. "Laminar Flame Speed and Oxidation Kinetics of iso-Octane/Air and n/Heptane/Air Flames," by S. G Davis and C. K. Law, *Twenty-Seventh Symposium (International) on Combustion* , in press.
4. "An Augmented Reduced Mechanism for Methane Oxidation with Comprehensive Global Parametric Validation," by C. J. Sung, C. K. Law and J.-Y. Chen, *Twenty-Seventh Symposium (International) on Combustion* , in press.
5. "Structure and Propagation of Premixed Flame in Nozzle-Generated Counterflow," by B. H. Chao, F. N. Egolfopoulos and C. K. Law, *Combustion and Flame*, Vol. 109, pp. 620-638 (1997).
6. "Ignition of Oscillatory Counterflowing Nonpremixed Hydrogen against Heated Air," by C. J. Sung and C. K. Law, *Combustion Science and Technology* **129**, 347-360 (1997).
7. "The Role of Chain Mechanisms in Some Fundamental Combustion Phenomena," by C. K. Law, *Physical and Chemical Aspects of Combustion: A Tribute to Irvin Glassman, Combustion Science and Technology Book Series,* Vol. 4 (Eds.: F. L. Dryer and R. F. Sawyer), Gordon and Breach, pp. 3-27 (1997).
8. "On the Aerodynamics of Flame Surfaces," by C. K. Law, C. J. Sung and C. J. Sun, Annual Review of Heat Transfer, Vol. VIII, (Ed.: C.-L.Tien), Begell House, pp. 93-151 (1997).

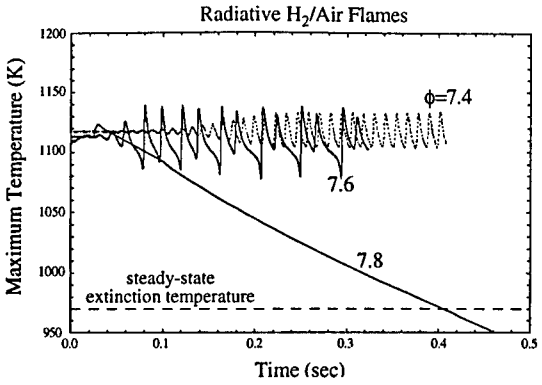

Figure 1

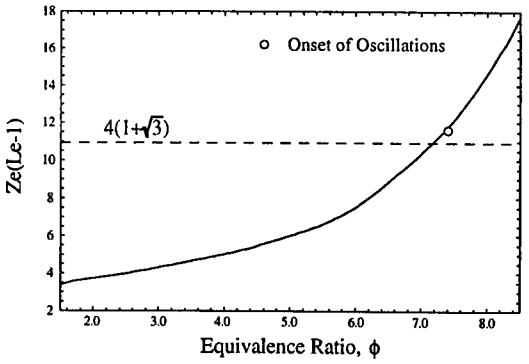

Figure 2

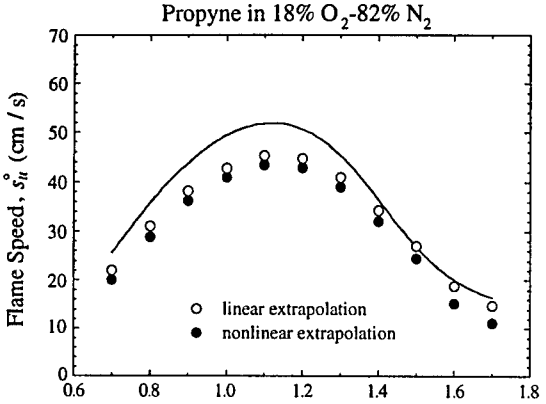

Figure 3

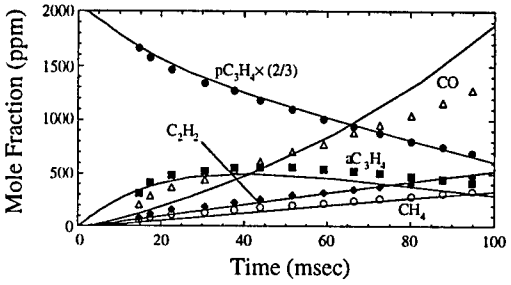

Figure 4

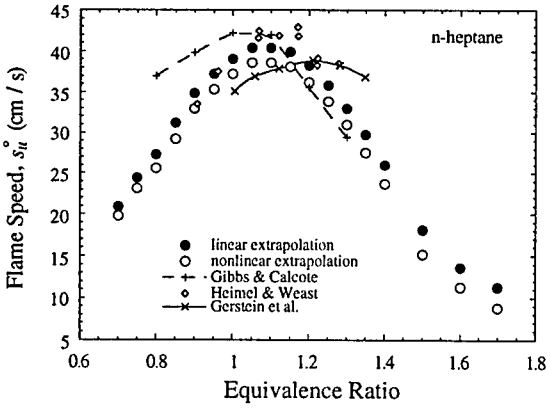

Figure 5

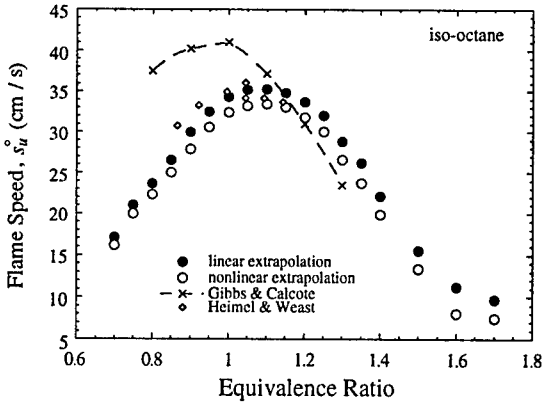

Figure 6

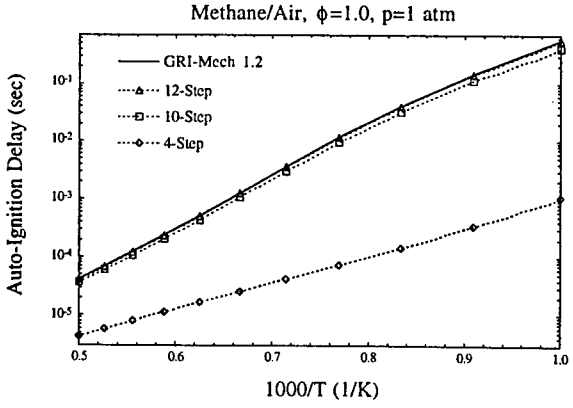

Figure 7

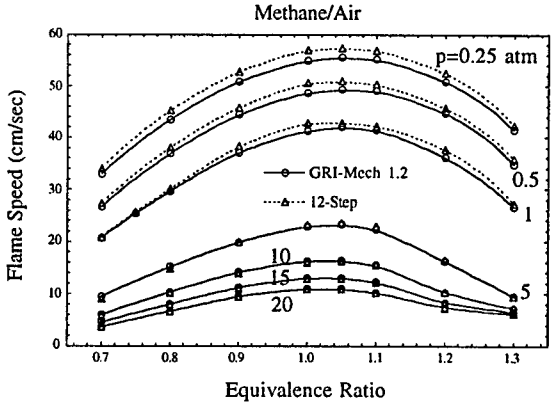

Figure 8

MULTI-SCALAR IMAGING IN TURBULENT NONPREMIXED FLAMES

AFOSR Grant No. 97-1-0096

Principle Investigator: Marshall B. Long

Yale University
Department of Mechanical Engineering and Center for Laser Diagnostics
New Haven, Connecticut 06520-8284

SUMMARY/OVERVIEW

The present research deals with improving confidence in the two-scalar mixture fraction formulation based on fuel concentration and enthalpy currently applied in turbulent nonpremixed flames. Adding a third scalar measurement to the required fuel Raman and Rayleigh scattering can reduce uncertainty around the stoichiometric contour, where fuel concentration approaches zero and the Rayleigh signal remains relatively constant. Nitrogen concentration from Raman scattering provides a simultaneous, independent, passive scalar, which has been used to modify the way functional dependences are assigned for terms appearing in the iterative calculation of mixture fraction.[1]

TECHNICAL DISCUSSION

Within the last year, a series of experiments has been focused on investigating multi-scalar measurements in turbulent nonpremixed flames. A major goal in studying such flames is to provide quantitative images of mixture fraction ξ, defined as the mass fraction of all atoms originating from the fuel stream. This allows calculation of axial and radial gradient information, and in particular the scalar dissipation χ, which controls the rate of molecular mixing. Extensive single-point measurements have been made[2], however scalar dissipation cannot be extracted because of the lack of spatial gradient data.

One method for constructing a conserved scalar suitable for imaging experiments in reacting flows has been through the simultaneous measurement of temperature (T) and fuel concentration.[3] The conserved scalar β, is defined based on fuel mass fraction (Y_F) and enthalpy and takes the form:

$$\beta = Y_F + c_p \mathrm{T}/Q \tag{1}$$

where Q is the lower heat of combustion and c_p is the specific heat at constant pressure. This can be cast into an expression for mixture fraction:

$$\xi^{FT} \equiv \frac{\beta - \beta_{air}}{\beta_{fuel} - \beta_{air}} = \frac{Y_F + c_p\left(\mathrm{T} - \mathrm{T}_{air}\right)/Q}{Y_{F,fuel} + c_p\left(\mathrm{T}_{fuel} - \mathrm{T}_{air}\right)/Q} \tag{2}$$

This two-scalar approach, which assumes unity Lewis number and idealized one-step reaction between fuel and oxidizer, relates to the measured signals through:

$$\xi^{FT} = \frac{\mathrm{C}_1 \sigma}{W\,Ra} Rm + \mathrm{C}_2 \frac{c_p}{Q}\left(\frac{\sigma}{Ra} - \mathrm{T}_{air}\right) \tag{3}$$

where Rm is the measured fuel Raman scattering and Ra is the Rayleigh scattering. The parameter σ, which is proportional to the Rayleigh cross section, the mixture molecular weight W, and the specific heat c_p, are dependent on the mixture fraction. Strained counterflow flame calculations provide appropriate functional forms for these parameters which are incorporated into an iterative

scheme for determining ξ. The remaining constants C_1 and C_2 must be determined from calibration experiments.

This approach has been applied successfully[4-6], however there is a need to improve the certainty in the mixture fraction calculation around the stoichiometric contour. At this location, the fuel concentration approaches zero and the Rayleigh signal remains nearly constant. The present work has examined Raman scattering from nitrogen as a third scalar measurement to improve confidence in the two-scalar mixture fraction calculation.

In order for the N_2 Raman channel to provide an independent conserved scalar with sufficient signal variation between regions of pure air and pure fuel, experiments were performed in which the fuel stream contained no nitrogen. Assuming no significant nitrogen consumption occurs during reaction, we can write the conserved scalar in terms of nitrogen mass fraction:

$$\beta^{N_2} \equiv Y_{N_2} \tag{4}$$

with the mixture fraction:

$$\xi^{N_2} = 1 - \frac{Y_{N_2}}{Y_{N_2,\text{air}}} = 1 - \frac{C_3\,\sigma}{W\,Ra} Rm_{N_2} \tag{5}$$

where Rm_{N_2} is the nitrogen Raman signal, and C_3 is an additional calibration constant. This formulation requires measurement of the temperature and nitrogen concentration, and thus, represents an additional two-scalar approach. The fuel mixture (25% methane, 59% argon, and 16% oxygen by volume), has a stoichiometric mixture fraction ξ_s=0.41, putting the reaction zone well inside the shear layer.

Simultaneous planar Rayleigh, fuel Raman, and nitrogen Raman images have been collected in experiments using three cameras and a single laser. Figure 1 shows the experimental facility, which is described in detail elsewhere and summarized here.[1] A flashlamp-pumped dye laser is employed in an intracavity configuration to generate single-shot energies up to 4.7 J at 532 nm. The beam is focused into a sheet over a 6.1 mm diameter piloted burner. Scattered light is collected on both sides of the flame by low *f#* camera lenses oriented perpendicular to the laser sheet. The Rayleigh scattering and fuel Raman scattering are collected along the same optical path and divided with a 50/50 pellicle beam splitter, while the weaker nitrogen Raman scattering is collected along the opposite optical path. Image intensifiers are lens-coupled to liquid-cooled CCD cameras and isolated with appropriate interference filters. The spatial resolution for this setup has been measured by imaging a uniformly illuminated 25 μm wire. The resolutions reported are approximately 2-4 times the estimated Kolmogorov scale, which should be sufficient to capture much of the scalar dissipation.

Figure 2 shows line plots of mixture fraction from a laminar flame (Re=1600) at a location 15 nozzle diameters downstream (*D*=6.1 mm). Two curves are shown for ξ^{FT}, which differ in the parameterization of the mixture fraction dependent terms appearing in Eqn. 3 (i.e. σ, W, c_p). The curve marked "No lean correction" uses flame calculation terms parameterized by "actual" mixture fraction determined from the Bilger formula[7].

Figure 3 shows that this approach incorporates a departure of ξ^{FT} from the more rigorous formulation, as indicated by strained laminar flame calculations (strain rate=100 s^{-1}). Deviation from one-step chemistry (i.e. loss of parent fuel to intermediate species) is compensated in the curve marked ξ^{FT}_{cor} by using a weighting term involving reactivity[8]. The curve for ξ^{N_2} exhibits little deviation from the actual mixture fraction. By assigning functional dependences based on the predicted ξ^{FT} from flame calculations, the ξ^{FT} curve shown in Fig. 2 is obtained showing improved agreement with ξ^{N_2}. The flame computations are insensitive to variations in the strain rate over the range 10-200 s^{-1}, which is expected to be representative of the scalar dissipation values measured in the turbulent flame, based on existing data in similar flames.[8,9]

Applying this technique to single-pulse imaging in turbulent nonpremixed flames provides similar results, although the N_2 Raman signal is affected by noise, especially in regions of high mixture fraction where there is little nitrogen. Figure 4 shows images taken 25*D* downstream from a *Re*=15,000 turbulent flame; the Raman images have been contour smoothed.[10] Qualitatively, the scalar dissipation fields, χ (defined as $\chi \equiv 2\mathcal{D}\nabla\xi\cdot\nabla\xi$, where $\mathcal{D}$ is the diffusivity), appear similar, revealing the same main structural features, with significant scalar dissipation apparent along the edge of the main jet. The position of the stoichiometric mixture fraction contour is highlighted (black lines) in these images.

In summary, recent experiments measuring nitrogen-temperature mixture fraction have served as a guide for correcting the fuel-temperature mixture fraction for values around and lean of stoichiometric. It has been shown that parameterizing specific heat, molecular weight, and Rayleigh cross section as a function of ξ^{FT} predicted from counterflow flame calculations, rather than the actual mixture fraction, improves the performance of this two-scalar approach. Under turbulent conditions (*Re*=15,000), the two approaches reveal differences close to the centerline, most likely a result of noise limitations of the nitrogen Raman signal. This work increases confidence in employing ξ^{FT} for mixture fraction determination, which remains the most attractive approach because of its superior signal-to-noise characteristics. Further details of the results are documented in the paper accepted to the Twenty-Seventh Symposium on Combustion, which will be published later this year.[1]

REFERENCES

1. Fielding, J., Schaffer, A.M., Long, M.B.,*Twenty-Seventh Symposium (International) on Combustion*, (in press) The Combustion Institute, Pittsburgh, PA, 1998.
2. Masri, A.R., Dibble, R.W., and Barlow, R.S., *Prog. Energy Combust. Sci.* 22:307-362 (1996).
3. Stårner, S.H., Bilger, R.W., Dibble, R.W., and Barlow, R.S., *Combust. Sci. and Tech.* 86:223-236 (1992).
4. Stårner, S.H., Bilger, R.W., Lyons, K.M., Frank, J.H., and Long, M.B., *Combust. Flame.* 99:347-354 (1994).
5. Frank, J.H., Lyons, K.M., Marran, D.F., Long, M.B., Stårner, S.H., and Bilger, R.W., *Twenty-Fifth Symposium (International) on Combustion*, The Combustion Institute, Pittsburgh, PA, 1994, pp. 1159-1166.
6. Long, M.B., Frank, J.H., Lyons, K.M., Marran, D.F., and Stårner, S.H., *Ber. Bunsenges. Phys. Chem.*, 97:1555-1559 (1993).
7. Bilger, R.W., Stårner, S.H., and Kee, R.J., *Comb. and Flame*, 80:135-149 (1990).
8. Stårner, S.H., Bilger, R.W., Long, M.B., Frank, J.H., and Marran, D.F., *Combust. Sci. Tech.* 129:141-163 (1997).
9. Kelman, J.B., and Masri, A.R., *Combust. Sci. and Tech.* 129:17-55 (1997).
10. Stårner, S.H., Bilger, R.W., and Long, M.B., *Combust. Sci. and Tech.* 107:195-203 (1995).

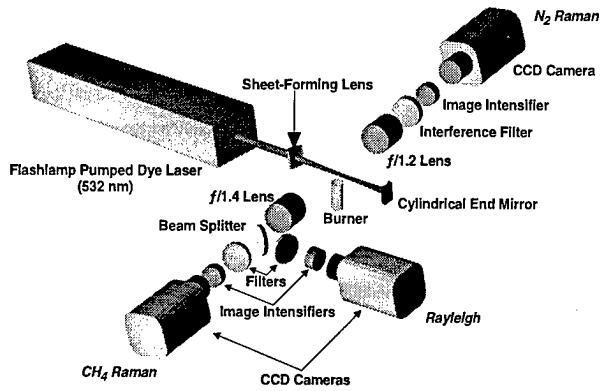

Figure 1. Schematic of the three-scalar intracavity turbulent flame imaging experiment.

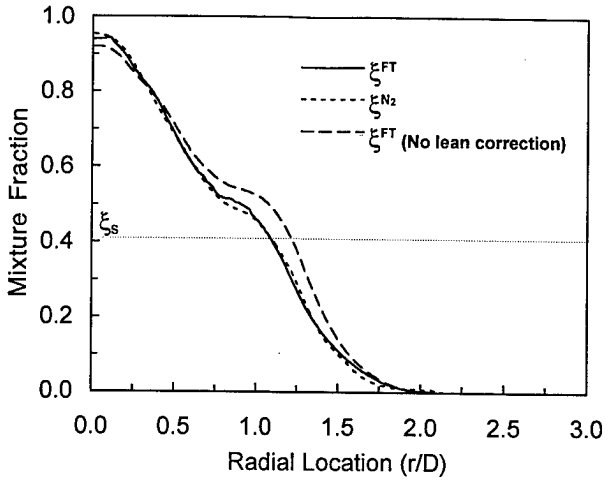

Figure 2. Radial variation of mixture fraction calculated from fuel-temperature (solid line) and nitrogen-temperature (short dashes) two-scalar approaches 15*D* downstream in a laminar flame (Re=1600). ξ^{FT} overpredicts the fuel-temperature mixture fraction in regions around and lean of stoichiometric (long dashes).

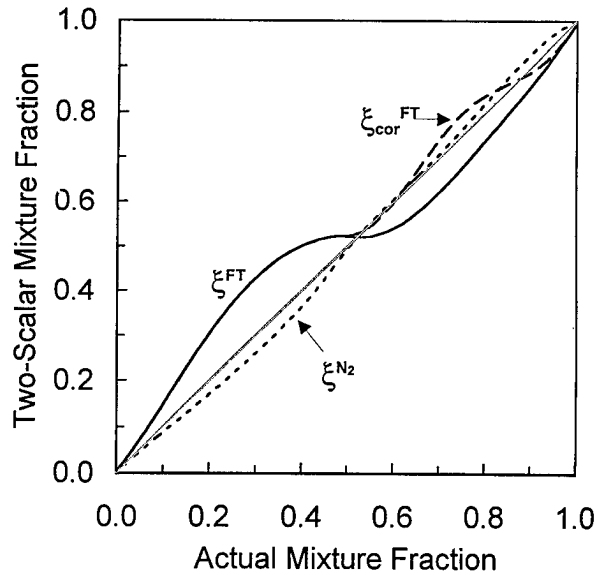

Figure 3. Mixture fraction calculated from strained laminar flame calculations (100 s^{-1}) using the fuel-temperature (solid line) and nitrogen-temperature (short dashes) two-scalar approaches plotted against mixture fraction calculated using the formula proposed by Bilger [7]. The effect of fuel correction on ξ^{FT} is shown (long dashes).

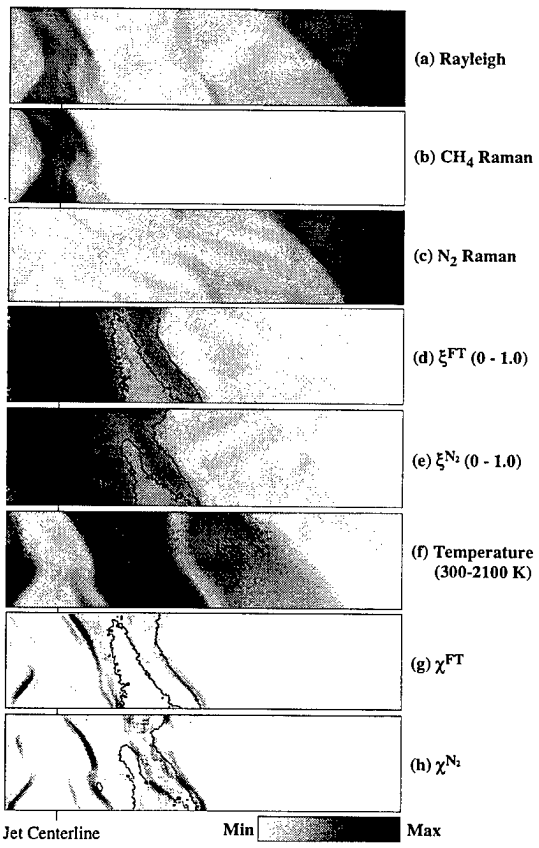

Figure 4. Instantaneous (a) Rayleigh, (b) CH_4 Raman, (c) N_2 Raman images of the turbulent flame taken 25 jet diameters (*D*=6.1 mm) downstream. Also shown are the computed mixture fraction images (d) ξ^{FT}, (e) ξ^{N_2}, (f) temperature, and scalar dissipation images (g) χ^{FT}, and (h) χ^{N_2}. Each image size is $4.3D \times 1D$.

MODELLING MIXING AND REACTION IN TURBULENT COMBUSTION

AFOSR Grant F-49620-97-1-0126
Principal Investigator: S. B. Pope

Mechanical & Aerospace Engineering
Cornell University
Ithaca, NY 14853

SUMMARY

Computer modelling of performance is an integral part of the design methodology for aerospace propulsion systems. In order to make calculations of the flow and reactions inside a combustion chamber, it is necessary to have a turbulent-combustion model. Increasingly, such models are based on PDF methods, in which the turbulent fluctuations are fully represented in terms of the joint probability density function (PDF) of the flow and thermochemical properties. The objectives of this research are to obtain numerically-accurate solutions to the PDF model equations, and to assess the physical accuracy of different sub-models by comparing PDF calculations with reliable experimental data.

RECENT ADVANCES

The significant advances in PDF modelling made recently at Cornell are:

1. the quantification and reduction of the numerical errors in the particle/mesh methods used to solve the PDF equations (Xu & Pope 1998)

2. the implementation and assessment within PDF methods (Saxena & Pope 1988a,b) of the ISAT algorithm (Pope 1997) for the efficient implementation of combustion chemistry

3. the development of more advanced PDF turbulence models, and their testing in application to swirling jets (Van Slooten, Jayesh & Pope 1998, Van Slooten & Pope 1998)

4. development, implementation and demonstration of the EMST mixing model, which overcomes serious deficiencies in previous models (Subramaniam & Pope 1997, 1998, Masri, Subramaniam & Pope 1996).

The first three of these topics are described in the following sections.

NUMERICAL ACCURACY

Every numerical method involves numerical errors. In order to make accurate model calculations, and in order to assess the attributes of different physical sub-models, it is essential that the numerical errors are below tolerable limits.

In time-accurate CFD methods there are time-stepping errors and spatial truncation errors. For second-order accurate methods, these errors are of order Δt^2 and Δx^2, respectively, where Δt

and Δx are the time step and the characteristic grid size. These same errors exist in particle/mesh methods; but in addition there are errors related to the average number of particles per cell, N. Comprehensive tests performed by Xu & Pope (1998) show that the time-stepping errors in the particle/mesh method are negligible, and that the remaining errors can be expressed as

$$\varepsilon = a\Delta x^2 + \frac{b}{N} + \frac{c\xi}{\sqrt{NM}}. \tag{1}$$

The last term is the *statistical error*. The coefficient c is the "standard error"; ξ is a standardized random variable ($\langle\xi\rangle = 0$, $\langle\xi^2\rangle = 1$); and M denotes the effective number of independent calculations. (Usually time averaging is used to reduce the statistical error: M is proportional to the number of time scales over which time averaging is performed.) The contribution with coefficient b represents the *bias*. This is a deterministic error due to N being finite, and it is not reduced by time averaging. The term with coefficient a is the spatial *truncation error*.

The tests performed verify this behavior of the error and hence demonstrate the convergence of the scheme, i.e., ε tends to zero as Δx tends to zero and N tends to infinity. The rate of convergence is quantified by "measuring" the coefficients, a, b and c.

An extrapolation scheme (an extension of Richardson extrapolation) has been devised to eliminate the primary truncation error and bias. Two calculations are performed, with grid spacings Δx and $\sqrt{\alpha}\,\Delta x$, and numbers of particles N and αN, where α is a constant greater than one (e.g., $\alpha = 2$). Let Q_1 and Q_2 denote the value of some quantity obtained from the two calculations. It is apparent from Eq. (1) that the truncation error and bias in Q_2 is greater than that in Q_1 by a factor α. Consequently (to leading order), the quantity

$$Q_0 \equiv \frac{\alpha Q_1 - Q_2}{\alpha - 1}, \tag{2}$$

is free of these errors.

The efficacy of the extrapolation scheme is illustrated in Fig. 1. For the test case of a nonpremixed piloted jet flame, the triangles show the numerical errors in calculations before extrapolation (i.e., in Q_1 and Q_2). The cases $A-E$ are for different choices of N, Δx and α. The circles and squares show (two variants of) the error in the extrapolated value (i.e., Q_0). Taking the turbulent kinetic energy (Fig. 1 d) cases $A - D$ as an example, before extrapolation the errors are in the range $7 - 22\%$: after extrapolation they are at most 3%.

NONPREMIXED PILOTED JET FLAMES

Saxena & Pope (1998a,b) have performed PDF calculations of nonpremixed piloted jet flames for comparison with experimental data. These computations include the EMST mixing model, and use the ISAT algorithm. A 16-species skeletal reaction mechanism for methane is used.

The most important result of this work is to demonstrate that, with the use of the ISAT algorithm, quite detailed chemistry can be included at affordable computational cost. Compared to performing a direct numerical integration of the chemical kinetic equations, the use of ISAT yields a speed-up of a factor of 40. Most importantly, only 60% of the total CPU time is consumed by chemistry computations.

SWIRLING JETS

Swirl is frequently used in combustion devices, to stabilize flames and to augment mixing. It is well known that simple turbulence models (e.g., the k-ε turbulence model) have difficulty in accurately representing swirling flows. To assess the accuracy of PDF methods for such flows, Van

Slooten & Pope (1998) made calculations of the swirling jet studied experimentally by Takahashi et al. (1991). As an example of the results, Fig. 2 shows mean circumferential velocity profiles at different axial locations for the case of 30° swirl calculated using three variants of the PDF model. These and other results show that the wavevector model (solid line)—which is exact in the limit of rapid distortions—performs quite well, and is clearly superior to the less sophisticated Simplified Langevin Model.

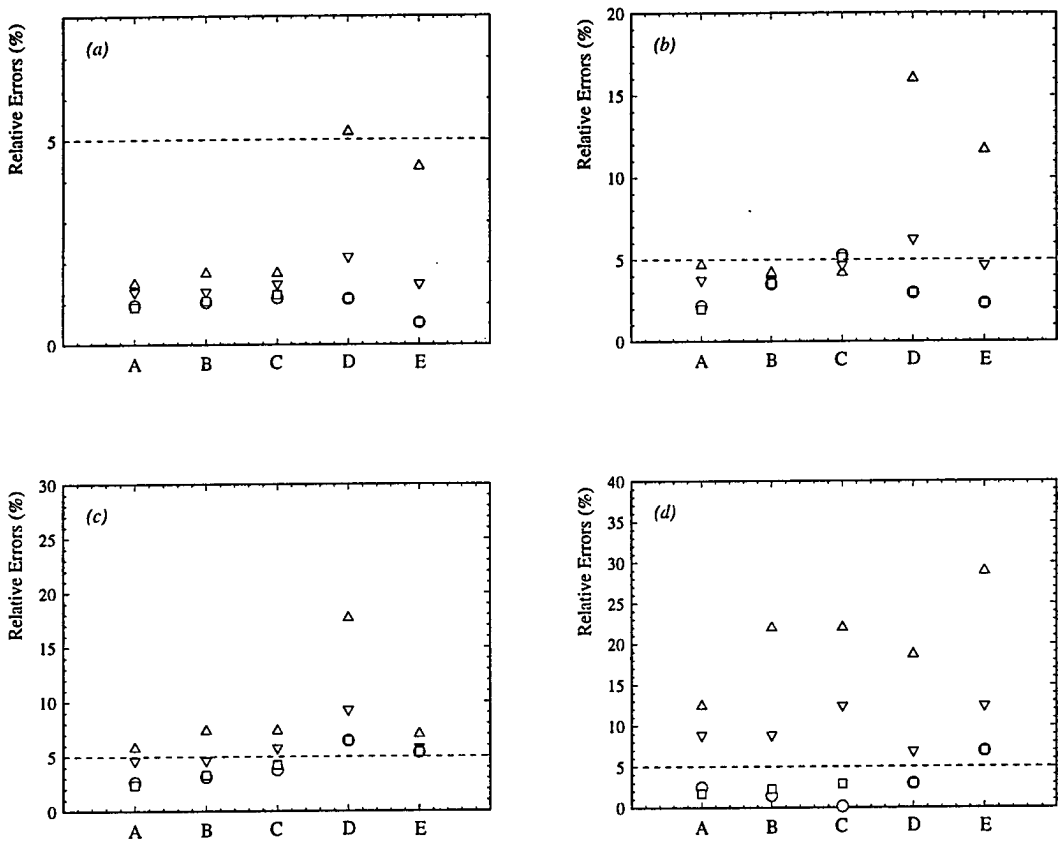

Figure 1: Relative errors in selected quantities in the non-premixed piloted jet flame test (a) mean velocity (b) mean mixture fraction (c) turbulence frequency (d) turbulent kinetic energy. Symbols: triangles, basic calculation; squares and circles, extrapolated quantities.

REFERENCES

A.R. Masri, S. Subramaniam and S.B. Pope (1996) "A mixing model to improve PDF simulation of turbulent diffusion flames," Twenty-Sixth Symp. (Int'l) on Combust., pp. 49–57.

S.B. Pope (1997) "Computationally Efficient Implementation of Combustion Chemistry using In Situ Adaptive Tabulation," Combustion Theory and Modelling, **1**, 41–63.

V. Saxena and S.B. Pope (1998a) "PDF Calculations of Major and Minor Species in a Turbulent Piloted Jet Flame," Twenty-seventh Symposium (Int'l) on Combustion (to be published).

V. Saxena and S.B. Pope (1998b) "PDF Simulations of Turbulent Combustion Incorporating Detailed Chemistry," Combustion and Flame (to be published).

S. Subramaniam and S.B. Pope (1997) "Comparison of PDF mixing models for nonpremixed turbulent reacting flow," Combustion and Flame, (submitted).

S. Subramaniam and S.B. Pope (1998) "A mixing model for turbulent reactive flows based on Euclidean minimum spanning trees," Combustion and Flame, (in press).

F. Takahashi, M.D. Vangsness and V.M. Belovich (1991) "Measurements in swirling and non-swirling coaxial air jets: No. 3, 30-degree swirl, 100m/s, Technical Report UDR-TR-91-162, University of Dayton, Ohio.

P.R. Van Slooten, Jayesh and S.B. Pope (1998) "Advances in PDF modeling for inhomogeneous turbulent flows," Physics of Fluids, **10**, 246–265.

P.R. Van Slooten and S.B. Pope (1998) "Application of PDF Modeling to Swirling and Non-Swirling Turbulent Jets," Flow, Turbulence and Combustion (submitted).

J. Xu and S.B. Pope (1998) "Numerical Accuracy of PDF Particle/Mesh Methods" J. Comp. Phys. (to be submitted).

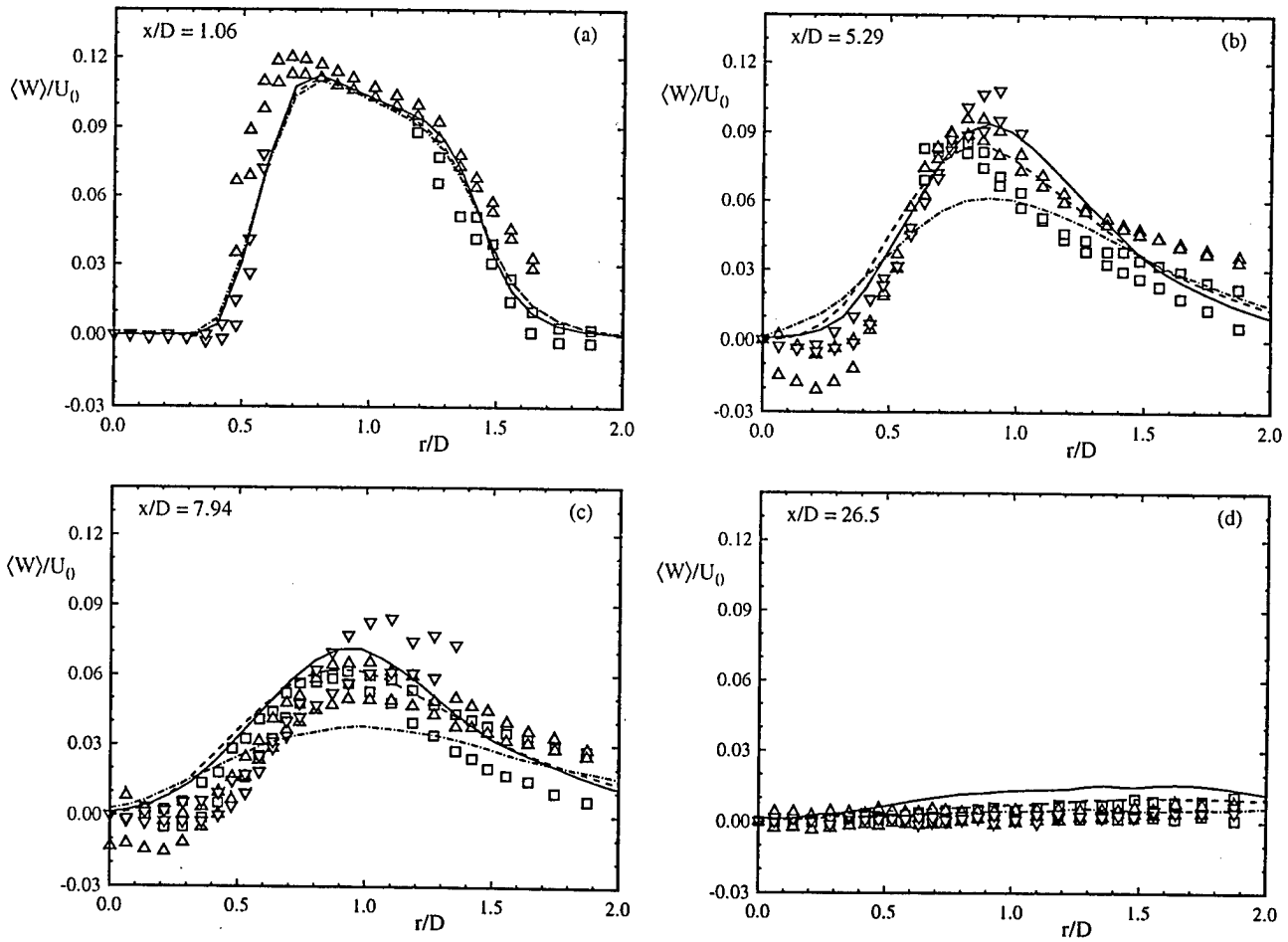

Figure 2: Mean circumferential velocity profiles at different axial distances in a 30° swirling jet. Symbols, experimental data of Takahashi et al. (1991); solid line, wavevector PDF model; dashed line, Lagrangian isotropization of production (LIPM) PDF model; dot-dashed line, Simplified Langevin PDF model.

COMBUSTION RESEARCH

AFOSR Task # 93WL036/92WL031

Principal Investigators: W. M. Roquemore, J. R. Gord, and R. D. Hancock

Air Force Research Laboratory
AFRL/PRSC Bldg 490
1790 Loop Rd N
Wright Patterson AFB OH 45433-7103

SUMMARY/OVERVIEW:

This combustion research program encompasses experimental and computational activities that range from fundamental vortex-flame interaction studies to the investigation of advanced gas turbine combustor concepts. Vortex-flame interactions represent the fundamental building blocks of turbulent flames, while advanced combustors depend on high levels of turbulence for proper mixing and combustion. This report summarizes some of the recent results from studies of vortex-flame interactions and of a Trapped-Vortex (TV) combustor concept.

TECHNICAL DISCUSSION

Studies on individual vortex-flame interactions constitute important elements for the understanding of the turbulent-flame structure. Vortices having sufficiently high normal velocity can pass through the flame by extinguishing it locally. In several circumstances, they deform the flame surface significantly before attaining extinction conditions. The development of curvature on the flame surface, especially in hydrogen flames, could lead to different quenching patterns. An experimental/numerical investigation is performed to explore possible quenching patterns in opposed-jet diffusion flames.

A diluted hydrogen-nitrogen mixture is used as the fuel. Vortices are driven toward the flame surface with different velocities from the air side. The changes in the structure of the flame, during its interaction with the incoming vortex, are recorded by measuring instantaneous OH-concentration fields using the Laser-Induced-Fluorescence (LIF) technique. A time-dependent CFDC code that incorporates 13 species and 74 reactions is used for the simulation of these vortex-flame interactions. Both the experiments and calculations have identified two types of quenching patterns; namely, point and annular. It is found that when an air side vortex is forced toward the flame at a relatively high speed, then the flame at the stagnation line quenches, resulting in a well-known point-quenching pattern. On the other hand, when the vortex is forced at a moderate speed, the flame surface deforms significantly and quenching develops in an annular ring away from the stagnation line, resulting in the unusual annular-quenching pattern shown in Figure 1. This unusual effect was predicted about a year before it was observed in the laboratory. Detailed analyses performed just before the development of annular quenching and one ms later suggest that this unusual annular quenching did not result from the strain rate. Based on the understanding gained from previous investigations on curvature effects in coaxial hydrogen jet flames and the findings made in the

present study, it is argued in Ref. 1 that such quenching develops as a result of the combined effect of preferential diffusion and flame curvature.

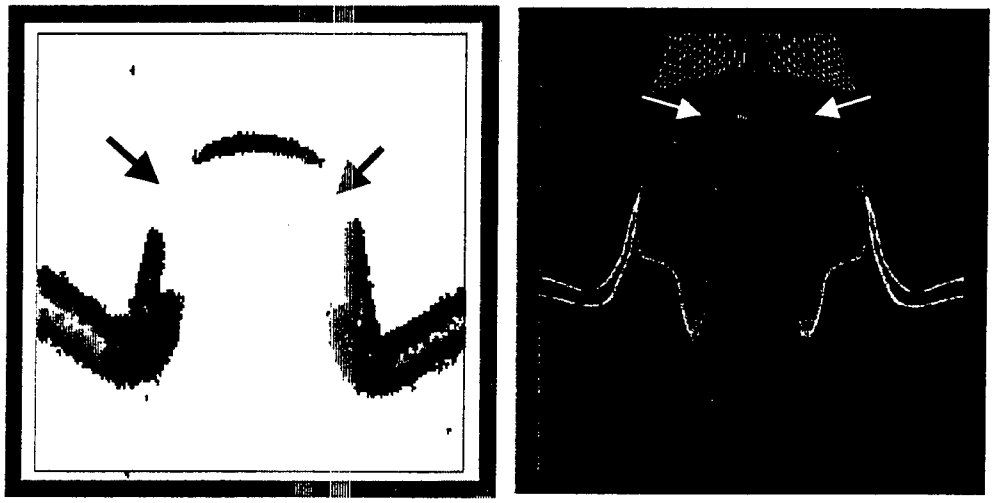

Experimental: OH Image Computed: OH/Streakline Images

Figure 1. Annular quenching during a vortex-flame interaction of a hydrogen-air flame.

Combustion stability is often achieved using recirculation zones to provide continuous sources of ignition by mixing hot products and burning gases with the incoming fuel and air. Swirl vanes, bluff-bodies, and rearward-facing steps are commonly used methods of establishing recirculation zones for flame stabilization. To our knowledge, the flame-stability characteristics of cavities that are aerodynamically designed to trap a vortex have not been investigated. One reason for this may be that when a vortex is trapped in a cavity, very little exchange of main flow and cavity fluid occurs. This constitutes a problem since flame stability requires a continuous exchange of mass and heat between the cavity and main flow. This problem can be solved by directly injecting both fuel and air into the cavity in a manner that reinforces the vortex. The goal of the study described in Ref. 2 is to investigate the flame-stability characteristics of a Trapped Vortex (TV) combustor in which fuel and air are injected directly into the cavity from the face of the afterbody.

The cavity is formed between two axisymmetric disks mounted in tandem (see Figure 2). The upstream disk is referred to as the forebody and the downstream disk, the afterbody. With co-flowing annular air, a vortex is trapped in the cavity for a specific separation between the forebody and the afterbody. Primary air and gaseous propane are injected directly into the cavity through multiple jets located on the upstream face of the afterbody.

The wake region behind the afterbody provides a low-speed region for further consumption of excess fuel; however, vortex shedding can cause local quenching which can lead to reduced combustion efficiency. Little and Whipkey[3] have shown that adding a second afterbody results in a significant reduction in drag. The second cavity seems to reduce the unsteady wake motion

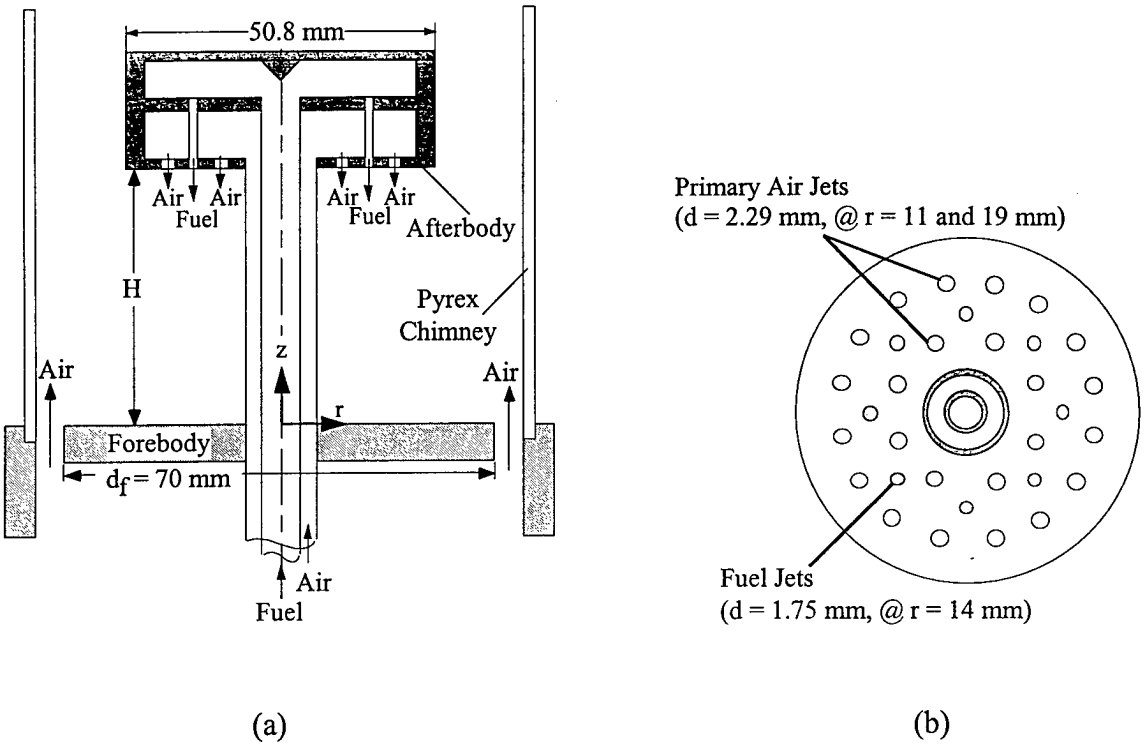

Figure 2. Schematic diagrams of (a) Trapped-Vortex combustor and (b) injection plane of afterbody

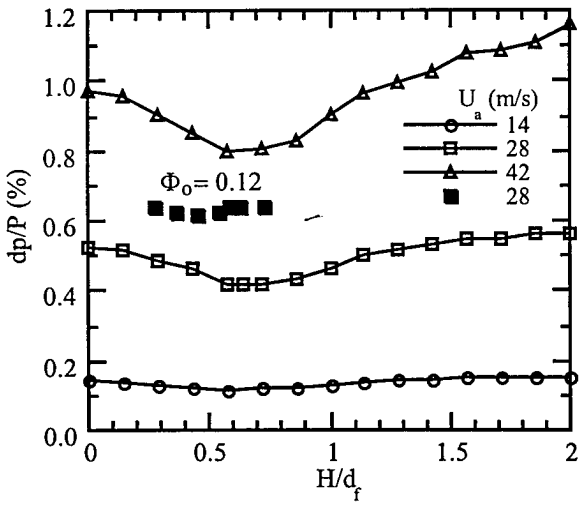

Figure 3. Impact of cavity length H/d_f on pressure drop under cold (open) and combusting (solid) flows.

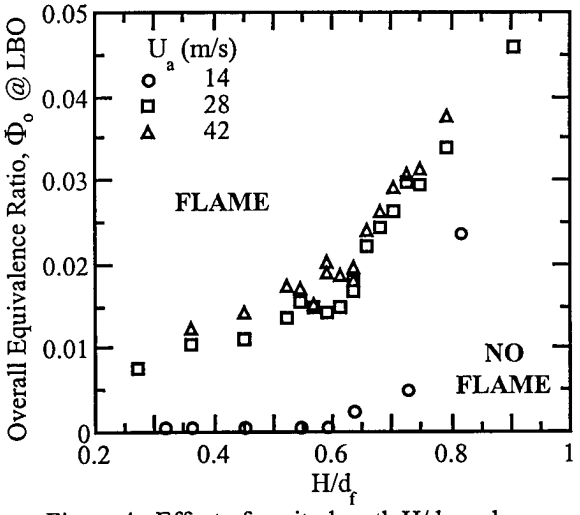

Figure 4. Effect of cavity length H/d_f on lean blow-out under various annular-air flows.

created behind the first afterbody in a one-cavity configuration. In a combusting flow, the second cavity should also improve the combustion efficiency by eliminating some of the unsteady combustion in the wake region. Experiments were also conducted with a two-cavity configuration that involved adding a second, passive, cavity to the burner shown in Fig. 2.

A feature of the TV combustor is its low-pressure drop. This feature may provide significant reductions in specific fuel consumption. The pressure drop was found to be a minimum at an H/d_f of about 0.6 as noted in Figure 3.

The TV combustor has a low lean-blow-out (LBO) limit over a wide operating range due to the cavity being shielded from the high-speed annular air. This is shown in Figure 4. Cavity length has a strong impact on the LBO limit. A cavity length of 0.6 d_f was found to be optimal under various annular-air flows when no primary air (air injected directly into the cavity) is used. The primary air has a direct impact on the LBO limit because of mixing and residence time in the cavity. The lowest LBO limits were achieved at low primary-air flow rates. At higher primary-air flows, the fuel flow rate at the LBO limit was found to increase linearly with the primary-air flow rate.

Figure 5 shows the results of combustion efficiency and emissions measurements for both the single and double cavity burners. Combustion efficiencies of ~ 99% were recorded at a low annular-air velocity of 14 m/s over a wide range of primary air flows. At a higher annular-air velocity of 42 m/s, the peak efficiency was ~ 97% and increased to ~ 99% when a second cavity was added to the combustor. Combustion is sensitive to the primary air flow and has a narrower high-efficiency range at higher annular-air flows. These results are noted in Figure 5(a).

Figures 5(b) and (c) show that inefficiency in the combustion process is the result of both unburned hydrocarbons (UHC) and carbon monoxide (CO). Even more interesting is the fact that the improvements in efficiency obtained by adding the second afterbody are mainly the result of the reduction of UHC emissions. It was also observed that CO increases slightly with the two-cavity configuration, which is due to additional consumption of UHC. It is also evident in comparing Figures 5(a) and (d) that the NO_X and combustion efficiency peak and decay at the same values of Φ_p. The lowest NO_X and combustion efficiency occur at the highest annular-air flow rate because of the short residence time. The addition of the second cavity produces only a small difference in NO_X. Therefore, it is thought that the CO and NO_X are produced mainly in the first cavity.

In conclusion, Ref. 2 presents an investigation of a simple, compact, low-pressure-drop combustor utilizing the Trapped-Vortex concept. This TV combustor exhibited good stability limits and reasonable combustion efficiencies under high flow conditions. However, considerable work is required before the practical aspects of a TV combustor can be demonstrated. Recently, the TV concept was used for flame stabilization in developing an advanced gas-turbine combustor. In optimizing cavity performance, it was found that the combustion efficiency and LBO limits were significantly improved over a wide range of operating conditions. The aspect ratio of the cavity and the fuel and air injection scheme in the cavity has a strong impact on cavity performance. Future investigations will continue to focus on methods of improving the performance characteristics while substantially reducing NO_X. The fuel residence time and cavity entrainment, which can impact practical designs, will be investigated. The impact of using air to cool the cavity walls on combustion characteristics will be evaluated.

REFERENCES

1. V. R. Katta, C. D. Carter, G. J. Fiechtner, J. R. Gord, J. C. Rolon, and W. M. Roquemore, "Interaction of a Vortex with a Flat Flame Formed Between Opposing Jets of Hydrogen and Air",

Accepted for publication at The Twenty-Seventh International Symposium on Combustion, The Combustion Institute, August 2-7, 1998, Boulder, Colorado.

2. K.-Y. Hsu, L. P. Goss, and W. M. Roquemore, "Characteristics of a Trapped-Vortex Combustor", J. Prop. and Power, Vol. 14, No. 1, pp. 57-65, February, 1998.

3. Little, B. H. Jr., and Whipkey, R. R., "Locked Vortex Afterbodies," *Journal of Aircraft*, Vol. 16, No. 5, pp. 296-302, May 1979.

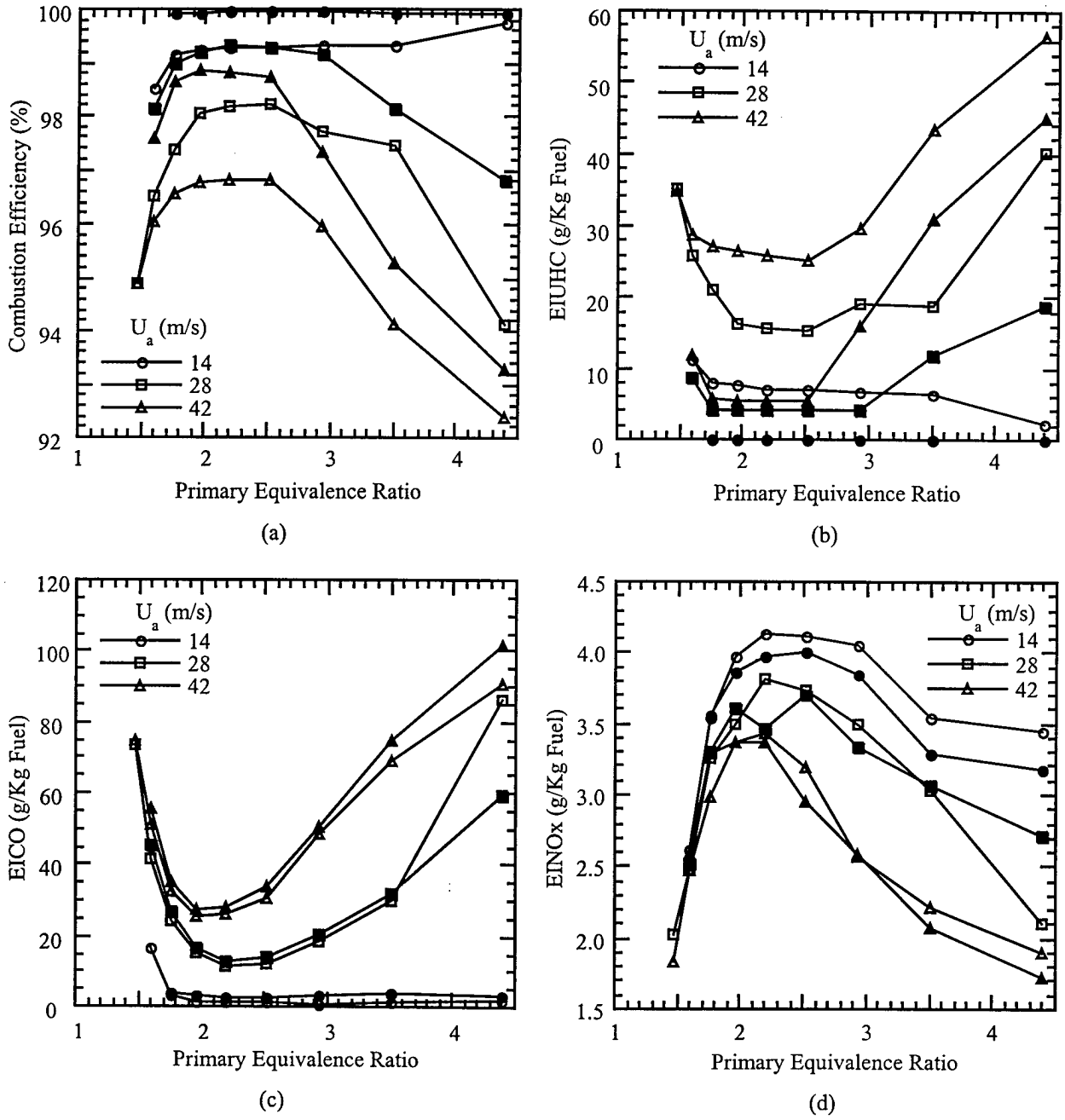

FIGURE 5

Figure 5. Impact of primary-air and annular-air flows on (a) combustion efficiency and on emission indices of (b) unburned hydrocarbon, (c) carbon monoxide, and (d) oxides of nitrogen at a fixed fuel flow. The open and solid symbols denote the results from one-cavity and two-cavity configurations, respectively.

COMPRESSIBLE TURBULENT REACTING FLOWS

(AFOSR Grant No. F49620-96-1-0106)

Principal Investigators: F. A. Williams, P. A. Libby and S. Sarkar

Department of Applied Mechanics and Engineering Sciences
University of California San Diego, La Jolla, CA 92093-0411

SUMMARY/OVERVIEW

The objective of this research is to advance fundamental understanding of reacting flows relevant to Air Force needs in high-speed airbreathing propulsion. Specific areas investigated in the past year include direct numerical simulation (DNS) of compressible turbulent combustion, analysis of subgrid-scale modeling for large eddy simulation (LES), and Reynolds-averaged Navier-Stokes (RANS) modeling of high-speed turbulent Couette flow. The results obtained here should improve the capability to analyze and design propulsion systems involving high-speed turbulent combustion.

TECHNICAL DISCUSSION

The compressible, reacting, shear layer

Three-dimensional, unsteady DNS [1, 2] of the shear layer has been performed for various values of the convective Mach number, $M_c = (U_1 - U_2)/(c_1 + c_2)$ on grids with up to 10 million points. The objective is to understand and model the coupling between flow, thermodynamic variables and chemistry. Unlike previous numerical studies, self-similar development of the flow in the fully nonlinear regime has been achieved. Fig. 1 shows that the reduced growth of the thickness growth rate observed in numerous physical experiments is seen in the DNS data. Experimental measurements of the Reynolds stresses, $R_{ij} = \overline{\rho u_i' u_j'}$, which are relatively scarce and not in agreement need to be supplemented by DNS data. Fig. 2 shows DNS results on the compressibility effect on streamwise (R_{11}), cross-stream (R_{22}), and shear (R_{12}) components. The inference is that all components decrease with M_c. In turbulent shear flow, the pressure-strain correlation is critical to transferring energy between the u_1, u_2 and u_3 fluctuations and maintaining the shear-stress, R_{12}, responsible for growth of the mixing layer thickness. In the high-speed regime, the reduced pressure fluctuations (see Fig. 3) leads to a lower magnitude of the pressure-strain term, the Reynolds shear stress decreases, and ultimately the thickness growth rate decreases.

Simulations of high-speed, methane-air combustion with infinitely-fast chemistry are being performed. Figs. 4-5 show temperature (normalized by the adiabatic flame temperature) contours at the same time for $M_c = 0.3$ and 0.8, respectively. The lower stream is methane while the upper one is air. Since the stoichiometric mass fraction, $\zeta_{st} = 0.05$, is low, the flame lies in the upper air side of the shear layer. The thickness of the temperature mixing region is smaller in the $M_c = 0.8$ case and so is the product formation rate. The turbulent transport of temperature is of interest; from the DNS, it is found that the approximation of turbulent Prandtl number, $Pr_t \simeq 0.8$, used in low-speed shear flows can be applied to the high-speed case.

Low-speed, variable density experiments have shown the variation in growth rate is not large. DNS is being used here to investigate the effect of nonuniform density in the high-speed regime. Three cases with $\rho_1/\rho_2 = 1$, 4, and 8 were simulated at $M_c = 0.8$. Fig. 6 shows that the growth rate has a large decrease with increasing density ratio. This suggests that the effect of unequal free-stream densities in the high-speed shear layer is fundamentally different from that in the low-speed case and is manifest as a compressibility effect (related to the ratio of free-stream Mach numbers M_1/M_2) and not a variable-density effect.

The turbulent jet

The evolution of the flow and scalar mixing in a turbulent plane jet ($M = 0.3, Re = 6{,}000$) has been simulated. The objective is to create a well-resolved database that is validated against experiments and then use it to develop subgrid-scale (SGS) models for LES. Two-dimensional simulations [3,4] have been completed and recent three-dimensional simulations [5] are discussed

here. Fig. 7 shows that the evolution of velocity half-width agrees well with experimental data. The shape of scalar pdf's in jets has generated controversy. Fig. 8a shows pdf's of the scalar ζ at various cross-stream locations in the initial region of the jet, $x/h = 3$. When the jet is traversed from the centerline ($y/\delta_U = 0$, $\zeta = 1$) to the upper edge ($y/\delta_U = 2.26$, $\zeta = 0$), the position of the local central maximum of the pdf's does not march from high to low values of ζ although the mean values (solid symbols) do. Such a so-called nonmarching pdf is indicative of mixing by large-scale coherent structures. However, the pdf has a qualitative change further downstream at $x/h = 17$ (see Fig. 8b) where the local central maximum of the pdf marches from high to low values of ζ during a cross-stream traverse. Fig. 9 shows that the r.m.s streamwise velocities compare well with experimental data. The DNS database is currently being used to evaluate SGS models for scalar mixing, models important for reacting flows.

Subgrid modeling

When applied to practical propulsion systems where the mean velocity gradient is nonuniform, LES must deal with filtering in inhomogeneous directions. The approximation of homogeneous, isotropic behavior of small sales is no longer valid. It is found that, in such a situation, the SGS (subgrid scale) stress tensor τ_{ij} has a rapid part τ_{ij}^R that depends explicitly on the mean velocity gradient and a slow part τ_{ij}^S that does not. The scaling properties associated with this new decomposition [6] are analytically derived and further quantified using the shear layer DNS database. The energy transfer, $\tau_{ij}' s_{ij}'$, between grid and subgrid scales is of interest. Figs. 10-11 show profiles of the normalized, Reynolds-averaged SGS transfer in the shear layer. The scale-similarity model captures the rapid contribution (see Fig. 10) while the Smagorinsky model represents well the slow contribution (see Fig. 11). This finding may be a reason for the observation in recent LES studies that the mixed model (scale-similarity plus Smagorinsky eddy viscosity) gives better results than either component model by itself. In ongoing work we are considering how SGS models may need to be altered to account for the effect of M_c and M_1/M_2 observed in the high-speed shear layer.

High-speed reacting Couette flow

Couette flow is of interest since it permits consideration of speeds up to the hypersonic regime and a broad range of rates of heat transfer within the context of a simple geometry. During the past year our research has been directed at two related issues. One study [7] involves an extension and exploitation of earlier research connected with laminar Couette flow in premixed systems. The extension involves consideration of the influence of wall cooling on extinction of the flame within the passage. The second issue concerns the theory of premixed turbulent flames; in an earlier impinging jet study we showed that the mean velocity components are accurately given by the mean Euler equations implying that the flows are dominated by mean pressure gradients. Extension of this strategy to the determination of Reynolds stresses and heat fluxes is now being examined; initial results have established that the standard second-moment theory, extended to apply to turbulent combustion, must be altered. In particular, flamelet dissipation which is operative only within the flame and which is not incorporated in the usual formulations appears to play an important role. This work is continuing and will involve comparison of theory and experiment from a variety of sources.

REFERENCES

[1] C. Pantano and S. Sarkar, "DNS of mixing in compressible turbulent shear layers," *Bulletin of the APS*, **42**, 2211 (1997)

[2] C. Pantano and S. Sarkar, "Compressibility effects in a self-similar, high-speed turbulent mixing layer," in preparation (1998)

[3] S. Stanley and S. Sarkar, "Simulations of spatially developing two-dimensional shear layers and jets," *Theor. Comput. Fluid Dyn.*, **9**, 121 (1997).

[4] S. Stanley and S. Sarkar, "Simulations of spatially developing plane jets," 28th AIAA Fluid Dynamics Conference, *AIAA 97-1922.*

[5] S. Stanley and S. Sarkar, "Direct simulation of turbulence evolution and scalar mixing in a spatially developing, turbulent plane jet," in preparation (1998).

[6] L. Shao, S. Sarkar, and C. Pantano, "On the relationship between the mean flow and subgrid stresses in LES of turbulent shear flows," submitted to *Phys. Fluids* (1998).

[7] K. N. C. Bray, M. Champion, P. A. Libby, "Premixed combustion in laminar Couette flow - extinction and mass burning rate," in preparation (1998).

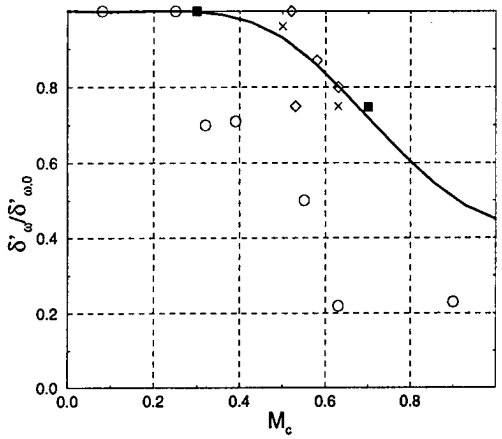

Figure 1: Compressibility effect on shear layer growth rate. The solid line is the Langley experimental curve, open symbols are other experiments, closed symbols are from our DNS.

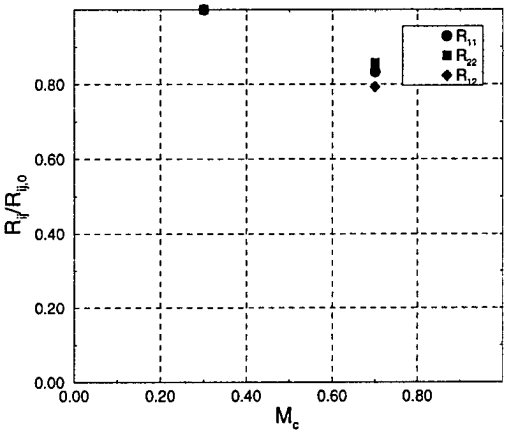

Figure 2: Compressibility effect on the Reynolds stresses.

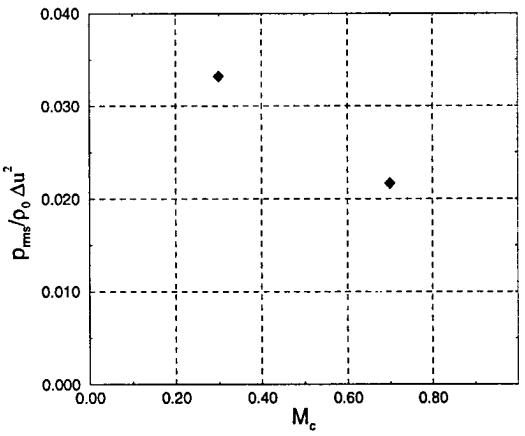

Figure 3: Normalized rms pressure fluctuations at the centerline.

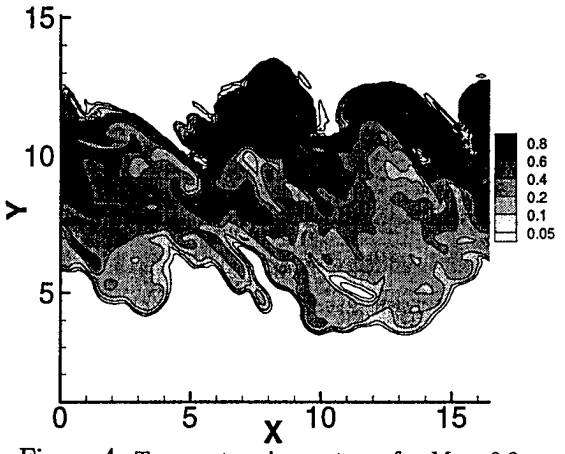

Figure 4: Temperature iso-contours for $M_c = 0.3$.

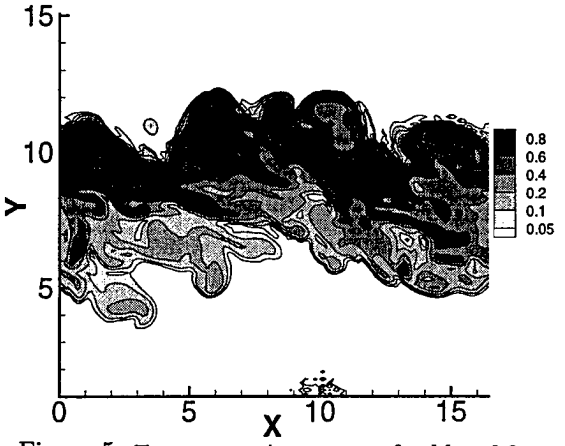

Figure 5: Temperature iso-contours for $M_c = 0.8$.

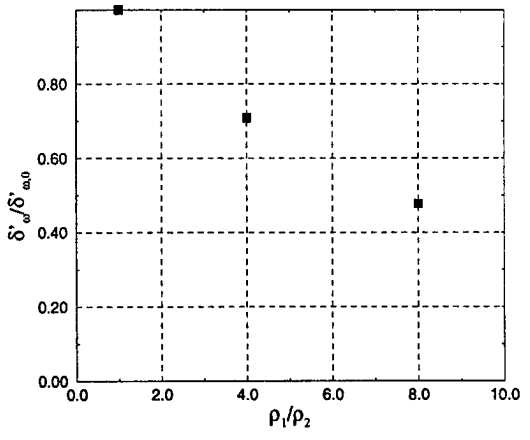

Figure 6: Shear layer growth rate as a function of the density ratio. $M_c = 0.8$ is held constant.

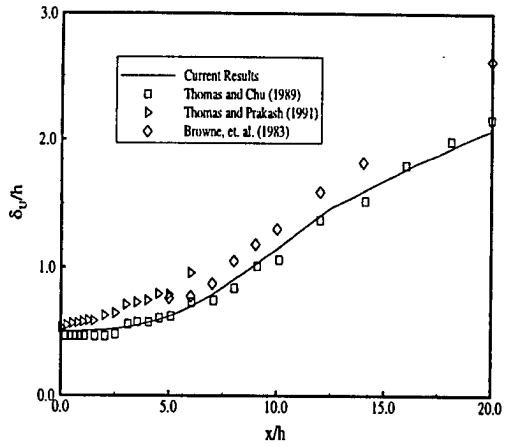

Figure 7: Downstream growth of the jet half-width based on velocity.

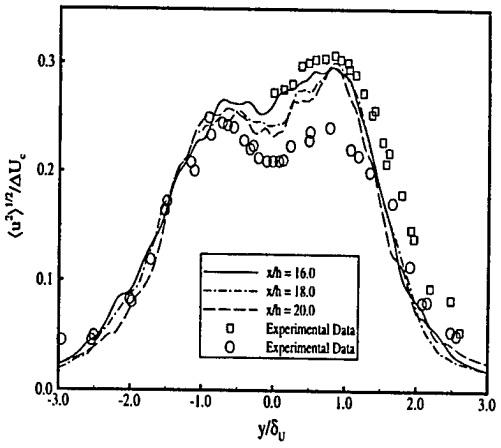

Figure 9: Profiles of rms streamwise velocity in the jet. □ - Gutmark and Wygnanski[1976], ○ - Ramaprian and Chandrasekhara[1985].

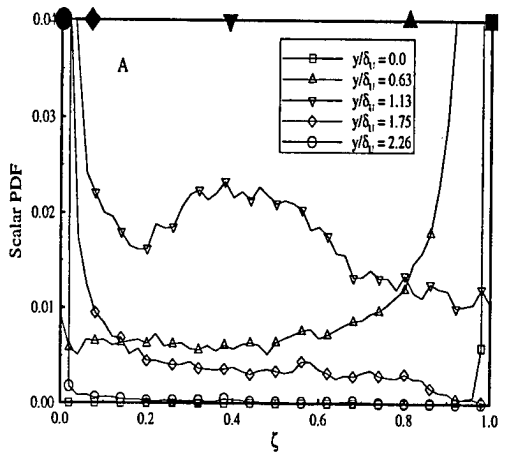

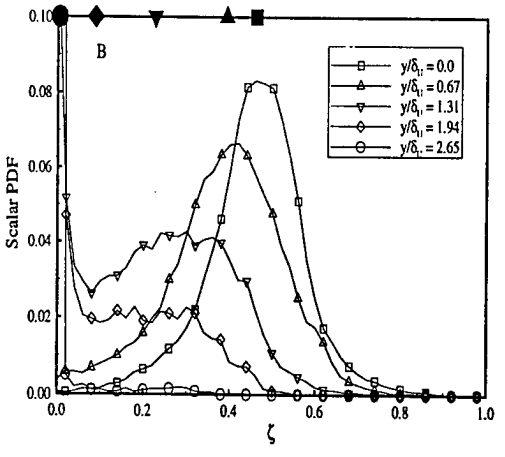

Figure 8: Scalar PDFs at (A) $x/h = 3.0$ and (B) $x/h = 17.0$ in a planar turbulent jet. The solid symbols across the top of the graphs indicate the local mean scalar values.

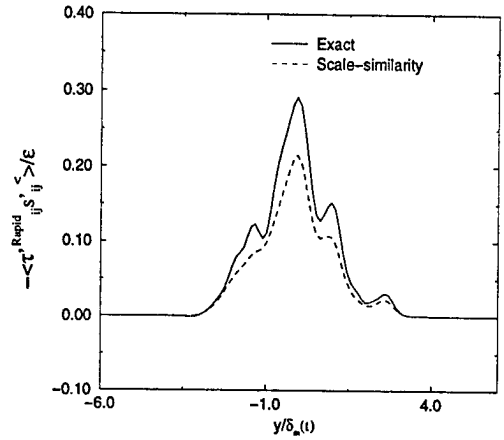

Figure 10: Rapid contribution to the normalized subgrid energy transfer $< \tau^{R'}_{ij} s'_{ij} > /\epsilon$.

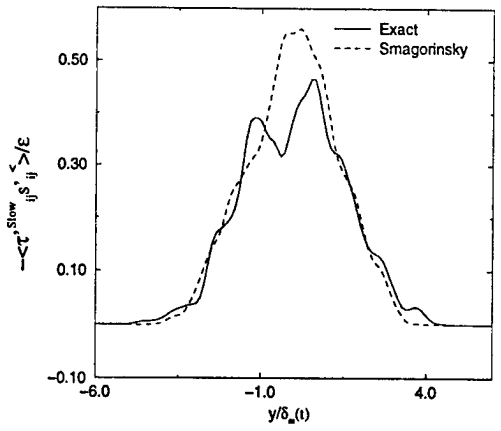

Figure 11: Slow contribution to the normalized subgrid energy transfer $< \tau^{S'}_{ij} s'_{ij} > /\epsilon$.

INVITEES

Dr. M. S. Anand
Allison Engine Company
P.O. Box 420
Speed Code T-14
Indianapolis IN 46206-0420
(317)230-2828
FAX:230-3691
iemsa@agt.gmeds.com

Dr Griffin Anderson
NASA Langley Research Center
M/S 168
Hampton VA 23681
(804)864-6238
FAX:864-6243
g.y.anderson@larc.nasa.gov

Dr. William Anderson
AMSRL-WT-PC
US Army Research Laboratory
Aberdeen Proving Ground MD 21005-5066
(410)278-9992
FAX: 278-7333
willie@arl.army.mil

Dr Kurt Annen
Aerodyne Research, Inc.
45 Manning Road
Manning Park Research Center
Billerica MA 01821-3976
(508)663-9500
FAX:663-4918
kannen@aerodyne.com

Dr Chris Atkinson
Dept of Mech. & Aerospace Eng.
West Virginia University
PO Box 6106
Morgantown WV 26506-6106
(304)293-4111
FAX:293-2582

Dr William Bachalo
Aerometrics, Inc.
755 North Mary Avenue
Sunnyvale CA 94086-9175
(408)738-6688
FAX:738-6871

Dr. Tiejun Bai
Engineering Department
Clark Atlanta University
223 James P Brawley Drive, SW
Atlanta GA 30314
(404)880-6983
FAX: 880-6853
tbai@cau.edu

Mr. Lee Bain
AFRL/PRS
Building 18
1790 Loop Road, North
Wright-Patterson AFB OH 45433-7103
(937)255-1237

Dr S L Baughcum
Boeing Company
P O Box 3707, MS 6H-FC
Seattle WA 98124
(425)965-0426
FAX:234-4543
baughcum@atc.boeing.com

Dr Howard Baum
National Institute of
Standards and Technology
Center for Fire Research
Gaithersburg MD 20899
(301)975-6668

Dr John Bdzil
Los Alamos National Laboratory
Los Alamos NM 87545

Dr. Bruce Beaver
Department of Chemistry
Duquesne University
Mellon Hall
Pittsburgh PA 15282-1503
(412)434-6340
FAX:434-5683

Mr. Steve Beckel
Pratt and Whitney
M/S 715-83
P.O. Box 109600
West Palm Beach FL 33410-9600

Dr Edward Beiting
Aerophysics Lab, Prop & Env Sc
The Aerospace Corporation
P O Box 92957, M5/754
Los Angeles CA 90009-2957
(310)336-7035

Dr Josette Bellan
Applied Technologies Section
Jet Propulsion Laboratory
4800 Oak Grove Drive
Pasadena CA 91109
(626)354-6959
FAX:393-1633
josette.bellan@jpl.nasa.gov

Dr Michael Berman
AFOSR/NL
110 Duncan Avenue, Suite B115
Bolling AFB DC 20332-8050
(202)767-4963
FAX:404-7475
michael.berman@afosr.af.mil

Dr. Robert Bill
Propulsion Dir, Army Res. Lab.
NASA Lewis Res. Ctr., MS 77-12
21000 Brookpark Road
Cleveland OH 44135-3191

Dr Mitat Birkan
AFOSR/NA
110 Duncan Avenue, Suite B115
Bolling AFB DC 20332-8050
(202)767-4938
FAX:767-4988
mitat.birkan@afosr.af.mil

Dr Kevin Bowcutt
North American Aircraft Div.
Rockwell International Corp.
P.O. Box 3644
Seal Beach CA 90740-7644

Dr C T Bowman
Department of Mechanical
Engineering
Stanford University
Stanford CA 94305-3032
(650)723-1745
FAX:723-1748
bowman@navier.stanford.edu

Dr Iain Boyd
Department of Mechanical and Aerospace Engineering
246 Upson Hall
Cornell University
Ithaca NY 14853
(607)255-4563
FAX:255-1222
boyd@scotch.mae.cornell.edu

Dr K N C Bray
University of Cambridge
Department of Engineering
Trumpington Street
Cambridge CB2 1PZ, England UK
0223 332744
FAX0223 332662

Dr Robert Breidenthal
Department of Aeronautics and
Astronautics
University of Washington, FS10
Seattle WA 98195
(206)685-1098

Dr Kenneth Brezinsky
Department of Chemical Engrg
University of Illinois-Chicago
810 S. Clinton St, Room 204
Chicago IL 60607-7000
(312)996-9430
FAX:996-0808
kenbrez@uic.edu

Dr Garry Brown
Department of Mechanical and
Aerospace Engineering
Princeton University
Princeton NJ 08544-5263
(609)258-6083
GLB@pucc.princeton.edu

Dr R C Brown
Aerodyne Research, Inc.
45 Manning Road
Manning Park Research Center
Billerica MA 01821-3976
(508)663-9500
FAX:663-4918

Dr. Adam Bruckner
Aerospace and Energ Rsrch Prog
University of Washington
120 Aero&Eng Rsrch Bldg FL-10
Seattle WA 98195
(206)543-6321
FAX:543-4719
bruckner@aa.washington.edu

Dr. Walter Bryzik
Propulsion Systems Division
ATTN: DRSTA-RGD
USA Tank-Automotive Command
Warren MI 48397-5000
(810)574-6461
FAX: 574-5054

Dr John D Buckmaster
Department of Aerospace
Engineering
University of Illinois
Urbana IL 61801

Dr Dennis Bushnell
NASA Langley Research Center
Mail Stop 110
Hampton VA 23681
(804)864-4546
d.m.bushnell@larc.nasa.gov

Dr Ron Butler
AFRL/PR
Building 490
1790 Loop Road, N
Wright-Patterson AFB OH 45433-7103

Dr T D Butler
Group T-3
Los Alamos National Laboratory
Los Alamos NM 87545
(505)667-4156
tdbutler@lanl.gov

Dr H F Calcote
Titan Corp, AeroChem Rsrch Lab
50 Washington Road
P. O. Box 2229
Princeton NJ 08543-2229
(609)716-1201
FAX:716-1204
hcalcote@titan.com

Dr George Caledonia
Physical Sciences, Inc
20 New England Business Center
Andover MA 01810
(508)689-0003
FAX:689-3232

Mr. Donald Campbell
NASA Lewis Research Center
21000 Brookpark Road
Mail Stop 3-2
Cleveland OH 44135
(216)433-2929
(216)433-5266

Dr Graham V Candler
Department of Aerospace
Engineering & Mechanics
University of Minnesota
Minneapolis MN 55455

Dr Brian Cantwell
Department of
Mechanical Engineering
Stanford University
Stanford CA 94305-3032
(650)723-4825

Dr. Ismail Celik
Department of Mechanical and
Aerospace Engineering
West Virginia University
Morgantown WV 26506

Dr. Nicholas Cernansky
Mechanical Engineering Dept.
Drexel University
32nd and Chestnut Streets
Philadelphia PA 19104-2884

Dr Richard Chang
Applied Physics Department
P. O. Box 208284
Yale University
New Haven CT 06520-8284
(203)432-4272
FAX: 432-4274
RK_CHANG@RAMAN.ENG.YALE.EDU

Dr Chine I Chang
AFOSR/NA
110 Duncan Avenue, Suite B115
Bolling AFB DC 20332-8050
(202)767-4987
FAX:767-4988
jim.chang@afosr.af.mil

Dr Tryfon Charalampopoulos
Mechanical Engineering Dept.
Louisiana State University
Baton Rouge LA 70803
(504)388-5792
FAX:388-5894

Dr. Harsha Chelliah
Department of Mechanical, Aero
and Nuclear Engineering
University of Virginia
Charlottesville VA 22903-2442
(804)924-6037
FAX:982-2037
harsha@virginia.edu

Dr. Jacqueline Chen
MS 9051
Sandia National Laboratories
P.O. Box 969
Livermore CA 94551-0969
(510)294-2586
FAX:294-1012
jhchen@sandia.gov

Dr Lea D Chen
Mechanical Engineering Dept
University of Iowa
Iowa City IA 52242
(319)335-5674
FAX:335-5669
ldchen@icaen.uiowa.edu

Dr Wai K Cheng
Department of Mechanical
Engineering
MIT
Cambridge MA 02139
(617)253-4531

Dr Robert Childs
Nielsen Engineering and
Research, Inc.
510 Clyde Avenue
Mountain View CA 94043-2287
(415)968-9457

Dr S Y Cho
Department of Mechanical and
Aerospace Engineering
Princeton University
Princeton NJ 08544-5263

Dr M-S Chou
Building R1, Room 1044
TRW Space and Technology Group
One Space Park
Redondo Beach CA 90278
(310)812-0469
FAX:812-7589

Mr R.W. Claus
NASA Lewis Research Center
21000 Brookpark Road
Cleveland OH 44135-3127
(216)433-5869

Dr M B Colket
United Technologies Research
Center
411 Silver Lane
East Hartford CT 06108
(860)610-7481
FAX:610-2151
colketmb@utrc.utc.com

Dr S M Correa
GE Corp. Research & Development
PO Box 8, K1ES112
Schenectady NY 12301
(518)387-5853
FAX:387-7258
correa@crd.ge.com

Dr David Crosley
Molecular Physics Department
SRI International
333 Ravenswood Avenue
Menlo Park CA 94025-3696
(415)326-6200

Dr Clayton Crowe
Department of Mechanical
Engineering
Washington State University
Pullman WA 99164-2920
(509)335-3214

Dr F E C Culick
Engrg. and Appl. Sci. Dept.
California Institute of
Technology
Pasadena CA 91125
(626)395-4470

Dr Eli Dabora
Mechanical Engineering Dept
University of Connecticut
Box U-139 ME
Storrs CT 06268
(203)486-2415

Dr Werner Dahm
Department of Aerospace
Engineering
The University of Michigan
Ann Arbor MI 48109-2118
(734)764-4318
FAX:763-0578
wdahm@engin.umich.edu

Dr John Daily
Center for Combustion Research
Mechanical Engineering Dept
University of Colorado
Boulder CO 80309
(303)492-7151

Dr Ron Davis
Chemical Science and Techn Lab
Building 221, Room B312
National Inst of Stds & Tech
Gaithersburg MD 20899

Dr. Peter A. DeBarber
MetroLaser
18006 Skypark Circle #108
Irvine CA 92714-6428

Dr Pablo G Debenedetti
Department of Chemical
Engineering
Princeton University
Princeton NJ 08544-5263
(609)258-5480
PDEBENE@princeton.edu

Dr George Deiwert
NASA Ames Research Center
MS 230-2
Moffett Field CA 94035
(415)604-6198

Dr R W Dibble
Department of Mechanical Eng
6159 Etcheverry Hall
University of California
Berkeley CA 94720
(415)642-4901
FAX:642-6163
rdibble@euler.vine.berkeley.edu

Dr Paul Dimotakis
California Institute of Tech
1201 East California Blvd.
MC 301-46
Pasadena CA 91125
(626)395-4456
(626)395-4447
dimotakis@caltech.edu

Dr. Glenn Diskin
NASA Langley Research Center
Hampton VA 23681
(757)864-6268
FAX:864-7923
g.s.diskin@larc.nasa.gov

Dr Richard Dobbins
Department of Engineering
Brown University
164 Angel Street
Providence RI 02912-9104
(401)863-2653
FAX:863-1157
richard_dobbins@brown.edu

Dr Gregory Dobbs
United Technologies Research
Center - Mail Stop 90
Silver Lane
East Hartford CT 06108
(860)610-7145

Mr Lee Dodge
Southwest Research Institute
P O Drawer 28510
San Antonio TX 78284
(512)684-5111

Dr Michael Drake
Physical Chemistry Department
General Motors Research Labs
Twelve Mile and Mound Roads
Warren MI 48090-9055

Dr. James F. Driscoll
Department of Aerospace Engrg
3004 FXB Building
University of Michigan
Ann Arbor MI 49109-2118
(734)936-0101
FAX:763-0578
jamesfd@engin.umich.edu

Dr. J. Philip Drummond
NASA Langley Research Center
Mail Stop 197
Hampton VA 23681-0001
(757)864-2298
FAX:864-7923
j.p.drummond@larc.nasa.gov

Dr Frederick Dryer
Department of Mechanical and
Aerospace Engineering
Princeton University
Princeton NJ 08544-5263
(609)258-5206

Dr C Dutton
Department of Mechanical and
Industrial Engineering
University of Illinois
Urbana IL 61801

Dr Harry Dwyer
Department of Mechanical
Engineering
University of California
Davis CA 95616

Dr A C Eckbreth
United Technologies Research
Center
411 Silver Lane
East Hartford CT 06108
(860)610-7269

Dr. Charles A. Eckert
Department of Chemical Engrg
Georgia Institute of
Technology
Atlanta GA 30332-0100
(404)853-9344
FAX:894-6956

Dr Raymond Edelman
WC 70
Rocketdyne
6633 Canoga Avenue
Canoga Park CA 91304
(818)586-1247

Dr J T Edwards
AFRL/PRSF
Building 490
1790 Loop Road, N
Wright-Patterson AFB OH 45433-7103
(937)255-3524
FAX:255-1125
edwardst@ward.appl.wpafb.af.mil

Dr. Fokion N. Egolfopoulos
Department of Mechanical Engrg
University of Southern Calif
Olin Hall 400B
Los Angeles CA 90089-1453
(213)740-0480
egolfopo@alnitak.usc.edu

Ms Charlotte Eigel
AFRL/PR
Building 490
1790 Loop Road, N
Wright-Patterson AFB OH 45433-7103
(937)255-5106

Dr Said Elghobashi
Department of Mechanical
Engineering
University of California
Irvine CA 92717
(714)856-6002

Dr Phillip Emmerman
Harry Diamond Laboratories
Attn. SLCHD-ST-RD
2800 Powder Mill Road
Adelphi MD 20783-1197
(301)394-3000

Dr K C Ernst
Pratt and Whitney Aircraft
Group
Government Products Division
West Palm Beach FL 33402

Dr G M Faeth
Department of Aerospace
Engineering
University of Michigan
Ann Arbor MI 48109-2118
(734)764-7202
FAX:936-0106
gmfaeth@umich.edu

Dr. Daniel Fant
South Carolina Energy Research
and Development Center
386-2 College Avenue
Clemson SC 29634-5180
(864)656-2267
FAX:656-1429

Dr Gregory W Faris
Molecular Physics Laboratory
SRI International
333 Ravenswood Avenue
Menlo Park CA 94025-3493
(650)859-4131
FAX:859-6196
faris@mplvax.sri.com

Mr Ted Fecke
WL/POTC
Building 18
1950 Fifth Street
Wright-Patterson AFB OH 45433-7251
(937)255-2351
fecket@wl.wpafb.af.mil

Dr Francis Fendell
TRW Space and Technology Group
Building R1, Room 1022
One Space Park
Redondo Beach CA 90278
(213)812-0327

Dr Richard Field
U. S. Army Armament R&D Center
DRSMC-LCA-G(D)
Building 382-S
Dover NJ 07801
(201)724-5844

Dr Farley Fisher
National Science Foundation
Chemical and Thermal Syst Div
4201 Wilson Boulevard
Arlington VA 22230
ffisher@nsf.gov

Dr Arthur Fontijn
Department of Chemical and
Environmental Engineering
Rensselaer Polytechnic Inst.
Troy NY 12180-3590
(518)276-6508
FAX:276-4030
fontijn@rpitsmts.edu

Dr. David E. Foster
Engine Research Center
University of Wisconsin
Madison WI 53706
(608)263-1617

Dr Michael Frenklach
Department of Mechanical
Engineering
University of California
Berkeley CA 94720-1740
(510)643-1676
FAX:642-6163
myf@euler.berkeley.edu

Mr Jack Fultz
AFRL/PR
Wright-Patterson AFB OH 45433-6563
(937)255-2175

Dr Bish Ganguly
AFRL/PRPS
2645 Fifth Street, Suite 13
Wright-Patterson AFB OH 45433-7919
(937)255-2923
FAX:476-4095
gangulbn@possum.appl.wpafb.af.mil

Dr Alon Gany
Faculty of Aerospace Engrg
Technion-Israel Institute of
Technology
32000 Haifa, ISRAEL
972-4-8292554
FAX:972-4-8230956
gany@aerodyne.technion.ac.il

Dr Alan Garscadden
AFRL/PR
1950 Fifth Street
Wright-Patterson AFB OH 45433-7251
(937)255-2246
FAX:986-4657
wl/ca@wl.wpafb.af.mil

Dr Ahmed Ghoniem
Department of Mechanical
Engineering
MIT
Cambridge MA 02139
(617)253-2295
FAX:253-5981
ghoniem@mit.edu

Mr R Giffen
General Electric Company
Aircraft Engine Group
Neumann Way
Cincinnati OH 45215

Dr P Givi
Department of Mechanical and
Aerospace Engineering
State University of New York
Buffalo NY 14260

Dr Irvin Glassman
Department of Mechanical and
Aerospace Engineering
Princeton University
Princeton NJ 08544-5263
(609)258-5199
FAX:258-5963
glassman@princeton.edu

Dr Mark Glauser
AFOSR/NA
110 Duncan Avenue, Suite B115
Bolling AFB DC 20332-8050
(202)767-4936
FAX:767-4988

Dr. Jay P. Gore
School of Mechanical Engrg
Purdue University
1003 Chaffee Hall
West Lafayette IN 47907-1003
(317)494-1500
FAX:494-0530

Dr. Sol Gorland
NASA Lewis Research Center
21000 Brookpark Road
Mail Stop 60-4
Cleveland OH 44135
(216)977-7561
FAX:977-7500
sol.h.gorland@lerc.nasa.gov

Dr A D Gosman
Department of Mechanical Engrg
Imperial College of Science
and Technology
London WS7 2BX UK

Dr Larry Goss
Research Applications Division
Systems Research Labs, Inc.
2800 Indian Ripple Road
Dayton OH 45440-3696
(513)252-2706

Dr Richard Gould
Department of Mechanical and Aerospace Engineering
Box 7910
North Carolina State University
Raleigh NC 27695-7910
(919)515-5236
FAX:515-7968
gould@eos.ncsu.edu

Dr Frederick Gouldin
Department of Mechanical and
Aerospace Engineering
Cornell University
Ithaca NY 14853-5692
(607)255-5280

Dr F Grinstein
Laboratory for Computational
Physics & Fluid Dynamics
Naval Research Laboratory
Washington DC 20375-5344

Dr. Mark Gruber
AFRL/PR
1950 Fifth Street, Suite 10
Wright-Patterson AFB OH 45433-7251
(937)255-4141
FAX:656-4659
grubermr@possum.appl.wpafb.af.mil

Dr Ephraim Gutmark
Mechanical Engineering Dept
2508 CEBA
Louisiana State University
Baton Rouge LA 70803
(504)388-5899
FAX:388-5924
gutmark@me.lsu.edu

Dr. Mark A. Hagenmaier
AFRL/PR
Building 18
1950 Fifth Street, Suite 10
Wright-Patterson AFB OH 45433-7251
(937)255-5210
FAX:476-4659
hagenma@possum.appl.wpafb.af.mil

Dr. Robert B. Hall
SAF/AQRT
1060 Air Force Pentagon
Washington DC 20330-1060
(703)588-7802
(703)588-8388
hall@aqpo.hq.af.mil

Dr Robert D. Hancock
AFRL/PR
Building 490
1790 Loop Road, N
Wright-Patterson AFB OH 45433-7103
(937)255-7487
FAX:255-1125
hancockr@ward.appl.wpafb.af.mil

Dr Ronald Hanson
Mechanical Engineering Department
Stanford University
Building 530, Room 112
Stanford CA 94305-3030
(650)723-4023
FAX:725-4862
hanson@cdr.stanford.edu

Dr Stephen Harris
Physical Chemistry Department
General Motors Research Labs
30500 Mound Road
Warren MI 48090-9055
(313)986-1305

Dr D L Hartley
Sandia National Laboratories
MS0735
Albuquerque NM 87185-5800

Dr. Stephen D. Heister
Department of Aeronautics
and Astronautics
Purdue University
West Lafayette IN 47907-1282
(765)494-5126
FAX:494-0307
stephen.d.heister.1@purdue.edu

Dr Simon Henbest
Airframes & Engines Division
Aero & Maritime Research Lab
P O 4331
Melbourne, Victoria AUSTRALIA 3001
(03)647 7585
FAX:646 6771
henbests@aedmel.arl.dsto.gov.au

Dr. Naeim Henein
Department of Mechanical Engrg
Wayne State University
2121 Engineering Building
Detroit MI 48201
(313)577-3887
FAX:577-8789
henein@me1.eng.wayne.edu

Dr Cecil F. Hess
MetroLaser
18006 Skypark Circle
Suite 108
Irvine CA 92714-6428
(714)553-0688
FAX:553-0495

Dr L Hesselink
Department of Aeronautics and
Astronautics
Stanford University
Stanford CA 94305-3032
(650)723-3466

Dr E D Hirleman
Department of Mechanical and
Aerospace Engineering
Arizona State University
Tempe AZ 85287
(602)965-3895
FAX:965-1384

Mr Norman Hirsch
AFRL/PR
Wright-Patterson AFB OH 45433-6563
(937)255-2175

Dr David Hofeldt
125 Mechanical Engineering
111 Church Street, S E
University of Minnesota
Minneapolis MN 55455
(612)625-2045

Mr Robert Holland
United Technologies Chemical
Systems Division
P O Box 49028
San Jose CA 95161-9028
(408)224-7656

Dr Hans G Hornung
Graduate Aeronautical Labs
California Institute of
Technology
Pasadena CA 91125
(626)395-4551
hans@galcit.caltech.edu

Dr David Huestis
Molecular Physics
SRI International
333 Ravenswood Avenue
Menlo Park CA 94025-3493
(650)859-3464
FAX:859-6196
huestis@mp1vax.sri.com

Dr Lawrence Hunter
Applied Physics Laboratory
Johns Hopkins University
Johns Hopkins Road
Laurel MD 20707-6099
(301)953-5000

Dr A K M F Hussain
Mechanical Engineering Dept
4800 Calhoun Road
University of Houston
Houston TX 77204-4792
(713)743-4545
FAX:743-4503
mece1w@jetson.uh.edu

Dr Essam A Ibrahim
Department of Mechanical
Engineering
Tuskegee University
Tuskegee AL 36088
(205)727-8974
FAX:727-8090
emeei@acd.tusk.edu

Dr Thomas Ishii
Department of Electrical
Engineering
Marquette University
Milwaukee WI 53233
(414)288-6998
FAX:288-7082

Dr. Thomas Jackson
AFRL/PRSS
Building 490
1790 Loop Road North
Wright-Patterson AFB OH 45433-7103
(937)255-2175
FAX:656-4659
jacksota@wl.wpafb.af.mil

Dr. Joseph Janni
AFOSR/CC
110 Duncan Avenue, Suite B115
Bolling AFB DC 20332-8050
(202)767-5017
FAX:767-6213
janni@afosr.af.mil

Dr Jay Jeffries
SRI International
333 Ravenswood Avenue
Menlo Park CA 94025-3493
(650)859-6341
FAX:859-6196
jeffries@mp1vax.sri.com

Mr. Jeff Jensen
Kaiser-Marquardt
16555 Staycoy Street
Van Nuys CA 91406

Mr Gordon Jensen
United Technologies Chemical
Systems Division
P O Box 49028
San Jose CA 95161-9028
(408)365-5552

Dr. William Johnson
BKM, Inc.
5141 Santa Fe Street
San Diego CA 92109
(619)270-6760

Dr Sheridan Johnston
Combustion Sciences
Sandia National Laboratories
Livermore CA 94551-0969
(510)294-2138

Mr. Craig Johnston
Lockheed Advanced Dev. Company
Lockheed-Martin Corporation
1011 Lockheed Way
Palmdale CA 93599-7212

Dr K Kailasanath
Code 6410, LCP&FD
US Naval Research Laboratory
4555 Overlook Avenue, SW
Washington DC 20375-5344
(202)767-2402
FAX:767-4798
KAILASANATH@lcp.nrl.navy.mil

Dr Ann Karagozian
Department of Mechanical and
Aerospace Engineering
University of California, LA
Los Angeles CA 90095-1597
(310)825-5653
FAX:206-4830
ark@seas.ucla.edu

Dr Laurence R Keefe
Nielsen Engineering and
Research, Inc.
510 Clyde Avenue
Mountain View CA 94043-2287
(415)968-9457
FAX:968-1410

Dr Dennis Keefer
University of Tennessee
Space Institute
Gas Diagnostics Research Div.
Tullahoma TN 37388-8897
(615)455-0631

Dr Arnold Kelly
Department of Mechanical and
Aerospace Engineering
Princeton University
Princeton NJ 08544-5263
(609)258-5221

Dr John Kelly
Altex Technologies Corporation
650 Nuttman Road
Suite 114
Santa Clara CA 95054
(408)980-8610

Dr Lawrence A Kennedy
Department of Mechanical
Engineering
The Ohio State University
Columbus OH 43210-1107
(614)292-5782

Dr Ian Kennedy
Mechanical & Aero Engrg
University of California,
Davis
Davis CA 95616-5294
(916)752-2796
FAX:752-4158
IMKENNEDY@ucdavis.edu

Dr James Kezerle
Gas Research Institute
8600 West Bryn Mawr Avenue
Chicago IL 60631
(312)399-8331

Dr G B King
Department of Mechanical
Engineering
Purdue University
West Lafayette IN 47907-1288
(765)494-6518
kinggb@ecn.purdue.edu

Dr Merrill K King
NASA Headquarters
Code SNB
300 E Street, SW
Washington DC 20546
(202)358-0818

Dr William H Kirchhoff
Division of Chemical Sciences
Office of Basic Energy Science
Department of Energy
Washington DC 20585
(301)903-5820
william.kirchhoff%er@mailgw.er.doe.gov

Dr. David E. Klett
Mechanical Engineering Dept
North Carolina Agricultural
and Technical State Univ
Greensboro IG 27401-3209

Dr Charles Kolb
Aerodyne Research, Inc.
45 Manning Road
Manning Park Research Center
Billerica MA 01821-3976
(508)663-9500
FAX:663-4918

Dr Wolfgang Kollmann
Mechanical & Aerospace Engrg
University of California,
Davis
Davis CA 95616-5295
(916)752-4152
FAX:752-4158
wkollmann@ucdavis.edu

Dr George Kosaly
Mechanical Engineering Dept
University of Washington
Box 352600
Seattle WA 98195-2600
(206)543-6933
FAX:685-8047
kosaly@u.washington.edu

Mr David Kruczynski
Attn SLCBR-IBA
Interior Ballistics Division
Army Research Laboratory
Aberdeen Proving Gnd MD 21005-5066
(410)278-6202

Dr Kenneth Kuo
Department of Mechanical
Engineering
Pennsylvania State University
University Park PA 16802
(814)865-6741
FAX:863-3203

Dr. Ming-Chia Lai
Department of Mechanical Engrg
Wayne State University
Detroit MI 48202

Dr Marshall Lapp
High Temperature Interfaces
Division
Sandia National Laboratories
Livermore CA 94551-0969
(510)294-2435

Dr John Larue
Department of Mechanical
Engineering
University of California
Irvine CA 92717

Dr A Laufer
Office of Energy Research
U. S. Department of Energy
1000 Independence Avenue, N.W.
Washington DC 20585
(202)903-5820
allan.laufer%er@mailgw.er.doe.gov

Dr Normand Laurendeau
Department of Mechanical
Engineering
Purdue University
West Lafayette IN 47907-1288
(765)494-2713
Laurende@ecn.purdue.edu

Dr Moshe Lavid
ML Energia, Inc.
P. O. Box 1468
Princeton NJ 08540
(609)799-7970

Dr C K Law
Department of Mechanical and
Aerospace Engineering
Princeton University
Princeton NJ 08544-5263
(609)258-5271
FAX:258-6233
cklaw@princeton.edu

Dr C C Lee
Environmental Protection
Agency
Cincinnati OH 45268
(513)569-7520

Dr Spiro Lekoudis
Office of Naval Research
Mechanics Division, Code 432
800 North Quincy Street
Arlington VA 22217-5660
(703)696-4403

Dr Anthony Leonard
Graduate Aeronautical Labs
California Institute of
Technology
Pasadena CA 91125
(626)395-4465

Dr Deborah Levin
Department of Chemistry
George Washington University
Washington DC 20013

Dr Jay Levine
AFRL/PR
10 East Saturn Boulevard
Edwards AFB CA 93524-7600
(805)275-6179
FAX:275-6233
levine@plablink.ple.af.mil

Dr Chiping Li
Naval Research Laboratory
Code 6910, CCP&FD
Washington DC 20375-5344
(202)767-3254
FAX:767-4078
LI@lcp.nrl.navy.mil

Dr Goang Liaw
Department of Civil Engineering
Alabama A&M University
PO Box 367
Normal AL 35762
(205)851-5565

Dr Paul Libby
Department of AMES 0310
9500 Gilman Drive
University of California
La Jolla CA 92093-0310
(619)534-3168
FAX:534-4543
libby@ames.ucsd.edu

Dr Wilbert Lick
Department of Mechanical and
Environmental Engineering
University of California
Santa Barbara CA 93106

Dr Hans Liepmann
Graduate Aeronautical Labs
California Institute of
Technology
Pasadena CA 91125
(626)395-4535

Dr. Charles L. Liotta
Department of Chemical Engrg
Georgia Institute of
Technology
Atlanta GA 30332-0100
(404)853-9344
FAX:894-6956

Dr Marshall Long
Mechanical Engineering Department
Yale University
PO Box 208284
New Haven CT 06520
(203)432-4229
FAX:432-6775
Marshall_Long@qm.yale.edu

Dr Lyle N Long
Department of Aerospace Engrg
233 Hammond Building
Pennsylvania State University
University Park PA 16802
(814)865-1172
FAX:865-7092
lnl@psu.edu

Dr F E Lytle
Department of Chemistry
Purdue University
West Lafayette IN 47907
(765)494-5261

Dr Bruce MacDonald
Research Applications Division
Systems Research Labs, Inc.
2800 Indian Ripple Road
Dayton OH 45440-3696
(513)252-2706

Dr Edward Mahefkey
AFRL/PR
Wright-Patterson AFB OH 45433-6563
(937)255-6241

Mr Nick Makris
SA-ALC/SFT
Kelly AFB TX 78241-5000
AV945-8212
FAX:945-9964

Dr David Mann
U. S. Army Research Office
P. O. Box 12211
4300 South Miami Boulevard
Research Triangle Pk NC 27709-2211
(919)549-4249
FAX:549-4310
dmann@aro-emh1.army.mil

Dr Nagi Mansour
Computational Fluid Mechanics
Branch, RFT 202A-1
NASA Ames Research Center
Moffett Field CA 94035
(415)604-6420

Dr Frank Marble
Engrg. and Appl. Sci. Dept.
California Institute of
Technology
Pasadena CA 91125
(626)395-4784
marble@cco.caltech.edu

Dr John Marek
NASA Lewis Research Center
Mail Stop 5-11
21000 Brookpark Road
Cleveland OH 44135-3127
(216)433-3584
FAX:433-3000
cecil.j.marek@lerc.nasa.gov

Dr. Jay Martin
University of Wisconsin-Madison
Engine Research Center
1500 Engineering Drive
Madison WI 53706
(608)263-9460
FAX:262-6707
martin@engr.wisc.edu

Dr James McDonald
Code 6110
Naval Research Laboratory
Chemistry Division
Washington DC 20375-5342
(202)767-3340

Dr D K McLaughlin
233 Hammond Building
Pennsylvania State University
University Park PA 16802
(814)865-2569

Dr Keith McManus
Physical Sciences, Inc
20 New England Business Center
Andover MA 01810
(508)689-0003
FAX:689-3232

Dr Constantine M Megaridis
University of Illinois-Chicago
Mechanical Engineering Dept
842 West Taylor Street
Chicago IL 60607-7022
(312)996-3436
FAX: 413-0447
cmm@dino.me.uic.edu

Dr Mehran Mehregany
Department of Electrical Engineering
Case Western Reserve University
10900 Euclid Avenue
Cleveland OH 44106-7221

Dr A M Mellor
Mech & Matls Engrg Dept
512 Kirkland Hall
Vanderbilt University
Nashville TN 37240
(615)343-6214
FAX:343-6687

Dr Lynn Melton
Programs in Chemistry
University of Texas, Dallas
P. O. Box 830688
Richardson TX 75080-0688
(972)883-2913
FAX:883-2925
melton@utdallas.edu

Dr R Metcalfe
Department of Mechanical
Engineering
University of Houston
Houston TX 77004
(713)749-2439

Dr Michael M Micci
Department of Aerospace Engrg
233 Hammond Building
Pennsylvania State University
University Park PA 16802
(814)863-0043
FAX:865-7092
micci@henry2.aero.psu.edu

Dr Richard Miller
Office of Naval Research
Mechanics Division, Code 432
800 North Quincy Street
Arlington VA 22217-5660
(703)696-4404
FAX:696-0934
millerr@onr.navy.mil

Dr Andrzej Miziolek
Ignition and Combustion Branch
Interior Ballistics Division
Army Research Laboratory
Aberdeen Proving Gnd MD 21005-5066
(410)278-6157
FAX:278-6094

Dr Parviz Moin
Center for Turbulence Research
Stanford University
Stanford CA 94305-3032
(650)725-2081

Dr H. C. Mongia
Manager, Combustion Technology
GE Aircraft Engines
One Neumann Way, M/D A404
Cincinnati OH 45215-6301
(513)243-2552
FAX:243-2538

Dr P J Morris
233-L Hammond Building
Pennsylvania State University
University Park PA 16802
(814)863-0157

Dr Edward Mularz
Attn: AMSRL-VP-C
NASA Lewis Res. Ctr., MS 77-12
21000 Brookpark Road
Cleveland OH 44135-3191
(216)433-5850
FAX:433-3720
Edward.Mularz@lerc.nasa.gov

Dr M G Mungal
Department of Mechanical
Engineering
Stanford University
Stanford CA 94305-3032
(650)725-2019
FAX:723-1748
mungal@leland.stanford.edu

Dr Phillip E Muntz
Department of Aerospace Engrg
Univ of Southern California
854 West 36th Place, RRB 101
Los Angeles CA 90089-1191
(213)740-5366

Dr Arje Nachman
AFOSR/NM
110 Duncan Avenue, Suite B115
Bolling AFB DC 20332-8050
(202)767-5028
FAX:404-7496
arje.nachman@afosr.af.mil

Dr Herbert Nelson
Code 6110, Chemistry Division
Naval Research Laboratory
4555 Overlook Avenue, SW
Washington DC 20375-5342
(202)767-3686

Dr David Nixon
NWING, Inc.
883 North Shoreline Boulevard
Suite B200
Mountain View CA 94043
(415)254-0202
FAX961-9286

Dr G B Northam
NASA Langley Research Center
MS 188B
Hampton VA 23681
(804)864-6248
g.b.northam@larc.nasa.gov

Dr Michael Nusca
AMSRL-WT-PC
US Army Research Laboratory
Aberdeen Proving Ground MD 21005-5066
(410)278-6108
FAX: 278-7333
nusca@arl.army.mil

Dr A K Oppenheim
Department of Mechanical
Engineering
University of California
Berkeley CA 94720
(415)642-0211

Dr Elaine Oran
LCP&FD, Code 6404
US Naval Research Laboratory
4555 Overlook Avenue, SW
Washington DC 20375-5344
(202)767-2960
FAX:767-4798
ORAN@lcp.nrl.navy.mil

Dr T E Parker
Engineering Division
Colorado School of Mines
Golden CO 80401-1887
(303)273-3657
FAX:273-3602
tparker@mines.colorado.edu

Dr Timothy Parr
Naval Air Warfare Center
Weapons Division
C02392
China Lake CA 93555-6001
(760)939-3367
FAX:939-6569
t.parr@genie.geis.com

Lt. John S. Paschkewitz
AFRL/VAVE
Building 45 Annex
2130 Eighth Street, Suite 1
Wright-Patterson AFB OH 45433-7542
(937)255-4640
FAX:656-7915
paschkjs@wl.wpafb.af.mil

Dr Phillip H. Paul
MS 9051
Sandia National Laboratories
P. O. Box 969
Livermore CA 94551-9051
(510)294-1465
FAX: 294-1012
phpaul@sandia.gov

Dr Alex Pechenik
AFOSR/NA
110 Duncan Avenue, Suite B115
Bolling AFB DC 20332-8050
(202)767-4962
FAX:767-4988
alex.pechenik@afosr.af.mil

Dr S S Penner
Center for Energy and
Combustion Research, 0411
University of California
La Jolla CA 92093-0411
(619)534-4284

Dr Richard Peterson
Department of Mechanical
Engineering
Oregon State University
Corvallis OR 97331-6001
(503)754-2567

Dr Lisa Pfefferle
Department of Chemical
Engineering
Yale University
New Haven CT 06520-8286
(203)432-2222
FAX:432-7232
pfefferle@htcre.eng.yale.edu

Dr Emil Pfender
Department of Mechanical Engrg
125 Mechanical Engineering
The University of Minnesota
Minneapolis MN 55455

Dr W M Pitts
National Institute of
Standards and Technology
Center for Fire Research
Gaithersburg MD 20899
(301)975-6486

Dr Robert Pitz
Department of Mechanical and
Materials Engineering
Vanderbilt University
Nashville TN 37235
(615)322-0209
FAX:343-8730
pitzrw@ctrvan.vanderbilt.edu

Dr S B Pope
Department of Mechanical and
Aerospace Engineering
Cornell University
Ithaca NY 14853-7501
(607)255-4314
FAX;255-1222
pope@mae.cornell.edu

Dr David Pratt
AFRL/VAVE
Building 45 Annex
2130 Eighth Street, Suite 1
Wright-Patterson AFB OH 45433-7542
(937)255-4640
FAX:656-7915
prattdm@wl.wpafb.af.mil

Dr C L Proctor II
Department of Mechanical
Engineering
University of Florida
Gainesville FL 32611
(904)392-7555

Dr Herschel Rabitz
Department of Chemistry
Princeton University
Princeton NJ 08544-1009
(609)258-3917
FAX:258-6746

Dr Larry Rahn
Sandia National Laboratories
7011 East Avenue
Mail Stop 9056
Livermore CA 94551-0969
(510)294-2091
FAX: 294-2276
rahn@sandia.gov

Dr S R Ray
National Institute of
Standards and Technology
Center for Chemical Engrg
Gaithersburg MD 20899

Dr Mohan K. Razdan
Allison Engine Company
P.O. Box 420
Speed Code T-14
Indianapolis IN 46206-0420
(317)230-6404
FAX:230-3691
iemkr@agt.gmeds.com

Mr Robert Reed
Sverdrup Technology, Inc.
AEDC
1099 Avenue C
Arnold AFB TN 37389-9013
(615)454-4648
(615)454-6317

Dr R G Rehm
National Institute of
Standards and Technology
Center for Fire Research
Gaithersburg MD 20899
(301)975-2704

Dr Rolf D Reitz
Mechanical Engineering Dept
University of Wisconsin
1500 Johnson Drive
Madison WI 53706
(608)262-0145
FAX:262-6717

Dr M Renksizbulut
Department of Mechanical
Engineering
University of Waterloo
Waterloo, Ontario CN N2L 3G1
(519)885-1211

Dr Eli Reshotko
Case Western Reserve Univ
Department of Mechanical and
Aerospace Engineering
Cleveland OH 44106
(216)368-6447
FAX:368-6445
exr3@po.cwru.edu

Dr David Reuss
Fluid Mechanics Department
General Motors Research Labs
30500 Mound Road
Warren MI 48090-9055
(313)986-0029

Dr William Reynolds
Department of Mechanical
Engineering
Stanford University
Stanford CA 94305-3032
(650)723-3840

Dr Kyung T. Rhee
Department of Mechanical and
Aerospace Engineering
Rutgers, The State Univ of NJ
Piscataway NJ 08854

Dr James Riley
Mechanical Engineering Dept
University of Washington
Seattle WA 98195
(206)543-5347
73671.737@Compuserve.com

Dr William Roberts
Department of Mechanical and Aerospace Engineering
Box 7910
North Carolina State University
Raleigh NC 27695-7910
(919)515-5294
FAX:515-7968
wrobert@eos.ncsu.edu

Dr Michael Roco
National Science Foundation
Chemical and Thermal Syst Div
4201 Wilson Boulevard
Arlington VA 22230
mroco@nsf.gov

Mr Wayne Roe
AFRL/PR
5 Pollux Drive
Edwards AFB CA 93523-5000
(805)275-5206
FAX:275-5852

Mr Gerald A. Roffe
GASL
77 Raynor Avenue
Ronkonkoma NY 11779

Dr Won B Roh
Department of Engrg Physics
Air Force Institute of
Technology
Wright-Patterson AFB OH 45433-6583

Dr U S Rohatgi
Department of Nuclear Energy
Brookhaven National Laboratory
Upton NY 11973
(516)282-2475

Dr Glenn Rolader
Science Applications
International Corporation
1247-B N Eglin Parkway
Shalimar FL 32579
DSN 872-0391

Dr W M Roquemore
AFRL/PRSC
Building 490
1790 Loop Road, N
Wright-Patterson AFB OH 45433-7103
(937)255-6813
FAX:255-1125
melr@ward.appl.wpafb.af.mil

Dr Anatol Roshko
Graduate Aeronautical Labs
California Institute of
Technology
Pasadena CA 91125
(626)395-4484

Dr Daniel Rosner
Department of Chemical
Engineering
Yale University
New Haven CT 06520-8286
(203)432-4391
FAX:432-7232
rosner@htcre.eng.yale.edu

Dr John Ross
Department of Chemistry
Stanford University
Stanford CA 94305-3032
(650)723-9203

Dr Gabriel Roy
Office of Naval Research
Mechanics Division, Code 1132
800 North Quincy Street
Arlington VA 22217-5660
(703)696-4406
FAX:696-2558
royg@onr.navy.mil

Mr Kurt Sacksteder
NASA Lewis Research Center
MS 500-217
21000 Brookpark Road
Cleveland OH 44135
(216)433-2857

Dr Michael Salkind
President
Ohio Aerospace Institute
22800 Cedar Point Road
Cleveland OH 44142
(216)962-3001
FAX:962-3120
MichaelSalkind@oai.org

Dr Mohammad Samimy
Ohio State University
Mechanical Engineering Dept
206 West 18th Street
Columbus OH 43210-1107
(614)422-6988
FAX:292-3163
msamimy@magnus.acs.ohio-state.edu

Dr G S Samuelsen
Department of Mechanical
Engineering
University of California
Irvine CA 92717
(714)856-5468

Dr Billy Sanders
University of California
Davis CA 95616

Dr Joseph Sangiovanni
United Technologies Research
Center
Silver Lane
East Hartford CT 06108
(860)610-7328

Dr Lakshmi Sankar
School of Aerospace Engrg
Georgia Institute of
Technology
Atlanta GA 30332
(404)894-3014

Dr Domenic Santavicca
Propulsion Engineering Research Center
Pennsylvania State University
106 Research Building East - Bigler Road
University Park PA 16802-2320
(814)863-1863

Dr R J Santoro
Department of Mechanical
Engineering
Pennsylvania State University
University Park PA 16802-2320
(814)863-1285
FAX:865-3389
rjs2@email.psu.edu

Dr Sutanu Sarkar
Department of Applied Mech
and Engr Science, MC 0411
University of California
La Jolla CA 92093-0411
(619)534-8243
FAX: 534-7599
sarkar@ames.ucsd.edu

Mr William Scallion
NASA Langley Research Center
Mail Stop 408
Hampton VA 23665
(804)864-5235

Dr Klaus Schadow
Naval Air Warfare Center
Code 3892
China Lake CA 93555-6001
(760)939-6532
FAX:939-6569
klaus_schadow@imdgw.chinalake.navy.mil

Dr John Schaefer
Energy and Environmental Div.
Acurex Corporation
555 Clyde Ave., P. O. Box 7555
Mountain View CA 94039

Dr W H Schofield
Aeronautical Research Labs
506 Lorimer St, Fishermen's Bn
Box 4331, P O
Melbourne, Victoria AUSTRALIA 3001

Maj Scott Schreck
AFOSR/NM
110 Duncan Avenue, Suite B115
Bolling AFB DC 20332-8050
(202)767-5028
FAX:404-7496
scott.schreck@afosr.af.mil

Dr Ernest Schwarz
Propulsion Systems Division
ATTN: DRSTA-RGD
USA Tank-Automotive Command
Warren MI 48397-5000

Mr Lee Scuderi
McDonnell Douglas Aerospace
P.O. Box 516
St. Louis MO 63166-0516

Dr D J Seery
United Technologies Research
Center
Silver Lane
East Hartford CT 06108

Dr Corin Segal
AeMES Department
University of Florida
P.O. Box 116250
Gainesville FL 32611-6250
(352)392-6132
FAX:392-7303
cor@AeMES.aero.ufl.edu

Dr Balu Sekar
AFRL/PRSC
Building 490
1790 Loop Road North
Wright-Patterson AFB OH 45433-7103
(937)255-5974
FAX: 255-2660
sekarb@possum.appl.wpafb.af.mil

Dr Hratch Semerjian
National Institute of
Standards and Technology
Chem Sci & Tech Laboratory
Gaithersburg MD 20899
(301)975-3145
FAX:975-3845
HRATCH@micf.nist.gov

Dr Robert V. Serauskas
Gas Research Institute
8600 West Bryn Mawr Avenue
Chicago IL 60631
(312)399-8208
FAX:864-2774
rserausk@gri.org

Dr Kalyanasundaram Seshadri
Center for Energy and
Combustion Research, 0407
University of California
La Jolla CA 92093-0407
(619)534-4876

Dr G S Settles
309 Mechanical Engrg Building
Pennsylvania State University
University Park PA 16802
(814)863-1504

Dr Robert Shaw
Division of Chemical and
Biological Sciences
U S Army Research Office
Research Triangle Park NC 27709-2211
(919)549-0641

Dr Adam Siebenhaar
Aerojet Propulsion Division
P.O. Box 13222
Sacramento CA 95813-6000

Mr David Siegel
Chief of Naval Research,
804 BCT1
800 North Quincy Street
Arlington VA 22217-5660
(703)696-4771
FAX:696-4274

Dr William Sirignano
Department of Mechanical and
Aerospace Engineering
University of California
Irvine CA 92717-3975
(714)824-3700
FAX:824-3773
sirignan@uci.edu

Dr Gregory Smith
Department of Chem Kinetics
SRI International
333 Ravenswood Avenue
Menlo Park CA 94025-3493
(415)859-3496

Mr Davey Smith
Northrop Grumman Corporation
B-2 Division Dayton Office
2850 Presidential Dr., Ste 100
Fairborn OH 45324

Dr Kenneth A. Smith
Department of Chemical Engrg.
Room 66-540
Massachusetts Inst. Of Technology
Cambridge MA 02139
(617)253-1973
FAX:253-2701
kas@mit.edu

Dr Alan Stanton
Southwest Sciences, Inc.
1570 Pacheco Street
Suite E-11
Santa Fe NM 87501
(505)984-1322

Dr F Dee Stevenson
Office of Basic Energy Science
U. S. Department of Energy
1000 Independence Avenue, N W
Washington DC 20585

Dr David Stewart
Department of Theoretical and
Applied Mechanics
University of Illinois
Urbana IL 61801

Dr Anthony Strawa
NASA Ames Research Center
MS 230-2
Moffett Field CA 94035
(415)604-3437

Dr Robert M. Stubbs
Mail Stop 5-11
NASA Lewis Research Center
21000 Brookpark Road
Cleveland OH 44135-3127
(216)433-6303
FAX:433-5802
rstubbs@lerc.nasa.gov

Dr Geoffrey J Sturgess
Innovative Scientific Solutions
2786 Indian Ripple Road
Dayton OH 45440-3638
(513)252-2706
FAX:056-4652
gsturgess@aol.com

Dr B Sturtevant
Engrg and Appl Sci Dept
California Institute of
Technology
Pasadena CA 91125

Dr G Sullins
Applied Physics Laboratory
Johns Hopkins University
Johns Hopkins Road
Laurel MD 20707-6099
(301)953-5000

Dr Larry Talbot
Department of Mechanical
Engineering
University of California
Berkeley CA 94720
(415)642-6780

Dr Douglas Talley
AFRL/PR
9 Antares Road
Edwards AFB CA 93524-7660
(805)275-6174

Dr Richard Tankin
Mechanical Engineering Dept
Northwestern University
Evanston IL 60208-3111
(847)491-3532
FAX:491-3915

Dr Jefferson W. Tester
M.I.T. Energy Laboratory
Room E40-455
Massachusetts Inst. Of Technology
Cambridge MA 02139
(617)253-3401
FAX:253-8013
testerel@mit.edu

Dr Julian Tishkoff
AFOSR/NA
110 Duncan Avenue, Suite B115
Bolling AFB DC 20332-8050
(202)767-0465
FAX:767-4988
julian.tishkoff@afosr.af.mil

Dr T Y Toong
Department of Mechanical
Engineering
MIT
Cambridge MA 02139
(617)253-3358

Dr Michael Trenary
Department of Chemistry
The University of Illinois
Chicago IL 60680

Dr Robert J Trew
Director for Research
Defense Research & Engineering
3040 Defense Pentagon
Washington DC 20301-3040

Dr James Trolinger
MetroLaser
18006 Skypark Circle
Suite 108
Irvine CA 92714-6428
(714)553-0688
FAX:553-0495
jtrolinger@vmsa.oac.uci.edu

Dr Timothy Troutt
Department of Mechanical
Engineering
Washington State University
Pullman WA 99164-2920

Dr Gretar Tryggvason
Dept of Mech Engrg & Appl Mech
2350 Hayward, Room 2250
The University of Michigan
Ann Arbor MI 48109-2125
(734)763-1049
FAX:764-4256
gretar@umich.edu

Dr Allen Twarowski
Rockwell International Sci Ctr
1049 Camino dos Rios
P O Box 1085
Thousand Oaks CA 91360
(805)373-4576
FAX:373-4775
ajtwarow@scimail.remnet.rockwell.com

Dr C J Ultee
United Technologies Research
Center
Silver Lane
East Hartford CT 06108

Dr A D Vakili
University of Tennessee
Space Institute
Tullahoma TN 37388

Dr John Vanderhoff
Ballistic Research Laboratory
DRSMC-BLI(A)
Aberdeen Proving Ground MD 21005
(410)278-6642

Dr S P Vanka
Department of Mechanical
and Industrial Engrg
University of Illinois
Urbana IL 61801

Dr James Verdieck
Rockwell International
Rocketdyne Div, M/S FA26
6633 Canoga Avenue
Canoga Park CA 91303
(818)700-4709

Dr Juan A. Vitali
AFRL/VA (Stop 37)
139 Barnes Drive, Suite 2
Tyndall AFB FL 32403-5323
(904)283-9708
FAX:283-9707
75023.56@compuserve.com

Dr Robert Vondra
PO Box 596
Wrightwood CA 92397
(619)249-3451

Dr P J Waltrup
Applied Physics Laboratory
Johns Hopkins University
Johns Hopkins Road
Laurel MD 20707-6099
(301)953-5000

Dr Joe Wanders
AFRL/MLQ
139 Barnes Drive
Tyndall AFB FL 32403-5319
(904)283-6026

Dr Charles Westbrook
Lawrence Livermore National
Laboratories
P. O. Box 808
Livermore CA 94550

Dr Phillip R. Westmoreland
Department of Chemical
Engineering
University of Massachusetts
Amherst MA 01003
(413)545-1750
(413)545-1647
westm@ecs.umass.edu

Dr James Whitelaw
Department of Mechanical Engrg
Imperial College of Science
and Technology
London SW7 2BX UK

Dr Forman Williams
Center for Energy and
Combustion Research, 0310
University of California
La Jolla CA 92093-0310
(619)534-5492
FAX: 534-5354
faw@ames.ucsd.edu

Dr Michael Winter
United Technologies Research
Center
411 Silver Lane, MS/90
East Hartford CT 06108
(860)610-7805
FAX:610-7911
mw@utrc.utc.com

Mr Steve Wirick
WL/AAWW-3
Wright-Patterson AFB OH 45433-6543
(937)255-4174
FAX:476-4642

Dr Bernard T Wolfson
Wolfson Associates
International
4797 Lake Valencia Blvd West
Palm Harbor FL 33563
(813)786-3007

Dr Joda Wormhoudt
Aerodyne Research, Inc.
45 Manning Road
Manning Park Research Center
Billerica MA 01821-3976
(508)663-9500
FAX:663-4918

Dr J M Wu
University of Tennessee
Space Institute
Tullahoma TN 37388

Dr Vigor Yang
Propulsion Engrg Rsrch Ctr
The Pennsylvania State Univ
111 Research Building East
University Park PA 16802-2320
(814)863-1502
FAX: 865-4784
vigor@arthur.psu.edu

Dr Yaw Yeboah
Engineering Department
Clark Atlanta University
223 James P Brawley Drive, SW
Atlanta GA 30314
(404)880-6619
FAX: 880-6615
yyeboah@cau.edu

Dr Richard Yetter
Department of Mechanical and
Aerospace Engineering
Princeton University
Princeton NJ 08544-5263
(609)258-2947
FAX:258-1939
rich@dante.princeton.edu

Dr Pui-kuen Yeung
School of Aerospace Engrg
Georgia Institute of
Technology
Atlanta GA 30332-0150
(404)894-9341
FAX:894-2760
yeung@peach.gatech.edu

Dr Shaye Yungster
Institute for Computational
Mechanics in Propulsion
NASA Lewis Research Ctr
Cleveland OH 44135
(216)433-6680

Dr Michael Zachariah
National Institute of
Standards and Technology
Center for Chemical Engrg
Gaithersburg MD 20899
(301)975-2063

Mr Fred Zarlingo
Code 3246
Naval Air Warfare Center
China Lake CA 93555-6001
(760)939-7395

Dr Ben Zinn
School of Aerospace Engineering
Georgia Institute of Technology
Atlanta GA 30332-0150
(404)894-3033
FAX:894-2760
ben.zinn@aerospace.gatech.edu